Dark Energy Tomography with the Euclid survey

Lisa Goh

université PARIS-SACLAY

Dark Energy Tomography with the *Euclid* survey

Tomographie de l'énergie sombre avec le satellite Euclid

Thèse de doctorat de l'université Paris-Saclay

École doctorale n° 127 : astronomie et astrophysique d'Île-de-France (AAIF)
Spécialité de doctorat : Astronomie et Astrophysique
Graduate School : Physique. Référent : Faculté des sciences d'Orsay

Thèse préparée dans l'unité de recherche **Astrophysique, Instrumentation et Modélisation de Paris-Saclay (Université Paris-Saclay, CNRS, CEA)**, sous la direction de **Valeria PETTORINO**, directrice de recherche, et la co-direction de **Martin KILBINGER**, directeur de recherche

Thèse soutenue à Paris-Saclay, le 07 octobre 2024, par

Lisa GOH

Composition du jury

Membres du jury avec voix délibérative

Filippo VERNIZZI Professeur, Université Paris-Saclay	Président
Mme Alkistis POURTSIDOU Professeure, University of Edinburgh	Rapporteure & Examinatrice
Martin KUNZ Professeur, Université de Genève	Rapporteur & Examinateur
Silvia GALLI Chargée de Recherche, Sorbonne Université	Examinatrice
Isaac TUTUSAUS Astronome Adjoint, Université de Toulouse	Examinateur
Alessandra SILVESTRI Professeure Associée, Universiteit Leiden	Examinatrice

THESE DE DOCTORAT
NNT : 2024UPASP091

université PARIS-SACLAY

ÉCOLE DOCTORALE
Astronomie
et Astrophysique
d'Île-de-France (AAIF)

Title : Dark Energy Tomography with the *Euclid* survey
Keywords : Dark energy, Weak lensing, Beyond-ΛCDM
Abstract :

The current ΛCDM concordance model has been widely successful in describing our Universe. However, crucial questions remain unanswered and are becoming increasingly critical with the continuous release of high-precision cosmological data. This has led to the exploration of modified ΛCDM models, one of them being the Coupled Dark Energy (CDE) model, whereby dark matter particles feel a force stronger than gravity, due to the fifth force mediated by a scalar field which plays the role of dark energy.
In my thesis, I introduce a new parametrisation of the CDE model where the coupling strength between the dark matter particles and the scalar field is allowed to evolve with redshift. To probe such a tomographic CDE model, I employ high redshift Cosmic Microwave Background (CMB) data from Planck, ACT and SPT, and a range of low redshift probes including, for the first time, Large Scale Structure (LSS) data from weak lensing, galaxy clustering, and their cross-correlation galaxy-galaxy lensing. I find that LSS data allows us to recover tight constraints on coupling at low redshifts, comparable to that obtained with highly precise CMB data, making it a promising probe to test CDE models at low redshifts.
I go on to develop other applications of the tomographic CDE model, such as investigations on an early coupled quintessence model whereby coupling is only activated during the radiation-dominated era, and constrain such a phenomenological model with observational data for the first time. I also explore whether deep learning techniques such as neural networks can differentiate between LSS data generated from a ΛCDM model and a tomographic CDE model.
Finally, I turn my attention to current stage IV galaxy surveys such as *Euclid*, which will map the LSS of the Universe and provide weak lensing and galaxy clustering data of unprecedented accuracy and precision. Within the consortium, I contribute to developing the official *Euclid* likelihood code, with the ultimate aim of obtaining constraints on extended ΛCDM models with *Euclid* data. I have also worked on developing the cosmic shear inference pipeline for UNIONS, a ground-based photometric galaxy survey in the northern hemisphere that will also complement *Euclid* observations. These LSS surveys thus usher in an exciting era of precision cosmology, allowing us to increase our understanding of the Universe and potentially uncover hints of new physics.

Titre : Tomographie de l'énergie sombre avec le satellite *Euclid*
Mots clés : Energie sombre, lentille gravitationelle faible, Au-delà de ΛCDM
Résumé :

Le modèle de concordance actuel, ΛCDM, a largement réussi à décrire notre Univers. Cependant, des questions cruciales restent sans réponse et deviennent de plus en plus critiques avec la publication continue de données cosmologiques de haute précision. Cela a conduit à l'exploration de modèles ΛCDM modifiés, parmi lesquels figure le modèle de l'énergie noire couplée, dans lequel les particules de matière noire sont sujettes à une force plus importante que la force gravitationnelle, en raison d'une cinquième force générée par un champ scalaire qui joue le rôle de l'énergie noire.

Dans ma thèse, j'introduis une nouvelle paramétrisation du modèle de l'énergie noire couplée où la force de couplage entre les particules de matière noire et le champ scalaire est autorisée à évoluer avec le décalage vers le rouge. Pour sonder un tel modèle de l'énergie noire couplée tomographique, j'utilise des données du fond diffus cosmologique à haut décalage vers le rouge provenant de Planck, ACT et SPT, ainsi qu'une gamme de sondes à bas décalage vers le rouge incluant, pour la première fois, des données de la structure à grande échelle issues de la lentille gravitationnelle faible, de l'agglomération des galaxies, et de leur corrélation croisée. Je constate que les données de la structure à grande échelle nous permettent d'obtenir des contraintes importantes sur le couplage à bas décalages vers le rouge, comparables à celles obtenues avec des données très précises du fonds diffus cosmologique, ce qui en fait une sonde prometteuse pour tester les modèles de l'énergie noire couplée à bas décalages vers le rouge.
Je développe ensuite d'autres applications du modèle de l'énergie noire couplée tomographique, comme un modèle de quintessence couplée précoce où le couplage n'est activé que pendant l'ère dominée par le rayonnement, et je contrains un tel modèle phénoménologique avec des données observationnelles pour la première fois. J'explore également des techniques d'apprentissage profond telles que les réseaux neuronaux, pour tester si elles peuvent différencier les données de la structure à grande échelle générées à partir d'un modèle ΛCDM et d'un modèle de l'énergie noire couplée tomographique.
Enfin, nous tournons notre attention vers les relevés actuels de galaxies de stage IV, tels que *Euclid*, qui realiseront une cartographie de la structure à grande échelle de l'Univers et fourniront des données de lentille gravitationnelle faible et d'agglomération des galaxies d'une précision sans précédent. Au sein du consortium, je contribue au développement du code de vraisemblance officiel *Euclid*, avec pour objectif final d'obtenir des contraintes sur les modèles ΛCDM étendus avec les données *Euclid*. J'ai également travaillé sur le développement de la chaîne de traitement pour l'inférence à partir de cisaillement cosmique pour UNIONS, un relevé photométrique de galaxies au sol dans l'hémisphère nord qui complétera également les observations *Euclid*. Ces relevés des structures à grande échelle inaugurent ainsi une ère passionnante de cosmologie de précision, nous permettant d'accroître notre compréhension de l'Univers et de potentiellement découvrir des indices de nouvelles physiques.

Acknowledgements

Since no one really reads this anyway, I shall keep this short and sweet.

Firstly, thank you to the members of my jury for agreeing to be on my jury, and for reading my thesis.

I would like to thank my supervisors Valeria Pettorino and Martin Kilbinger, for their guidance and support these past 3 years. Thank you to all the members of ComoStat for making my PhD journey such an enriching one (you know who you are). Thank you also to all the friends in France, London, Singapore, my family, and all the people I have crossed paths with in my life who have made me who I am today.

And finally, I would like to borrow the words of the man, the legend, Snoop Dogg himself :

"Last but not least, I wanna thank me
I wanna thank me for believing in me
I wanna thank me for doing all this hard work
I wanna thank me for having no days off
I wanna thank me for, for never quitting
I wanna thank me for always being a giver
And tryna give more than I receive
I wanna thank me for tryna do more right than wrong
I wanna thank me for just being me at all times."

Thank you Lisa, for completing this PhD. 17 year old you would be proud of you.

Acknowledgements for computing resources and data

Part of this work was carried out using the Feynman cluster of the Institut de recherche sur les lois fondamentales de l'Univers (Irfu) at CEA Paris-Saclay.

Part of this work was made possible by utilising the CANDIDE cluster at the Institut d'Astrophysique de Paris. The cluster was funded through grants from the PNCG, CNES, DIM-ACAV, the *Euclid* Consortium, and the Danish National Research Foundation Cosmic Dawn Center (DNRF140). It is maintained by Stephane Rouberol.

Part of this work is based on data obtained as part of the Canada-France Imaging Survey, a CFHT large program of the National Research Council of Canada and the French Centre National de la Recherche Scientifique. Based on observations obtained with MegaPrime/MegaCam, a joint project of CFHT and CEA Saclay, at the Canada-France-Hawaii Telescope (CFHT) which is operated by the National Research Council (NRC) of Canada, the Institut National des Science de l'Univers (INSU) of the Centre National de la Recherche Scientifique (CNRS) of France, and the University of Hawaii. This research used the facilities of the Canadian Astronomy Data Centre operated by the National Research Council of Canada with the support of the Canadian Space Agency.

Table des matières

Table des figures

Liste des tableaux

Acronyms

2**PCF**	2 Point Correlation Function
Λ**CDM**	Λ Cold Dark Matter
BAO	Baryonic Acoustic Oscillations
BBN	Big Bang Nucleosynthesis
CCH	Cosmic Chronometers
CDE	Coupled Dark Energy
CLOE	Cosmology Likelihood for Observables in *Euclid*
CMB	Cosmic Microwave Background
DE	Dark Energy
DM	Dark Matter
ECQ	Early Coupled Quintessence
EoS	Equation of State
FLRW	Friedmann-Lemaître-Robertson-Walker
GC	Galaxy Clustering
IA	Intrinsic Alignment
IST :L	Inter-Science Taskforce : Likelihood
LSS	Large Scale Structure
MCMC	Markov Chain Monte Carlo
MDE	Matter Dominated Era
NN	Neural Network
PSF	Point Spread Function
RDE	Radiation Dominated Era
RSD	Redshift Space Distortions
SNe1a	Type 1a Supernovae
SOM	Self Organising Map
SWG	Science Working Group
SSC	Super Sample Covariance
UNIONS	Ultraviolet Near-Infrared Optical Northern Survey
WL	Weak Lensing
WP	Work Package

1. Extended Abstract

The ΛCDM model postulates that the Universe is primarily comprised of a cosmological constant Λ, responsible for the late-time accelerated expansion of the Universe; dark matter, a slow-moving matter component which only interacts gravitationally, and ordinary matter. The model accounts for almost the entirety of the growth history of the Universe from the time of the Big Bang, and has been able to elucidate numerous observational phenomena such as the existence and structure of the Cosmic Microwave Background (CMB) and the Large Scale Structure (LSS), the observed late-time accelerated expansion of the Universe, and various other astrophysical processes. Hence it is still hailed as the concordance model within the cosmological community.

However, with the continuous release of high-precision data, tensions between datasets have arisen that could suggest possible insufficiencies of this model. For example, the most well-known and pressing tension currently being faced within the community is the H_0 *tension* : the significant difference between the present-day value of the expansion of the Universe, the Hubble constant H_0, measured by early-time probes such as the CMB, as opposed to using late-time probes such as Type 1a supernovae.

An attempt to reconcile these tensions has led to the exploration of modified ΛCDM models. Specifically, one such model is known as the *Coupled Dark Energy (CDE) model*. It proposes the existence of a scalar field in place of a cosmological constant, which is coupled to the dark matter particles, causing them to experience a fifth force apart from gravity. Such a model alters the growth history and structure formation of the Universe, and has been shown to be able to relieve the H_0 tension while still being compatible with current datasets.

In my thesis, I introduce a new parametrisation of the CDE model where the coupling strength between the dark matter particles and the scalar field is allowed to evolve with redshift. To probe such a tomographic CDE model, I employ various datasets across a range of redshifts, including for the first time, LSS data combining weak lensing, galaxy clustering, and their cross-correlation, galaxy-galaxy lensing, known as a '3x2pt' probe. I find that LSS data allows us to recover tight constraints on coupling even at low redshifts, comparable to that obtained with CMB data, making it a promising probe to constrain CDE models at low redshifts.

With this first proof of concept, I subsequently applied this tomographic CDE model to other avenues of investigation. Firstly, I studied a form of early coupled quintessence (ECQ) models, whereby coupling is only activated during primordial times, specifically during the radiation-dominated era. The dynamics of such a coupling can lead to interesting physical consequences, particularly the formation of primordial black holes, which could be a candidate for dark matter. I constrained this ECQ model with observational data for the first time. Secondly, I explore

whether deep learning techniques like neural networks can differentiate between LSS data generated from a ΛCDM model and a tomographic CDE model. I find promising results showing that neural networks can discern the effects of early-time, late-time or zero coupling on growth data created by adopting Stage-IV-like survey specifications, demonstrating the exciting potential of employing machine learning techniques in upcoming weak lensing analyses.

Lastly, I highlight my contributions to the various galaxy survey collaborations which I have been a part of during my PhD : namely the *Euclid* mission and UNIONS survey. The *Euclid* mission is an ambitious space-based galaxy survey commissioned by the ESA that will image more than a billion galaxies, ultimately aiming to shed light on the enigmatic dark sector of the Universe. I play an active role within the *Euclid* consortium by contributing to the development of the official *Euclid* likelihood code, Cosmology Likelihood for Observables in *Euclid* (CLOE). CLOE is a key piece of code which will be needed at the end of the data processing pipeline, as it will deliver cosmological constraints with *Euclid* data, with a functionality that will enable inference with extended ΛCDM models as well.

Furthermore, I have worked on developing the cosmic shear inference pipeline for the UNIONS collaboration, which brings together 3 ground-based photometric telescopes in Hawaii that, when completed, will provide the largest galaxy map in the northern hemisphere to date. I underline the various tests that I have carried out to obtain cosmological constraints from processed galaxy catalogues, which will form a fitting complement to those already available with current Stage III surveys such as the Dark Energy Survey (DES) and the Kilo-Degree Survey (KiDS).

This thesis is thus an amalgamation of the work that I have carried out in the 3 years of my PhD journey, spanning a considerable breadth of topics from both a theoretical and observational point of view. Therefore it is my hope that within the grand scheme of cosmological research, my efforts have, be it in some minuscule way, contributed to our attempts to understand this Universe which we call home.

2. Résumé étendu en français

Le modèle ΛCDM postule que l'Univers est principalement composé d'une constante cosmologique Λ, responsable de l'expansion accélérée de l'Univers à des époques tardives ; de matière noire, une composante de matière se déplaçant lentement et n'interagissant que gravitationnellement, et de matière ordinaire. Le modèle rend compte presque entièrement de l'histoire de la croissance de l'Univers depuis le Big Bang, et a permis d'élucider divers phénomènes observationnels, tels que l'existence et la structure du fond diffus cosmologique et la structure à grande échelle, l'expansion accélérée tardive de l'Univers observée, ainsi que divers autres processus astrophysiques. C'est pourquoi il est encore considéré comme le modèle de concordance au sein de la communauté cosmologique.

Cependant, avec la publication continue de données de haute précision, des tensions entre les ensembles de données ont émergé, suggérant des insuffisances possibles de ce modèle. Par exemple, la tension la plus connue et la plus pressante actuellement rencontrée au sein de la communauté est la tension sur H_0 : la différence significative entre la valeur actuelle de l'expansion de l'Univers, la constante de Hubble H_0, mesurée par des sondes de l'univers primordial telles que le fond diffus cosmologique, par opposition à des sondes de l'univers tardif telles que les supernovae de Type 1a.

Une tentative de concilier ces tensions a conduit à l'exploration de modèles ΛCDM modifiés. Plus précisément, l'un de ces modèles est connu sous le nom de modèle de *couplage de l'énergie noire* . Ce modèle propose l'existence d'un champ scalaire à la place d'une constante cosmologique, couplé aux particules de matière noire, leur faisant ressentir une cinquième force en plus de la gravité. Un tel modèle modifie l'histoire de la croissance et la formation des structures de l'Univers, et s'est avéré capable de réduire la tension sur H_0 tout en restant compatible avec les ensembles de données actuels.

Dans ma thèse, je présente une nouvelle paramétrisation du modèle de couplage de l'énergie noire où la force de couplage entre les particules de matière noire et le champ scalaire est autorisée à évoluer avec le décalage vers le rouge. Pour explorer un tel modèle couplage de l'énergie noire tomographique, j'utilise divers ensembles de données sur une gamme de décalages vers le rouge, incluant pour la première fois des données de la structure à grande échelle en combinant lentille faible, regroupement de galaxies et leur corrélation croisée, lentille galaxie-galaxie pour former une sonde '3x2pt'. Je constate que les données de la structure à grande échelle nous permettent de récupérer des contraintes strictes sur le couplage même à faible décalage vers le rouge, comparables à celles obtenues avec les données du fond diffus cosmologique, ce qui en fait une sonde prometteuse pour contraindre les modèles couplage de l'énergie noire à faible décalage vers le rouge.

Avec cette première preuve de concept, j'ai ensuite appliqué ce modèle couplage de l'énergie noire tomographique à d'autres axes de recherche. Tout d'abord, j'ai étudié une forme de modèles de quintessence couplée précoce, où le couplage n'est activé qu'à des époques primordiales, notamment pendant l'ère dominée par le rayonnement. Les dynamiques d'un tel couplage peuvent entraîner des conséquences intéressantes, notamment la formation de trous noirs primordiaux, qui pourraient être un candidat pour la matière noire. J'ai contraint ce modèle de quintessence couplée précoce avec des données observationnelles pour la première fois. Ensuite, j'explore si des techniques d'apprentissage profond comme les réseaux de neurones peuvent différencier les données structure à grande échelle générées par un modèle ΛCDM et un modèle couplage de l'énergie noire tomographique. Je trouve des résultats prometteurs montrant que les réseaux de neurones peuvent discerner les effets de couplage primordial, tardif ou nul sur les données de croissance créées en adoptant des spécifications de sondage de type Stage-IV, démontrant le potentiel excitant de l'utilisation des techniques de machine learning dans les analyses futures de lentilles faibles.

Enfin, je souligne mes contributions aux différentes collaborations de sondages de galaxies auxquelles j'ai participé pendant mon doctorat ; à savoir la mission *Euclid* et le sondage UNIONS. La mission *Euclid* est un ambitieux sondage de galaxies basé dans l'espace, commandé par l'Agence Spatiale Européenne, qui imagera plus d'un milliard de galaxies, visant en fin de compte à éclairer le secteur obscur et énigmatique de l'Univers. Je joue un rôle actif au sein du consortium *Euclid* en contribuant au développement du code officiel de vraisemblance *Euclid*, Cosmology Likelihood for Observables in *Euclid* (CLOE). CLOE est une pièce maîtresse de code qui sera nécessaire à la fin de la chaîne de traitement des données : il fournira des contraintes cosmologiques avec les données *Euclid*, avec une fonctionnalité permettant une inférence avec des modèles ΛCDM étendus également.

De plus, j'ai travaillé au développement de la chaîne d'inférence de cisaillement cosmique pour la collaboration UNIONS, qui réunit 3 télescopes photométriques terrestres à Hawaii qui, une fois achevés, fourniront la plus grande carte des galaxies de l'hémisphère nord à ce jour. Je souligne les divers tests que nous avons effectués pour obtenir des contraintes cosmologiques à partir des catalogues de galaxies traités, qui compléteront adéquatement ceux déjà disponibles avec les sondages actuels de la Stage III comme le Dark Energy Survey (DES) et le Kilo-Degree Survey (KiDS).

Cette thèse est donc une amalgamation des travaux que j'ai menés au cours des 3 années de mon doctorat, couvrant une large gamme de sujets à la fois d'un point de vue théorique et observationnel. Par conséquent, j'espère que dans le cadre de la recherche cosmologique, mes efforts ont, ne serait-ce que d'une manière minuscule, contribué à nos tentatives de comprendre cet Univers que nous appelons chez nous.

3. The Cosmological Principle

Sommaire

3.1 Introduction

In this first Chapter, we shall derive the relevant equations governing the evolution and perturbation history of the Universe. Then we move on to introduce several cosmological quantities that will be useful in the coming Chapters. Finally, we turn to the state-of-the-art in the current cosmological community, and delve into some issues it is presently facing. This shall set us up with the relevant background knowledge and mathematical know-how to proceed with the rest of this thesis, and will hopefully prove adequate in equipping us on this journey of discovering our Universe.

3.2 Einstein's Field Equations

In 1916, Einstein published his seminal theory on General Relativity in a series of papers [1], reinterpreting our understanding of the nature of spacetime and consequently, our Universe. He proposed a direct relationship between the curvature of spacetime and its energy-matter constituents, which is elegantly captured within the *Einstein Field Equations* :

$$R_{\mu\nu} - \frac{1}{2}Rg_{\mu\nu} = 8\pi G T_{\mu\nu} - \Lambda g_{\mu\nu} \tag{3.1}$$

Here $R_{\mu\nu}$ is the Ricci tensor, R the Ricci scalar, $g_{\mu\nu}$ the metric of the spacetime, Λ the cosmological constant, G the gravitational constant and $T_{\mu\nu}$ the energy-momentum tensor [2]. Note that we have taken the speed of light $c = 1$, which will also be the case for the rest of this thesis.

The left-hand side of Eq. (3.1) describes the geometry of spacetime through the Ricci tensor and the metric, while the right-hand side describes its matter-energy components, encapsulated in $T_{\mu\nu}$ with the inclusion of a cosmological constant Λ. The indices of μ and ν run across the 4 dimensions of space and time, condensing Eq. (3.1) into a set of 10 equations (since these tensors are symmetric). Solving the Field Equations then requires working out expressions for the metric $g_{\mu\nu}$, which then gives a complete description of the nature of the spacetime under study.

3.3 The Cosmological Model

Solutions to all 10 of Einstein's Field Equations constitute a metric that describes a characteristic spacetime and its matter-energy components. The solution most widely employed in cosmology is the Friedmann-Lemaître-Robertson-Walker (FLRW) metric. It describes a homogeneous and isotropic Universe, in accordance with the Cosmological Principle, where the line element is given by

$$ds^2 = -dt^2 + a^2(t)\left[dx^2 + dy^2 + dz^2\right], \tag{3.2}$$

with $a(t)$ being the *scale factor*, quantifying the rate of expansion of the Universe as a function of time. We can also re-express the spatial components x, y and z in polar coordinates χ, θ and ϕ, such that Eq. (3.2) becomes

$$ds^2 = -dt^2 + a^2(t)\left[d\chi^2 + f_K^2(\chi)d\Omega^2\right] \tag{3.3}$$

where χ is the radial comoving coordinate and $d\Omega^2 = d\theta^2 + \sin^2(\theta)\, d\phi^2$. Here, K is known as the curvature constant and $f_K(\chi)$ is dependent on the value it takes :

$$f_K(\chi) = \begin{cases} K^{-1/2} \sin\left(K^{1/2}\chi\right), & \text{for } K > 0 \text{ (open Universe),} \\ \chi, & \text{for } K = 0 \text{ (flat Universe),} \\ (-K)^{-1/2} \sinh\left((-K)^{1/2}\chi\right), & \text{for } K < 0 \text{ (closed Universe).} \end{cases} \tag{3.4}$$

We have thus established a form for the metric, $g = [-1, a^2(t), a^2(t), a^2(t)]$ that describes the geometry of our Universe, completing the left-hand side of Eq. (3.1). We can now turn to study its energy-matter content by specifying a form for $T_{\mu\nu}$, i.e. the right-hand side of Eq. (3.1). To do this, it is typical to assume a cosmological model for the Universe : in this thesis, we shall focus on the concordance model, known as Λ *Cold Dark Matter* (ΛCDM).

ΛCDM postulates the existence of 4 main components of the Universe : a cosmological constant term Λ, responsible for the late-time acceleration of the Universe; secondly, non-relativistic dark matter (DM) that only interacts through gravity; thirdly, baryonic matter, and lastly, radiation. This model has been widely successful in explaining observational phenomena such as the late-time accelerating expansion of the Universe [3, 4], the larger-than-expected value of galaxy rotation curves [5], and the detection of remnant radiation from primordial times [6]. Assuming a flat Universe (i.e. $K = 0$), this model specifies almost every aspect of the Universe's evolutionary history with just six parameters, making it the most fitting theory of our Universe to date.

We assume each component of the Universe as a perfect homogeneous fluid, with its energy-momentum tensor given by $T_{\mu\nu}$ taking on the form $T^{\mu}_{\nu} = \text{diag}(-\rho(t), p(t), p(t), p(t))$, where ρ denotes the energy density of the particular fluid and p, its pressure. By convention, $T_{\mu\nu}$ also obeys the conservation equation; i.e. $\nabla^{\mu} T_{\mu\nu} = 0$ for each fluid component.

Now we can explicitly solve Eq. (3.1), for both the temporal (00) and spatial (ii) components. This leads us to two equations respectively, known as *Friedmann's Equations*, describing the rate of expansion of the Universe as a function of the energy density of its constituents :

$$\left(\frac{\dot{a}}{a}\right)^2 + \frac{K}{a^2} - \frac{\Lambda}{3} = \frac{8\pi G}{3}\rho \tag{3.5}$$

$$\left(\frac{\ddot{a}}{a}\right) - \frac{\Lambda}{3} = -\frac{4\pi G}{3}\left(\rho + 3p\right) \tag{3.6}$$

where the dot denotes a derivative with respect to time t. It is convenient to define the Hubble parameter $H(t) = \frac{\dot{a}}{a}$, which by its definition quantifies the rate of expansion of the Universe.

Differentiating Eq. (3.5) with respect to time, we get

$$\frac{8\pi G}{3}\dot{\rho} = 2\,\frac{\dot{a}}{a}\left(\frac{\ddot{a}}{a} - \left(\frac{\dot{a}}{a}\right)^2 - \frac{K}{a^2}\right) \tag{3.7}$$

or more concisely,

$$\dot{\rho}_i + 3H(\rho_i + p_i) = 0 \tag{3.8}$$

which is known as the *continuity equation*, describing the evolution of each component i of the Universe as a function of the scale factor. We can hence obtain a general solution to Eq. (3.8) :

$$\rho_i \propto a^{-3(1+w)} \tag{3.9}$$

where $i =$ DM, radiation, baryons or Λ, and w is the *Equation of State (EoS)* parameter given by

$$w \equiv p/\rho\,, \tag{3.10}$$

whose value depends on the nature of the fluid under study. Since non-relativistic fluids are pressureless, we have $w = 0$ for DM and baryons, while $w = \frac{1}{3}$ for radiation. In the case of Λ, since it is responsible for the accelerating expansion of the Universe, this imposes a condition $w < -\frac{1}{3}$ from Eq. (3.6). In a ΛCDM model with a cosmological constant, $w = -1$. In extended models however, a different or even non-constant value for w_Λ is explored [7-10], in what is often termed dynamical dark energy models.

Thus for the specific expression for the evolution of a particular fluid, one just has to substitute the appropriate value for w. From Eq. (3.9), we can appreciate how each component evolves differently with time, and identify the different cosmological epochs based on the dominant element.

It is also useful to re-express Eq. (3.5) as the Hubble function, where we define the evolution of the Hubble parameter H in terms of the present-day value of the

energy densities :

$$H(a) = H_0\sqrt{\Omega_{\mathrm{DM},0}a^{-3} + \Omega_{\mathrm{b},0}a^{-3} + \Omega_{R,0}a^{-4} + \Omega_{K,0}a^{-2} + \Omega_{\Lambda}} \tag{3.11}$$

Here $\Omega_{i,0}$ represents the dimensionless density parameter of each component (DM, baryons, radiation, curvature and Λ respectively), with the 0 subscript denoting the present time. H_0 is then the present value of the Hubble parameter, oftentimes expressed as $100h$ km s^{-1}Mpc^{-1} as well. The various density parameters are thus defined as :

$$\Omega_i = \frac{8\pi G\rho_i}{3H^2} \tag{3.12}$$

$$\Omega_\Lambda = \frac{\Lambda}{3H^2} \tag{3.13}$$

$$\Omega_K = \frac{K}{aH^2} \tag{3.14}$$

where i here applies for DM, radiation and baryons. These quantities can also be expressed as a function of redshift; i.e. $\Omega_i(z) = \frac{8\pi G\rho_i(z)}{3H(z)^2}$. The reduced energy density parameter $\omega_i = \Omega_i h^2$ is also sometimes used as an alternative parameter to express the energy densities. In a flat Universe, we can define a critical density of matter $\rho_{\mathrm{crit}} = \frac{3H_0^2}{8\pi G}$, and thus $\Omega_i \equiv \frac{\rho}{\rho_{\mathrm{crit}}}$. Since Ω defines the fraction of each component present within the Universe, they must sum to unity. Thus the energy densities of only 4 components need to be measured in order to deduce the value of the last one.

3.4 Cosmological Quantities

After establishing our cosmological model, we can now introduce various other quantities widely used in cosmology.

3.4.1 Conformal Time

Due to the expansion of the Universe, time as measured by observers at different points in spacetime is different. To take this effect into account, we define a new quantity for time, known as *conformal time* τ. It is defined as

$$\tau = \int \frac{dt}{a} \tag{3.15}$$

where t is then the *proper time*, the time measured by an observer at rest with respect to the expanding Universe. The point where $\tau = 0$ occurs at the Big Bang. As we shall see in the next section, it is convenient to express the metric in terms of conformal time instead of proper time, especially when considering perturbations.

3.4.2 Cosmological Distances

An analogous approach can be taken to express cosmological distances in various manners. They can be thought of as proxies for distance measurements since we are unable to directly measure the distance to a particular object in the sky.

Redshift. Due to the expansion of the Universe, the wavelength of a photon gets 'stretched out', or Doppler-shifted, as it travels towards the observer. We term this effect *redshift*, which can be quantified as a measurable parameter z, and is related to the scale factor by

$$z = \frac{1}{a} - 1. \tag{3.16}$$

A redshift of $z = 0$ thus indicates present time, or present location. The larger the redshift of an object, the further away from the observer it is. The redshift of an object can be directly measured through spectroscopy, hence is an extremely useful measure of cosmological distance.

Comoving Distance. Just like how we have defined conformal time, we can similarly define a distance measure ignoring the effect of the expanding Universe. This quantity is known as the *comoving distance* χ, where it is the integration of the path given by the metric in Eq. (3.3) :

$$\chi = \int_{\text{obs}}^{\text{source}} ds. \tag{3.17}$$

However this quantity cannot be measured directly, hence it is deduced from angular distances, calculated from the size of objects that we observe through our telescopes.

Angular Diameter Distance. The angular diameter distance D_A is the ratio between the physical size of the object s to the angle that it subtends, θ. It can also be expressed in terms of redshift and curvature, where

$$D_A = \frac{s}{\theta} = \frac{S_K(\chi)}{1+z},$$
$$S_K(\chi) = \begin{cases} K^{-1/2}\sin\left(K^{1/2}\chi\right), & \text{for } K > 0 \text{ (open Universe)}, \\ \chi, & \text{for } K = 0 \text{ (flat Universe)}, \\ (-K)^{-1/2}\sinh\left((-K)^{1/2}\chi\right), & \text{for } K < 0 \text{ (closed Universe)}. \end{cases} \tag{3.18}$$

Comoving Angular Diameter Distance. The comoving angular diameter distance D_M is given by the comoving radial size of the object r to the angle it subtends θ. It is thus related to D_A by

$$D_M = (1+z)D_A. \tag{3.19}$$

3.5 Linear Perturbation Theory

Up till now, we have only considered the evolution of the mean energy densities of the various components of the Universe. However, that is only half of the picture. The theory of inflation postulates that the current observable structures of the Universe were seeded by *quantum fluctuations* during the inflationary era. These minute instabilities grow with the Hubble expansion as inhomogeneous perturbations against a homogeneous background, evolving into complex networks of galaxy clusters and dark matter halos, or what we term the *Large Scale Structure* (LSS) of the Universe. In this section, we shall thus concern ourselves with the evolution of these density perturbations.

3.5.1 The Perturbed Metric

It is simplest to assume a flat FLRW Universe at the background level, consisting of fluids with constant entropy. Perturbations in the metric are often expressed in gauges, with the two most commonly employed being the *Newtonian gauge* and the *synchronous gauge*. For completeness, we quote both here.

In the Newtonian gauge, the perturbed metric can be understood as a conse-

quence of the presence of gravitational potentials Φ and Ψ :

$$ds^2 = -(1+2\Phi)dt^2 + a(t)^2(1-2\Psi)\delta_{ij}^K\, dx^i\, dx^j \tag{3.20}$$

where δ_{ij}^K is the Kronecker delta.

In the synchronous gauge, we express the perturbations to the metric as a tensor h :

$$ds^2 = -dt^2 + a(t)^2[(1+h_{ii}/3)\delta_{ij}^K + h_{ij}]dx^i\, dx^j \tag{3.21}$$

where h_{ii} is its trace and h_{ij} its traceless part, denoting perturbations to the spatial components of the metric.

3.5.2 Perturbation Quantities

We can subsequently move on to specify several perturbed quantities of interest.

Density Perturbation. The energy density perturbations can be expressed as overdensities on top of the mean background density :

$$\delta_i(\chi,\tau) = \frac{\rho_i(\chi,\tau) - \bar{\rho}_i(\tau)}{\bar{\rho}_i(\tau)} \tag{3.22}$$

where ρ_i is a function of comoving distance χ and conformal time τ, $\bar{\rho}_i$ is the mean density, and i here can refer to baryons, DM, radiation or Λ. By definition, $\delta_\Lambda = 0$.

Particularly for the case of DM overdensities, we can define a σ_8 parameter as the amplitude of DM density fluctuations within a sphere of characteristic radius 8 Mpc$/h$:

$$\sigma_8^2(z) = \left\langle \left|\delta_{\mathrm{DM},8\mathrm{Mpc/h}}\right|^2 \right\rangle, \tag{3.23}$$

as well as the S_8 parameter, where $S_8 = \sigma_8\sqrt{\Omega_\mathrm{m}/0.3}$ (taking note that $\Omega_\mathrm{m} = \Omega_\mathrm{DM} + \Omega_\mathrm{b}$).

Pressure Perturbation. We can similarly define a perturbation to the pressure $\delta p_i(\chi,\tau)$, and the quantity $c_{s,i}^2 = \delta p_i/\delta\rho_i$ known as the *sound speed*, analogous to the EoS parameter w at the background level.

Velocity Perturbation. Gravitational instabilities induce, on top of perturbations to the energy densities, perturbations to the fluid velocities as well. Thus, we

can express a fluid's total velocity as the sum of its velocity due to Hubble expansion, v_H, and its velocity perturbation, v_P :

$$\vec{v}_T(\chi,\tau) = \vec{v}_H(\chi,\tau) + \vec{v}_P(\chi,\tau). \tag{3.24}$$

The perturbed velocity $\vec{v}_P = \dot{\chi} - H\chi$ is also referred to as the *peculiar velocity*. Hereafter, we drop the P subscript for clarity of notation.

3.5.3 Perturbation Growth

To understand the formation of the LSS, we track its main driver, the evolution of dark matter overdensities $\delta_{\rm DM}$. Within the Newtonian regime where we assume $|\delta| \ll 1$, the evolution of $\delta_{\rm DM}(\chi,\tau)$ can be derived by solving the linearised continuity and Euler equations, assuming a gravitational potential $\phi(\chi,\tau)$ evolving as Poisson's equation. We quote here the three equations respectively [11] :

$$\frac{\partial \delta_{\rm DM}(\chi,\tau)}{\partial \tau} + \theta_{\rm DM}(\chi,\tau) = 0 \tag{3.25}$$

$$\frac{\partial \vec{v}_{\rm DM}}{\partial \tau} + \mathcal{H}(\tau)\vec{v}_{\rm DM}(\chi,\tau) = -\nabla\phi(\chi,\tau) \tag{3.26}$$

$$\nabla^2\phi(\chi,\tau) = 4\pi G a^2 \bar{\rho}_{\rm DM}\delta_{\rm DM} \tag{3.27}$$

where we have defined the divergence of the velocity perturbation $\theta = \nabla \cdot \vec{v}$ and $\mathcal{H} = a'/a$. This yields a second-order differential equation for $\delta_{\rm DM}$:

$$\delta_{\rm DM}^{''} + \mathcal{H}\delta_{\rm DM}^{'} = 4\pi G \rho_{\rm DM}\delta_{\rm DM} \tag{3.28}$$

where we use a prime superscript to denote a derivative with respect to τ. Eq. (3.28) has two solutions : one mode that decreases with time and another that increases. Since the decreasing function merely decays, it is of no interest, hence we consider only the increasing mode, writing $\delta_{\rm DM}(\chi,\tau)$ in the form

$$\delta_{\rm DM}(\chi,\tau) = D^+(\tau)\delta_{\rm DM}(\chi,0) \tag{3.29}$$

where $D^+(\tau)$ is known as the *growth factor* and $\delta_{\rm DM}(\chi,0)$ is $\delta_{\rm DM}$ at present time.

We can also define a *growth rate* parameter $f \equiv \frac{d\ln D^+}{d\ln a}$ which has been shown to be approximately $f(z) \approx \Omega_{\rm m}(z)^{0.545}$ [12] in the regime of General Relativity.

3.5.4 The Matter Power Spectrum

It is easier to consider these density perturbations as waves in Fourier space, and as a function of redshift. Hence we can express a particular wave mode of $\delta_{\rm DM}$ as :

$$\delta_{\rm DM}(\vec{k}, z) = \frac{1}{2\pi^2} \int d^3\chi \, e^{-i\vec{k}\cdot\vec{\chi}} \, \delta(\chi, z). \tag{3.30}$$

From here, we can define the *matter power spectrum* $P_{\delta\delta}(k, z)$ as the variance of the overdensities :

$$\left\langle \delta_{\rm DM}(\vec{k}, z) \delta_{\rm DM}(\vec{k'}, z) \right\rangle = (2\pi)^3 P_{\delta\delta}(k, z) \, \delta_D(|\vec{k} - \vec{k'}|) \tag{3.31}$$

where the δ_D symbol on the right-hand side of the equation denotes the Dirac delta function. Hereafter, we shall denote the absolute magnitude of the wavevector $\vec{k}$ as k, and drop the directional dependence due to isotropy.

In the early Universe, theories of inflation [13, 14] assume a dimensionless primordial power spectrum $P_\zeta(k)$ given by

$$P_\zeta(k) = A_{\rm s} \left(\frac{k}{k_p} \right)^{n_{\rm s}-1} \tag{3.32}$$

where $A_{\rm s}$ is the *amplitude of the primordial power spectrum* and k_p is known as the pivot scale. The variation of $P_\zeta(k)$ with respect to scale is quantified by the *spectral index* $n_{\rm s}$. The matter power spectrum is related to its primordial counterpart through the *transfer function* $\mathcal{T}_m(k, z)$, which describes the evolution of the perturbations throughout the various epochs [15] :

$$P_{\delta\delta}(k, z) = 2\pi^2 k \, \mathcal{T}_m^2(k, z) P_\zeta(k) \tag{3.33}$$

3.6 Cosmological Tensions

As we have shown, the ΛCDM model, specified by the parameters $\{\Omega_{\rm DM}, \Omega_{\rm b}, n_{\rm s}, A_{\rm s}, \tau_{\rm reio}, H_0\}$ where $\tau_{\rm reio}$ is the optical depth of reionisation, gives a complete picture of the expansion history of the Universe. It has been remarkably successful in explaining observations such as the formation of the LSS (see Sect. 4.3), the anisotropies of the Cosmic Microwave Background (CMB, see Sect. 4.4), and the observed accelerated expansion of the Universe.

Yet with the release of more observational data, which continues to become

increasingly precise, tensions have emerged that cannot seem to be reconciled within the framework of ΛCDM. We briefly explore the two most pressing tensions currently faced by the cosmological community.

3.6.1 H_0 Tension

Perhaps the most well-known tension is the H_0 *tension* [16] : the discrepancy between the value of H_0 measured indirectly by early time probes such as the CMB [17-19] (while assuming a ΛCDM model), and late time probes such as Type 1a Supernovae and strong lensing time-delays [20-22] (measured through a direct model-independent approach). This difference is almost $\sim 5\sigma$ in magnitude, hence it cannot solely be due to statistical variance. In Fig. 3.1, we plot the values of H_0 reported by various experiments using different probes. Unless this inconsistency is due to systematic errors in the measurement, this could hint at the necessity of new physics beyond ΛCDM.

3.6.2 S_8 Tension

Another tension that has recently come under scrutiny is the S_8 *tension* : the discrepancy between the value of S_8, i.e. the degree of 'clumpiness' of our Universe, as measured by the CMB and late-time LSS probes. For comparison,

$$S_8 = \begin{cases} 0.829 \pm 0.012, & \text{Planck + Lensing [17]}, \\ \hline 0.759^{+0.024}_{-0.021}, & \text{KiDS-1000 Cosmic Shear [24]}, \\ 0.772^{+0.018}_{-0.017}, & \text{DES Y3 Cosmic Shear [25, 26]}, \\ 0.769^{+0.031}_{-0.034}, & \text{HSC Y3 Cosmic Shear [27]} \end{cases} \tag{3.34}$$

which equates to an average discrepancy of $\sim 2.5\sigma$ between CMB and Cosmic Shear probes. Explanations have been proposed to explain this tension while still adhering to the ΛCDM framework : attributing it to inadequate modelling of cosmic shear calibration [28-30] or inaccurate modelling of the matter power spectrum at nonlinear scales [31, 32].

The emergence of these two tensions has in part led to explorations of alternative ΛCDM models, albeit to varying degrees of success (for a comprehensive review, see for example [33]). In the following Chapters of this thesis, we shall focus on one particular class of modified ΛCDM models, with the ultimate aim of confronting it with state-of-the-art data from upcoming LSS galaxy surveys.

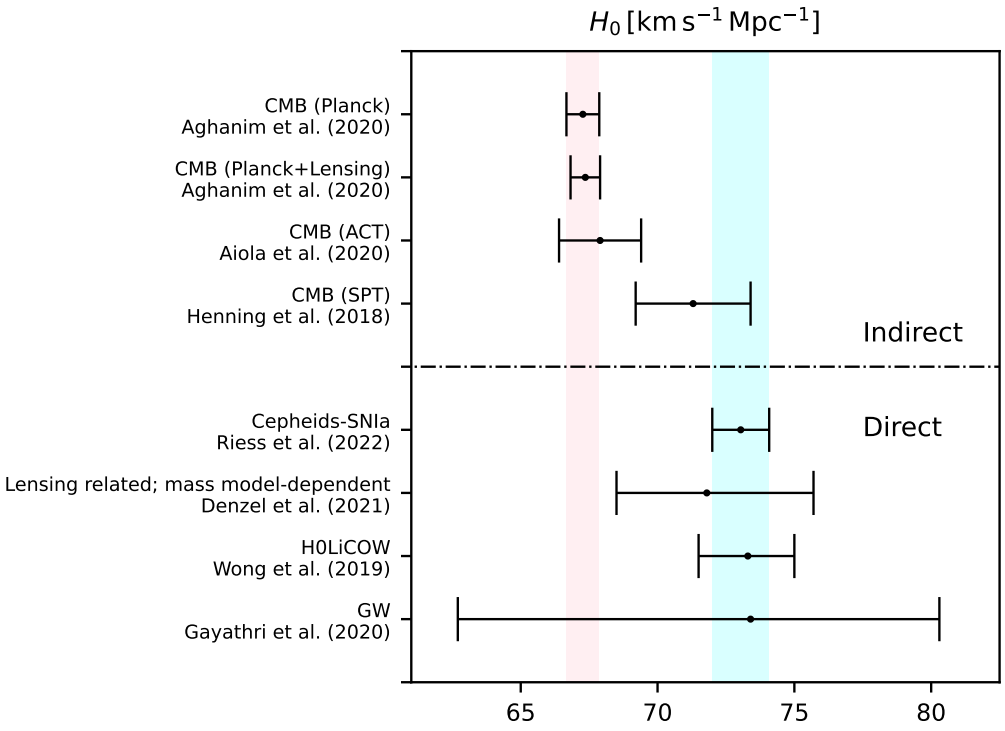

Fig. 3.1. Whisker plot of the mean and 1σ values of H_0 as measured by a select number of experiments. We make a distinction between direct and indirect measurements. The pink vertical band follows the constraints from Planck 2018 results [17] while the blue vertical band follows the latest SH0ES prior [21]. This figure was produced using code accompanying [23].

IN BRIEF

In this Chapter, I have introduced the Cosmological Principle of the Universe and its concordance ΛCDM model, deriving the relevant equations dictating the evolution of the background and perturbation energy densities. I have also introduced various cosmological quantities often measured in observations, and lastly presented the two most critical tensions faced by the cosmological community today.

After introducing the theory, we can turn towards what current data can offer. In the next Chapter, we shall delve into the various state-of-the-art cosmological data probes and discuss their potential strength in constraining the various cosmological parameters.

4. Cosmological Probes

Sommaire

4.1 Introduction

After introducing the theoretical model of our Universe, it is now useful to discuss the observational data we currently have at our disposal to probe our hypotheses. In this Chapter, we shall mainly concern ourselves with the probes of the LSS and the CMB : explaining their physical features and focusing on how we can extract useful information from them to constrain the various cosmological parameters of our model. Finally, we will touch on important statistical concepts such as *Bayesian Inference*, which we employ to carry out our cosmological analyses.

4.2 The Cosmological Random Field

Cosmological fields are important concepts in cosmology as they give a largely fitting picture of various physical quantities in the Universe. At first order, most cosmological fields can be approximated as *Gaussian random fields*, which associate a random variable, sampled from a Gaussian distribution, to each point in real space $\vec{r}$.

To study the properties of such a field, we calculate the 2*-point correlation function* (2PCF) $\xi(\vec{r})$, which gives the correlates the value of a field at 2 points in space by

calculating its expectation squared[34] :

$$\xi(\vec{r}) = \langle \delta(\vec{x})\delta(\vec{x}+\vec{r}) \rangle \tag{4.1}$$

Comparing it to Eq. (3.31), is simply the real space analogue of the power spectrum in Fourier space.

4.3 Large Scale Structure

The LSS of the Universe consists of a complex web of galaxy clusters, superclusters, filaments and voids, residing within dark matter halos. It originated from minute density fluctuations during primordial times, imprinted during the period of cosmic inflation and amplified by gravitational instability as the Universe expanded. Hence the LSS can shed light on the expansion and perturbation history of the Universe, especially by allowing us to probe the small-scale perturbations at low redshifts.

In this section, we explain 3 different techniques for studying the LSS : weak lensing, photometric galaxy clustering, and their cross-correlation known as '3x2pt'. All these methods, to a first-order approximation, rely on calculating the 2 point auto- or cross-correlation function of one or two fields, whose nature we shall discuss in the next subsections.

4.3.1 Weak Lensing

The presence of a foreground matter distribution (referred to as the 'lens') causes light rays travelling from background galaxies (referred to as 'sources') to be deflected due to their gravitational field. This results in the measured shape of the galaxy being distorted, a phenomenon known as *gravitational weak lensing*, as demonstrated in Fig. 4.1. By tracing these light rays back to the galaxy source, the distribution of the foreground dark matter can thus be deduced, allowing gravitational lensing analysis techniques to emerge as powerful tools to probe the dark matter distribution.

Following the notation of Fig. 4.1, we can define the separation between two unperturbed light rays as their transverse comoving separation $\vec{x}(\chi)$ [36],

$$\vec{x}(\chi) = f_K(\chi)\vec{\theta} - \frac{2}{c^2}\int_0^{\chi} d\chi' f_K(\chi-\chi')\Delta\left[\nabla_\perp \Phi(\vec{x},\chi')\right] \tag{4.2}$$

while the actual comoving separation that we measure is instead $d\vec{x} + \vec{x} = f_K(\chi)\vec{\theta}$,

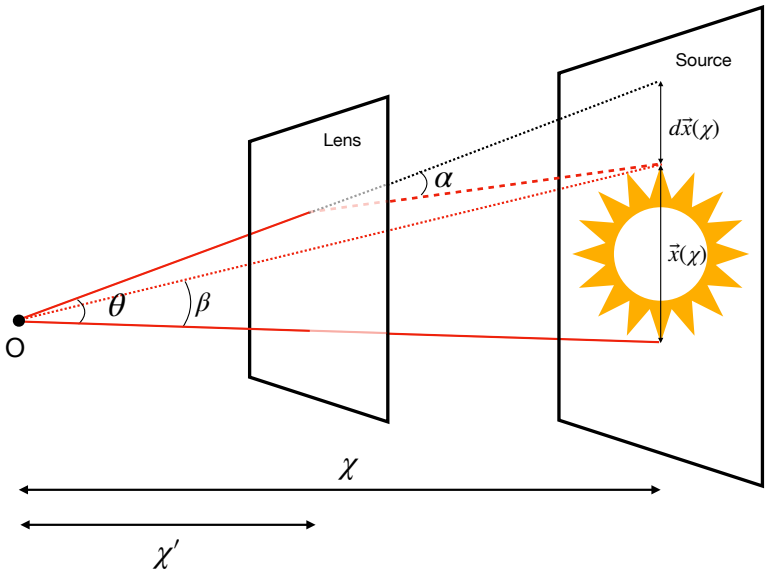

Fig. 4.1. A matter distribution on the lens plane at a distance χ' deflects light rays with transverse separation $\vec{x}(\chi)$, at comoving distance χ. The solid red lines show the direction they are perceived to have originated from, subtended by an angle $\vec{\theta}$. Without the lensing mass, the light rays would have subtended an angle $\vec{\beta}$, as drawn out by the dotted line. The deflection angle is then $\vec{\alpha}$, and the shift in separation is $d\vec{x}$. Figure adapted from [35, 36].

due to a distortion caused by the presence of a mass distribution on the lens plane at comoving distance χ'. It induces a difference in the perpendicular gravitational potential of the two light rays, expressed as $\Delta\left[\nabla_\perp \Phi(\vec{x}, \chi')\right]$.

Assuming $d\vec{x} \ll \vec{x}$, we can use the *Born approximation* to replace $\vec{x}$ by $f_K(\chi)\vec{\theta}$ within the perpendicular gravitational potential $\nabla_\perp \Phi(\vec{x}, \chi')$ of Eq. (4.2). We can also express the deflection angle $\vec{\alpha}$ as an integral of the gravitational potential along the line-of-sight :

$$\vec{\alpha}(\vec{\theta}) = \frac{2}{c^2}\int_0^\chi d\chi' \frac{f_K(\chi - \chi')}{f_K(\chi)} \nabla_\perp \Phi\left(f_K(\chi')\vec{\theta}, \chi'\right) . \tag{4.3}$$

Then, from the lens equation

$$\vec{\beta} = \vec{\theta} - \vec{\alpha}(\vec{\theta}) , \tag{4.4}$$

we can linearise it and invoke Eq. (4.3) to define a *distortion matrix* $\mathbf{A} = \partial\beta/\partial\theta$ that

maps the lensed image to its original unlensed image coordinates :

$$A_{ij} = \frac{\partial \beta_i}{\partial \theta_j} = \delta_{ij}^{\mathrm{D}} - \frac{\partial \alpha_i}{\partial \theta_j} \tag{4.5}$$

$$= \begin{pmatrix} 1 - \kappa - \gamma_1 & -\gamma_2 \\ -\gamma_2 & 1 - \kappa + \gamma_1 \end{pmatrix} \tag{4.6}$$

where κ is a scalar quantity known as the *convergence*, while γ_1 and γ_2 are the two components of the spin-2 quantity *shear*, where $\gamma = \gamma_1 + i\gamma_2$. Intuitively, convergence quantifies the magnification of the galaxy image, while shear quantifies its distortions along the major and minor axes.

In real surveys, the observable that is measured is the galaxy's *ellipticity* ϵ. It is expressed as a sum of various contributing factors [37] :

$$\epsilon = \gamma + \gamma_I + \epsilon_{\mathrm{int}} \tag{4.7}$$

where γ is its shear from Eq. (4.5), γ_I is the intrinsic shear, quantifying its alignment due to the surrounding gravitational field, and ϵ_{int} is the galaxy's intrinsic ellipticity. For perfectly circular galaxies, $\epsilon_{\mathrm{int}} = 0$. It is not possible to measure the intrinsic ellipticities of each individual galaxy; however, given the statistical nature of weak lensing, we can assume that the galaxies are randomly aligned such that on average $\langle \epsilon_{\mathrm{int}} \rangle = 0$ for an ensemble of galaxies. Its variance $\sigma^2(\epsilon_{\mathrm{int}})$ is then known as the *shape noise*. The γ_I contribution comes from *intrinsic alignment* (IA) [38, 39]. This effect arises when the tidal forces of the lensing matter cause the nearby galaxy sources to be aligned with each other, or with the underlying gravitational potential.

In the regime of weak lensing, the magnitude of the distortion of individual galaxy images is too small to be detected. Hence a large ensemble of galaxies must be analysed by calculating the correlation of their alignments and measured shapes, in order to deduce the dark matter distribution present among them and hence derive constraints on the cosmological parameters.

For a pair of lens and source galaxies, we can further decompose the shear signal into its tangential and cross components respectively :

$$\gamma_t = -\mathrm{Re}(\gamma e^{-2i\phi}) \tag{4.8}$$

$$\gamma_\times = -\mathrm{Im}(\gamma e^{-2i\phi}) \tag{4.9}$$

where ϕ is the angle between the horizontal axis of the source galaxy and the lens galaxy.

The shear 2PCF in real space can then be expressed as the expectation value of the tangential and cross components of the shear squared[40] :

$$\xi_{\pm}(\theta) = \langle \gamma_t \gamma_t \rangle (\theta) \pm \langle \gamma_\times \gamma_\times \rangle (\theta) \,, \tag{4.10}$$

which is a function of the 2D angle of separation in the sky θ.

On the other hand, it is more straightforward to arrive at the theoretical prescription of the shear correlation function in Fourier space, i.e. with the shear *angular power spectrum*. For any two observable fields A and B measured in redshift bins i and j respectively, it is given by an integration of their 3D power spectrum $P_{AB}(k, z(\chi))$ along the line of sight :

$$C_{ij}^{AB}(\ell) = \int_0^\infty d\chi \, \frac{W_i^A(\chi) W_j^B(\chi)}{f_K^2(\chi)} P_{AB}(k, z(\chi)), \tag{4.11}$$

where $W_{i,j}^{A,B}$ is the weight function of each field. In most cosmic shear analyses, it is common to bin the observed galaxies in redshift bins and cross-correlate the shear signals between two bins.

The total angular power spectrum measured from the data is that of the ellipticity field, which is then a sum of the underlying shear field and the IA contributions (ignoring noise contributions) :

$$C_{ij}^{\epsilon\epsilon}(\ell) = C_{ij}^{\gamma\gamma}(\ell) + C_{ij}^{\gamma I}(\ell) + C_{ij}^{II}(\ell) \tag{4.12}$$

where in the last two terms, the γI and II superscripts denote the contributions due to the shear-IA and IA-IA power spectra respectively. Models exist which give an approximate theoretical prescription for them, with one of the most widely employed models being the nonlinear alignment model (NLA;[41, 42]). Here, the 3D power spectrum $P^{\gamma I}(k, z)$ and $P^{II}(k, z)$ are expressed as a rescaling of the nonlinear matter power spectrum $P_{\delta\delta}^{\rm nl}(k, z)$:

$$P^{\gamma I}(k, z) = -\mathcal{A}_{\rm IA} C_1 \rho_{\rm crit} \frac{\Omega_m}{D(z)} P_{\delta\delta}^{\rm nl}(k, z) \tag{4.13}$$

$$P^{II}(k, z) = \left(\mathcal{A}_{\rm IA} C_1 \rho_{\rm crit} \frac{\Omega_m}{D(z)} \right)^2 P_{\delta\delta}^{\rm nl}(k, z) \tag{4.14}$$

where $\mathcal{A}_{\rm IA}$ is a dimensionless IA amplitude parameter, $D(z)$ is the growth factor and $C_1 = 5 \cdot 10^{-14} h^{-2} M_\odot^{-1}\text{Mpc}^3$.

Assuming a flat Universe such that $f_K(\chi) = \chi$, we focus on the cosmic shear angular power spectrum, which is given by :

$$C_{ij}^{\gamma\gamma}(\ell) = \int_0^{\chi_H} d\chi \, \frac{q_i^\gamma(\chi) q_j^\gamma(\chi)}{\chi^2} P_{\delta\delta}(k, z(\chi)), \tag{4.15}$$

where χ_H is the comoving distance to the horizon, and in this case, the weight function is given by $q^\gamma(\chi)$, the cosmology-dependent lensing efficiency :

$$q_i^\gamma(\chi) = \frac{3}{2}\Omega_{\rm m}\frac{H_0}{c^2}\int_\chi^{\chi_H} d\chi' n_i(\chi')\frac{\chi - \chi'}{\chi'} \tag{4.16}$$

with $n_i(\chi')$ the redshift distribution of the source galaxies in bin i. It is typically the case to assume the Limber approximation at small enough scales (i.e. not too large values of ℓ) such that we can easily express the k scales in the 3D matter power spectrum in terms of the 2D ℓ scales [43, 44] :

$$k = \frac{\ell + 1/2}{\chi} \tag{4.17}$$

The real space 2PFCs are then related to their Fourier space power spectrum counterparts via the Hankel transformation

$$\xi_{\pm,ij}(\theta) = \frac{1}{2\pi}\int_0^\infty d\ell \, \ell \, J_{0,4}(\ell\theta)[C_{ij}^E(\ell) \pm C_{ij}^B(\ell)] \tag{4.18}$$

where $J_{0,4}(\ell\theta)$ are the Bessel functions of the first kind at zeroth and fourth order, and $C_{ij}^{E/B}(\ell)$ are the angular power spectra of the E and B modes respectively. Here θ is then the 2D angular separation between two points in real space. Since the shear field is a spin-2 field, it can be decomposed into a curl-free and divergence-free component, respectively known as E and B modes in Fourier space. At first order, and if systematic effects are ignored, the shear field should not produce a B mode signal, therefore $C_{ij}^B(\ell) = 0$ and $C_{ij}^{\gamma\gamma} = C_{ij}^E$.

Here we have briefly presented the 2 most commonly used summary statistics, the 2PCF and angular power spectrum, to probe the correlations of the shear field and derive cosmological constraints. They are highly complementary probes that each have their advantages and disadvantages. Additionally, it should be noted that they cannot capture the non-Gaussian information embedded within the

shear field, since they only calculate second-order moments of the field.

4.3.2 Galaxy Clustering

Galaxies form in regions of matter overdensities due to gravitational collapse. Hence we can express the galaxy overdensity field $\delta_g(k, \chi)$ as a function of the underlying matter overdensity field [45] :

$$\delta_g(k, \chi) = f(\delta_{\rm DM}(k, \chi)) \tag{4.19}$$

The spatial distribution of galaxies does not necessarily trace the underlying dark matter overdensities precisely [46], necessitating a bias factor to relate these two fields. On large enough scales, we can sufficiently assume that the relation between the two fields is linear, such that $\delta_g = b_g \delta_{\rm DM}$, where b_g is known as the linear galaxy bias factor.

However when transitioning to the nonlinear regime, this approximation no longer holds, thus we have to introduce a new correlation coefficient function $r(k, \chi)$ that encapsulates the *stochastic biasing* between the two fields [47, 48] :

$$r(k, \chi) = \frac{P_{g\delta}(k, \chi)}{\sqrt{P_{gg}(k, \chi) \times P_{\delta\delta}(k, \chi)}} \tag{4.20}$$

where $P_{g\delta}$ is the cross power spectrum between the galaxy and matter overdensity, $P_{\delta\delta}$ is the matter power spectrum and P_g is the galaxy power spectrum, given by $P_{gg} = b_g^2 P_{\delta\delta}$.

Galaxy clustering (or more specifically *photometric* galaxy clustering) is thus the study of the correlation between galaxy positions on a 2D plane. The observable in this case is the real space galaxy clustering correlation function often denoted as$w(\theta)$, where one commonly used estimator is the Landy-Slazay estimator [49] :

$$w(\theta) = \frac{DD(\theta) - 2DR(\theta) + RR(\theta)}{RR(\theta)} \tag{4.21}$$

where given the data catalogue and a random catalogue, DD is the number of galaxy pairs, DR is the number of galaxy-random pairs and RR the number of random pairs with angular separation between θ and $\theta + \delta\theta$.

Ignoring higher-order effects such as magnification and redshift space distortions (RSD), we can obtain the theoretical expression for the galaxy clustering an-

gular power spectrum :

$$C_{ij}^{gg}(\ell) = \int_0^{\chi_H} d\chi \, \frac{q_i^g(\chi) q_j^g(\chi)}{\chi^2} P_{\delta\delta}\left(\frac{\ell + 1/2}{\chi}, z(\chi)\right) \tag{4.22}$$

where we have once again assumed the flat-sky and Limber approximations. The clustering weight function in redshift bin i, $q_i^g(\chi)$ is the product of the lens galaxy redshift distribution and the galaxy bias :

$$q_i^g(\chi) = b_g\left(\frac{\ell + 1/2}{\chi}, \chi\right) n_i(\chi). \tag{4.23}$$

Once again the galaxy clustering power spectrum is then related to its real space counterpart by :

$$C_{ij}^{gg}(\ell) = 2\pi \int_0^{\infty} d\theta \, \theta \, w(\theta) J_0(\ell\theta). \tag{4.24}$$

4.3.3 Galaxy - Galaxy Lensing

Finally, we can cross-correlate the shear signal of the source galaxies at higher redshifts with the positions of the lens galaxies at lower redshifts, to obtain a probe known as *galaxy-galaxy lensing*.

The main observable is the tangential shear $\gamma_t(\theta)$. Analogous to the cosmic shear and galaxy clustering correlation functions, it can be expressed in terms of the galaxy-galaxy lensing cross-correlation function through a Hankel transform :

$$\gamma_{ij,t}(\theta) = \frac{1}{2\pi} \int_0^{\chi_H} d\ell \, \ell \, J_2(\ell\theta) C_{ij}^{g\gamma}(\ell) \tag{4.25}$$

where $J_2(\ell\theta)$ is the Bessel function of the first kind at second order, and the theoretical expression for $C_{ij}^{g\gamma}$ is given by

$$C_{ij}^{g\gamma}(\ell) = \int_0^{\chi_H} d\chi \, \frac{q_i^g(\chi) q_j^{\gamma}(\chi)}{\chi^2} r\left(\frac{\ell + 1/2}{\chi}, \chi\right) P_{\delta\delta}\left(\frac{\ell + 1/2}{\chi}, z(\chi)\right). \tag{4.26}$$

The three probes of cosmic shear, galaxy clustering, and galaxy-galaxy clustering thus form a highly complementary set of observables, known as '3x2pt', with which to study the LSS and especially probe the expansion history of the Universe at small scales. In the past two decades, a wealth of data has been built up from numerous past and ongoing ground-based and space-based galaxy surveys. The Baryonic Observation Spectroscopic Survey (BOSS ;[50]), the Dark Energy Survey (DES ;

[51]) and the Dark Energy Spectroscopic Instrument (DESI, [52]) have been collecting both photometric and spectroscopic data on galaxy clustering. Weak lensing surveys include the Canada-France-Hawaii Telescope Lensing Survey (CFHTLenS; [53]), the Kilo-Degree Survey (KiDS; [54]), and ongoing surveys such as the Hyper-Suprime Cam (HSC; [55]), the Dark Energy Survey (DES; [56]), *Euclid* [57] and the forthcoming Legacy Survey of Space and Time (LSST;[58]) will continue to push the boundaries of weak lensing and galaxy clustering measurement techniques, with improved systematics and larger datasets that will refine measurement accuracy and precision.

4.4 Cosmic Microwave Background

The CMB is an important probe that contains a wealth of information about the Universe at early times. At redshift $z \sim 1100$, the Universe had expanded and cooled sufficiently such that electrons and baryons *recombined*, causing photons to decouple from this opaque plasma and stream freely towards us. The original point from which these photons came can be thought of as a spherical surface also known as the *surface of last scattering*. These photons carry information about the temperature and velocity of the primordial plasma, informing us about the history and composition of the early Universe as far back as we can ever go.

The CMB is a blackbody spectrum at 2.75K. These CMB photons propagate through a perturbed Universe towards us, hence we can theoretically derive an expression for their temperature anisotropies as a function of direction $\vec{n}$, with 4 main contributions [59] :

$$\frac{\Delta T}{T_0} = \frac{\delta_r(\tau_*)}{4} + \Psi(\tau_*) - \Psi_0 + \vec{n}\cdot(\vec{v_0} - \vec{v}) + \int_{\tau_*}^{\tau_0} d\tau(\Psi' - \Phi') \tag{4.27}$$

The first term $\frac{\delta_r(\tau_*)}{4}$ is the contribution due to the radiation perturbation δ_r to the temperature anisotropies at recombination time τ_*; the $(\Psi(\tau_*) - \Psi_0)$ term accounts for the difference in the gravitational potential at the surface of last scattering $\Psi(\tau_*)$ and at present (denoted by a 0 subscript), which is dependent on the direction the photon is propagating from. This is known as the Sachs-Wolfe effect. The third term $\vec{n}\cdot(\vec{v_0} - v)$ is the Doppler shift due to the photons having different peculiar velocities $\vec{v}$ depending on their direction of propagation. Lastly, the integration term arises from the *integrated* Sachs-Wolfe effect, which takes into account the change in the

gravitational potential as the photons are travelling in and out of a gravitational well. Hence we see how the temperature anisotropies are sensitive to many different aspects of the expansion history : the primordial density and velocity perturbations, the evolution of gravitational potentials, which in turn are dictated by the matter content of the Universe, as well as the curvature of the Universe, which will impact the path of the photons.

Since we are mapping these temperature anisotropies on a spherical sky, it is more convenient to express ΔT in spherical harmonics :

$$\Theta(\vec{n}) = \frac{\Delta T}{T_0}(\vec{n}) = \sum_{\ell m} T_{\ell m} Y_{\ell m}(\vec{n}) \tag{4.28}$$

where the CMB temperature angular power spectrum is then defined as

$$C_\ell^{TT} = \left\langle |T_{\ell m}|^2 \right\rangle \, , \tag{4.29}$$

which is the primary observable when measuring the CMB. Here, the TT superscript indicates that it is the auto-correlation of the temperature-temperature fields. Since we expect perturbations to be Gaussian distributed and very small during the Radiation-Dominated Era (RDE), it is hence reasonable to assume that the CMB temperature anisotropy field can be fully specified by its variance, i.e. by its C_ℓ's.

The space-based *Planck* experiment [60] mapped the most precise values of the CMB power spectrum to date. In Fig. 4.2 we show the latest results from the *Planck* 2018 Data Release 4 (DR4) [61]. We see that the data points in red are in excellent agreement with a ΛCDM model (best fit in blue). From the shape and amplitude of the CMB power spectrum, we are able to very tightly constrain various cosmological parameters, such as A_s, n_s, τ_reio and Ω_b, evident also from Eq. (4.27).

Additionally, these CMB photons get *polarised* as they propagate through the Universe, due to Thomson scattering off of free electrons at the surface of last scattering as well as during the *epoch of reionisation* ($6 \lesssim z \lesssim 10$) when the first galaxies formed, creating regions of ionised hydrogen and electrons. We can decompose the spin-2 polarisation field into a 'gradient' and 'curl' mode (i.e. the E and B modes), measure their amplitudes, and express them as polarisation auto- and cross-correlation power spectra :

$$C_\ell^{EE} = \langle E_{\ell m}^* E_{\ell m} \rangle \tag{4.30}$$

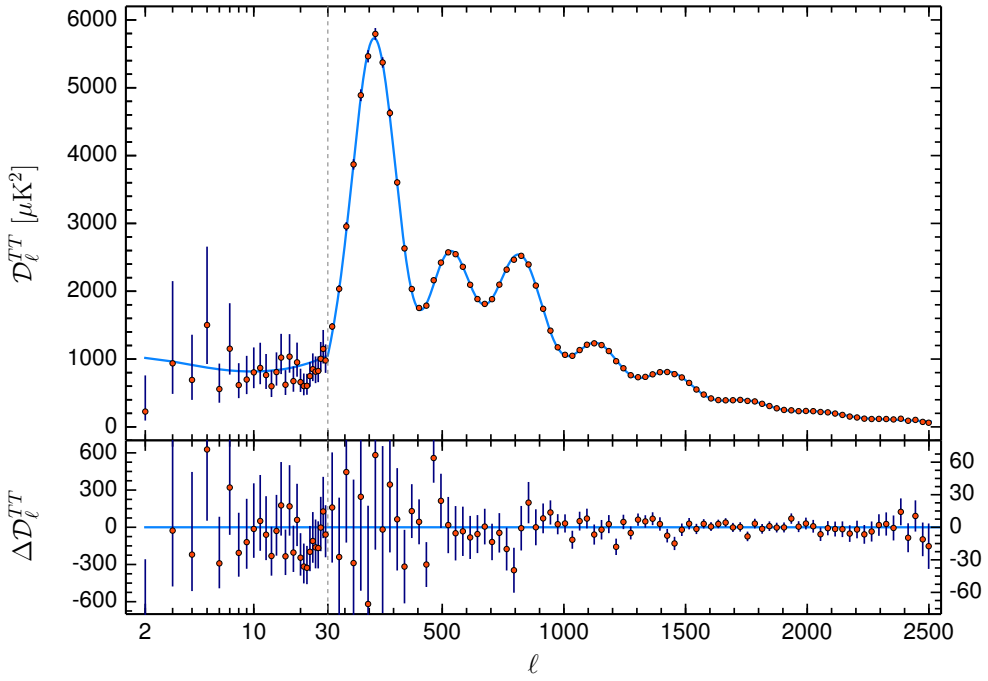

Fig. 4.2. Top panel : CMB temperature power spectrum (denoted here as $\mathcal{D}_\ell^{TT}$) as reported in *Planck* DR4 [61]. The red dots denote the data points binned in ℓ, while the blue solid line represents the ΛCDM best-fit with the *Planck* TTTEEE+low l+lensing likelihood. Bottom panel : Residuals with respect to the best-fit model. Plot taken from [61].

$$C_\ell^{BB} = \langle B_{\ell m}^* B_{\ell m} \rangle \tag{4.31}$$

$$C_\ell^{TE} = \langle E_{\ell m}^* T_{\ell m} \rangle \tag{4.32}$$

From theory, Thomson scattering due to density perturbations produces only E-mode polarisation, thus the presence of B-modes could only be due to systematics or indicate the presence of tensor perturbations such as gravitational waves and gravitational lensing.

The CMB photons are also subject to gravitational lensing due to the Large Scale Structure at low redshifts. For example, this will shift both the temperature and polarisation anisotropies by [62] (here we only quote the temperature anisotropies for simplicity) :

$$\tilde{\Theta}(\vec{n}) = \Theta(\vec{n} + \nabla\phi(\vec{n})) \tag{4.33}$$

where $\phi(\vec{n})$ is the lensing potential (as seen in Sect. 4.3.1), the line-of-sight projection

of the gravitational potential :

$$\phi(\vec{n}) = -2 \int d\tau \frac{\chi(\tau - \tau_*)}{\chi(\tau_*)\chi(\tau)} \Phi(\chi\vec{n}, \tau) \tag{4.34}$$

As such we can define a quadratic CMB lensing power spectrum [63]

$$C_\ell^{\phi\phi} = \langle \phi_{\ell m} \phi^*_{\ell m} \rangle \,, \tag{4.35}$$

thus allowing us to constrain the dynamics of late-time physics with the CMB as well.

Other recent ground-based CMB experiments, such as the Atacama Cosmology Telescope (ACT; [64]) and the South Pole Telescope Third Generation (SPT-3G; [65]), have also measured the CMB temperature power spectrum up to higher ℓ multipoles than *Planck*. Fig. 4.3 shows the 2D marginalised posterior distributions of the cosmological parameters $\{H_0, \Omega_{\rm b}h^2, \Omega_{\rm DM}h^2, A_{\rm s}, \tau_{\rm reio}, n_{\rm s}, 100\theta_{\rm MC}\}$ as obtained by the three different experiments, where $\theta_{\rm MC}$ is the ratio r_s/D_M and r_s is the distance travelled by sounds waves up until recombination, or the *sound horizon* at recombination. Interestingly, we see a slight tension between ACT and *Planck*/SPT at $\sim 2\sigma$ level, assuming a ΛCDM model.

We thus see how the CMB has proven to be an extremely useful probe in constraining the various parameters of our cosmological model, insofar as being one of the most precise probes to date. It is also the highest redshift dataset we have observed to date, giving us an insight into the physics of the early time Universe. Hence it would be of interest to exploit the power of the CMB in constraining extended ΛCDM models, as we shall discuss in the next Chapter.

4.5 Bayesian Inference

In the past two decades, Bayesian statistics have been increasingly adopted as the standard method of cosmological inference, whereby the parameters of interest are assumed to be random variables following probability distributions [67, 68]. Bayesian statistical analyses rely on *Bayes' Theorem*, which gives the probability distribution of the parameters θ given a model M and the observed data d. This probability distribution $P(\theta|d, M)$, called the *posterior distribution*, is defined as

$$P(\theta|d, M) = \frac{\mathcal{L}(d|\theta, M)\Pi(\theta|M)}{\mathcal{Z}(d|M)}, \tag{4.36}$$

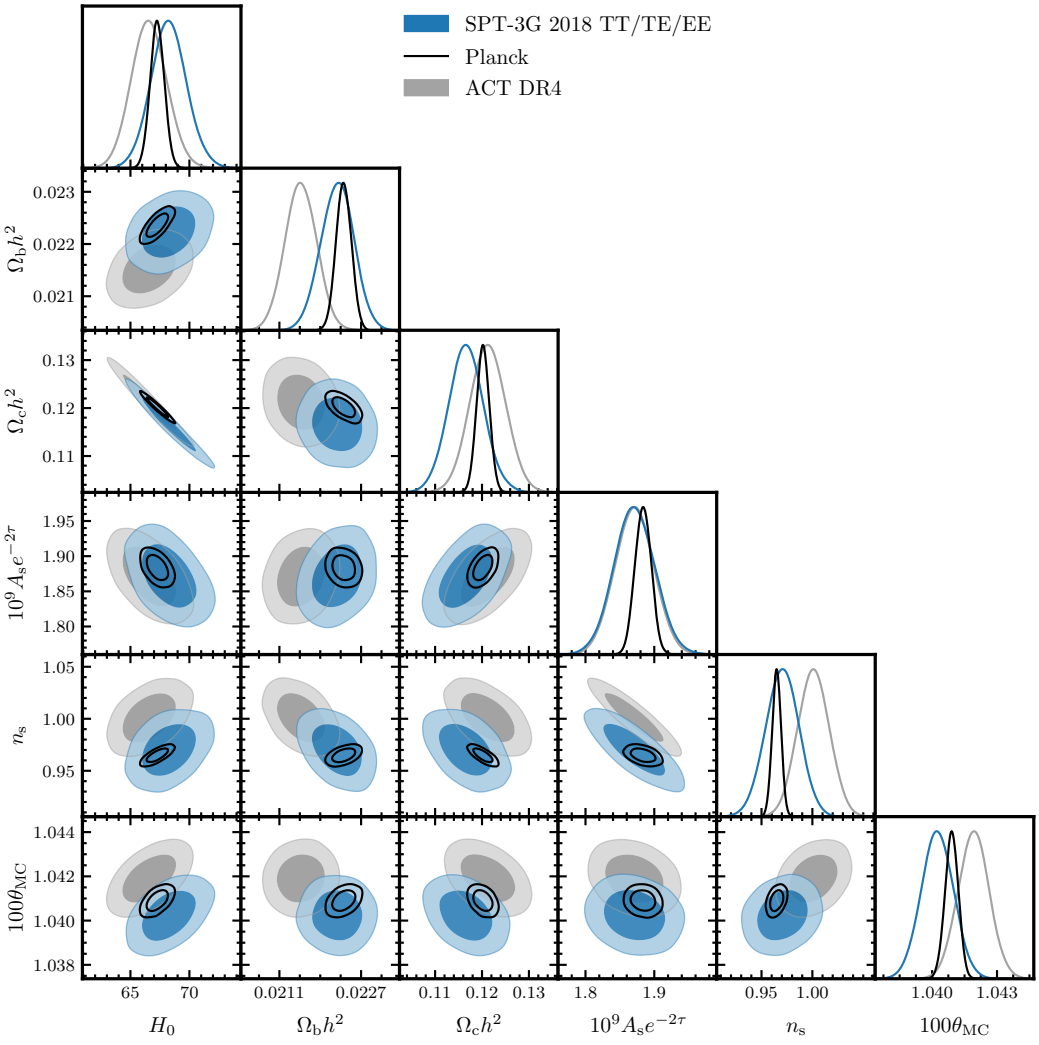

Fig. 4.3. Marginalised 2D posterior constraints on the various cosmological parameters, derived from SPT-3G (blue), *Planck* (black solid line) and ACT (grey). Plot taken from [66].

where $\Pi(\theta|M)$ is the *prior distribution*, quantifying our initial knowledge of the distribution of θ; $\mathcal{Z}(d|M)$ is the *evidence*, which gives the probability of observing the data given M; $\mathcal{L}(d|\theta, M)$ is known as the *likelihood function* : the probability of observing the data d given the model M with parameter values θ.

The likelihood $\mathcal{L}$, which incorporates the underlying assumptions of the model M, serves as a probability distribution assessing the goodness-of-fit between that model, characterised by a specific set of parameter values θ, and the observed experimental data d. A primary focus in cosmology is determining the compatibility of cosmological models, such as the concordance model or its variants, with the avai-

lable data. Hence, it is imperative to establish a link between the observed data d and its theoretical predictions derived from the model.

In most cases, it is sufficient to express the likelihood $\mathcal{L}$ as a multivariate Gaussian distribution function :

$$-2\log\mathcal{L} \propto [d - T(\theta)]^T C^{-1}[d - T(\theta)], \tag{4.37}$$

where d is the data vector, $T(\theta)$ is the theory vector derived from the model, C is the covariance matrix of the data d which captures the correlations between the parameters, and i is the number of variables of the dataset d.

4.5.1 Sampling the Posterior Distribution

The primary objective of contemporary cosmological analyses involves deriving the posterior distribution $P(\theta|d, M)$ to find the best-fit set of parameters given the data. This entails exploring the parameter space and assessing the model-data fit across a broad range of values within the prior. However, having to evaluate the posterior distributions $P(\theta|d, M)$ in a large dimensional parameter space that is sometimes highly correlated poses considerable challenges. Hence, numerical techniques are indispensable for sampling the posterior distribution computationally.

Markov Chain Monte Carlo Methods

One of the most common methods to numerically derive the posterior distribution is by exploring the parameter space iteratively, and drawing independent random samples from it to build up the desired distribution : this process is also known as the Monte Carlo method. The resultant ensemble of points makes up what is known as a Markov chain, which then, when converged, matches the target posterior distribution. The most common algorithm for Markov Chain Monte Carlo (MCMC) techniques is the *Metropolis-Hastings* random walk [69-71]. This algorithm involves first drawing samples from the prior distribution and at each iteration, determining whether to "jump" to a new set of parameters x_{i+1} or stay at the current step x_i, with a probability

$$A(x_{x+i}|x_i) = \min\left(1, \frac{P(x_{i+1})q(x|x_{i+1})}{P(x_i)q(x_{i+1}|x_i)}\right) \tag{4.38}$$

where $q(x_{i+1}|x_i)$ is some specified proposal distribution, usually considered Gaussian.

To test for convergence (i.e. if the points drawn adequately mimic the true posterior distribution), one can calculate the Gelman-Rubin R statistic [72, 73], which is the ratio of the variation between chains to the variation within a chain. Specifically, for J number of chains with L number of samples $x_1^{(j)}, x_2^{(j)}, ..., x_L^{(j)}$(after burn-in has been discarded),

$$\bar{x}_j = \frac{1}{L}\sum_{t=1}^{L} x_t^{(j)} \tag{4.39}$$

$$\bar{x} = \frac{1}{J}\sum_{j=1}^{J} \bar{x}_j \tag{4.40}$$

$$B = \frac{L}{J-1}\sum_{j=1}^{J}(\bar{x}_j - \bar{x})^2 \tag{4.41}$$

$$s_j^2 = \frac{1}{L-1}\sum_{t=1}^{L}(x_t^{(j)} - \bar{x}_j)^2 \tag{4.42}$$

$$W = \frac{1}{J}\sum_{j=1}^{J} s_j^2 \tag{4.43}$$

$$R = \frac{\frac{L-1}{L}W + \frac{1}{L}B}{W}\,. \tag{4.44}$$

Typically, a chain with $R-1$ value of $R-1 < 0.02$ is considered to be converged.

Several implementations of the *Metropolis-Hastings* MCMC algorithm exist that are widely used in cosmology, such as within the `MontePython` [74], `CosmoMC` [75], its updated Python version `Cobaya` [76] and `CosmoSIS` [77] libraries.

Nested Sampling

In a high dimensional space, simultaneously drawing samples from the posterior distributions of multiple parameters can be a slow and computationally intensive task, especially in light of Stage IV survey analysis requirements. Hence alternatives in place of conventional MCMC methods have been proposed, notably the technique of *nested sampling* [78]. In nested sampling algorithms, the evidence $\mathcal{Z}(d|M)$ is the main quantity of interest. It is given by the integral

$$\mathcal{Z} = \int \mathcal{L}(\theta)\Pi(\theta)\, d\theta\,. \tag{4.45}$$

Calculating the evidence has the added advantage of allowing one to conduct *model comparison*– determining which of two competing models the observed data is a better fit to. Model comparison requires calculating *Bayes factor* B, the ratio of the evidence of the two models in question :

$$B \equiv \frac{\mathcal{Z}(d|M_1)}{\mathcal{Z}(d|M_2)}, \tag{4.46}$$

hence necessitating the value of $\mathcal{Z}$.

There are currently several state-of-the-art implementations of nested sampling for Bayesian inference, notably `PolyChord` [79, 80]. This algorithm implements a *slice sampling* method [81] to efficiently sample from within the iso-likelihood contour. First, the multidimensional sample space is affine transformed (or "*whitened*") such that it is of size $\sim \mathcal{O}(1)$ in every direction. Then a new sample is drawn from within this sampling space by "slicing" it in one dimension, and drawing the new sample within the slice. This allows sampling in a high dimensional space while taking into account degeneracies between correlated parameters. `PolyChord` has been used in the latest Stage III LSS survey analyses [82, 83] and has proven to give robust and accurate posteriors [84].

IN BRIEF

In this Chapter, I introduced the main probes of 3x2pt and the CMB, which I will be using to constrain a new cosmological model in the following Chapter. I explained how the LSS and the CMB are sensitive to the physics of the late time and early time Universe respectively, and discussed how we can obtain constraints from them. Moreover, it is worth noting that the LSS and CMB, since they probe distinctly different epochs in cosmic evolution, can form highly complementary datasets that have the potential to break degeneracies between the cosmological parameters, while possessing completely independent systematics.

Finally, I touched on Bayesian statistical theory, an important concept when conducting cosmological parameter inference. With these two Chapters, the stage is set to introduce the main thrust of this thesis : using a range of datasets including LSS and CMB to derive constraints for a new cosmological model.

5. Tomographic Coupled Dark Energy

Sommaire

5.1 Introduction

In this Chapter, we shall introduce a cosmological model alternative to ΛCDM : the *coupled dark energy* (CDE) model, which was first proposed almost three decades ago [85, 86]. The CDE model postulates the existence of a *quintessence*, or scalar field ϕ, as a candidate for dark energy, responsible for the late time accelerating expansion of the Universe. The concept of scalar fields is prevalent in many aspects of fundamental physics, and the case of a cosmological quintessence field has been shown to provide an elegant solution to the *'coincidence problem'* [87], the question of why the current energy densities of dark energy and dark matter should be of equal magnitude, and the *'cosmological constant problem'*, why the measured value of the vacuum energy density ρ_Λ should differ from theoretical derivations based on quantum field theory by up to 120 orders of magnitude [88].

All these reasons make coupled quintessence models a noteworthy alternative to ΛCDM, which also explains why it is still an active field of study today [89-120]. Thus in this Chapter, I shall investigate the CDE model in more detail and highlight its differences from ΛCDM. I will also introduce a novel parameterisation that I have developed [121], which I term the *tomographic CDE model*, and describe how I have obtained constraints on it by employing a range of observational datasets.

5.2 Theoretical Framework

CDE cosmologies suppose that a non-minimal coupling exists between the canonical scalar field ϕ and the matter components of the Universe, which we take to be fermionic DM particles.

We begin with the Einstein-Hilbert action of a scalar field :

$$\mathcal{S} = \int d^4x \sqrt{-g} \left[-\frac{1}{2\kappa^2} R + \mathcal{L}_{\rm dark} \right] \tag{5.1}$$

where $\kappa = \sqrt{8\pi G}$, g is the determinant of the metric tensor $g_{\mu\nu}$, and $\mathcal{L}_{\rm dark}$ is the Lagrangian for the dark sector, expressed as

$$\mathcal{L}_{\rm dark} = -\partial_\mu \phi \partial^\mu \phi - V(\phi) - m_{\rm DM}(\phi)\bar{\phi}\phi + \mathcal{L}_{\rm kin}[\phi] \,, \tag{5.2}$$

with ϕ the wavevector of the DM particle, $\mathcal{L}_{\rm kin}[\phi]$ the DM kinetic term and $V(\phi)$ the potential of the field. Hence ϕ mediates an interaction between the DM particles, causing them to experience a fifth force in addition to the standard gravitational attraction. We also note that the baryonic sector is not coupled to ϕ, so the model automatically fulfils the very stringent local constraints on the weak equivalence principle and screened fifth forces [122-125].

We can define the following two covariant conservation equations of the energy-momentum tensor $T_{\mu\nu}$, concerning the scalar field and DM components respectively :

$$\nabla^\mu T^\phi_{\mu\nu} = \kappa\beta T^{\rm DM} \nabla_\nu \phi \quad ; \quad \nabla^\mu T^{\rm DM}_{\mu\nu} = -\kappa\beta T^{\rm DM} \nabla_\nu \phi \,, \tag{5.3}$$

with $T^{\rm DM} = g^{\mu\nu} T^{\rm DM}_{\mu\nu}$. The total energy-momentum tensor of the dark sector is thus conserved; i.e. $\nabla^\mu (T^\phi_{\mu\nu} + T^{\rm DM}_{\mu\nu}) = 0$.

As we can see on the right-hand side of Eq. (5.3), we have introduced a new

dimensionless coupling parameter β, defined as

$$\beta \equiv -\frac{1}{\kappa}\frac{\partial \ln m(\phi)}{\partial \phi}. \tag{5.4}$$

This coupling parameter quantifies the strength of coupling between ϕ and the DM particles.

The DM particles thus interact with the field through their field-dependent mass term, $m_{\rm DM} = m_{\rm DM}(\phi)$. In this model, we assume a dilaton-like interaction $m_{\rm DM}(\phi) = m_0 \exp(-\beta\kappa\phi)$ [126-129], with $\beta(\phi) = \beta\, m_0 \exp(-\beta\kappa\phi)/m_{\rm DM}(\phi)$, allowing for a transition from $\beta(\phi) \sim \beta$ to $\beta(\phi) \sim 0$.

5.2.1 Background Modifications

Here, we highlight the modifications to the cosmological background equations due to the presence of such a coupling between DM and ϕ. Once again assuming a flat FLRW metric where DM and the scalar field behave as perfect fluids, we can solve the Einstein Field equations with a modified $T_{\mu\nu}^{\rm DM;\phi}$, arriving at the relevant conservation equations for DM and ϕ respectively :

$$\rho'_{\rm DM} + 3\mathcal{H}\rho_{\rm DM} = -\kappa\beta\rho_{\rm DM}\phi'\,, \tag{5.5}$$

$$\rho'_{\phi} + 3\mathcal{H}(\rho_{\phi} + p_{\phi}) = \kappa\beta\rho_{\rm DM}\phi'\,, \tag{5.6}$$

where the prime denotes a derivative with respect to conformal time τ, and $\kappa = \sqrt{8\pi G}$ is the reduced Planck mass. The right-hand side of Eqs. (5.5) and (5.6) tell us that a non-zero coupling has a considerable impact on the background dynamics only when the DM fraction is non-negligible, i.e. from the matter-dominated era (MDE) onwards.

From Eq. (5.3) we can also derive the energy density and pressure terms of the scalar field, ρ_ϕ and p_ϕ :

$$\rho_\phi = \frac{(\phi')^2}{2a^2} + V(\phi) \quad ; \quad p_\phi = \frac{(\phi')^2}{2a^2} - V(\phi)\,, \tag{5.7}$$

Substituting Eq. (5.6) into Eq. (5.7), we obtain the modified Klein-Gordon equation governing the evolution of the scalar field :

$$\phi'' + 2\mathcal{H}\phi' + a^2\frac{\partial V}{\partial \phi} = \kappa\beta a^2\rho_{\rm DM}\,, \tag{5.8}$$

The scalar field potential $V(\phi)$ can also accelerate ϕ at different epochs of the cosmic expansion, depending on its form. For simplicity, however, we will only consider a constant potential, i.e.

$$V(\phi) = V_0, \tag{5.9}$$

which is responsible for the late-time acceleration of the Universe and has no impact on the scalar field dynamics at high redshifts. Thus CDE models can be considered as a class of 'thawing' dark energy models, whereby the field is initially frozen due to the dominance of the Hubble damping term, only recently starting to roll down to the potential minima [130].

5.2.2 Perturbation Modifications

We now highlight the relevant perturbation equations in CDE cosmologies. Here, we express the overdensities of DM and ϕ as $\delta\rho_{\rm DM} \equiv \delta_{\rm DM}$ and $\delta\phi$.

We work in the synchronous gauge. Consider the modified perturbations of DM and ϕ by solving

$$\delta(\nabla^\mu T^\phi_{\mu\nu}) = \delta(\kappa\beta T^{\rm DM}\nabla_\nu\phi). \tag{5.10}$$

This leads to a second-order ODE for the evolution of the perturbed scalar field $\delta\phi$:

$$\delta\phi'' + 2\mathcal{H}\delta\phi' + \left(k^2 + a^2\frac{\partial^2 V}{\partial\phi^2}\right)\delta\phi + \frac{h'}{2}\phi' = \kappa\rho_{\rm DM}a^2\left(\beta\delta_{\rm DM} + \frac{\partial\beta}{\partial\phi}\delta\phi\right), \tag{5.11}$$

whereas the evolution of the DM density contrast $\delta_{\rm DM}$ and velocity divergence $\theta_{\rm DM}$ take the following form, respectively :

$$\delta'_{\rm DM} = -\theta_{\rm DM} - \frac{h'}{2} - \kappa\beta\delta\phi' - \kappa\frac{\partial\beta}{\partial\phi}\phi'\delta\phi \tag{5.12}$$

$$\theta'_{\rm DM} = (-\mathcal{H} + \kappa\beta\phi')\theta_{\rm DM} - k^2\kappa\beta\delta\phi. \tag{5.13}$$

The perturbed density and pressure terms of the scalar field are then

$$\delta_\phi = \frac{\phi'\delta\phi'}{a^2} + \frac{\partial V}{\partial\phi}\delta\phi \quad ; \quad \delta p_\phi = \frac{\phi'\delta\phi'}{a^2} - \frac{\partial V}{\partial\phi}\delta\phi \tag{5.14}$$

and its velocity divergence is given by

$$\theta_\phi = k^2\delta\phi/\phi'\,. \tag{5.15}$$

At subhorizon scales, i.e. for $k \gg \mathcal{H}$, under a reasonably slow evolution of β satisfying $\partial\beta/\partial(\kappa\phi) \leq \mathcal{O}(1)$, we can approximate the following equation for the evolution of $\delta_{\rm DM}$:

$$\delta''_{\rm DM} + \left[\mathcal{H} - \beta\kappa\phi'\right]\delta'_{\rm DM} - \frac{\kappa^2 a^2}{2}\left[\rho_{\rm b}\delta_{\rm b} + \rho_{\rm DM}\delta_{\rm DM}(1+2\beta^2)\right] = 0\,. \tag{5.16}$$

Regardless of the sign of β, the last term of Eq. (5.16) is enhanced by the presence of a non-minimal coupling. On the other hand, the friction term (the factor in front of $\delta'_{\rm DM}$) decreases if the sign of β does not change throughout cosmic history. These two effects lead to a change in the clustering of matter in the Universe as compared to ΛCDM, for fixed initial conditions. For a constant β the DM density contrast evolves as $\delta_{\rm DM} \sim a^{1+2\beta^2}$ during the MDE.

Another point worth noting is the possibility of the sign of β changing in time, since, from a phenomenological point of view, it is not impossible to consider a negative coupling. This could lead to periods of cosmic history with a larger friction term, which would slow down the evolution of $\delta_{\rm DM}$. However, we restrict ourselves to $\beta \geq 0$ in this study for simplicity.

5.2.3 Tomographic Coupling

As we have demonstrated, studies of CDE cosmologies have evolved into a mature and robust field of research. Yet in almost every case, the coupling parameter β has only been considered as a non-varying parameter. However, varying couplings have already been considered in other paradigms, such as in the case of a vacuum dark energy interaction with dark matter particles [131, 132], between dark matter particles themselves (see eg. [133-136]) and analogously, between neutrino particles [137, 138]. So, *why not in CDE cosmologies too?*

Hence, we set out to investigate the following questions : what is the impact of a varying coupling on the main cosmological observables? Up to what extent can we constrain this evolution with current data? Is the coupling strength similarly bounded in all the stages of cosmic expansion? Would we be able to achieve a similar, or even better, degree of alleviation of the H_0 tension with a varying coupling?

To this end, I propose a new phenomenological *'tomographic coupling'* parameterisation, in which we allow for different amplitudes of coupling at different epochs of cosmic evolution. Instead of exploring specific functional forms of $\beta = \beta(\phi)$, we opt to make use of a more general expression for the coupling, written directly in

terms of the redshift, i.e. $\beta = \beta(z)$, which is easy to interpret and visualise.

We bin the coupling strength parameter in different redshifts and constrain the amplitude of coupling within each redshift bin independently. To do this, we consider a smooth function built from hyperbolic tangents,

$$\beta(z) = \frac{\beta_1 + \beta_n}{2} + \frac{1}{2}\sum_{i=1}^{n-1}(\beta_{i+1} - \beta_i)\tanh[s_i(z - z_i)]\,, \tag{5.17}$$

where n is the number of redshift bins and z_i is the redshift upper limit of the $i_{\rm th}$ bin. We can easily express the derivatives of β appearing in Eqs. (5.11) and (5.12) as follows,

$$\frac{\partial\beta}{\partial\phi} = -\frac{\partial\beta}{\partial z}\frac{\mathcal{H}}{a\phi'}\,, \tag{5.18}$$

with

$$\frac{\partial\beta}{\partial z} = \frac{1}{2}\sum_{i=1}^{n-1}\frac{s_i(\beta_{i+1} - \beta_i)}{\cosh^2[s_i(z - z_i)]}\,. \tag{5.19}$$

The constants s_i are smoothing factors that control the steepness of $\beta(z)$ when transitioning between tomographic bins. They have to be chosen such that they allow to reach the values of β_i in the $i_{\rm th}$ bin $\forall i \in [1, n]$. In Fig. 5.1 we plot an example form that $\beta(z)$ could take, assuming a 3-bin model with bin edges $z = \{0, 100, 1000\}$.

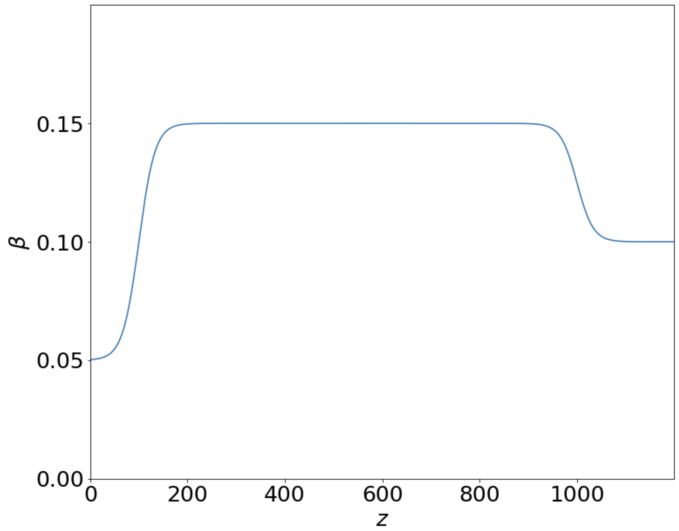

Fig. 5.1. Example of $\beta(z)$ with three bins, using $s_i = 0.03$ for $i = 1, 2$ and arbitrarily chosen values of $\beta_1 = 0.05$ ($z \lesssim 10^2$), $\beta_2 = 0.15$ ($10^2 \lesssim z \lesssim 10^3$), $\beta_3 = 0.10$ ($z \gtrsim 10^3$).

In Fig. 5.2 we plot the linear matter power spectrum and the CMB temperature

power spectrum obtained when we switch on the coupling in only one bin of the 3 bins to understand the effects that an early-, mid- and late-time coupling can have on these cosmological observables. To ensure a fair comparison between the resulting curves, we fix in all the cases studied in this figure the same values of the standard cosmological parameters $n_{\rm s}$, $A_{\rm s}$, $\tau_{\rm reio}$, $\omega_{\rm b}$, the cosmological constant V_0, and the initial value of the DM energy density (at $z_{\rm ini} = 10^{14}$) following *Planck* ΛCDM best-fit cosmology. Thus, the differences between these curves are only due to the activation of the different coupling windows and the value they take on.

Fig. 5.2 shows that the matter power spectrum is most sensitive to the coupling in the first two tomographic bins and, more conspicuously, in the first one, i.e., at $z < \mathcal{O}(10^2)$. This is because this is the period of the cosmic expansion at which the scaling solution is typically reached by the scalar field (cf. the lower left plot of Fig. 5.3) and, hence, when the fifth force leaves a larger imprint on the structure formation processes. In all cases, we see that a non-null coupling generates an increase in the amplitude of matter fluctuations regardless of the activation bin, as already discussed in Sect. 5.2.2. Regarding the CMB TT power spectra, we observe that the peaks are enhanced and move to larger multipoles for larger values of the coupling. The enhancement is bigger when the coupling is activated in the pre-recombination epoch, since it decreases the ratio $\rho_{\rm DM}/\rho_{\rm b}$, whereas the shift to larger multipoles is more important when the coupling is switched on at $z < 1000$, in the first two bins. This is because, for fixed initial conditions, we have a lower amount of dark matter at the decoupling time and very small redshifts. The lowering of $H(z)$ leads to a larger sound horizon at the baryon-drag epoch r_s and a larger angular diameter distance to the last scattering surface, but the late-time effect is more important and this is why the angle subtended in the sky by r_s decreases. When the coupling is only activated in the third bin, i.e. at $z \gtrsim 1000$, the shifts induced in the power spectra are in general much smaller than those found when the coupling is switched on after decoupling, as the DM fraction in the pre-recombination epoch is smaller and so are the source terms in the background conservation equations for DE and DM, i.e. the right-hand side of Eqs. (5.5) and (5.8).

Subsequently, in Fig. 5.3, we show the evolution of several background quantities obtained again with the 3-bin tomographic model, fixing the initial conditions in all cases as in Fig. 5.2. In particular, we highlight the effect that initialising the coupling β at different redshifts has on the late-time evolution of $H(z)$ and the ϕ and

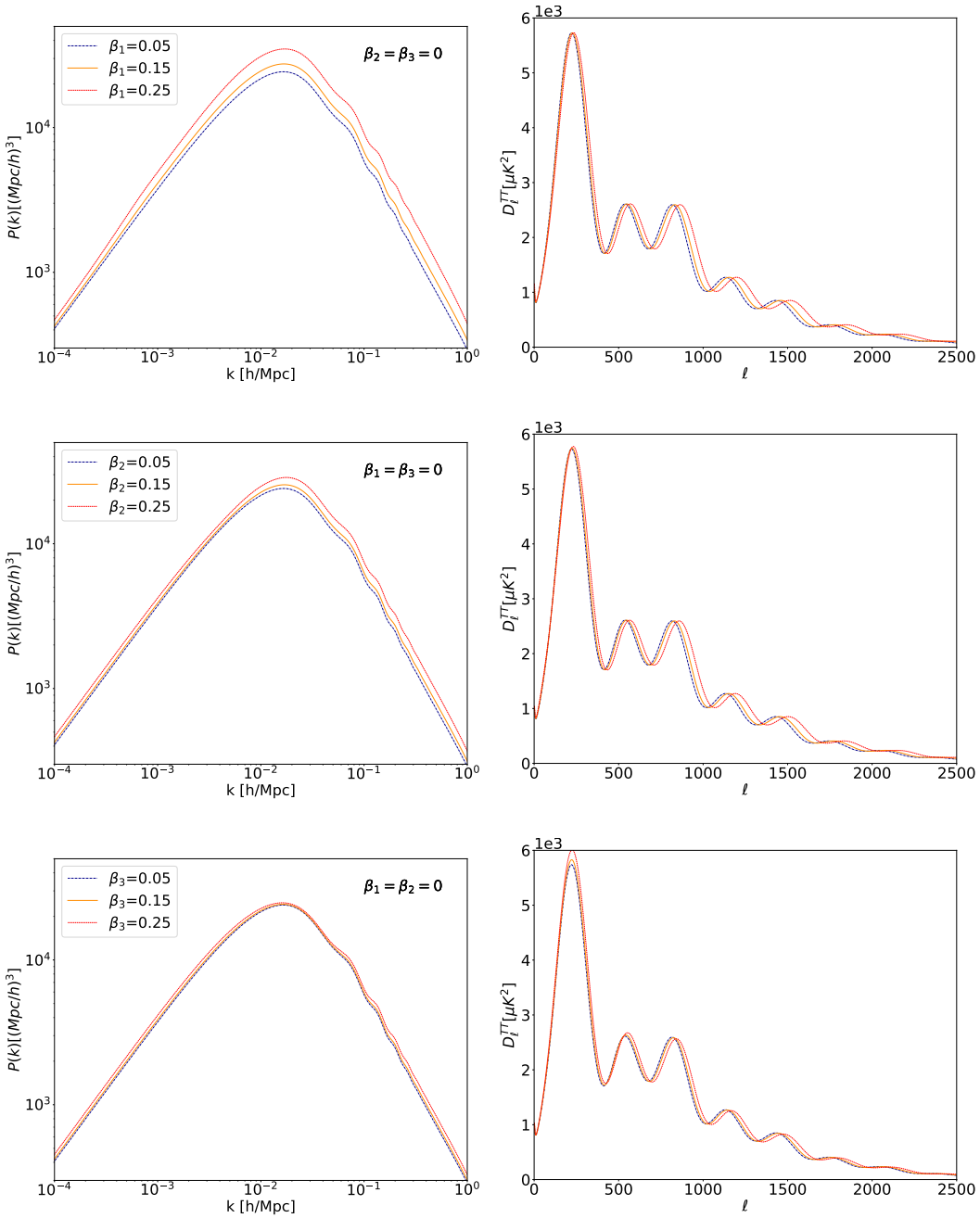

Fig. 5.2. Matter power spectra $P(k)$ (left column) and CMB temperature spectra D_ℓ^{TT} (right column) obtained with different values of β_1 (top row), β_2 (middle row) and β_3 (bottom row), while setting the other β_i's to zero. This is to show the impact of a non-null coupling at each bin. We use in all cases the same primordial power spectrum, $\tau_{\rm reio}$, $\omega_{\rm b}$, V_0 and the initial value of DM energy density as in the *Planck* TT+TE+EE ΛCDM best-fit cosmology.

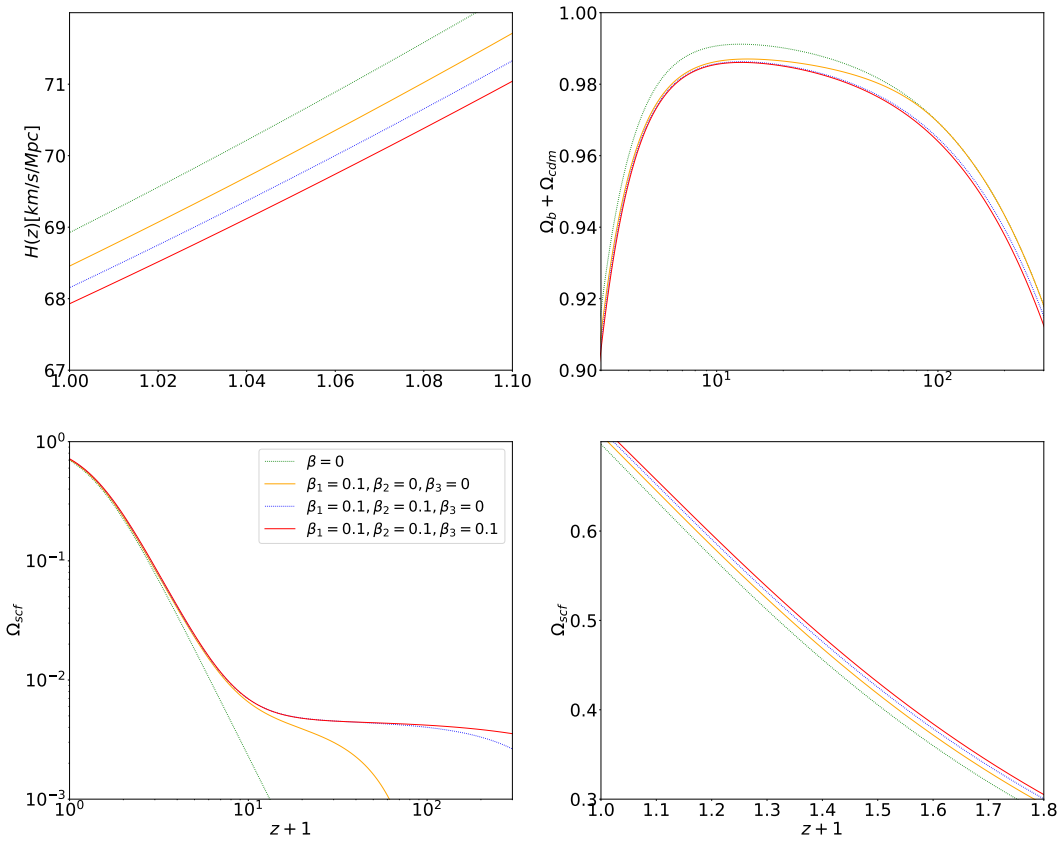

Fig. 5.3. We plot (clockwise from top left) the evolution of $H(z)$ and the values of $\Omega_{\rm b}(z) + \Omega_{\rm DM}(z)$ and $\Omega_\phi(z)$ when we subsequently switch on the coupling strength at increasing redshifts by activating the corresponding coefficient of β from 0 to 0.1. The green dotted line with $\beta = 0$ represents the ΛCDM model. The plot of $\Omega_\phi(z)$ at the bottom right is a zoom-in of the bottom left plot, in the window $0.1 \leq z \leq 0.8$, which allows us to grasp the differences between the various curves.

DM energy fractions $\Omega_i(z)$. Since $\rho_{\rm DM}$ decreases with increasing β, as seen from Eq. (5.5), the activation of the coupling leads to lower values of H_0.

To better understand the dynamics of the scalar field, we also plot its evolution, the evolution of its derivative and the resultant equation of state parameter w in Fig. 5.4. We see that ϕ and ϕ' become non-zero at the redshift when coupling is activated, following Eq. (5.8). During the period of non-zero coupling, the field typically behaves like those in 'freezing' dynamical dark energy models (as introduced in [130]), whereby it rolls to a minimum and slows down during the onset of accelerated expansion during late times (as seen from the decrease of ϕ'). We see this in the evolution of w as well : it is initially positive, slowly decreasing and asymptoting to a value of $w = -1$ to mimic the behaviour of a cosmological constant at present

times.

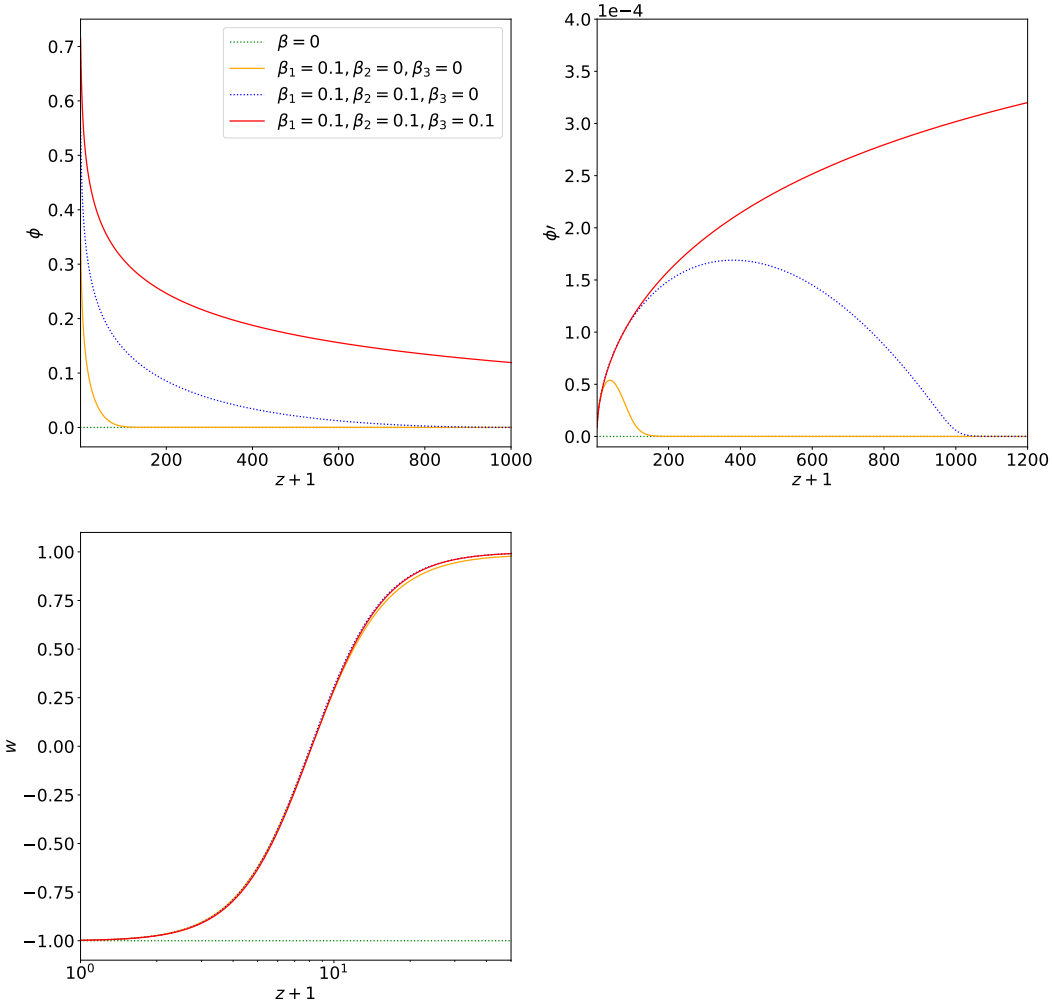

Fig. 5.4. Plot of (clockwise from top left) : the evolution of the scalar field and its derivative, and the EoS w, with the same coupling activation setup as in Fig. 5.3. ϕ and ϕ' are given in units of the reduced Planck mass.

5.3 Methodology

5.3.1 Modifying `CLASS`

We subsequently develop a modified version of the code, the Cosmic Linear Anisotropy Solving System (`CLASS`; [139]), to accommodate a redshift-dependent coupling $\beta(z)$.[1] Our code allows us to solve the Einstein-Boltzmann system of cosmo-

1. Our modified version of `CLASS` is publicly available at the following link : https://github.com/LisaGoh/CDE.

logical equations, to obtain the theoretical quantities of interest at the background and linear perturbation levels, which is crucial to confront the model with observations and subsequently constrain model parameters. The code has been validated against the one used in [140-143], for constant coupling (and previously with a modified version of CMBfast used in [144]). The present version allows us to reach exactly ΛCDM in the limit of constant potential and zero coupling.

We employ `MontePython` to explore the parameter space of our CDE models. We use the regular Metropolis-Hastings sampling algorithm and stop the Monte Carlo when the Gelman-Rubin convergence statistic $R-1 < 0.02$. On top of the β_i's, we vary the reduced baryon density, $\omega_{\rm b}$, the reionization depth $\tau_{\rm reio}$, the potential of the scalar field V_0, $\omega_{\rm DM,ini}$ the reduced initial DM density at redshift $z_{\rm ini} = 10^{14}$, $A_{\rm s}$ and the spectral tilt $n_{\rm s}$. In this study, we are interested in setting the initial conditions in the past, evolving quantities under the effect of the varying coupling, in order to see the effect on present quantities. We keep the Hubble parameter, H_0, the present day reduced DM energy density $\omega_{\rm DM,0}$, σ_8, and S_8 as derived parameters. We consider two massless neutrinos and one massive neutrino of 0.06 eV.

For the initial conditions of the scalar field, we are allowed to set $\phi_{\rm ini} = 0$ and $\phi'_{\rm ini} = 0$, since the scalar field has no dynamics during the radiation-dominated epoch due to the null impact of the potential in that era, and the equations do not depend on ϕ, but only on its time derivatives.

We choose uninformative flat priors for all the parameters, wide enough to not influence the posterior distribution. In particular, we vary the couplings in the range $\beta_i = (0, \beta_{\rm max})$, where the value of $\beta_{\rm max}$ is chosen depending on the particular dataset. It has to be sufficiently large to not cut the tail of the posterior artificially. The MCMC chains are then analysed using the `GetDist` [145] Python package.

5.3.2 Data

Here we detail the different datasets we employ, ranging from high-redshift to low-redshift data, to constrain our model under investigation.

Cosmic Microwave Background We test our tomographic CDE model on *Planck* 2018 low-ℓ and high-ℓ TT, TE and EE CMB spectra [61], covering the multipole range $\ell = (2, 2508)$ for the TT, and $\ell = (2, 1996)$ for the TE and EE power spectra. We call this dataset Planck, in short. For completeness, in one of our datasets, we also include the CMB lensing power spectrum in the multipole range $\ell = (8, 400)$ and

combine it with the Planck TT,TE,EE data. We denote it as Planck+PlanckLens.

We also study four additional combinations of CMB data, by including the information from ACT and SPT-3G surveys, which cover a multipole range larger than *Planck* :

1. ACT Data Release 4 [18] :
   We use CMB temperature anisotropy and polarisation (TT, EE and TE) power spectra from the latest ACT DR4, measured with the ACTPol receiver. We use the full ℓ-range of $600 \leq \ell \leq 4125$ for the TT power spectra and $350 \leq \ell \leq 4125$ for the TE/EE power spectra. Data from ACT complements the Planck dataset in the high ℓ range. Following the recommendation of [18], we use a Gaussian prior on the optical depth of reionisation, $\tau_{\rm reio} = 0.065 \pm 0.015$, which is only relevant when ACT is employed without including the low multipoles from *Planck* since in this case $\tau_{\rm reio}$ is basically unconstrained by the likelihood. All the results reported in this paper, though, are obtained by combining the ACT data with the low-multipole information from *Planck*, so the impact of this prior is in practice negligible.
2. *Planck* + ACT (TT cut at $\ell_{\rm min} = 1800$) :
   We combine ACT and *Planck* data. After a Fisher matrix analysis carried out by [18], the authors found it necessary to truncate the ACT TT power spectrum at multipoles $\ell < 1800$ to avoid double counting issues caused by the overlap of the multipole ranges covered by the two experiments. The addition of the *Planck* information has the potential to greatly tighten cosmological constraints with respect to the case in which only ACT data is considered (see e.g. Figs. 12 and 17 in [18]). We denote this truncated ACT dataset as ACT1800, and its combination with the full *Planck* temperature and polarisation likelihoods as Planck+ACT1800.
3. *Planck* + ACT1800 + SPT-3G :
   As a next step, we include TE and EE power spectra from the SPT-3G [19], covering a multipole range of $300 \leq \ell \leq 3000$. Constraints from SPT-3G CMB data have shown to be in good agreement with *Planck*, hence providing further independent validation of *Planck* results. In addition, SPT data has much better constraining power at high ℓ's compared to *Planck* and also covers a separate area of the sky than ACT, so is highly complementary to the former two datasets [146]. Since the overlap between SPT-3G and *Planck* is small and

there is no overlap of the SPT survey area with ACT, there is no need to truncate their power spectra when used in combination. We denote this dataset as Planck+ACT1800+SPT.

4. *Planck* (TT cut at $\ell_{\rm max} = 650$) + ACT +SPT-3G :
   Following [147], we also consider an alternative way to combine Planck and ACT : we combine again the ACT, *Planck* and SPT-3G data, but this time limiting the *Planck* TT power spectrum to $\ell_{max} = 650$. The exclusion of higher multipoles of the *Planck* TT spectrum has shown to give rise to a preference for early dark energy models and a higher value of H_0, see [147-149]. Hence, it will be interesting to look into whether this dataset suggests a stronger preference for CDE as well. We denote this dataset as Planck650+ACT+SPT. With respect to the previous choice 3, this combination includes a larger part of ACT data.

Baryonic Acoustic Oscillations (BAO) We use the following BAO data points :

- $D_V/r_s(z = 0.122)$ [150] from the 6dF Galaxy Survey (6dFGS) and Sloan Digital Sky Survey (SDSS) Main Galaxy Sample
- $D_M/r_s(z = 0.32)$ and $r_s H(z = 0.32)$ [151] from the BOSS DR12 LOWZ samples
- $D_M/r_s(z = 0.57)$ and $r_s H(z = 0.57)$ [151] from the BOSS DR12 CMASS samples
- $D_V/r_s(z = 0.44, 0.60, 0.73)$ [152] from the WiggleZ Dark Energy Survey
- $D_M/r_s(z = 0.835)$ [153] from the DES Year3 Data Release
- $D_M/r_s(z = 1.19, 1.50, 1.83)$ and $r_s H(z = 1.19, 1.50, 1.83)$ [154] from the extended BOSS (eBOSS) DR14 quasar sample (DR14Q)
- $D_M/r_s(z = 2.34)$ [155] obtained by the correlations between Ly-α absorption and eBOSS quasar spectra

where $D_M(z)$ is the comoving angular diameter distance, r_s the sound horizon at the baryon-drag epoch, and

$$D_V(z) = \left[D_M^2(z) \frac{cz}{H(z)} \right]^{1/3} \tag{5.20}$$

the dilation scale. The covariance matrices of the BOSS DR12 LOWZ and CMASS samples and eBOSS DR14Q have been taken into account.

Type Ia supernovae (SNe1a) We employ the following SNe1a data :

- 6 effective points on the Hubble rate, i.e. $E(z) = H(z)/H_0$, and their associa-

ted covariance. They compress the data from the 1048 SNe1a of the Pantheon compilation [156] and the 15 SNe1a at $z > 1$ from the Hubble Space Telescope Multi-Cycle Treasury programs [157]. The compression effectiveness of the information contained in such SNe1a samples is excellent, see Ref. [157]

- Combination of the lightcurve data from 251 spectroscopically confirmed SNe1a in the redshift range of $0.02 < z < 0.85$, measured by the Dark Energy Survey Supernova Programme (DES-SN) [158]

Cosmic Chronometers (CCH) We use the 31 data points of the Hubble function $H(z)$ in a redshift range of $0.07 \leq z \leq 1.905$, obtained by making use of passively-evolving galaxies : i.e. galaxies with old stellar populations and low star formation rates, whose evolution can be modelled considerably accurately. By employing the differential age technique [159], where we observe the evolutionary state of each pair of such galaxies at different redshifts, the value of dz/dt and thus $H(z)$ can be inferred. These probes are known as cosmic chronometers (CCH). These values were calculated without assuming any fiducial cosmology. We take reference from [160] for the CCH data points, and present them in Table 5.1.

Redshift Space Distortions (RSD) We use the following data from redshift space distortions (RSD), expressed in terms of the product of the growth rate $f(z)$ and σ_8. We note that in the case of a CDE model, the modified evolution of the density contrast $\delta_{\rm DM}$ adds a contribution to f, such that the effective growth rate becomes $f_{\rm eff} = f - \kappa\phi'\beta/\mathcal{H}$ [131]. However, we have explicitly checked that this correction is very small : using a test value of $\beta = 0.04$, the ratio $|f_{\rm eff} - f|/f \sim 10^{-3}$ in the redshift range of the RSD data points, while the uncertainties of the data are on the order $\sigma_{f\sigma_8}/f\sigma_8 \sim 0.1 - 0.2$.

We use the following data points :

- $f\sigma_8(z = 0.03)$ [161] derived by combining results from the 2MASS Tully-Fisher (2MTF) and 6dFGS surveys
- $f\sigma_8(z = 0.1)$ [162] from the SDSS DR7
- $f\sigma_8(z = 0.18, 0.38)$ [163] [164] from the Galaxy and Mass Assembly survey (GAMA)
- $f\sigma_8(z = 0.22, 0.41, 0.60, 0.78)$ [152] from WiggleZ
- $f\sigma_8(z = 0.32)$ [151] from BOSS DR12 LOWZ

z	$H(z)$ [km s^{-1}Mpc^{-1}]
0.07	69.0 ± 19.7
0.09	69.0 ± 12.1
0.12	68.6 ± 26.3
0.17	83.0 ± 8.3
0.1791	77.8 ± 8.1
0.1993	77.7 ± 8.7
0.2	72.9 ± 29.7
0.27	77.0 ± 14.1
0.28	88.8 ± 36.7
0.3519	85.2 ± 16.9
0.3802	86.0 ± 15.6
0.4	95.0 ± 17.2
0.4004	79.8 ± 12.3
0.4247	90.3 ± 13.6
0.4497	96.1 ± 15.3
0.47	89.0 ± 49.6
⋮	⋮
0.4783	83.8 ± 10.8
0.48	97.0 ± 62.0
0.5929	106.7 ± 16.4
0.6797	94.6 ± 11.9
0.7812	96.3 ± 21.0
0.8754	124.5 ± 17.3
0.88	90.0 ± 40.1
0.9	117.0 ± 23.2
1.037	132.5 ± 45.8
1.3	168.0 ± 17.5
1.36	160.0 ± 33.8
1.43	177.0 ± 18.5
1.53	140.0 ± 14.4
1.75	202.0 ± 40.3
1.965	186.5 ± 50.6

Table 5.1. Table of collated $H(z)$ values and their 1σ uncertainties at 31 different redshifts, referenced from [160].

- $f\sigma_8(z = 0.57)$ [151] from BOSS DR12 CMASS
- $f\sigma_8(z = 0.60, 0.86)$ [165] from the Visible Multi-Object Spectrograph (VIMOS) Public Extragalactic Redshift Survey
- $f\sigma_8(z = 0.77)$ [166] from the VIMOS Very Large Telescope (VLT) Deep Survey
- $f\sigma_8(z = 1.19, 1.50, 1.83)$ [154] from eBOSS DR14Q
- $f\sigma_8(z = 1.36)$ [167] from Subaru FMOS galaxy redshift survey (FastSound)

We correct for the Alcock-Paczynski effect by multiplying $f\sigma_8$ by the ratio $[H(z)D_A(z)]/[H^{\rm fid}(z)D_A^{\rm fid}(z)]$, as in [168], where *fid* denotes the fiducial cosmology used in the particular survey. In the CMASS, LOWZ and eBOSS DR14Q samples we take into account the correlations between the BAO and RSD data through the corresponding covariance matrices.

Supernova Ho for the Equation of State (SHoES) We include the most updated prior on the Hubble constant obtained by the SHoES team using the cosmic distance ladder method, $H_0 = (73.04 \pm 1.04)$ km s^{-1}Mpc^{-1} [21], which is in $\sim 5\sigma$ tension with the value obtained by the *Planck* collaboration under the assumption of the flat

ΛCDM model.

Weak Lensing We employ cosmic shear data from the latest data release of KiDS-1000 [169], covering an effective area of 777deg^2 with photometric galaxies spanning the redshift range $0.1 < z \leq 1.2$. We have validated our pipeline by conducting runs with the ΛCDM model, making use of our modified version of `CLASS` (while setting $\beta(z) = 0$) and verifying that we are able to reproduce the results reported in [170]. In this study, we follow the fiducial analysis settings keeping an ℓ range of $\ell = (100, 1500)$ in the calculation of the cosmic shear angular power spectrum $C^{\ell}_{\epsilon\epsilon}$. Here, we acknowledge that although fitting functions exist to model the nonlinear matter power spectrum $P_{nl}(k)$ for a constant coupled dark energy model [171], an accurate recipe for the tomographic coupling case has yet to be developed and would need Nbody simulations for varying coupling which are not publicly available at present; we leave this task for future work. For this reason, we conservatively use only scales up to $\ell < 1500$; while this already cuts a large part of nonlinear scales that may be interesting to include in future studies, we also use HMCode [172] to approximate $P_{nl}(k)$ within this range; this approximation is good enough for our purposes, under the assumption that in this regime and for the values of β considered in this paper, the difference between the nonlinear spectra obtained with HMCode corrections, and the spectra in a CDE model, is small. We leave a more refined analysis at nonlinear scales, including smaller scales than the ones included here, for future studies.

Spectroscopic Galaxy Clustering We consider spectroscopic galaxy clustering data from the SDSS-III BOSS DR12 [173], following the methodology of [174], where they calculate the anisotropic redshift space correlation function $\xi_{gg}(s, \mu, z)$ in 3 three-dimensional 'wedges' (transverse, intermediate and parallel to the line of sight), split into 2 tomographic bins of $0.2 < z \leq 0.5$ and $0.5 < z \leq 0.75$.

$3\mathbf{x}2$ **pt** We also include, for the first time, the cross-correlations of the aforementioned KiDS-1000 'source' galaxies, split into 5 tomographic bins, with 'lens' galaxies obtained by combining both BOSS DR12 and 2DFLenS [175] data to obtain the galaxy-galaxy lensing angular power spectra $C^{\ell}_{n\epsilon}$ to constrain our model. The combination of cosmic shear, galaxy clustering and galaxy-galaxy lensing will then make up our

3x2pt probe. Since the overlap between the KiDS and BOSS surveys only accounts for 4% of the BOSS footprint, the galaxy clustering covariance matrix has been assumed to be independent of the covariance matrix of cosmic shear and galaxy-galaxy lensing, which was derived analytically in [176]. In the case of galaxy-galaxy lensing, we follow [170] to limit the contribution of nonlinear scales with $k \gtrsim 0.3\,h$Mpc^{-1}. The authors argue that beyond these scales, their theoretical model of the galaxy-galaxy lensing power spectrum becomes significantly inaccurate due to nonlinearities. This cut in scale corresponds, based on calculations of the data and the real space correlations functions $\xi_{\pm}(s, \mu)$, to an ℓ range of $\ell = (100, 300)$. We will thus also use this ℓ range in our 3x2pt analysis.

5.3.3 Binning Parametrisations

When binning the coupling, we need to make a choice on the bins to be considered. We start from the consideration that, depending on the datasets we include in the analysis, different choices may be more or less adequate. For example, if we are interested in including CMB data, it is interesting to consider bins which differentiate between late and early times. If instead we only include late-time probes, we may rather be interested in increasing the number of bins within a redshift range which overlaps with where the data are available. While there is no unique choice, we specify here different typical choices, depending on the datasets.

Here we describe the different binning models we test, and the datasets we have chosen to constrain each of them.

3-bin Tomographic β

We first consider CMB data alone, to evaluate the impact of different choices which can be made when using Planck alone, or in combination with ACT and SPT. For this purpose, we test a binning with 3 tomographic bins, using bin edges $\{0, 100, 1000\}$. This choice roughly identifies the structure formation, post-recombination and pre-recombination eras. We fix $s_1 = s_2 = 0.03$ to allow for a smooth, gradual transition between amplitudes in the various bins. Here we study if the data prefer a different value of the coupling in the pre- and post-recombination epochs, allowing also for a change in β at $z < 100$.

We test this model with CMB data alone, namely : Planck, Planck+PlanckLens, Planck650+ACT+SPT, Planck+ACT1800 and Planck+ACT1800+SPT, since we would like

to test the constraining power of these alternative CMB datasets as compared to a purely Planck dataset.

7-bin Tomographic β

Next, we aim to combine CMB data with background datasets from BAO, supernovae and cosmic chronometers, with or without RSD. We then test a binning with 7 tomographic bins, using bin edges $\{0, 1, 2, 5, 100, 500, 1000\}$. In this case we use $s_i = 10$ for $i = (1, 3)$, and $s_i = 0.03$ for $i = (4, 6)$. This finer binning will let us study to what extent the constraints on the coupling are sensitive to the large variety of data at low redshifts and to the physical processes around the decoupling time of the CMB photons. Our definition of the tomographic bin edges is largely motivated by the redshift ranges that are being covered by the datasets we employ.

We begin with a baseline CMB dataset, to which we include other probes to see how constraints might be affected, namely : BAO+SNe1a+CCH datasets (denoted as 'BSC'), RSD data, and finally a SH0ES prior to see if its inclusion could potentially increase the coupling strength at various epochs.

Our two baseline datasets are Planck+ACT1800+SPT and Planck650+ACT+SPT. It is interesting to run our analyses on both combinations of CMB data cuts (cut on ACT versus cut on Planck) to study how these different cuts impact the constraints on our model.

In conclusion, we list the datasets here that we will employ in the following sections :

1. Planck+ACT1800+SPT+BSC
2. Planck+ACT1800+SPT+BSC+RSD
3. Planck+ACT1800+SPT+BSC+SH0ES
4. Planck+ACT1800+SPT+BSC+RSD+SH0ES
5. Planck650+ACT+SPT+BSC
6. Planck650+ACT+SPT+BSC+RSD
7. Planck650+ACT+SPT+BSC+SH0ES

4-bin Tomographic β

Lastly, we concentrate on late-time probes only; for this purpose, we test a binning with 4 tomographic bins, using bin edges $z = \{0, 0.5, 1, 2\}$ and $s = 10$ in the

case of weak lensing (KiDS-1000 cosmic shear), BOSS spectroscopic galaxy clustering and the 3x2pt datasets. Since the redshift ranges of KiDS-1000 source galaxies are between $0.1 \leq z \leq 1.2$ and the BOSS and 2DFLenS lens galaxies are between $0.2 < z < 0.75$, we alter our tomographic binning model to only vary $\beta(z)$ at this range, ensuring that the data can be fully exploited to constrain our model. Moreover, since the first three tomographic bins are very narrow in this binning model and only vary at low redshifts, the impact of larger β_i's on the matter power spectrum is less significant.

We use the cosmic shear, spectroscopic galaxy clustering, and 3x2pt datasets to test both a constant and tomographic coupling model, and subsequently combine cosmic shear with the Planck+ACT1800+SPT+BSC dataset in a tomographic framework, to see if $\beta(z)$ can become more constrained at higher redshifts. We only do this for cosmic shear and not galaxy clustering and 3x2pt, to avoid double counting when combining galaxy clustering with BAO and RSD. Additionally, when using only cosmic shear, we follow [170] by imposing a flat prior on H_0 encompassing $\pm 5\sigma$ of distance ladder constraints [20], given by $64 < H_0 < 82$ km s^{-1} Mpc^{-1}.

Weak lensing has been used to constrain a constant CDE model in previous literature [177], however it is the first time we cross-correlate it with full-shape galaxy clustering to probe coupled dark energy models, hence it is interesting to assess their combined constraining power.

5.4 Observational Constraints on Tomographic CDE

5.4.1 Constraints with High-Redshift Data

We show in Fig. 5.5 the posterior distribution of the standard cosmological parameters $\theta = \{\omega_{\rm b}, \omega_{\rm DM}, \ln 10^{10} A_{\rm s}, n_{\rm s}, \tau_{\rm reio}, H_0, \sigma_8\}$, as well as the constraints on β_{1-3}, for a 3-bin tomographic model. In this model, we only consider CMB datasets and we fit our model with Planck, Planck+ACT1800, Planck+ACT1800+SPT and Planck650+ACT+SPT. For a detailed list of the best-fit, mean and 68% confidence level (C.L.) uncertainties for each parameter, we refer the reader to Table A.1 in Appendix A.

We see that the differences between the contour plots obtained from the analyses with Planck alone and Planck+ACT1800 when the scale cut includes more of Planck and less of ACT data are not substantial, and also do not differ considerably from the one derived with a constant coupling model. This is expected since,

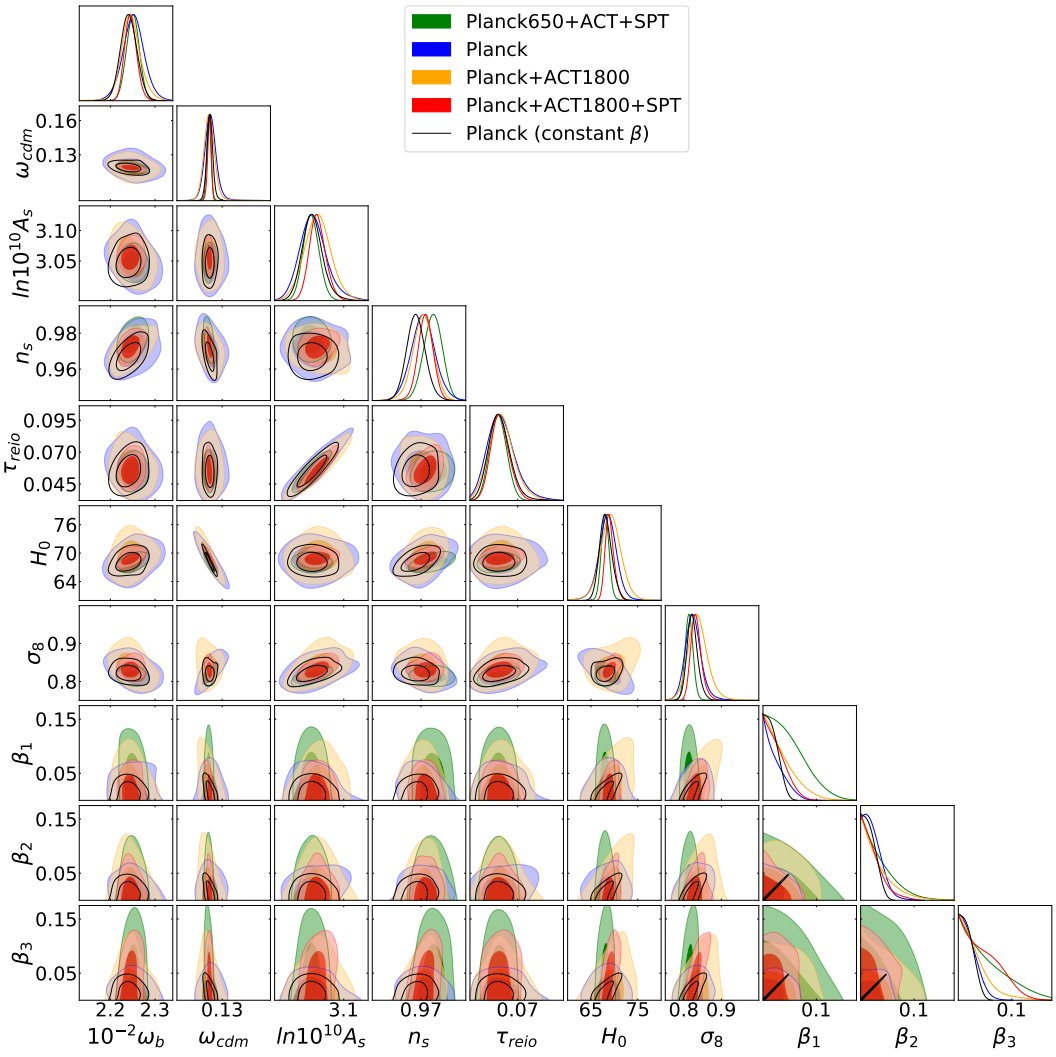

Fig. 5.5. Triangular plot of 68% and 95% C.L. posterior distributions obtained with the CMB datasets Planck650+ACT+SPT (green), Planck (blue), Planck+ACT1800 (yellow) and Planck+ACT1800+SPT (red) for the 3-bin tomographic model. The binning is defined by the edges $z = \{0, 100, 1000\}$. We include the contours derived for a constant β model, using Planck data, in black. In this case, the contours for β_{1-3} correspond to the same constant β.

as mentioned, *Planck* data carries the bulk of the statistical power. When instead high multipoles of the Planck spectrum are excluded, i.e. when we consider the Planck650+ACT+SPT dataset, the constraints loosen considerably for every coupling coefficient β_{1-3}. In all cases, we find that the interaction strength is compatible with 0 (i.e. with ΛCDM) at 68% C.L.

There is a positive correlation between H_0, σ_8 and the coupling coefficients β_{1-3}, especially in the case Planck+ACT1800. The correlation is stronger for β_1, i.e. in the

redshift range $0 < z < 100$. This behaviour ties in with the results presented in Fig. 5.2 : an increase in β_1 leads to an increase of the matter power spectrum and hence, to σ_8, and requires larger values of H_0 to respect the position of the first acoustic peak of the CMB temperature spectrum.

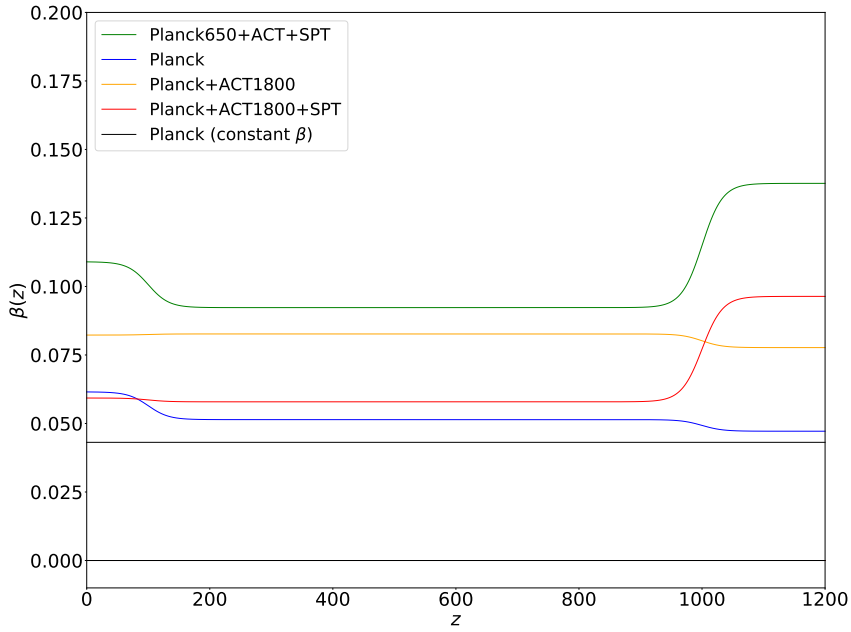

Fig. 5.6. 95% C.L. on $\beta(z)$ for the 3-bin tomographic model. The binning is defined by edges $z = \{0, 100, 1000\}$. For reference, we also include the constraint for the case of a constant coupling β, obtained with Planck data, in black.

In Fig. 5.6 we plot the 95% C.L. constraints on the evolution of the coupling strength $\beta(z)$, reconstructed from β_{1-3} via Eq. (5.17) : constraints are derived for the various CMB datasets, and compared to the case of a constant coupling, as studied in [142, 143]. We see that in all cases, CMB constraints on $\beta(z)$ are weaker than for a constant coupling, going from $\beta_3 < 0.045$ at 95% C.L. to a maximum of $\beta_3 < 0.14$ at 95% C.L. for the case of Planck650+ACT+SPT. Interestingly, adding ACT and SPT data to Planck loosens constraints at all epochs, and for all scale cuts, with respect to Planck alone. Constraints in β_3 bin, around recombination mainly come from Planck data. This is due to the fact that Planck data tightly constrain the amplitude of the first acoustic peak, to which, as we have seen in Fig. 5.2, a change in β_3 is most sensitive. The inclusion of SPT further loosens constraints around recombination.

Fig. 5.7 summarises our results for the 3-bin scenario : we show the mean and 68% C.L. of the cosmological parameters of our 3-bin model, as constrained by dif-

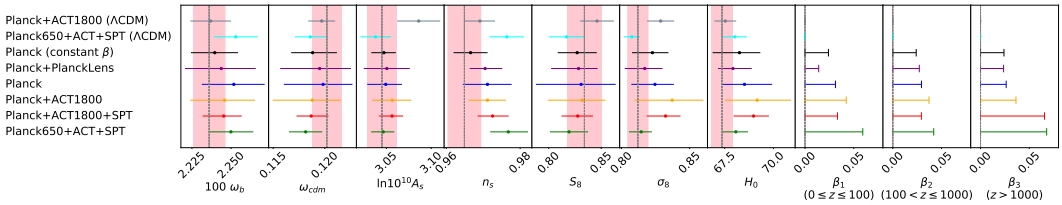

Fig. 5.7. Comparison of the mean and 68% C.L. of the various cosmological parameters, for the different CMB datasets with a 3-bin model. Here the grey vertical dashed lines and pink bands denote respectively the mean and 1σ of *Planck* ΛCDM TTTEEE+lowE fiducial cosmology (cf. Table 2 of [61]), and the results obtained for the Planck+ACT1800 (ΛCDM) dataset in grey were taken from Table 4 of [18]. We also make a comparison to the constant β model with Planck data (in black).

ferent choices of CMB datasets, and compare them with those obtained for ΛCDM and for a constant coupling ($\beta_1 = \beta_2 = \beta_3 = \beta$) model. The pink band represents the mean and 1σ uncertainty on ΛCDM cosmological parameters as obtained from *Planck*. We note that ACT and SPT are in better agreement with Planck data within a CDE cosmology (red and orange vs blue lines) than in ΛCDM (grey and cyan vs pink band); however this may also be due to the fact that the analysis was run with a different prior on τ as compared to that in [18]. As shown before, when the coupling is allowed to vary in redshift, as in a tomographic model, it is less constrained than when it is forced to be constant at all redshift bins, and in particular near recombination. The inclusion of ACT and SPT further loosens the constraints.

Interestingly, we see that a tomographic CDE model shifts H_0 towards slightly higher mean values for all datasets, when compared to ΛCDM. Using the Planck dataset as a basis for comparison, we find that a tomographic model gives very similar results compared to the constant coupling case, with $H_0 = (68.15^{+1.21}_{-1.43})$ km s^{-1} Mpc^{-1} for the constant coupling model and $H_0 = (68.51^{+1.42}_{-1.17})$ km s^{-1} Mpc^{-1} for the tomographic case. Including ACT, as in Planck+ACT1800, increases this value to $H_0 = (69.17^{+1.75}_{-1.65})$ km s^{-1} Mpc^{-1}. If we take the results obtained only with Planck and compare them to the SH0ES value, the Hubble tension decreases from $\sim 4.8\sigma$ (assuming ΛCDM) to $\sim 2.9\sigma$ (assuming CDE with $\beta =$ const.). In the case of the tomographic model, the H_0 tension decreases even more, to $\sim 2.7\sigma$. However we note that the uncertainties in H_0 are increased by a factor of 2 going from ΛCDM to a CDE model, which is the main cause of this reduction of the tension.

Finally, we also note that the tension between the value of $n_{\rm s}$ measured with Planck and Planck650+ACT+SPT when assuming ΛCDM disappears in the context

of a tomographic CDE model; the error bars overlap (dark blue and green) and thus the corresponding values of $n_{\rm s}$ are compatible. Similarly, the mild tension between the value of $A_{\rm s}$ found with Planck and Planck+ACT1800 in the ΛCDM is also washed out in the tomographic model (cf. the dark blue and yellow bars).

Finally, we present results derived from additionally employing the *Planck* lensing likelihood in Fig. 5.8. We see that the inclusion of the lensing likelihood leads to tighter constraints, especially for the coupling at the lowest redshift bin, β_1. This is to be expected, since the CMB lensing potential power spectrum $C_\ell^{\phi\phi}$ probes the large scale structure at redshifts in that range, and has also been shown to lend a preference towards ΛCDM [178].

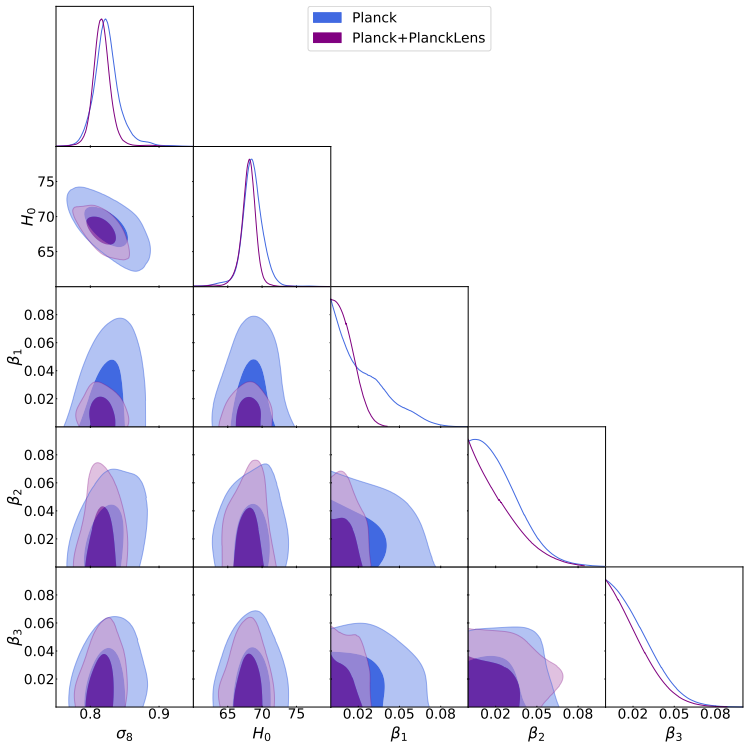

Fig. 5.8. Comparison between the results obtained for the 3-bin tomographic model using Planck with (purple) and without (blue) the Planck CMB lensing likelihood. We recall that all spectra (in both cases) are always lensed, even when the Planck lensing (4-point) likelihood is not included.

In summary, the results obtained with the 3-bin tomographic model when using only CMB data allow for larger couplings at all epochs; none of the current datasets detects a non-zero coupling in any bin, and data are consistent with ΛCDM predictions; the CDE model though, allows for slightly larger values of σ_8 and H_0 with

respect to ΛCDM. On the other hand, a non-zero coupling works to decrease $\omega_{\rm DM}$, which compensates the increase in σ_8 to give a value of S_8 similar to the one we would have for *Planck* ΛCDM. We will see in the next section whether this is still compatible with other background datasets.

5.4.2 Constraints with Low-Redshift Data

It is natural to wonder whether shifts observed in σ_8 and H_0 and the corresponding slight decrease in $\omega_{\rm DM}$ for a CDE model, are still compatible with background data, such as BAO and low redshift data from RSD. We present results for the 7 different datasets as listed in Sect. 5.3.3, adapting the binning to a 7-bin model, which is finer at low redshifts. We then add to the Planck+ACT1800+SPT baseline lower redshift data, namely BAO, SNe1a, cosmic chronometers, RSD and a SH0ES prior, and check their impact on the coupling strength.

In Fig. 5.9 we use Planck+ACT1800+SPT+BSC as a baseline and plot the constraints on H_0, σ_8 and the 7 coupling coefficients obtained for datasets 1-4, namely combining Planck$+$ACT1800$+$SPT with BSC, BSC$+$RSD, BSC$+$SH0ES and BSC$+$RSD$+$SH0ES. We recall that BSC refers to the combination BAO+SNe1a+CCH. A list of the best-fit, mean and 68% C.L. uncertainties for each parameter is given in Table A.2 of Appendix A.

We see that when we combine our baseline CMB dataset with BSC data, the coupling strengths at low redshifts ($z < 5$) are not well constrained (green contours for β_1, β_2 and β_3). The addition of either RSD or SH0ES leads to tighter constraints : $\beta_1 < 0.017$ for Planck+ACT1800+SPT+BSC+RSD+SH0ES with respect to $\beta_1 = 0.146^{+0.075}_{-0.081}$ for Planck+ACT1800+SPT+BSC at 68% C.L. Couplings at larger redshifts are instead mainly unaffected with respect to Planck+ACT1800+SPT+BSC. We also see a considerable loosening of constraints for all parameters in general in the tomographic coupling case as compared to a constant coupling (in black), and a shift towards larger values of H_0 and σ_8.

In Fig. 5.10 we plot the 95% C.L. on $\beta(z)$ as derived from the seven β_i described above, for the baseline Planck+ACT1800+SPT with different background data, as compared to the constant coupling case with a Planck+ACT1800+SPT+BSC dataset. We see once again that the constraints on the coupling strength are weaker in the tomographic scenario, especially in high redshift bins, reaching $\beta_7 = 0.063^{+0.023}_{-0.054}$ at 68% C.L. around recombination for Planck+ACT1800+SPT+BSC, with respect to $\beta_7 = 0.015^{+0.005}_{-0.014}$ for the same dataset, when a constant coupling is assumed (i.e.

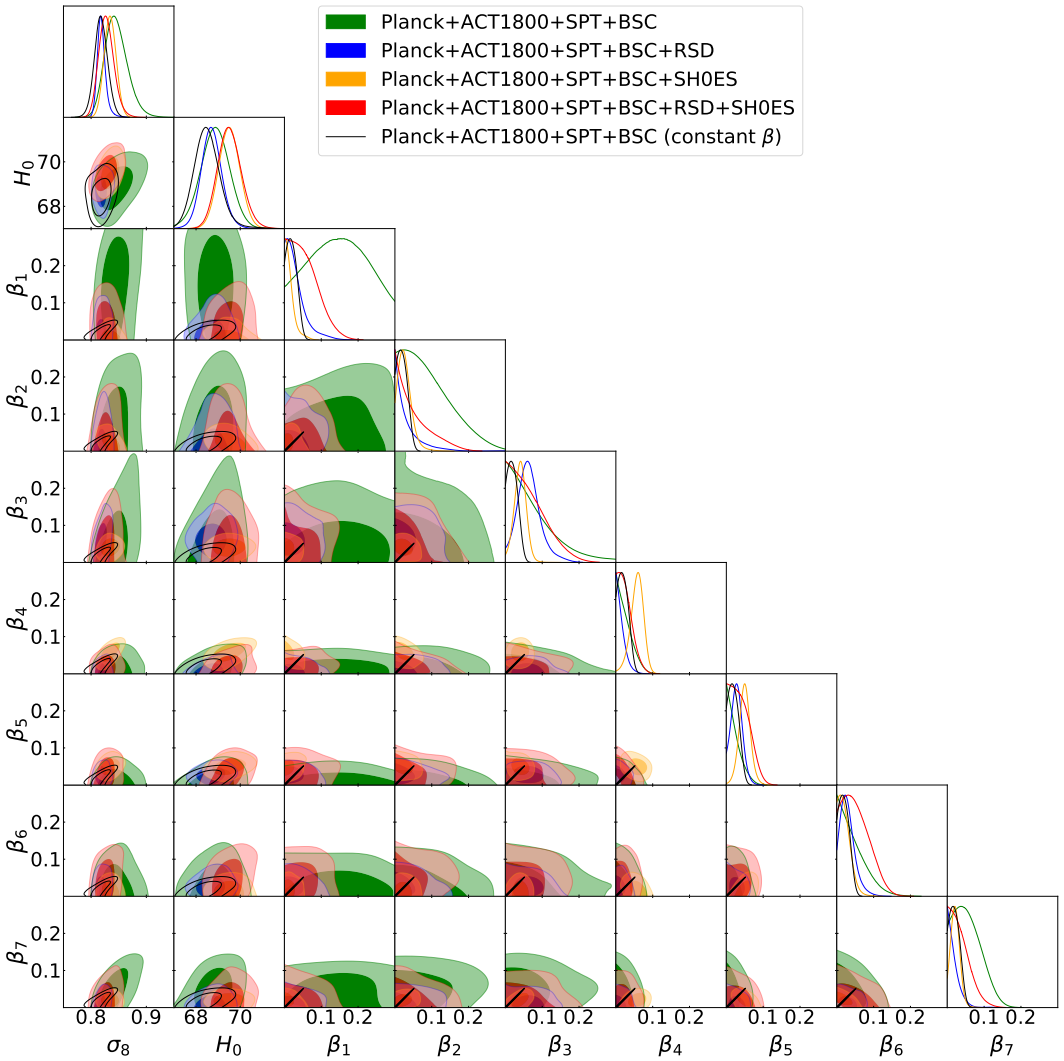

Fig. 5.9. Triangular plot of 68% and 95% C.L. posterior distributions of σ_8, H_0, and the 7 tomographic coupling coefficients β_{1-7} derived from datasets Planck+ACT1800+SPT+BSC (green), Planck+ACT1800+SPT+BSC+RSD (blue), Planck+ACT1800+SPT+BSC+SH0ES (yellow) and Planck+ACT1800+SPT+BSC+RSD+SH0ES (red). For reference, the binning is defined by edges $z = \{0, 1, 2, 5, 100, 500, 1000\}$. We include, in black lines, the contours obtained for a constant β case with Planck+ACT1800+SPT+BSC data. In this case, the contours for all β_{1-7} are the same.

nearly 5 times greater). Interestingly, when either RSD or SH0ES data are considered on top of Planck+ACT1800+SPT (blue and yellow curves in Fig. 5.10, respectively), a non-null-coupling seems to be preferred in some redshift bins : in particular, the inclusion of a SH0ES prior appears to favour a non-zero coupling at more than 95% C.L. for $5 < z < 500$ (right panel, zoom in z). This is consistent with the results found in [142], who find a $> 2\sigma$-level preference for a non-zero coupling coefficient when

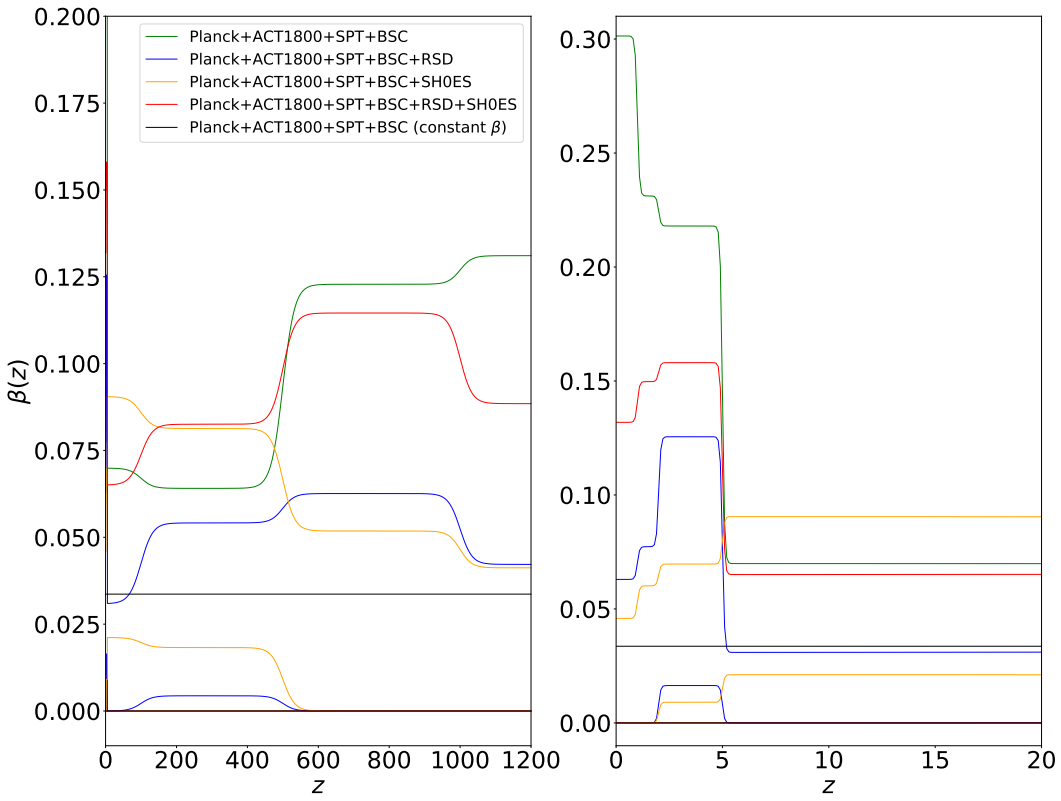

Fig. 5.10. 95% C.L. on $\beta(z)$ for a 7-bin coupling model constrained with different datasets that incorporate the baseline combination Planck+ACT1800+SPT. The right plot is a low-redshift zoom of the plot on the left. For reference, we include the constraints for a constant β with Planck+ACT1800+SPT+BSC, in black. The binning is defined by edges $z = \{0, 1, 2, 5, 100, 500, 1000\}$.

including a SH0ES prior and data from strong-lensing time delays from HoLICOW. However, when we use the combination RSD+SH0ES (in red) this evidence for a non-null coupling disappears.

In Fig. 5.11, we also present the results obtained with the baseline CMB dataset of Planck650+ACT+SPT, which corresponds, as explained above, to a larger cut of Planck data. We report the best-fit, mean and 68% C.L. uncertainties for each parameter in Table A.3 of Appendix A. We see that when we add BSC we are unable to constrain the coupling strength at redshifts $z < 5$ (i.e. coupling parameters β_1, β_2 and β_3), similar to the case with Planck+ACT1800+SPT CMB dataset; but when RSD data is included, constraints become tighter in all tomographic bins, and a lower value of σ_8 is favoured. Also, comparing with the contours obtained for a constant coupling case, and for the same dataset Planck650+ACT+SPT+BSC, in the 7-bin to-

mographic model, we no longer see any correlation between σ_8 and the coupling coefficient.

We also see that contours derived with the Planck650+ACT+SPT+SH0ES dataset are much less constrained than that of the Planck+ACT1800+SPT+SH0ES dataset, with an interesting point that in the case of the former dataset, there is no significant evidence for a non-null coupling in any redshift bin. A cut on large *Planck* TT multipoles has shown to lend a preference for a higher value of H_0 already in the context of the ΛCDM [61], thus making the Planck650+SH0ES combination less in tension with SH0ES. This could explain why a nonzero coupling becomes less necessary. Furthermore, comparing between datasets, we see that a change between the Planck650+ACT+SPT and Planck+ACT1800+SPT dataset mainly affects coupling constraints at high redshifts, with the Planck650 cut allowing for larger values of β_7. This is analogous to the 3-bin model, where β_3, the amplitude of the bin at the highest redshift $z > 1000$, is the least constrained when the Planck650+ACT+SPT dataset is used.

In Fig. 5.12 we plot $\beta(z)$ as a function of redshift, where similar to Fig. 5.10, constraints for every tomographic coupling bin are considerably loosened compared to a constant coupling model, especially at high redshifts. However, in all 3 datasets, results for β are still compatible with 0 at all redshifts, unlike with the CMB baseline Planck+ACT1800+SPT dataset.

In Fig. 5.13 we present a comparison of the mean and 68% C.L. of the various parameters derived for all the different datasets used to probe our 7-bin tomographic coupling model, comparing it to *Planck* fiducial cosmology, a ΛCDM model with the same datasets, and a constant coupling model. Comparing across models, we see that a tomographic coupling generally gives lower values of $\omega_{\rm DM}$, and higher values of σ_8 and H_0 than the constant coupling case by allowing for a stronger coupling at low and high redshifts. We see this reflected in our results for the case of σ_8 : when we compare the same dataset analysed with a ΛCDM model and a CDE model, we see that with CDE, σ_8 (and thus S_8) increases, even if $\omega_{\rm DM}$ decreases. For example, with a Planck+ACT1800+SPT+BSC dataset, $S_8 = 0.812^{+0.011}_{-0.010}$ in ΛCDM, while $S_8 = 0.834^{+0.015}_{-0.017}$ in a tomographic CDE case.

For almost every dataset, the most tightly constrained bins are β_4 and β_5, where $5 < z < 100$. This can be explained by the fact that this redshift bin encompasses the era of structure formation, to which a DE-DM coupling would be most sensitive,

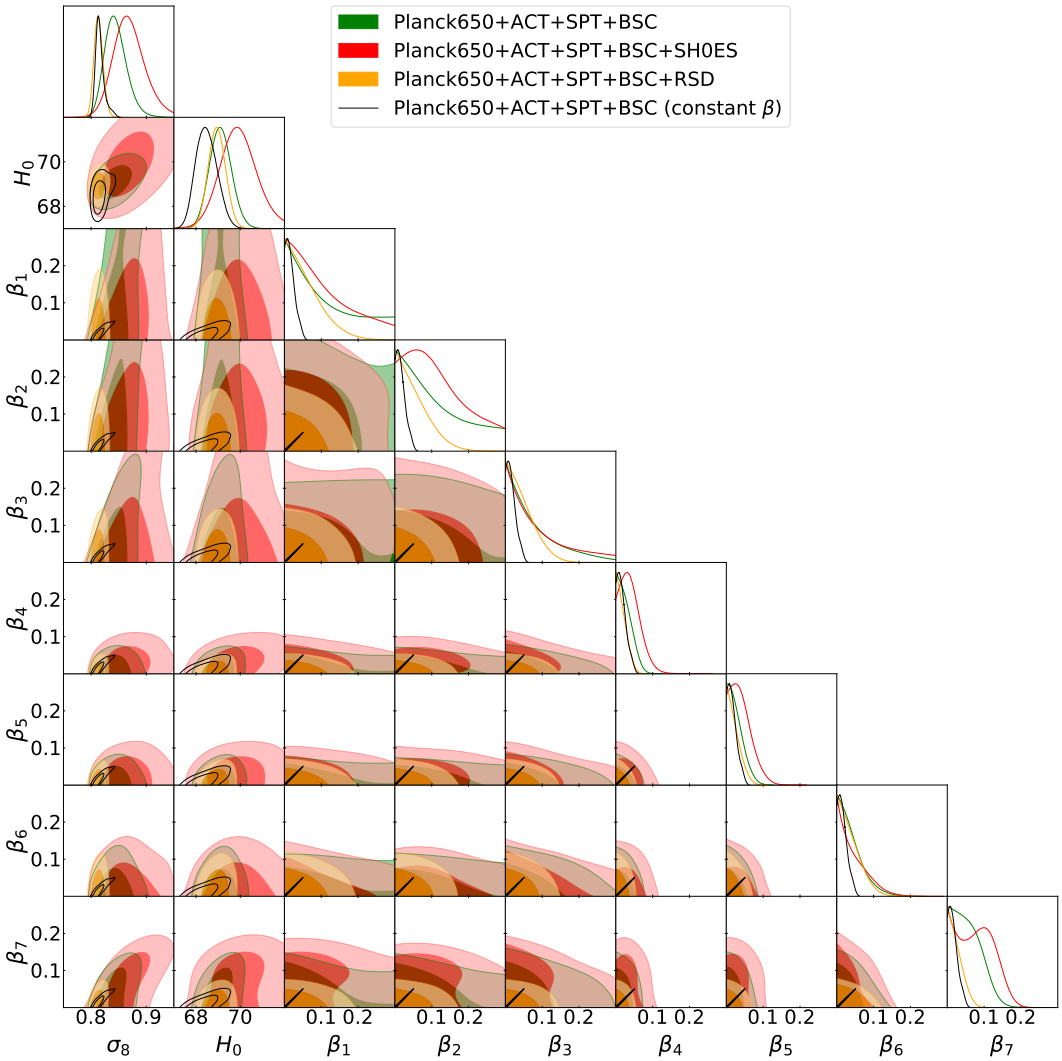

Fig. 5.11. Triangular plot of 68% and 95% C.L. posterior distributions of σ_8, H_0, and the 7 tomographic coupling coefficients β_{1-7} derived from datasets Planck650+ACT+SPT+BSC (green), Planck650+ACT+SPT+BSC+RSD (yellow) and Planck650+ACT+SPT+BSC+SH0ES (red). For reference, the binning is defined by edges $z = \{0, 1, 2, 5, 100, 500, 1000\}$. We include, in black lines, the contours obtained for a constant β case with Planck650+ACT+SPT+BSC data. In this case, the contours for all β_{1-7} are the same.

since as seen from Eqs. (5.5) and (5.16), coupling significantly affects the amount of dark matter and the amplitude of clustering. We further illustrate this in Fig. 5.14, where we plot the resultant $P(k)$ as we activate the coupling at each subsequent bin from 1 to 7. We see that increasing β_4 and β_5 from 0 to 0.1 gives the largest increase in $P(k)$. On the other hand, at lower redshifts (within tomographic bins β_1, β_2 and β_3), the impact of coupling on the matter power spectrum is much less significant,

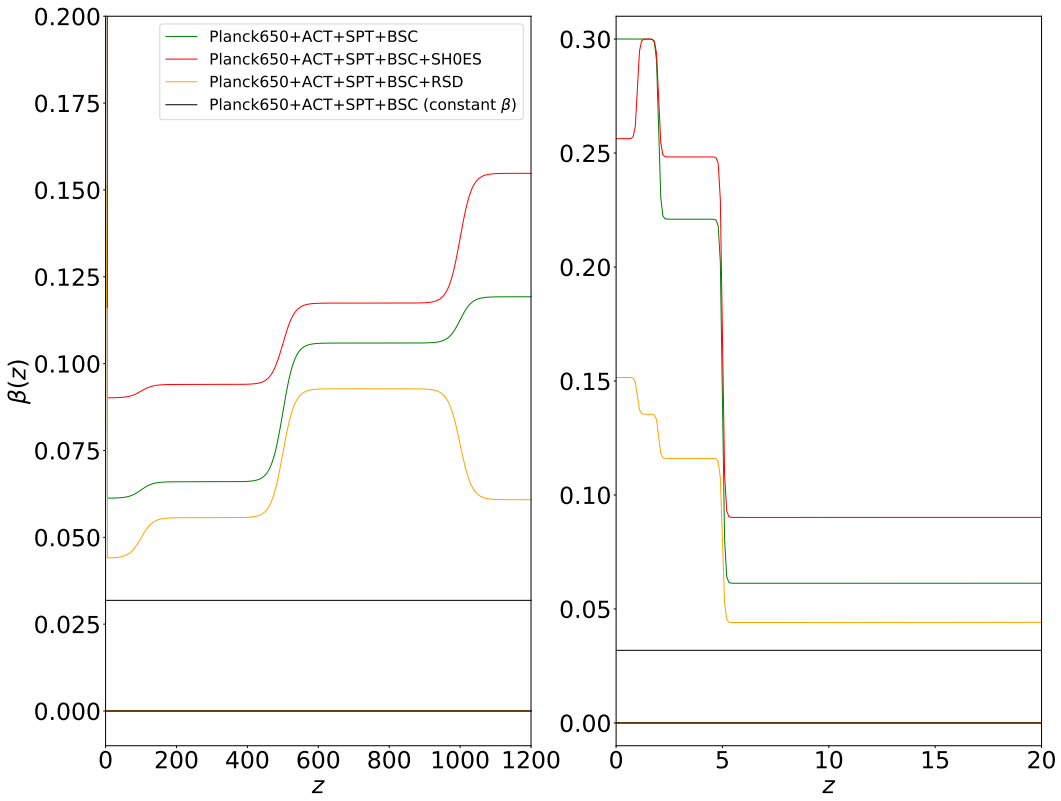

Fig. 5.12. 95% C.L. on $\beta(z)$ for a 7-bin coupling model, with base CMB dataset Planck650+ACT+SPT. The right plot is a low-redshift zoom of the plot on the left. For reference, we include the constraints for β in the case of a constant coupling derived from a dataset Planck650+ACT+SPT+BSC in black. The binning is defined by edges $z = \{0, 1, 2, 5, 100, 500, 1000\}$.

as seen from the inset of the same figure, which shows how activating β_1, β_2 and β_3 leads to only a slight increase in $P(k)$. Hence this could be why β_{1-3} can take on larger values and are thus much less constrained.

The 7-bin model allows us to better understand how the coupling affects the universe dynamics at different redshifts. A larger coupling is allowed at low redshifts ($z < 5$) and high redshifts ($z > 1000$), outside of the period of LSS formation in the MDE.

5.4.3 Constraints with Large Scale Structure Data

Finally, we consider constraints from galaxy surveys, using cosmic shear, galaxy clustering and 3x2pt : we use these datasets here for the first time in the context of CDE cosmologies, both for a constant coupling and for a tomographic coupling. The case of a constant coupling is shown in Fig. 5.15 : β is mainly constrained by galaxy

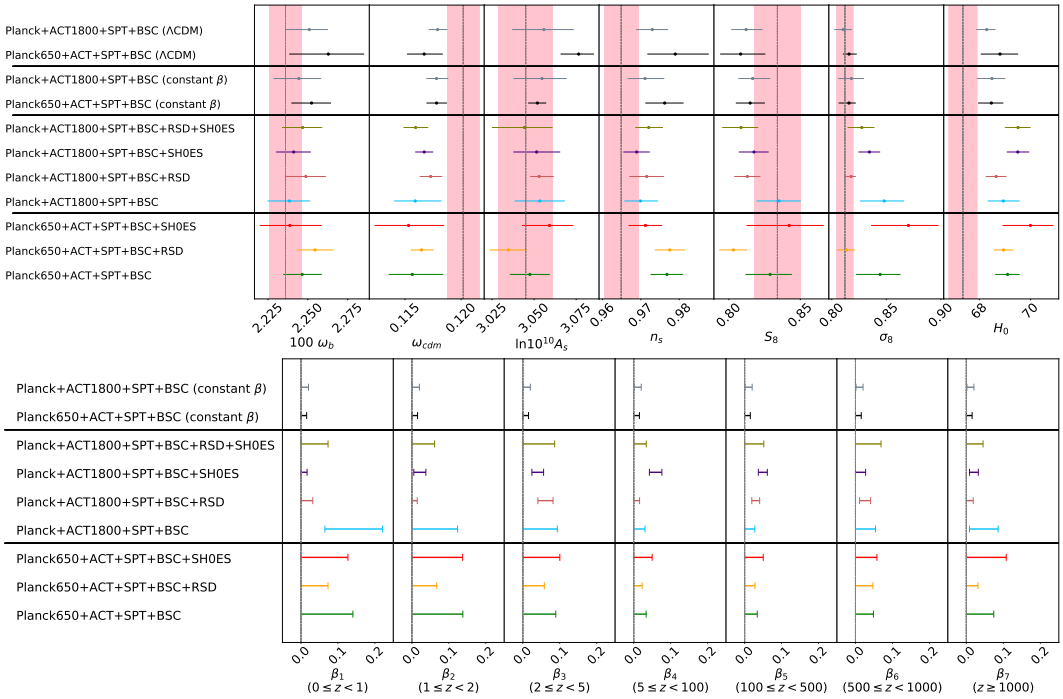

Fig. 5.13. Comparison of the mean and 68% C.L. values of the various cosmological parameters (top) and β coupling coefficients (bottom), for the various datasets in a 7-bin tomographic CDE model. In the top plot, the grey vertical dotted lines and pink band denote respectively the mean and 1σ of *Planck* fiducial cosmology. We also make a comparison with ΛCDM and a constant β model, for datasets Planck+ACT1800+SPT+BSC (grey) and Planck650+ACT+SPT+BSC (black).

clustering and 3x2pt probes, rather than by cosmic shear from KiDS alone (at least for the conservative cut we use at nonlinear scales, cf. Sect. 5.3.2).

Next, we present results using the same probes, but for a 4-bin tomographic coupling, in Fig. 5.16. We see that once again, similar to the constant coupling case, coupling strength is relatively unconstrained when using Cosmic Shear (CS) from KiDS alone (with a conservative cut), even more so than in the constant coupling case. Also, coupling at the highest redshift bin, β_4, is more constrained than the lower redshift bins. The lack of constraining power at $z < 2$ could be due to the fact that, as shown in Fig. 5.14, the increase of $P(k)$ caused by the coupling at such low redshifts is too small for CS to be sensitive towards. Moreover, cosmic shear is able to constrain S_8 but exhibits a strong degeneracy in the $\sigma_8 - \Omega_{\rm m}$ plane, which works in the same direction as β : larger values of β increase σ_8 while decreasing $\Omega_{\rm m}$. This also explains why larger values of the coupling are allowed by this dataset.

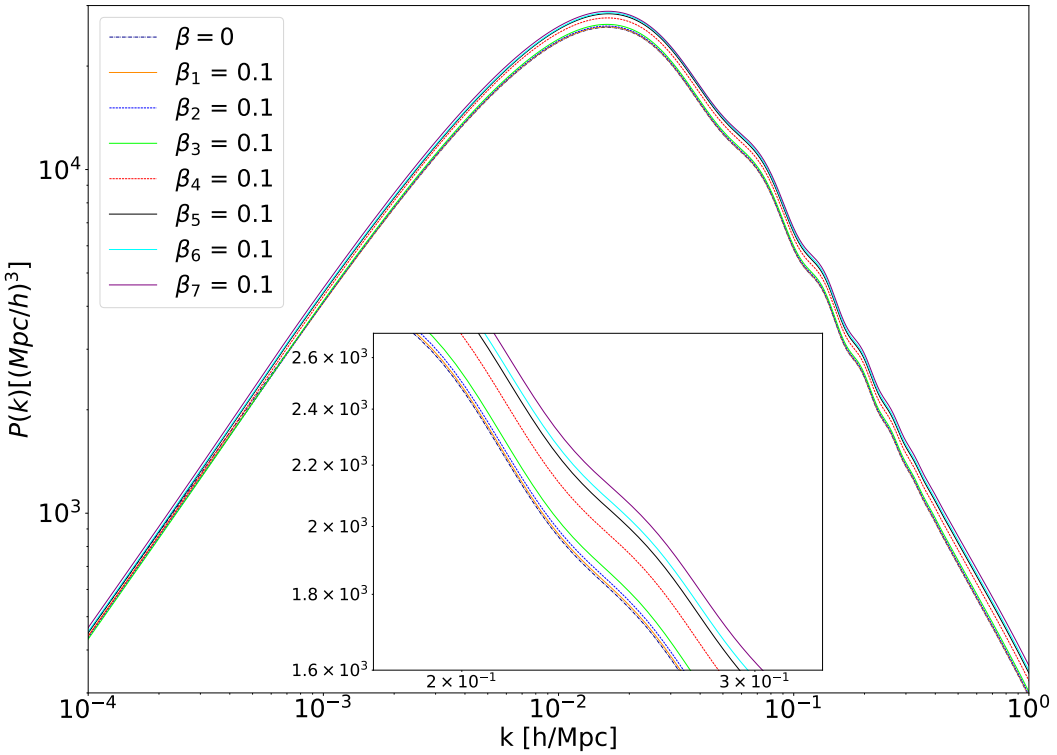

Fig. 5.14. Plot of the matter power spectrum $P(k)$ when activating coupling at each redshift bin (increasing subsequent values of coupling from 0 to 0.1 as done in Fig. 5.3), in the tomographic 7-bin case, keeping initial conditions fixed. The dashed dark blue line with $\beta = 0$ corresponds to ΛCDM. The inset plot is a zoom-in at small k scales. The binning is defined by edges $z = \{0, 1, 2, 5, 100, 500, 1000\}$.

On the other hand, galaxy clustering and subsequently 3x2pt are able to give tight constraints on the coupling at all redshifts, as they are able to break this degeneracy.

In Fig. 5.17 we plot the reconstruction of $\beta(z)$ at 95% C.L. for the various datasets we have employed. We see that when considering only the weak lensing probe, $\beta(z)$ is once again less constrained at low redshifts. However, when Planck+ACT1800+SPT+BSC data is included, constraints are tightened significantly (going from CS to the Planck+ACT1800+SPT+BSC+CS dataset). Moreover, comparing CDE models, we see that although constraints become much weaker going from a constant to a tomographic coupling model in the case of cosmic shear, constraints on β remain very similar for galaxy clustering (GC) and 3x2pt. Remarkably, GC and 3x2pt exhibit comparable, or even stronger, constraining power compared to CMB probes. Hence weak lensing and galaxy clustering are powerful tools to constrain coupled dark energy models, as they are sensitive to large-scale structure formation during late times and give

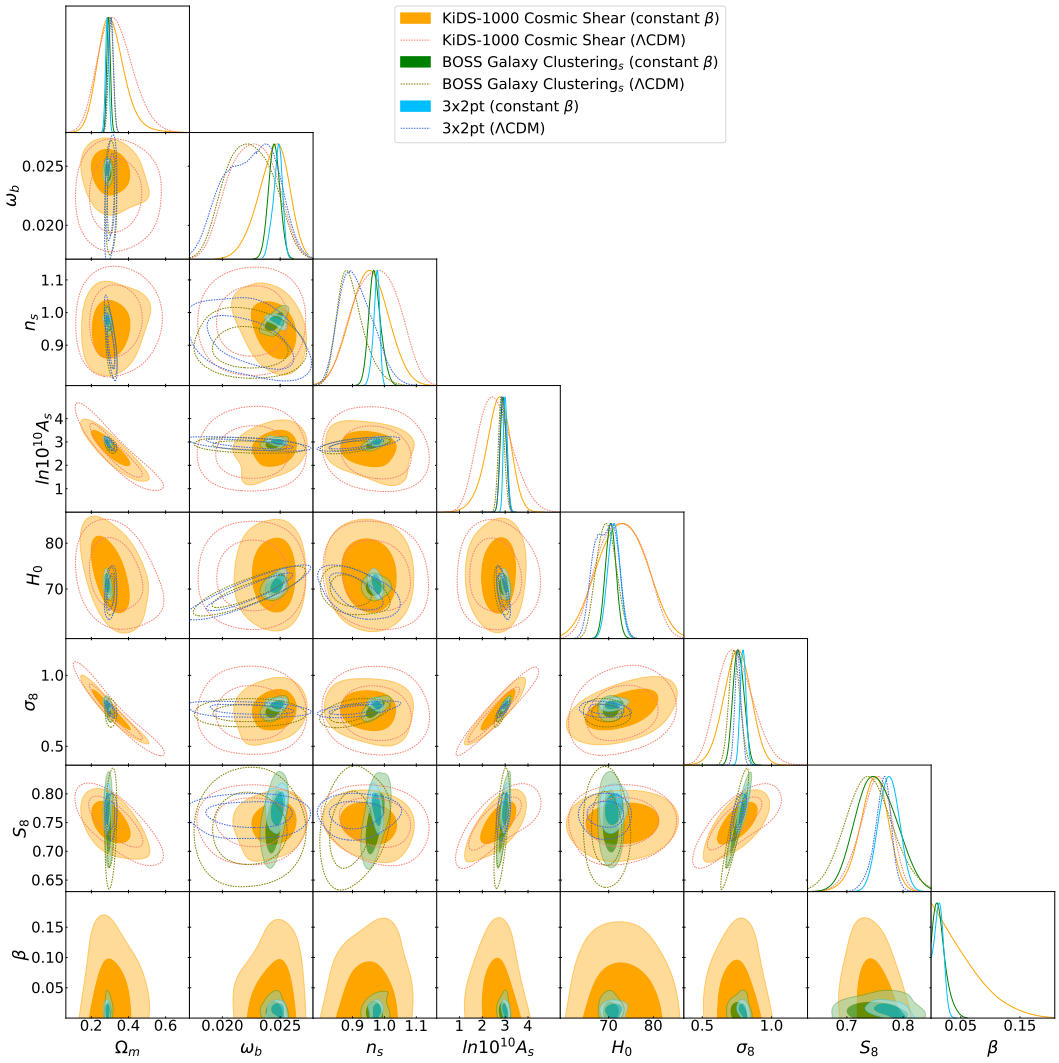

Fig. 5.15. Triangular plot of 68% and 95% C.L. posterior distributions of the various cosmological parameters, using datasets : KiDS-1000 cosmic shear (orange), BOSS spectroscopic galaxy clustering (green) and their 3x2pt (blue), for the ΛCDM (unfilled contours) and the constant coupling model.

considerable constraints on coupling at higher redshifts.

In Fig. 5.18 we plot the mean and 68% C.L. of the full set of cosmological parameters for each dataset, comparing them to the results obtained assuming ΛCDM. We see that in the case of a combined CMB and cosmic shear dataset, the bulk of the statistical power comes from Planck data : the mean value of each parameter is now more in agreement with *Planck* fiducial cosmology. Moreover, with a CDE model, the tension between the measurement of the S_8 parameter from CMB and weak lensing is eased : for ΛCDM, $S_8 = 0.764^{+0.017}_{-0.014}$ with the 3x2pt probe, and

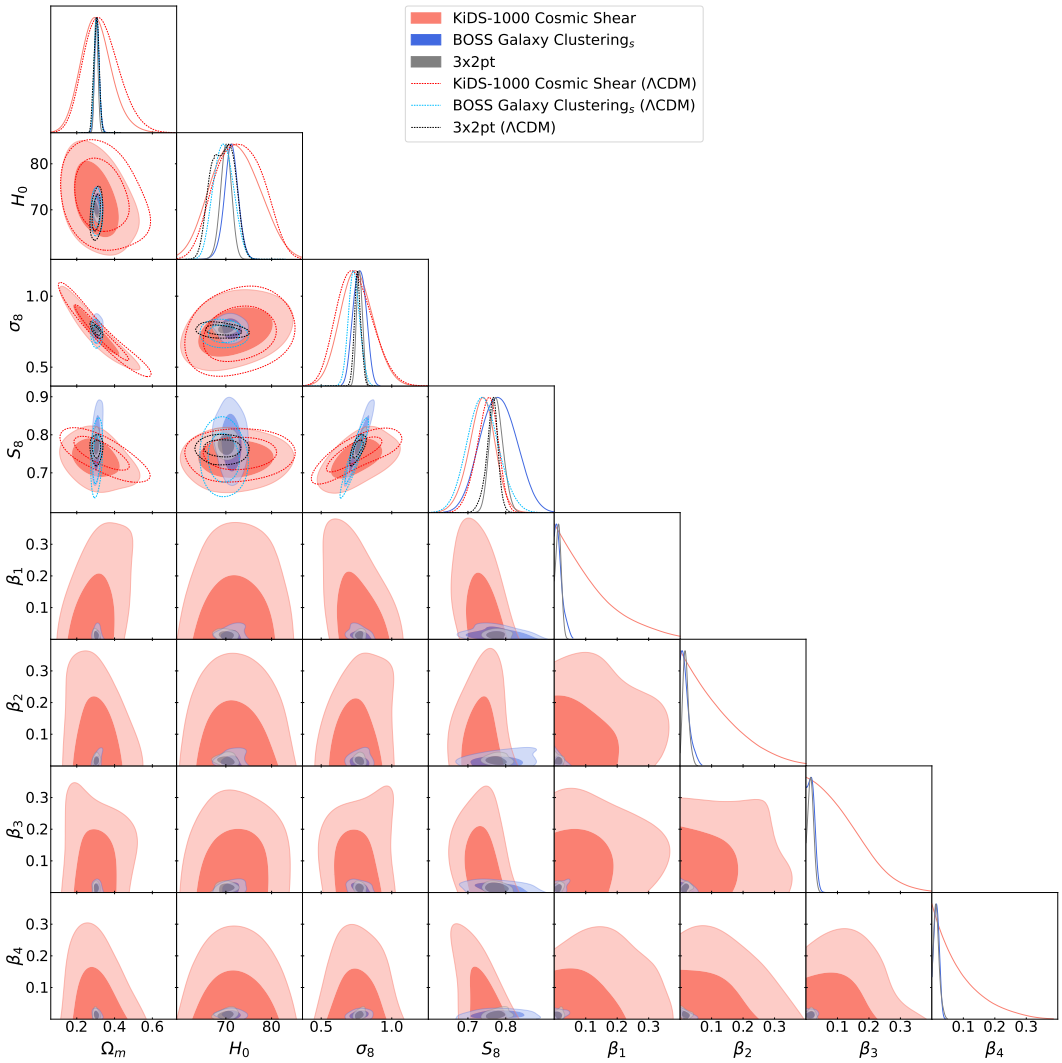

Fig. 5.16. Triangular plot of 68% and 95% C.L. posterior distributions of the various cosmological parameters, for both ΛCDM and the 4-bin tomographic model using datasets : KiDS-1000 cosmic shear (red), BOSS spectroscopic galaxy clustering (blue) and their 3x2pt (grey). For reference, the bin edges are defined as $z = \{0, 0.5, 1, 2\}$.

$S_8 = 0.834 \pm 0.016$ with the Planck dataset, which is a $\sim 3.1\sigma$ tension. In a constant coupling model, $S_8 = 0.775 \pm 0.018$ using 3x2pt and $S_8 = 0.829^{+0.023}_{-0.026}$ with Planck, thus reducing this tension to $\sim 1.8\sigma$. The decrease of the tension is due to the increase of S_8 obtained from the 3x2pt dataset and also to the increase of the uncertainties. Both effects are induced by the coupling. On the other hand, the values for the other parameters remain within 1σ agreement : for example, in a constant coupling case, $\omega_{\rm DM} = 0.119 \pm 0.002$ and $\sigma_8 = 0.822^{+0.013}_{-0.015}$ for the Planck dataset, while $\omega_{\rm DM} = 0.120^{+0.007}_{-0.006}$ and $\sigma_8 = 0.795^{+0.020}_{-0.015}$ for the 3x2pt dataset. However, we

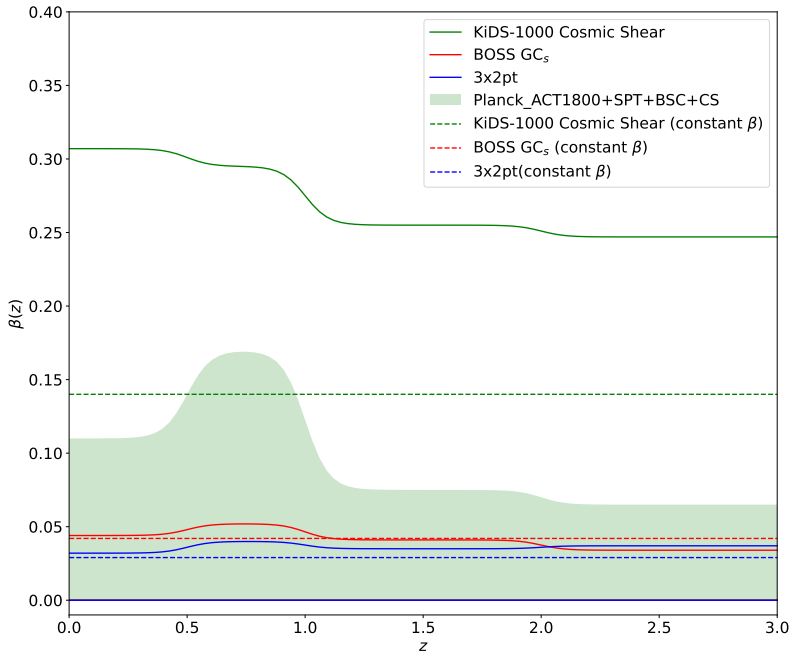

Fig. 5.17. 95% C.L. on $\beta(z)$ for a 4-bin coupling model, for cosmic shear (green), galaxy clustering (red) and 3x2pt (blue) datasets, tested on CDE with a constant coupling (dotted lines) and tomographic CDE (solid lines). The Planck+ACT1800+SPT+BSC+CS dataset, tested with a tomographic CDE model, is shaded in green. The binning is defined by edges $z = \{0, 0.5, 1, 2\}$.

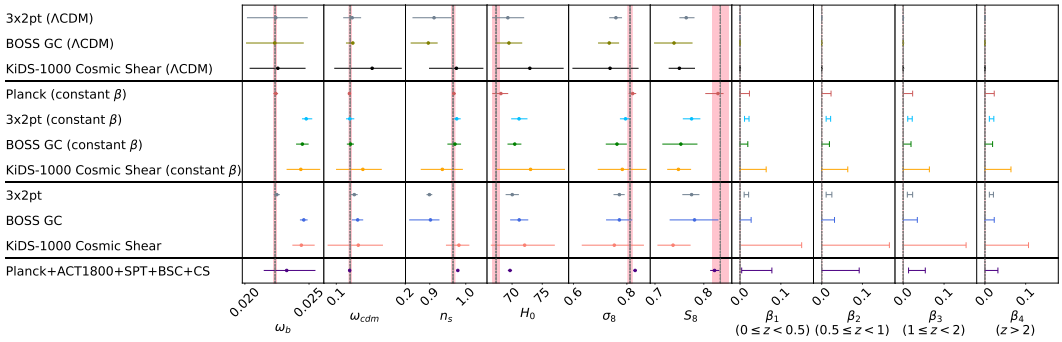

Fig. 5.18. Mean and 68% C.L. values for the various cosmological parameters and coupling coefficients obtained with the three weak lensing and galaxy clustering datasets only, for the ΛCDM, the constant β and the 4-bin tomographic models. For ease of comparison, we put in the same figure results obtained from our earlier analysis of a Planck dataset in a constant coupling case, and results from the analysis of Planck+ACT1800+SPT+BSC+CS in a 4-bin tomographic model.

note that these calculations are only estimates as they assume Gaussian posterior distributions for the cosmological parameters.

These calculations have been made based on the values quoted in Tables A.1 and

A.4 of Appendix A. We also include the best-fit, mean and 68% C.L. uncertainties for each parameter in these tables.

5.4.4 Bayesian Model Comparison

We conduct a rough model comparison by calculating the $\Delta\chi^2_{\rm min} = \chi^2_{\rm cde,min} - \chi^2_{\Lambda{\rm CDM,min}}$ of each of the datasets used in each model with respect to ΛCDM, and report their values in Table 5.2. We see that across all models and datasets, the CDE model (be it constant or tomographic) is able to reduce the $\chi^2_{\rm min}$ value with respect to ΛCDM. This difference is generally not large enough to signify a statistically significant preference for CDE over ΛCDM; moreover, the large number of parameters varied especially in the tomographic CDE scenario will penalise the model.

Thus we also calculate the Bayes factor, a more robust method of quantifying the goodness of fit of the data to the model as it takes into account the number of parameters varied in the model. Its logarithm is given by

$$\ln B = \ln \mathcal{Z}({\rm CDE}|D) - \ln \mathcal{Z}(\Lambda{\rm CDM}|D), \tag{5.21}$$

where $\mathcal{Z}(M_i|D)$ is the Bayesian evidence of the model M_i under the dataset D. We use the code `MCEvidence` [179] to numerically calculate the evidence estimated using the kth Nearest Neighbour method, for one chosen dataset in each CDE model (3-bin, 7-bin, 4-bin and constant coupling when using cosmic shear). We report their values in Table 5.2. We see that $\ln B < -3$ for all models which, based on the Jeffreys' scale, shows substantial evidence for ΛCDM over CDE models [180]. Thus even when constant or tomographic CDE models give a smaller $\chi^2_{\rm min}$, the data does not show a preference towards CDE.

Dataset + Model	χ^2	$\ln B$
Constant β		
Planck	-2.59	–
Planck+ACT180o+SPT+BSC	-0.80	–
Planck65o+ACT+SPT+BSC	-7.98	–
Cosmic Shear	-2.48	-11.35
Galaxy Clustering	-3.64	–
3x2pt	-3.56	–
3-bin β		
Planck	-1.99	-3.73
Planck+PlanckLens	-1.72	–
Planck+ACT180o	-1.12	–
Planck+ACT180o+SPT	-5.96	–
Planck65o+ACT+SPT	-6.11	–
7-bin β		
Planck+ACT180o+SPT+BSC	-2.66	-10.61
Planck+ACT180o+SPT+BSC+RSD	-2.56	–
Planck+ACT180o+SPT+BSC+SH0ES	-9.88	–
Planck+ACT180o+SPT+BSC+RSD+SH0ES	-1.92	–
Planck65o+ACT+SPT+BSC	-14.06	-10.56
Planck65o+ACT+SPT+BSC+RSD	-17.84	–
Planck65o+ACT+SPT+BSC+SH0ES	-13.74	–
4-bin β		
Cosmic Shear	-2.81	-6.73
Galaxy Clustering	-2.57	–
3x2pt	-3.54	–

Table 5.2. Table of χ^2 values and $\ln B$ values for selected models and datasets.

IN BRIEF

In this Chapter, I introduced a *coupled dark energy* (CDE) model, an alternative to the concordance ΛCDM model. I then proposed a new parameterisation for the CDE model, where I allowed the coupling parameter to vary with cosmic evolution. To do this, I binned the coupling in redshift z, and investigated three binning parameterisations, to see how well different datasets, varying from early to late times, can constrain coupling strength at various cosmological epochs. In order to calculate the cosmological observables, I also modified an existing Einstein-Boltzmann code, `CLASS`, according to my model.

In the case of a 3-bin model probed only with high-redshift CMB data, constraints on β are looser in a tomographic model compared to in a constant β model. With the inclusion of low-redshift data probes and a finer 7-bin parametrisation, the tightest constraints on coupling occur at redshifts corresponding to the era of LSS formation, while constraints on late-time coupling enlarge by almost one order of magnitude. However, when employing LSS probes, I was able to recover tight constraints on β at $z < 2$, demonstrating for the first time the promising potential of these datasets in constraining coupled dark energy models.

I have thus laid the framework for a tomographic CDE model in this Chapter, and established constraints on this model based on current observational data. In the subsequent Chapters, I move on to discuss how I have applied this model in various other studies.

6. Early Coupled Quintessence

Sommaire

6.1 Introduction

In this Chapter, I introduce a subclass of the CDE model, which I term an *Early Coupled Quintessence* (ECQ) model [181]. As its name suggests, the coupling between the scalar field and the DM particles, which I have introduced in the previous Chapter, only occurs at early times, i.e. during the RDE. This class of coupled quintessence models are of particular interest as [182] showed that if the strength of this coupling is large enough, the system approaches an *attractor solution* in the RDE, whereby the scalar and DM energy densities evolve as the radiation one, such that Ω_R, $\Omega_{\rm DM}$, and Ω_ϕ remain constant over the epoch where coupling is activated. This induces a rapid growth of DM overdensities. Subsequently, this can lead to the formation of compact primordial structures, such as primordial black holes [129, 182] or primordial dark matter halos [183], which can be enticing candidates for dark matter.

6.2 Theoretical Framework

The mechanics of coupling in the ECQ model are the same as that of CDE models, hence we shall delve straight into the discussion of its specific features at the background and perturbation levels.

6.2.1 Background Modifications

Once again considering a flat FLRW Universe, we evoke the modified conservation equations for the DM and scalar field respectively :

$$\dot{\rho}_{\rm DM} + 3H\rho_{\rm DM} = -\kappa\beta\rho_{\rm DM}\dot{\phi}, \tag{6.1}$$

$$\dot{\rho}_{\phi} + 3H(\rho_{\phi} + p_{\phi}) = \kappa\beta\rho_{\rm DM}\dot{\phi}, \tag{6.2}$$

with the Friedmann equation being

$$H^2 = \frac{\kappa^2}{3}\left(\frac{\rho_{\rm DM,0}}{a}e^{-\beta\phi} + \frac{\rho_{R,0}}{a^2} + \frac{1}{2}\dot{\phi} + V(\phi)a^2\right) \tag{6.3}$$

where the dot denotes a derivative with respect to cosmic time t, and we have assumed a flat potential of the form $V(\phi) = V_0$, as was the case in the previous Chapter.

The coupling is effectively active whenever the fermions are non-relativistic (i.e. when $\rho_{\rm DM} \neq 3p_{\rm DM}$). In the limit when $\beta > 1/\sqrt{2}$, the system presents an attractor solution in which the DM and ϕ energy densities follow the evolution of radiation, i.e. $\rho_{\rm DM} \sim \rho_{\phi} \sim \rho_R \propto a^{-4}$.

We can find this scaling solution to Eqs. (6.1)and (6.2) following the methodology of [184]. From Eq. (6.3), we define the variables

$$x = \frac{\kappa}{H}\frac{\dot{\phi}}{\sqrt{6}}, \qquad y = \frac{\kappa a}{H}\sqrt{\frac{V_0}{3}} \qquad z = \frac{\kappa a}{H}\sqrt{\frac{\rho_R}{3}}, \tag{6.4}$$

where $\Omega_{\phi} = x^2 + y^2$, $\Omega_{\rm r} = z^2$ and $\Omega_{\rm DM} = 1 - x^2 - y^2 - z^2$. Differentiating the set of equations in (6.4) with respect to $\ln a$,

$$x' = x\left(\frac{z'}{z} - 1\right) - \sqrt{\frac{3}{2}}\beta(1 - x^2 - y^2 - z^2) \tag{6.5}$$

$$y' = y\left(2 + \frac{z'}{z}\right) \tag{6.6}$$

$$z' = -\frac{z}{2}(1 - 3x^2 + 3y^2 - z^2) \tag{6.7}$$

The scaling solutions exist when $x' = y' = z' = 0$. In the case where all 3 components of the scalar field, dark matter and radiation are non-negligible, we arrive at a critical point that is a solution to the system of equations (6.5) $-$ (6.7). We then arrive at the expressions for the density parameters of the scalar field ϕ, DM and

radiation components, which depend purely on the strength of coupling β :

$$\Omega_\phi = \frac{1}{6\beta^2}, \qquad \Omega_{\rm DM} = \frac{1}{3\beta^2}, \qquad \Omega_R = 1 - \frac{1}{2\beta^2}. \tag{6.8}$$

In this regime, the scalar field energy is dominantly kinetic. Taking the general form of the solution for Eq. (6.1) and assuming it scales as a^{-4} [85, 185-187],

$$\rho_{\rm DM,0} a^{-4} = \rho_{\rm DM,0} a^{-3} e^{-\kappa\beta\phi}, \tag{6.9}$$

we have

$$\phi' = \frac{1}{\kappa\beta}, \tag{6.10}$$

where the dot signifies a derivative with respect to the number of e-folds $dN \equiv d\ln a$, and $\phi' = \dot{\phi}H$.

Additionally, we note that Big Bang Nucleosynthesis (BBN) constraints require that the coupling must satisfy $\beta^2 \gg 1$ to have $\Omega_R \gg \Omega_{\rm DM}, \Omega_\phi$ in the RDE, if scaling starts before BBN ($z \sim 10^9$).

6.2.2 Perturbation Modifications

The evolution of the matter density contrast $\delta_{\rm DM}$ can be derived from the Navier-Stokes equations [93]. If there are no shear or rotational components in the initial velocity field, during RDE, these equations condense into a single differential equation governing the nonlinear growth at subhorizon scales [183],

$$\delta''_{\rm DM} + \left(1 + \frac{\mathcal{H}'}{\mathcal{H}} - \kappa\beta\phi'\right)\delta'_{\rm DM} - \frac{4}{3}\left(\frac{\delta'^2_{\rm DM}}{1+\delta_{\rm DM}}\right) - \frac{3}{2}\left(Y\Omega_{\rm DM}\delta_{\rm DM} + \Omega_R\delta_R\right)\left(1+\delta_{\rm DM}\right) = 0, \tag{6.11}$$

where $Y \equiv 1 + 2\beta^2$ is the effective coupling strength resulting from gravity plus the fifth force. Hence, for $|\beta| \approx 1$, the fifth force is of gravitational order.

In the scaling regime during RDE, $\mathcal{H}' \approx -\mathcal{H}$. Since $\Omega_R\delta_R$ is small, if $\beta^2 \gg 1$, Eq. (6.11) reduces to

$$\delta''_{\rm DM} - \delta'_{\rm DM} - \delta_{\rm DM}\left(1+\delta_{\rm DM}\right) - \frac{4}{3}\left(\frac{\delta'^2_{\rm DM}}{1+\delta_{\rm DM}}\right) = 0, \tag{6.12}$$

where we have also used Eq. (6.8). The DM overdensities are small at early times,

so Eq. (6.12) can be linearised and analytically solved, leading to

$$\delta_{\rm DM} = \delta_{\rm DM,in} \left(\frac{a}{a_{\rm in}}\right)^p \text{, with } p = \frac{1+\sqrt{5}}{2} \equiv \varphi \approx 1.618, \tag{6.13}$$

where the growth rate coincides with the golden ratio φ and $a_{\rm in}$ is the scale factor at the beginning of the scaling regime, when $\delta_{\rm DM}(a_{\rm in}) = \delta_{\rm DM,in}$. The scaling solution in Eq. (6.8) remains valid till the coupling is effectively switched off. Afterwards, the model behaves as ΛCDM.

6.3 Methodology

To reach the scaling solution, the energy of the scalar field must be kinetically dominated, which is achievable via a field-dependent potential with a cross-over phase or a sufficiently small constant potential. Here we mainly consider a constant potential $V = V_0 \sim \mathcal{O}(M_P^2 H_0^2)$ to produce acceleration at late times. Since this value is much lower than the critical energy density during the RDE, ϕ is naturally kinetically dominated and the system approaches the scaling solution if $\beta > 1/\sqrt{2}$.

We set the initial conditions (denoted by the subscript 'ini') for $\dot{\phi}$ and the DM density to the scaling solution values (recall Eqs. (6.8) and (6.10))

$$\dot{\phi}_{\rm ini} = \frac{1}{\kappa\beta}, \quad \text{and} \quad \rho_{\rm DM,ini} = \frac{\rho_{R,\rm ini}}{3\left(\beta^2 - \frac{1}{2}\right)}, \tag{6.14}$$

at $z_{\rm ini} = 10^{14}$, i.e. we assume that the system starts in the scaling regime at $z_{\rm ini}$. Moreover, we set $\phi_{\rm ini} = 0$ since, given the considered flat potential, the dynamics of the scalar field do not depend on its initial value.

To mimic a transition from $\beta(\phi) \sim \beta$ to $\beta(\phi) \sim 0$, we employ a similar parametrisation introduced in the previous Chapter (Eq. (5.17)), but for only 2 bins :

$$\beta(z) = \frac{\beta \tanh\left[s_z(z - z_{\rm OFF})\right] + \beta}{2}, \tag{6.15}$$

with s_z a crossover rapidity that we set to a fiducial value $s_z = 0.3$, ensuring a smooth and rapid enough transition as compared to $H^{-1}(z_{\rm OFF})$ in cosmic time, and $z_{\rm OFF}$ the redshift when coupling is deactivated and the fifth force becomes negligible.

From the scaling solution Eq. (6.8), we expect an important degeneracy between

β and $z_{\rm OFF}$. By matching the expressions of the DM and radiation energy densities before and after the transition at $z_{\rm OFF}$ and considering (for now) massless neutrinos, we obtain

$$z_{\rm OFF} = -1 + 3\frac{\Omega_{\rm DM,0}}{\Omega_{R,0}}\left(\beta^2 - \frac{1}{2}\right). \tag{6.16}$$

A larger value for the coupling necessitates a larger redshift at which it is deactivated. This is consistent with the fact that a larger β implies a stronger fifth force driving an intensified structure growth. Assuming *Planck* best-fit values for $\Omega_{\rm DM,0}$ and $\Omega_{R,0}$ [61], we expect $z_{\rm OFF} \sim 10^4\beta^2$, regardless of the redshift at which the scaling begins.

As we did in the previous Chapter for a tomographic CDE model, we modify the Einstein-Boltzmann code `CLASS` by implementing the background and linear perturbation equations described in the previous 2 subsections, considering Eq. (6.15), with the initial conditions discussed above.

We plot the ΛCDM and ECQ density parameters Ω_i in Fig. 6.1. For ECQ, we set the current energy fractions close to the *Planck* fiducial ΛCDM values ($n_{\rm s} = 0.9649$, $\ln(10^{10}A_{\rm s}) = 3.044$, $\omega_{\rm b,0} = 0.02237$, $V_0 = 2.64 \cdot 10^{-47}$ GeV^4) and fix $\beta = 13$ and $z_{\rm OFF} = 1.69 \times 10^6$, making the model lie almost exactly along the degeneracy curve given in Eq. (6.16). We observe the presence of the scaling solution during the RDE (at $z > z_{\rm OFF}$) in the ECQ model. To better understand the individual impact of and the relationship between β and $z_{\rm OFF}$, we plot the evolution of the density parameters and the Hubble function for a fixed $z_{\rm OFF}$ and different β values, corresponding to ECQ models out of the degeneracy curve of Eq. (6.16), in Appendix B.

In Fig. 6.2, we present the growth of DM overdensities at scale $k = 45\,h$Mpc^{-1} as a function of the scale factor a, for both an ECQ model and ΛCDM. We notice that, for superhorizon modes in ECQ, the DM density contrast follows the ΛCDM prediction $\delta_{\rm DM} \sim a^2$. After mode re-entry, it follows the predicted golden ratio growth (6.13) until the coupling is turned off.

We subsequently plot the matter and CMB temperature spectra for $\beta = [11, 12, 13, 15]$ and fixed $z_{\rm OFF} = 1.69\times10^6$ in Fig. 6.3. We include again the ΛCDM curves for comparison. At $z_{\rm OFF}$ we expect that only wave modes with $k \gtrsim 5\,h$Mpc^{-1} have reentered the horizon, and hence be directly affected by the fifth force. Indeed, during scaling, we can derive the relation between the mode k and its re-entry redshift z :

$$k \approx \sqrt{\frac{\Omega_{R,0}}{\Omega_R}}\frac{z}{3000}\,h\,{\rm Mpc}^{-1}. \tag{6.17}$$

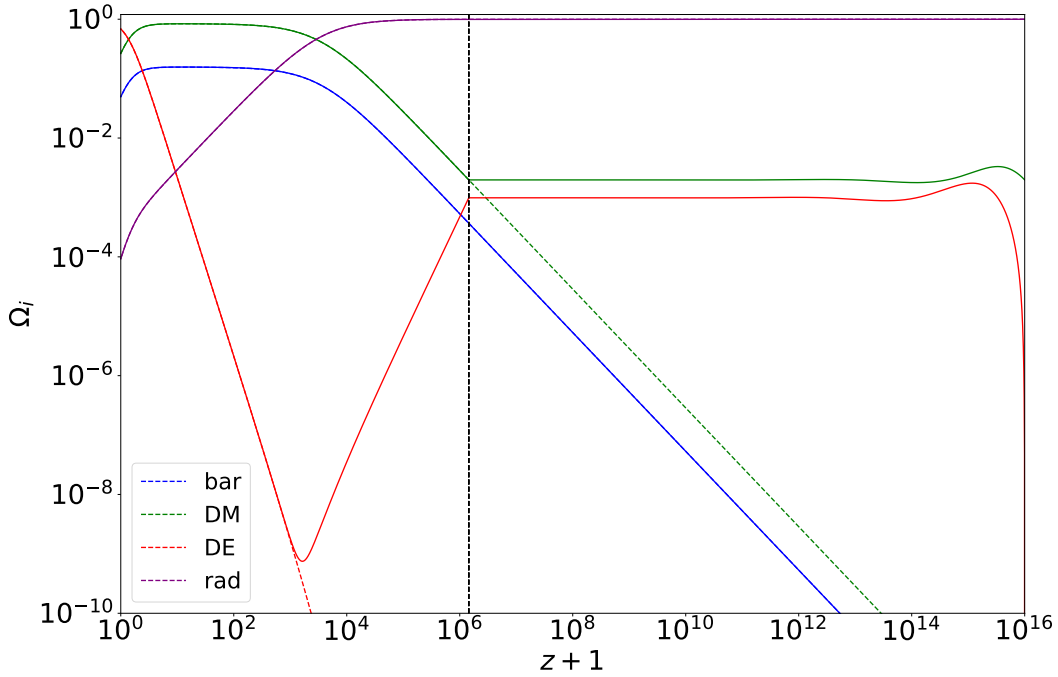

Fig. 6.1. Background evolution of the density fractions Ω_i's of baryons (blue), DM (green), DE (red), and radiation (purple) for ECQ (solid lines) and ΛCDM (dotted lines). We fix the values of $\omega_{\mathrm{b},0}$, V_0, and H_0 to the *Planck* 2018 TTTEEE+lowE+lensing ΛCDM best-fit cosmology [61], and set $\beta = 13$ and $z_{\mathrm{OFF}} = 10^4\beta^2 = 1.69 \times 10^6$ to obtain the ΛCDM background evolution at $z < z_{\mathrm{OFF}}$ in the ECQ model. The grey dashed vertical line indicates z_{OFF}.

However, smaller wave modes are also sensitive to the coupling through the changes induced at the background level. In Fig. 6.3, we still observe an increase of $P(k)$ at $k \gtrsim \mathcal{O}(0.1)\,h\mathrm{Mpc}^{-1}$ and a shift of its peak. This is because Ω_{DM} increases and matter-radiation equality happens at larger redshifts for decreasing values of β and a fixed z_{OFF}. However, when β becomes sufficiently large, Ω_{DM} decreases such that $P(k)$ becomes smaller than in ΛCDM at small scales and larger at large scales (we show this for $\beta = 15$).

Concerning the CMB TT spectrum, we see that the amplitude of the peaks decreases and they shift to lower multipoles for lower values of β, considering again a fixed z_{OFF}. The decrease in amplitude can be explained by the increase in Ω_{DM} at pre-recombination times. Furthermore, this also alters the baryon fraction $\rho_{\mathrm{b}}/\rho_{\mathrm{DM}}$, thereby changing the ratio between the amplitudes of the odd and even peaks. Finally, the observed shifts of the peaks to lower multipoles are again due to the increase of the DM energy density, which changes the sound horizon at the baryon-drag epoch, $r_s(z_d)$, and the angular diameter distance to the last scattering surface.

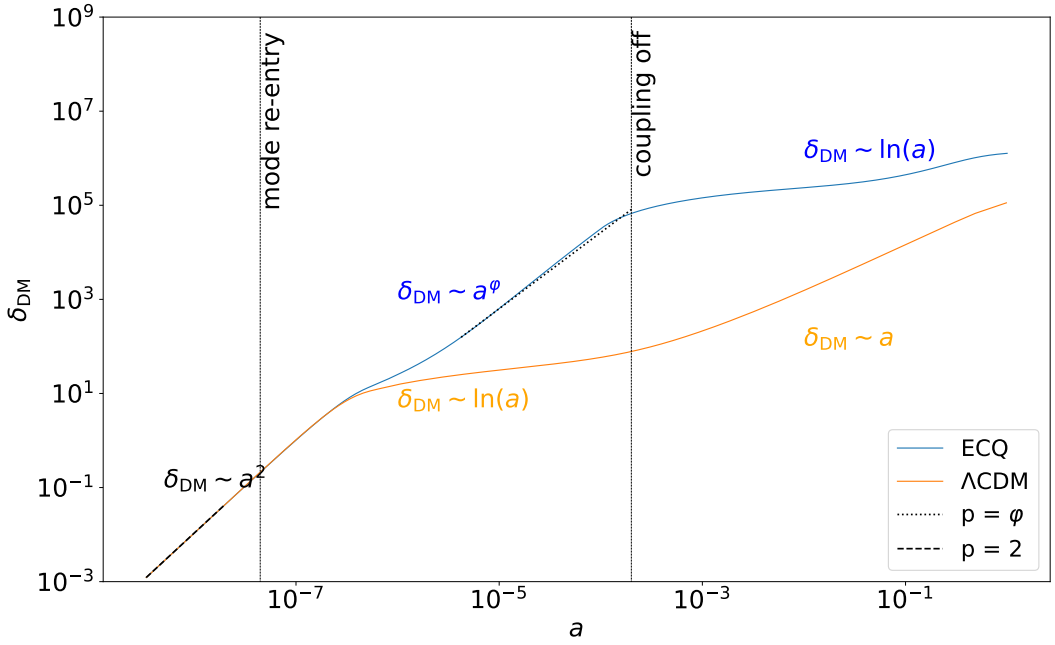

Fig. 6.2. Evolution of DM density contrast $\delta_{\rm DM}$ in ECQ (blue) and ΛCDM (orange) as a function of scale factor a, for the scale $k = 45\,h$Mpc^{-1}, for the cosmological parameter values as in Fig. 6.1. We include the theoretical $\delta_{\rm DM} \sim a^2$ growth at superhorizon scales during the RDE in black dashed lines and the one during the ECQ scaling regime $\delta_{\rm DM} \sim a^{\varphi}$ at subhorizon scales (Eq. (6.13)) in black dotted lines. Vertical lines denote the time of mode re-entry and when the coupling is turned off. Notice that after turning the coupling off the universe is still strongly dominated by radiation. This is why $\delta_{\rm DM} \sim \ln(a)$ even at $a > 10^{-3}$, deep inside the MDE of the ΛCDM. This is because this model lies far from the degeneracy curve (6.16), such that $z_{\rm OFF}$ is too low for the ECQ model to be realistic. Thus, the recombination time would significantly change with respect to ΛCDM. This figure illustrates the fulfilment of theoretical growth and the potential to enhance the power of matter fluctuations in ECQ during the RDE at sufficiently small scales.

The latter has a more significant relative effect, moving the peaks to the left.

6.3.1 Inference and Data

We conduct an MCMC analysis to constrain the parameter space of the model : sampling across the suite of parameters $\{n_{\rm s}, \ln(10^{10}A_{\rm s}), \tau, \omega_{\rm b}, V_0, \beta^2, z_{\rm OFF}\}$ and obtaining H_0, $\Omega_{\rm DM,0}$, σ_8 and S_8 as derived parameters. We assume a flat universe with two massless neutrinos and a massive one with $m_\nu = 0.06$ eV. We sample β^2 instead of β to expedite convergence, taking advantage of the linear relationship (6.16) between $z_{\rm OFF}$ and β^2. Additionally, we highlight that since we want the system to begin in the scaling regime, we impose the initial conditions as described in the previous section (specifically Eq. (6.14)); hence we do not directly sample $\omega_{\rm DM}$, instead

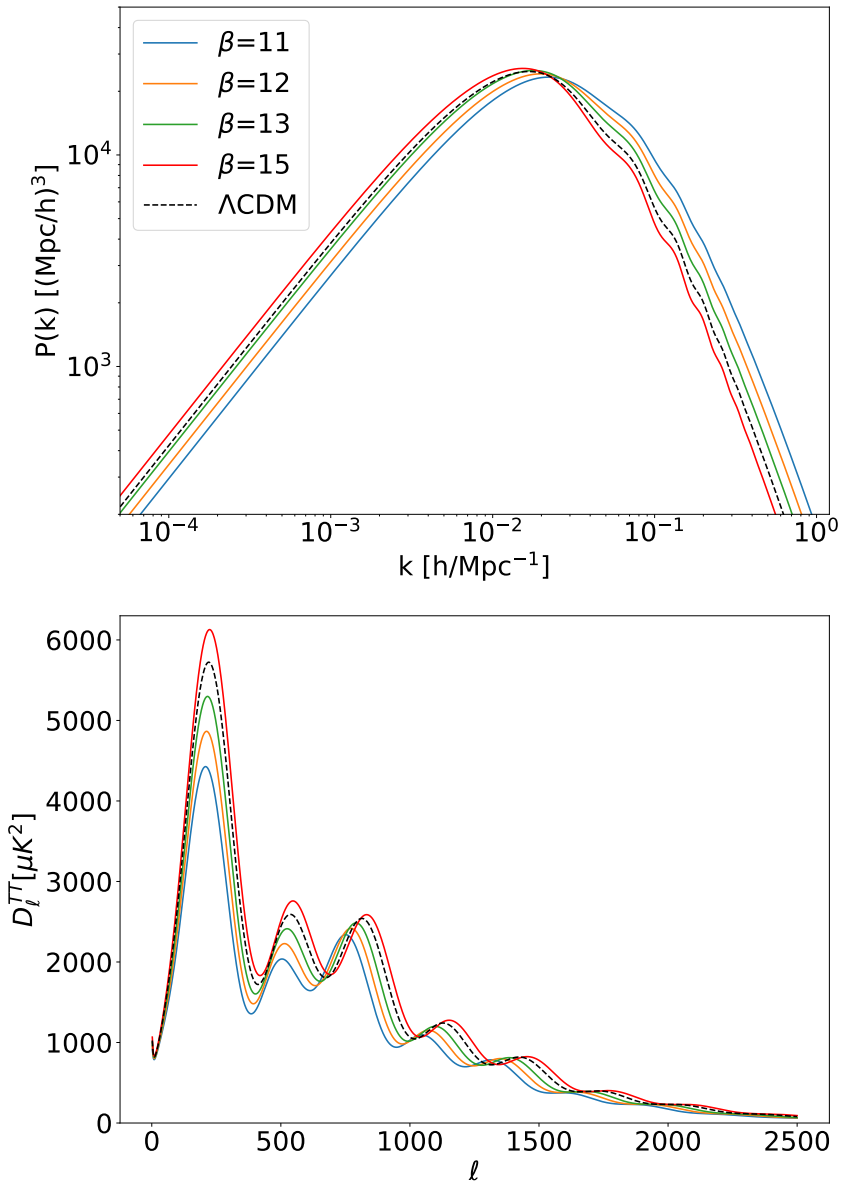

Fig. 6.3. Matter (top) and CMB (bottom) temperature power spectra for both ΛCDM (black dashed) and ECQ (coloured solid). Here, we fix $z_{\rm OFF} = 1.69 \times 10^6$ and vary $\beta = \{11, 12, 13, 15\}$.

deriving its value based on β.

The relative abundance of light elements just after BBN places tight constraints on the expansion rate value [188] and consequently, on the density parameters $\Omega_{\rm DM}$, Ω_ϕ and Ω_R during the scaling regime [189]. This translates to a rough lower bound of $\beta \gtrsim 3$ in ECQ [183]. This restriction indicates that one cannot recover ΛCDM from ECQ by setting $\beta = 0$: the two models are not nested. We also employ the prior

upper bound $\beta < 30$ since we have verified that this value is well above the range of β to which the data is sensitive.

We also impose a flat prior on $z_{\rm OFF}$ with a range $10^5 < z_{\rm OFF} < 10^7$, where the lower bound is close to that of matter-radiation equality, and the upper bound is obtained from Eq. (6.16) using the prior upper bound on β. Moreover, based on BBN constraints, we consider a Gaussian prior for the baryon density, $\omega_{\rm b,0} = 0.023 \pm 0.002$, following [190]. However, its impact on our results is minimal, as the width of its uncertainty exceeds that of the one derived from CMB data by an order of magnitude [61].

We constrain our model with the following CMB and background datasets, covering a range from low to high redshifts :

- We use CMB TT, TE and EE power spectra data from the *Planck* 2018 data release [61, 191], ranging from multipoles $0 \leq \ell \leq 2508$ (for TT), and $0 \leq \ell \leq 1996$ (for TE and EE) : more specifically, the `simall lowl` EE and `commander lowl` TT likelihoods for $0 < \ell < 29$, and the fast `Plik_lite` likelihood for larger multipoles, which already includes marginalization over foregrounds and residual systematics. The differences between the contours obtained with the full likelihood are marginal.
- We include data on the product $H(z)r_s(z_d)$ and the ratio involving the comoving angular diameter distance $D_M(z)/r_s(z_d)$ at the three effective redshifts $z = [0.38, 0.51, 0.61]$, obtained through the reconstructed measurement of the BAO peak from the BOSS DR12 data [173].
- We employ the Pantheon+ dataset [192], consisting of 1550 distinct SNe1a ranging in redshift $z = (0.001, 2.26)$. We allow the absolute magnitude of the SNe1a to vary freely as a nuisance parameter in the Monte Carlo analyses. This dataset gives us constraints on the current DE and DM energy fractions, which subsequently fixes the degeneracy curve in the $\beta^2 - z_{\rm OFF}$ plane through Eq. (6.16).

We run our version of `CLASS` to obtain the various background and perturbation quantities in the ECQ framework. Since accurate models for the nonlinear power spectrum in an ECQ framework are yet to be developed, we present results for both a linear and a nonlinear case : for the former, we opt to impose a cut in the CMB spectra at $\ell_{\rm max} = 1400$ to avoid biases in the computation of the CMB lensing effects at small scales. We also set a conservative scale cut at $k_{max} = 0.1h{\rm Mpc}^{-1}$ to avoid

biasing the power spectrum. For the latter, we consider the entire range of *Planck* multipoles, using `Halofit` [193] to model the nonlinear power spectrum without the scale cut at $k_{max} = 0.1h\text{Mpc}^{-1}$.

We sample the posterior distributions using `CosmoSIS`, employing a standard Metropolis-Hastings sampling algorithm and stopping the sampling when the Gelman-Rubin convergence statistic R fulfils $R - 1 < 0.02$. We analyse our chains using `GetDist`.

6.4 Observational constraints on ECQ

We present our main results for the ΛCDM and ECQ models in Fig. 6.4, showing the 1D and 2D marginalised posterior distributions of the most relevant parameters. We report their mean and 1σ uncertainties in Table 6.1.

We regain the expected strong degeneracy in the $\beta^2 - z_{\rm OFF}$ plane of the ECQ model, determined by Eq. (6.16) and the constraint on $\Omega_{\rm DM,0}$ imposed by the data. The 1D posteriors for β^2 and $z_{\rm OFF}$ are largely prior dominated. Our datasets cannot discriminate among points $(z_{\rm OFF}, \beta^2)$ on the degeneracy line. There is a peak in the posterior distribution of β^2, but we believe that this is due to volume effects. This is clear from Fig. 6.5, which shows that the minimum value of χ^2 remains constant within the range of β^2 covered by the MCMC.

Comparing the linear and nonlinear cases (blue vs yellow and red vs green), we see that all the contours are consistent within 2σ, with the largest discrepancy being between the posteriors for $n_{\rm s}$. We argue that this is within expectation, as small multipoles favour larger values of $n_{\rm s}$ and H_0, and smaller values of σ_8 (see Fig. 22 in [61]). We recover this behaviour for both ΛCDM and our ECQ model.

The CMB temperature and polarisation data are only mildly sensitive to values of $\beta > 3$ even if we include the entire range of *Planck* multipoles, since in this case, the fifth force affects scales that fall out of the range probed by *Planck* [17]. The prior (BBN) bound of $\beta > 3$, together with Eq. (6.16), lead to the lower bound $z_{\rm OFF} \gtrsim 8 \times 10^4$, which means that even in the extreme case of $\beta = 3$ only wave modes $k \gtrsim 0.25\, h\text{Mpc}^{-1}$ are directly affected by the fifth force. This is also reflected in the fact that all the best-fit values of the parameters present in both models are compatible within 1σ and that the value of $\chi^2_{\rm min}$ in ECQ is only slightly smaller than in ΛCDM. The value of H_0 does not deviate considerably from the ΛCDM one, as

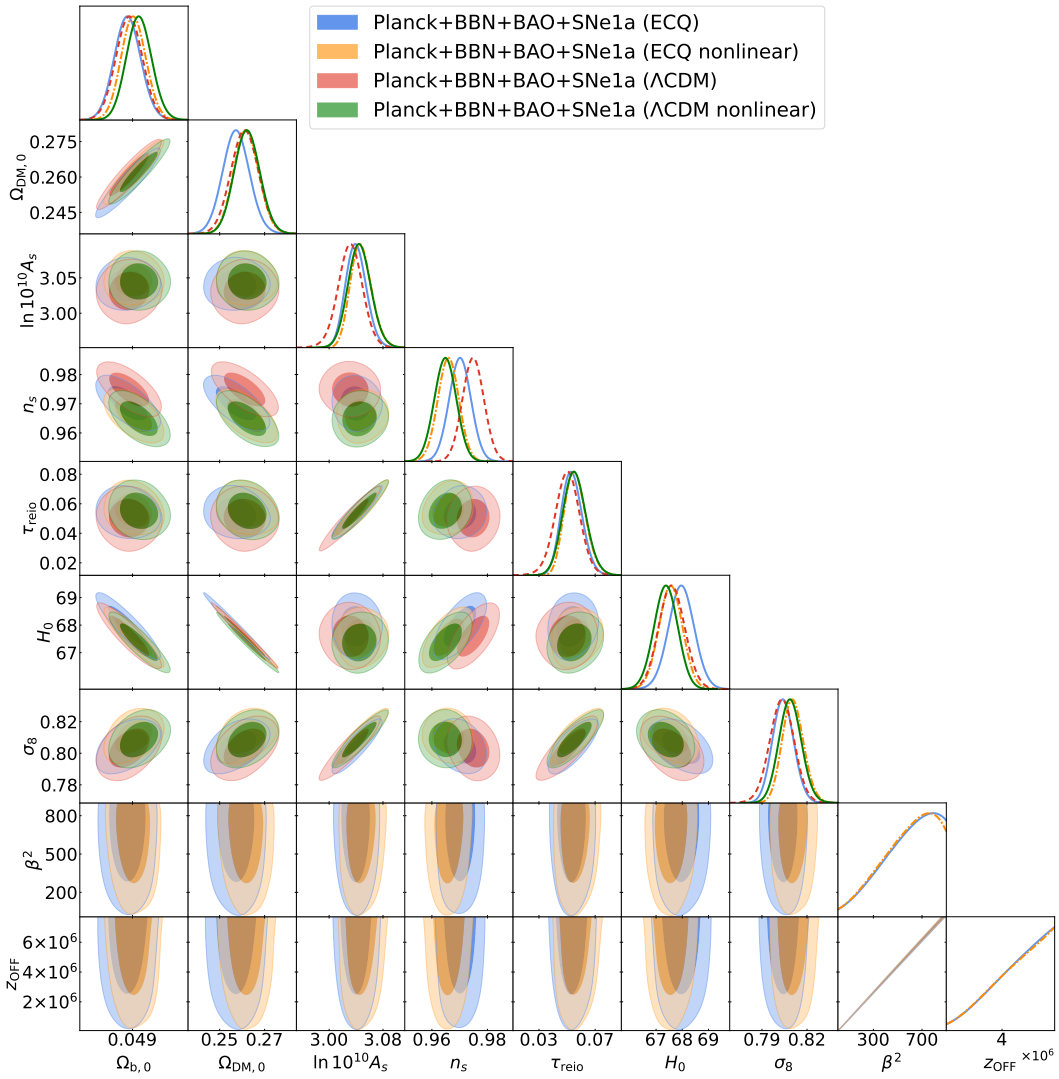

Fig. 6.4. Comparison of the 2D contours and 1D marginalised posteriors of the main cosmological parameters obtained for the ΛCDM and ECQ models in the following two setups : (i) considering the linear scales, with $\ell < 1400$, and using `Halofit` with the cut at $k_{max} = 0.1h/\text{Mpc}^{-1}$. Here we plot them in red (red dashed line in 1D) and blue (blue solid line in 1D) for the ΛCDM and ECQ, respectively; (ii) considering nonlinear scales (i.e. without the cuts in k and ℓ), in green (green solid line in 1D) for ΛCDM and yellow (yellow dashed-dotted line in 1D) for ECQ.

the allowed values of $z_{\rm OFF}$ are too large to introduce significant departures from the typical ΛCDM shape of $H(z)$ at $z < 10^5$ and therefore cannot induce important changes in the value of $r_s(z_d)$. This consequently makes H_0 take on the ΛCDM value to keep the location of the CMB peaks stable and respect the good description of the BAO data. The model has no bearing on the cosmological tensions.

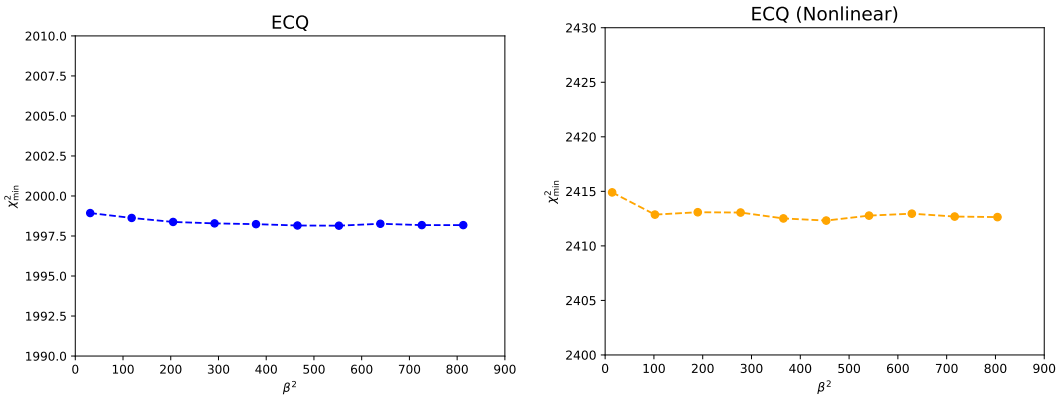

Fig. 6.5. Minimum values of χ^2 as a function of β^2, for a linear (left, blue) and nonlinear (right, yellow) ECQ run. We have obtained them directly from our Markov chains, applying the method of [194]. We see that the value of $\chi^2_{\rm min}$ remains roughly constant, even for those values of β^2 for which we find the peak in the 1D posterior, see Fig. 6.4. That peak is due to volume effects.

If we turn on the coupling at $z_{\rm BBN} < z < 10^{14}$ with β and $z_{\rm OFF}$ on the degeneracy line, the effects on the matter power spectrum can be softened since we decrease the interval when the fifth force is active, yet these changes affect scales that have no impact on the observables employed in this paper. Hence once again, we can only constrain the slope of the degeneracy line in this case.

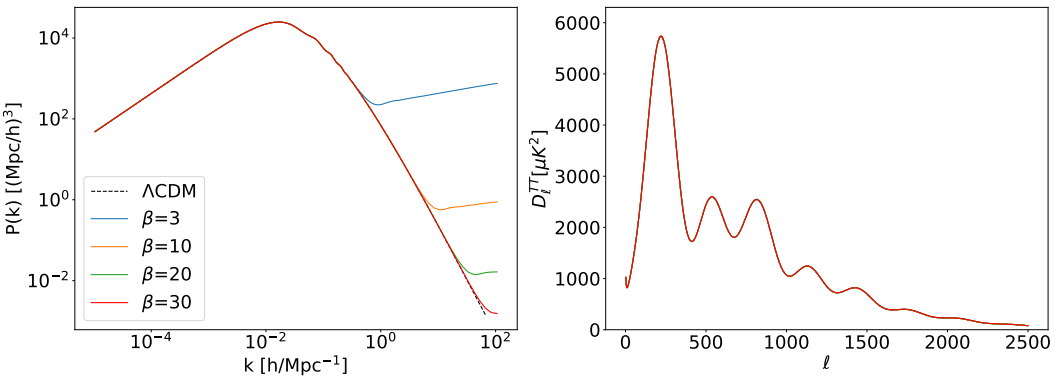

Fig. 6.6. Matter (left) and CMB temperature (right) power spectra obtained using the same parameter values as in previous figures, i.e. using again values of β and $z_{\rm OFF}$ lying on the degeneracy line. We include the ΛCDM case in black dashed-dotted lines for reference. In the left plot, we show a larger range of k's than in Fig. 6.3 to appreciate the impact of the large values of $\beta \gtrsim \mathcal{O}(10)$ on $P(k)$.

We can see this better illustrated in Fig. 6.6 : the matter power spectrum diverges at higher k's for increasing values of β. However, the datasets employed in this work, including the CMB spectra, are not sensitive to these small-scale effects. We could

Parameter	ΛCDM	ECQ
$\Omega_{\rm b,0}$	0.0489 ± 0.0005	0.0488 ± 0.0005
$\Omega_{\rm DM,0}$	0.261 ± 0.006	$0.257^{+0.005}_{-0.006}$
$\ln(10^{10} A_{\rm s})$	3.030 ± 0.016	$3.040^{+0.014}_{-0.015}$
$n_{\rm s}$	0.975 ± 0.004	0.970 ± 0.004
$\tau_{\rm reio}$	0.050 ± 0.008	0.054 ± 0.007
β^2	–	Unconstrained
$z_{\rm OFF}$	–	Unconstrained
$\beta^2/z_{\rm OFF}$	–	$(11.41^{+0.11}_{-0.13})\times 10^{-5}$
H_0 [km s^{-1}Mpc^{-1}]	67.60 ± 0.46	67.96 ± 0.45
σ_8	0.803 ± 0.008	0.804 ± 0.007
$\chi^2_{\rm min}$	2000.59	1998.14
$\ln B$	–	-2.29

Table 6.1. Mean and 1σ uncertainties of ΛCDM and ECQ parameters, as well as the minimum χ^2 and $\ln B$ values. Since β^2 and $z_{\rm OFF}$ are individually unconstrained, we present the value of their ratio instead, which determines the slope of their degeneracy line.

improve the lower bounds on β by using newer CMB data from SPT-3G [19] or ACT [18], which involve larger multipoles than *Planck*, or data from the Lyα-forest (see e.g. Fig. 19 of [17]). Nevertheless, these datasets require highly accurate modelling of the nonlinear matter power spectrum, which shall be left as future work.

6.4.1 Bayesian Model Comparison

Lastly, we perform a model comparison by calculating the Bayes factor of both models. As was described in the previous Chapter, we use `MCEvidence` to compute the evidence $\mathcal{Z}(M_i|D)$ numerically, following Eq. (5.21). We report the χ^2 and $\ln B$ values in Table 6.1. Despite the fact that $\chi^2_{\rm min,ECQ} \lesssim \chi^2_{\rm min,\Lambda CDM}$, we find that $\ln B = -2.29$, which shows that ECQ is not preferred over the ΛCDM, according to Jeffreys' scale. We have also explicitly verified that similar results hold for non-constant polynomial potentials of the form $V(\phi) = V_0 \phi^{-\alpha}$ leading to a fast-rolling field ϕ.

IN BRIEF

In this Chapter, I investigated an *early coupled quintessence* (ECQ) model, a subset of the tomographic CDE model where coupling is only activated during the radiation-dominated era. Such models have been of interest from a theoretical standpoint, as past literature has shown that a presence of coupling between the scalar field and DM particles during the RDE can lead to an attractor solution in the background equations, and significantly larger growth of DM overdensities, forming primordial compact objects that could be candidates for dark matter.

I implemented our ECQ model with `CLASS`, and for the first time employed observational data such as CMB, BAO and SNe1a to obtain constraints on such a model. While current data is incapable of setting individual significant constraints on the model parameters, i.e. the coupling strength β and the redshift at which it is deactivated, $z_{\rm OFF}$, I was able to recover the distinct degeneracy in the $\beta^2 - z_{\rm OFF}$ plane, that has been, up to now, only derived from first principles.

7. Neural Networks as Classifiers of Cosmological Models

Sommaire

7.1 Introduction

In the previous 2 Chapters, we have introduced the tomographic CDE model and studied a subclass ECQ model, where we have performed Bayesian inference to constrain these models, especially using data from Stage III LSS surveys like KiDS and BOSS. With the current Stage IV surveys such as *Euclid*, DESI and LSST, it is expected that measurements with sub-percent level uncertainties can be achieved. Thus the upcoming decade will witness an exponential increase in the quantity, variety, and quality of observations of the LSS, requiring more sophisticated computational resources. There is hence a need to improve analysis methods alongside the data quality and quantity. In this aspect, *machine learning* (ML) techniques have emerged as a valuable tool capable of addressing some of the computational limitations of conventional statistical methods [195, 196]. In this Chapter, I shall investigate if we can apply such deep learning techniques to a tomographic CDE framework.

To this end, we employ Neural Networks (NN) to perform model classification, where we assess their accuracy in differentiating between datasets generated from two different cosmological models [197, 198]. Investigations of a similar nature have been carried out in past literature [199-201], hence it would be of interest to build upon these efforts of investigating how accurately deep learning methods can detect hints of beyond ΛCDM physics, especially in this era of precision cosmology.

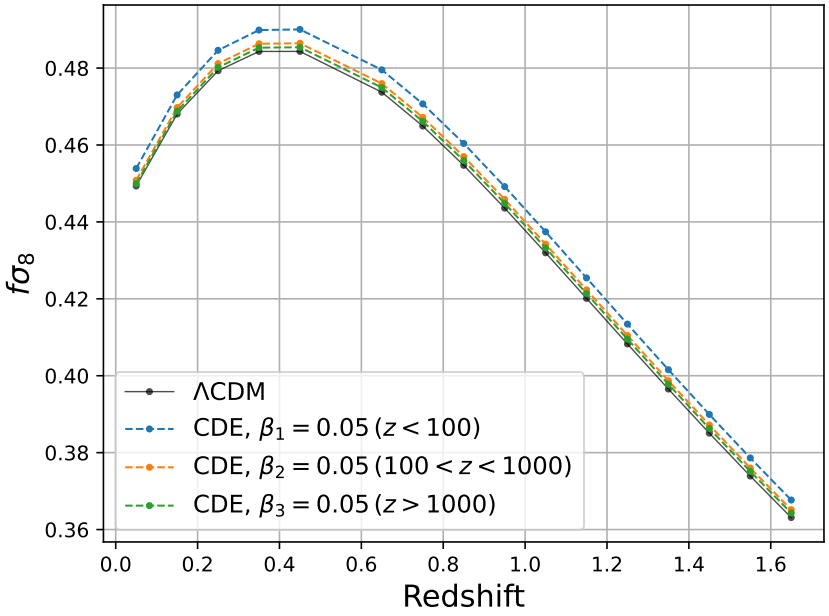

Fig. 7.1. Plot of the growth rate $f\sigma_8$ against redshift z for the 16 redshift bins, for both the ΛCDM model (black solid line) and the CDE model (coloured lines). We keep the same cosmological parameters, but in the CDE case, set the coupling at the 3 different redshift bins $z = \{0, 100, 1000\}$ to a value of $\beta_i = 0.05$.

7.2 Data Generation

We employ the LSS observable $f\sigma_8(z)$, the product of the growth rate $f(z)$ and $\sigma_8(z)$, as our input dataset to the NN. Stage IV spectroscopic galaxy surveys such as DESI and *Euclid* will be able to obtain values of $f\sigma_8(z)$ through measurements of RSD, with forecasts of $\sigma(f\sigma_8)/f\sigma_8$ at less than 5% [202]. It could hence be an effective probe in testing for deviations from the concordance model, by tracing the growth history of the Universe.

For a ΛCDM model, we use `CLASS` to generate 8000 training and 750 testing datasets of the product $f\sigma_8(z)$, varying $\Omega_{\mathrm{m},0}$ between the range $\Omega_{\mathrm{m},0} = (0.01, 0.7)$ and fixing the rest of the parameters to a fiducial cosmology of $\Omega_{\mathrm{b},0} = 0.02225$, $\ln 10^{10} A_\mathrm{s} = 3.044$, $n_\mathrm{s} = 0.966$, $\tau_\mathrm{reio} = 0.0522$, $V_0 = 2.64 \cdot 10^{-47}\mathrm{GeV}^4$ where in ΛCDM, $V_0 = \rho_\Lambda$. To be conservative, we set a $k_{max} = 0.1\,h\,\mathrm{Mpc}^{-1}$ to exclude highly non-linear scales, and only consider the linear matter power spectrum. For the tomographic CDE model, we employ a modified version of `CLASS` (which was used in the previous 2 Chapters) to generate the same number of training and testing datasets with the same cosmological parameters, additionally varying the strength of cou-

pling within each redshift bin $\beta_i = (0.001, 0.5)$. In this study, we have chosen to adopt a 3-bin parameterization, with bin edges $z = \{0, 100, 1000\}$.

We plot the function of $f\sigma_8(z)$ in Fig. 7.1, where we separately activate coupling within the 3 tomographic bins, and compare it with the case of ΛCDM. We see that for each CDE case, non-zero coupling increases DM clustering, which is also evident from the perturbation equations of Sect. 5.2.2. Late-time coupling (i.e. $\beta_1 = 0.05$) has the largest impact on this increase, followed by β_2 and β_3. Hence we would expect that models with late-time coupling would be the most easily distinguished from ΛCDM.

We simulate a DESI-like setup of 16 redshift bins with mean redshifts equally spaced between $z = (0.05, 1.65)$, and employ values of the galaxy bias $b(z)$ and galaxy number densities $\frac{dn}{dz}$ as specified in [202].

We also include, in our training and testing data, uncertainties in the $f\sigma_8(z)$ measurement at each redshift. To do this, we build a covariance matrix by first calculating the Fisher matrix for the observed galaxy power spectrum in each redshift bin z_i [203, 204], given by

$$F_{\alpha\beta}(z_i) = \frac{1}{8\pi^2}\int_{-1}^{1} d\mu \int_{k_{min}}^{k_{max}} k^2\, dk \left[\frac{\partial P_{\delta\delta}(k,\mu;z_i)}{\partial\alpha}\frac{\partial P_{\delta\delta}(k,\mu;z_i)}{\partial\beta}\right] \times V_{\rm eff}(z_i;k,\mu) \quad (7.1)$$

where α and β are the parameters of concern, $P_{\delta\delta}$ is the linear matter power spectrum and $V_{\rm eff}$ is the effective volume of the survey. We calculated the power spectrum using our Boltzmann solver, then evaluated its derivatives via a two-point central difference formula with respect to the cosmological parameters, $\theta_{\rm cosmo} = \left\{\Omega_{\rm b,0}, \Omega_{\rm m,0}, h, n_{\rm s}, \ln\left(10^{10}A_{\rm s}\right)\right\}$, and the nuisance parameters, $\theta_{\rm nuis} = \{\sigma_{\rm P}, P_s\}$, where $\sigma_{\rm P}$ parametrises the nonlinear contribution to the matter power spectrum due to galaxy velocity dispersion [205],

$$\sigma_{\rm P}^2 = \frac{1}{6\pi^2}\int dk\, P_{\delta\delta}(k,z)\,, \quad (7.2)$$

and P_s is the shot noise term dictated by survey specifications.

Subsequently, we obtain the total Fisher matrix summing over all the redshift bins as :

$$F_{\alpha\beta} = \sum_{i=1}^{N_{\rm bins}} F_{\alpha\beta}^{\rm bin}(z_i) \quad (7.3)$$

Finally, the Fisher matrix is projected from the $\theta_{\rm cosmo}$ and $\theta_{\rm nuis}$ parameters to

$f\sigma_8(z_i)$ in the redshift bins and then inverted to obtain the covariance matrix $C_{f\sigma_8 f\sigma_8}$, which is used to generate an additional Gaussian sampled noise component added to the values of $f\sigma_8(z)$ output by the Boltzmann code. This method was compared with other approaches [203, 206], finding excellent agreement and providing confidence in its robustness.

7.3 Neural Network Architecture

NNs are a popular machine learning technique which simulates the learning mechanism of biological systems, by extracting information from relationships and patterns from data [207]. Every neuron (unit) has a weighted connection with each other. Its architecture can vary depending on the problem at hand; generally, it involves having an input and output layer, with an arbitrary number of hidden layers between. Various packages have been developed to optimise, test and choose the most appropriate architecture; for the present study, we employ `Optuna`[1] [208] to optimise the number of hidden layers and the hyperparameters of the NN, which we will explain below. This agnostic framework works by training several times the same dataset with different architectures and extracts the one that has the highest accuracy and lowest loss.

In Fig. 7.2 we plot a diagram of the general setup of the NN : We first implemented feature normalisation (of the 16 $f\sigma_8$ datapoints with its associated uncertainties) with a batch size of 32 [209], using it as our input layer. It then passes through the first hidden dense layer with n number of nodes, where n is a hyperparameter that we vary with `Optuna`. Subsequently, it goes through an activation layer (for which we have chosen a Rectified Linear Unit, or ReLU, function [210]) and a regularisation dropout layer commonly used in the literature as a regularisation technique [211] to avoid overfitting. Here, the dropout rate, the probability of a node being 'deactivated' going to the subsequent layer, is another hyperparameter that will be optimised. The number of hidden layers can be defined arbitrarily and is something that we vary as a hyperparameter as well. Having more layers allows the network to better capture the intricacies of the relationship between the features of the model, hence it is highly dependent on the nature of the problem. Finally, in the output layer, we implement a sigmoid activation function to enable the classification task :

1. https://github.com/optuna/optuna

the NN will associate a class '0' for ΛCDM and class '1' for CDE. We use an `nadam` [212] optimiser for our NN. Lastly, we implement early stopping regularisation, a practice whereby the training of the NN stops once the accuracy does not increase by a given amount after a certain number of epochs. This step also prevents overfitting of the network, by ensuring it is not *overtrained*. We also train the network by batch sizes of 32, i.e. splitting our training dataset into sets of 32 in order to consume less memory during the training.

We have used the `TensorFlow Keras` library [213] to build, train and test our network. Since the goal is to probe for deviations from ΛCDM using the NN, we worked with 3 different network architectures, designed to discriminate growth rate $f\sigma_8$ data coming from the two models being considered at hand : $\{\Lambda$CDM, CDE(β_1)$\}$, $\{\Lambda$CDM, CDE(β_2)$\}$ and $\{\Lambda$CDM, CDE(β_3)$\}$, bearing in mind that we varied the coupling within each tomographic bin independently. We present in Table 7.1 a list of the NN hyperparameters, their prior ranges and best-fit values as found by `Optuna`.

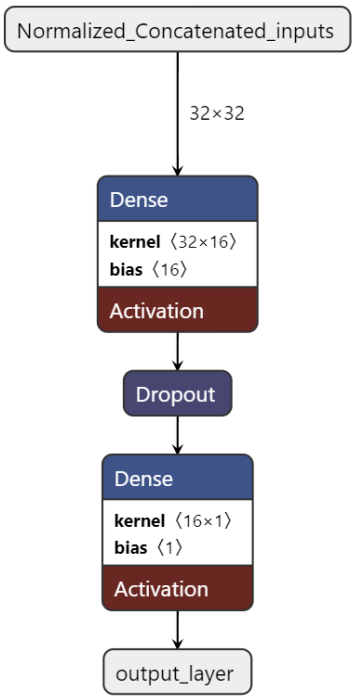

Fig. 7.2. Graphic of the general structure of the NN architecture implemented. The normalisation of features and their concatenation as an input array was performed within the architecture. Here 32×32 as denoted beside the topmost arrow, represents the 32 features (16 datapoints of $f\sigma_8(z)$ with its standard deviation), with a batch size of 32. Graphic produced by `Netron`[2].

We perform several robustness tests on our network. Firstly, we verified the impact of randomness during the training procedure : we trained and tested the network with the same architecture and dataset multiple times, and determined the error of the performance. We find a standard deviation of ± 0.002 on the classification accuracy in the case of varying β_1. Secondly, after the data generation step, we divided the training and test set randomly, and found a standard deviation of the percentage of accurately classified datasets with similar magnitude. These tests prove that our NN architecture is robust to randomness.

Finally, we test the effect of increasing the number of training datasets, for five different values $[4050, 5000, 6400, 8200, 9800]$, where half of the dataset are samples from ΛCDM, and the other half is generated from a CDE model. From Fig. 7.3 we see that the NN can accurately distinguish almost all of the ΛCDM cases regardless of the number of training datasets. In the CDE case, results improve with an increasing number of datasets up to an optimum value of about 8000, after which performance plateaus, indicating that the network does not learn any more new information with the increase in the number of datasets.

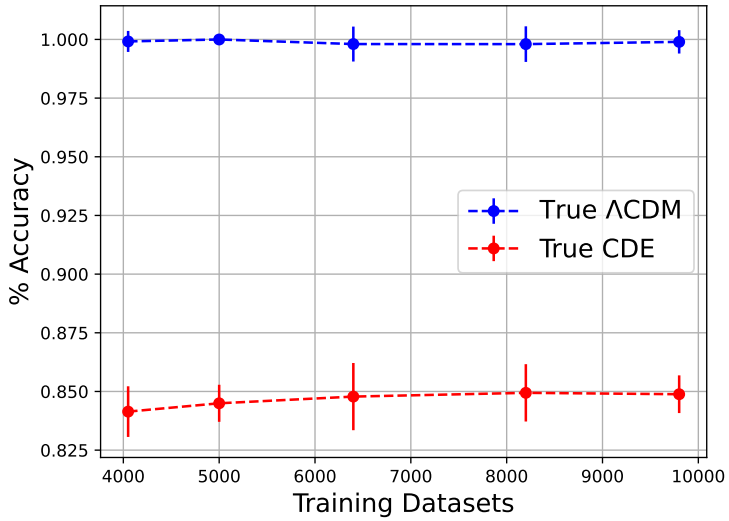

Fig. 7.3. Plot of percent accuracy of the NN against the number of training datasets used. The circular points mark the average values out of 50 runs, with the error bars denoting 1σ standard deviation.

7.4 Neural Network Performance

2. https://github.com/lutzroeder/netron

7.4.1 Binary Model Classification

Here we present the results for the case where we switch on coupling in only one of the 3 tomographic bins β_1, β_2 or β_3. Since it is a case of classification between two models, we use a binary cross-entropy loss function as provided within `Keras`. Hereafter, for brevity, we shall refer to the model where the coupling is activated within the ith tomographic bin as the β_i model.

In Table 7.1, we present the best-fit hyperparameters obtained with `Optuna` and the number of training epochs when early stopping is invoked. We see that in all cases, having one hidden layer is sufficient, although the number of nodes within the layer varies widely between models. Interestingly, the best-fit dropout fraction is relatively low : at around 20% for all cases.

	Hyperparameter			
	Hidden layers	**Nodes**	**Dropout rate**	**Training epochs**
Prior	$(1, 4)$	$(1, 128)$	$(0.0, 0.5)$	< 2000
β_1 best-fit	1	38	0.224	660
β_2 best-fit	1	116	0.218	683
β_3 best-fit	1	82	0.215	673

Table 7.1. Table of prior ranges and best-fit hyperparameters as obtained by `Optuna` for each model : number of hidden layers, number of nodes in the hidden layer, dropout fraction, as well as the number of training epochs when utilising early stopping.

We present the learning curves for each model in Fig. 7.4, where we have additionally split our training dataset into a training and validation set. In the case where only late-time coupling is activated (i.e. β_1 is non-zero), our NN performs well, reaching a high accuracy of over 90% and losses of $< 20\%$, while being sufficiently trained after just 660 epochs. From the loss curve, we also see that the training and validation losses stabilise and reach roughly equality, implying that the model has been able to learn all the features from the training dataset and can generalise to unseen datasets. The same behaviour is exhibited for the cases of β_2 and β_3.

We present the classification results of our NN in the form of confusion matrices in Fig. 7.5, for each model $\beta_{1,2,3}$. We see that the NN can accurately classify 100% of the ΛCDM cases, and also has a high accuracy of 86.4% in capturing CDE cases. We see similar performance in the cases of β_2 and β_3, where the coupling is activated between redshifts of $100 < z < 1000$ and $z > 1000$ respectively. For the β_2 model, we

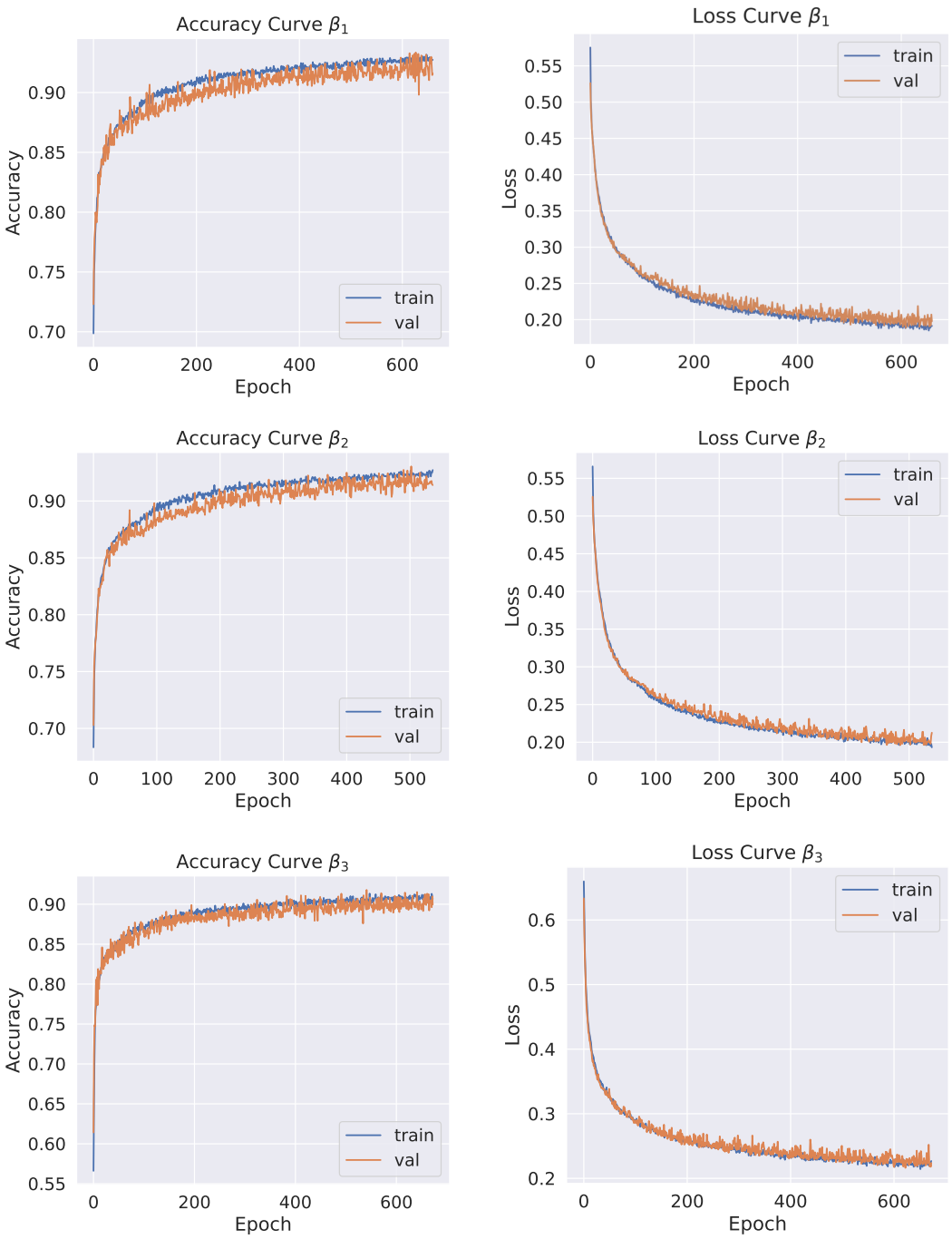

Fig. 7.4. Left column : Accuracy curve for both the training (blue) and validation (orange) datasets, where each row corresponds to the model investigated (top : β_1, middle :β_2, bottom : β_3). Right column : Its corresponding loss curve.

once again achieve 100% accuracy in identifying $f\sigma_8$ datasets coming from a ΛCDM model, and 86.1% accuracy for CDE. In the case of β_3, we see that the accuracy of

the NN is 99.6%. This might be because activating coupling at early times ($z > 1000$) has the least impact on the increase in $f\sigma_8$, as illustrated in Fig. 7.1. Hence, since the discrepancy between a ΛCDM dataset and a CDE dataset is marginal, the NN might not have been able to differentiate between the two as accurately as in the cases of β_1 and β_2.

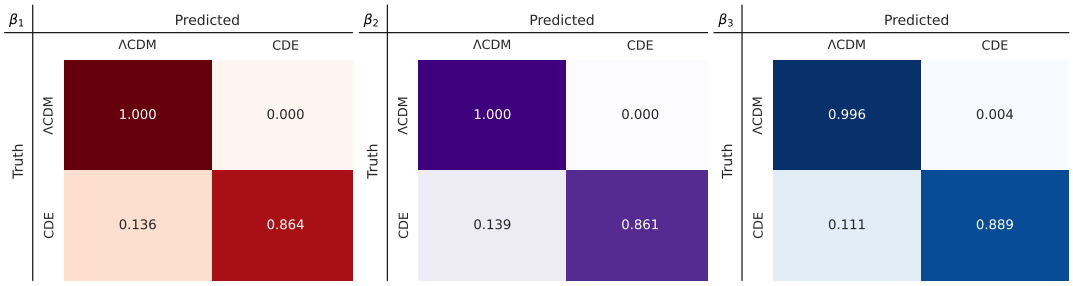

Fig. 7.5. NN classification results in the form of confusion matrices, for the case of switching on coupling at (left) β_1, (middle) β_2 and (right) β_3. As a reminder, the tomographic bins for each coupling parameter are $z\,(\beta_1) < 100$, $100 < z\,(\beta_2) < 1000$ and $z\,(\beta_3) > 1000$.

7.4.2 Multiclass Classification

Here we also explore the implementation of an NN architecture capable of performing multi-class classification. For this, we created a dataset from the aforementioned cases of each tomographic bin, with the classes defined as follows : '0' for ΛCDM, '1' for β_1 and '2' for $\beta_2 + \beta_3$, where for the last case we activated these two couplings independently, and combined the generated datasets into one class (i.e. coupling at high redshift $z > 100$). The motivation comes from the fact that we are simulating DESI-like data, where the redshift bins in which this survey operates are between $z = (0.05, 1.65)$. Hence we do not expect the NN to be able to differentiate between low-redshift data generated with a coupling at $100 < z < 1000$ and $z > 1000$.

We similarly implemented feature normalisation with a batch size of 32 (see a summary of the architecture in Fig. 7.6), while highlighting that we added one more hidden layer with a ReLU activation function and 16 neurons as we found that this improved the multi-class accuracy, as can be seen in Fig. 7.8. The optimal dropout rate found by `Optuna` was 0.1 and the number of training epochs obtained by the early stopping callback was 1021. Another difference with respect to the previous architectures was that the output layer contained 3 units for each category and a

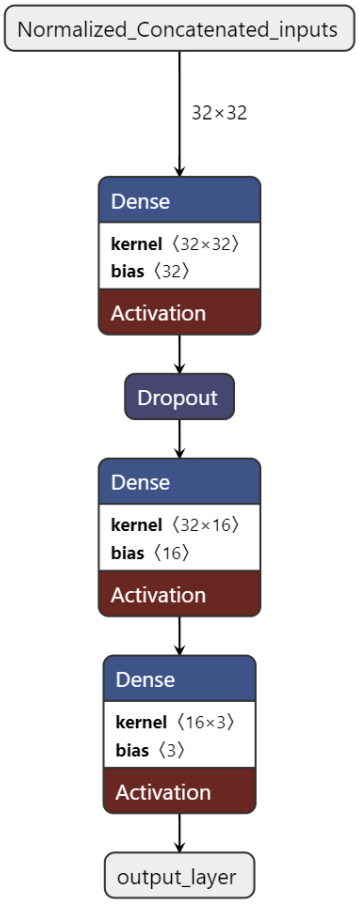

Fig. 7.6. NN architecture implemented for the multiclassification task. The normalisation of features and their concatenation as an input array was performed within the architecture before training. Graphic produced with `Netron`.

softmax activation function. We compiled this model using an `nadam` optimiser and a sparse categorical cross-entropy loss function.

The learning curves for this multi-class task are illustrated in Fig. 7.7, where we can see that the accuracy reached by our model is approximately 68% and the loss 65%. The results of this multi-class classification task are shown in Fig. 7.8. We also computed the errors of the predictions performed by the NN, since the impact of randomness in the training was found to be slightly more significant than the previous cases. We can see that the prediction of ΛCDM data achieves very high accuracy compared to the CDE models. 99% of the ΛCDM data samples were correctly classified. The growth data coming from the β_1 and $\beta_2 + \beta_3$ activation models are respectively 79% and 84% correctly classified, which is slightly lower than in the binary classification scenario.

We separately performed the test to evaluate whether our architecture could be able to discriminate between 4 classes, i.e. separating the class '2' (combination of β_2 and β_3 data) into '2' (β_2 data only) and '3' (β_3 data only), however, the NN performs poorly. This is to be expected since we do not anticipate being able to probe dynamics at high redshifts with DESI-like data, which falls within a redshift range $z = (0.05, 1.65)$. We argue that our architecture being able to differentiate $f\sigma_8$ data coming from the activation of low and high redshift tomographic couplings is a substantial result in itself.

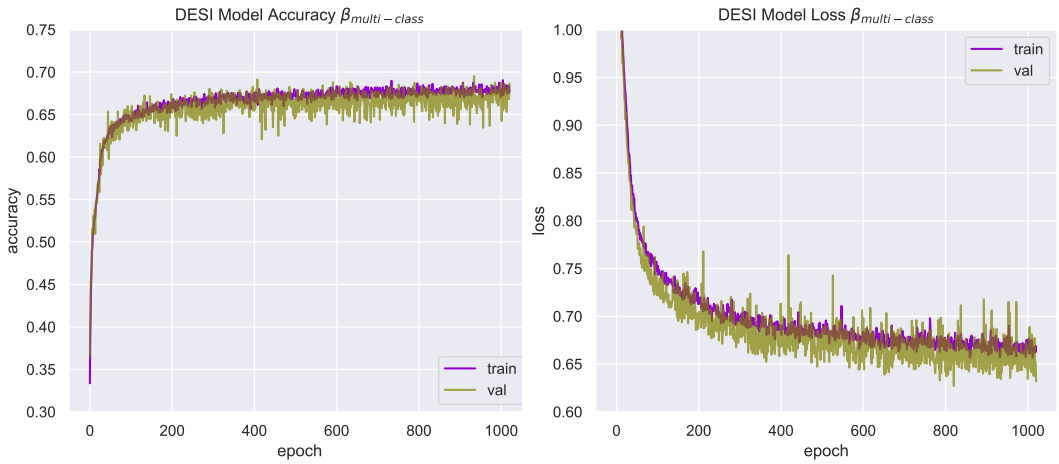

Fig. 7.7. Left : Accuracy curve for both the training (purple) and validation (green) datasets, for the model where the three parameters β_1, β_2 and β_3 are activated. Right : The corresponding loss curve. We considered a 3 class dataset : ΛCDM, CDE(β_1) and CDE(β_2+β_3).

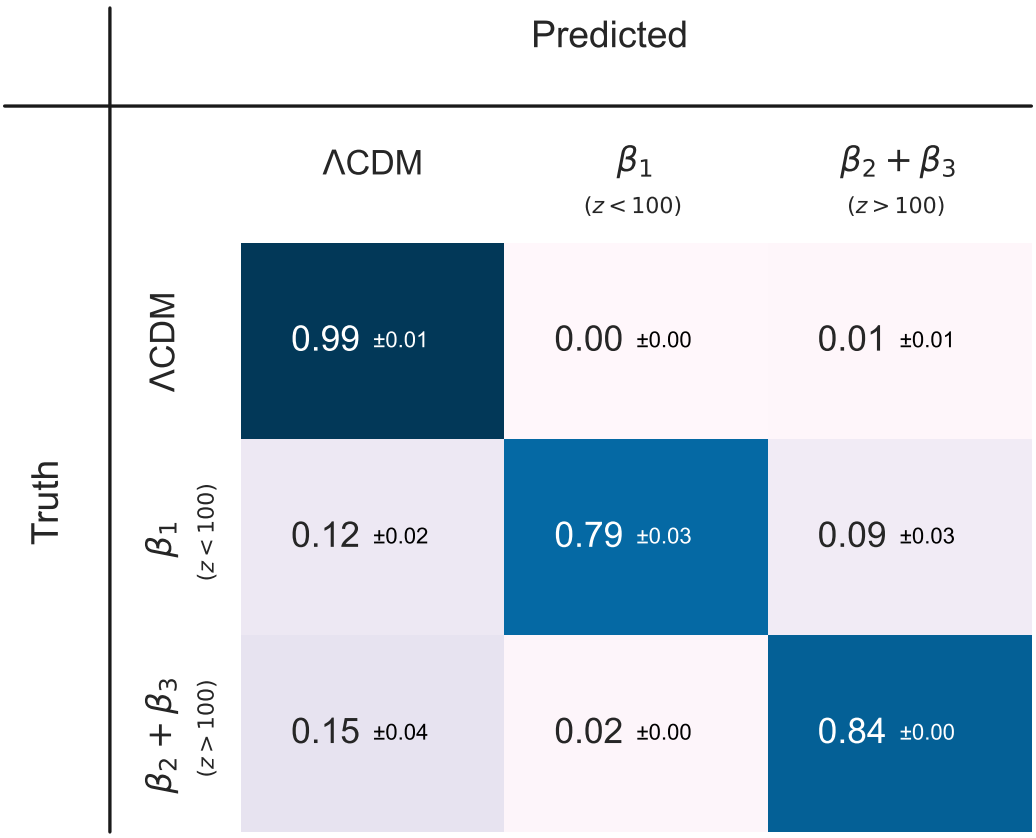

Fig. 7.8. Confusion matrix for the NN multiclassification performance and its errors. In this case, the distinction between 3 classes : ΛCDM, CDE through the activation of couplings in β_1 (low redshift coupling at $z < 100$), and in $\beta_2 + \beta_3$ (high redshift coupling at $z > 100$). As a reminder, the tomographic bins for each coupling parameter are $z(\beta_1) < 100$, $100 < z(\beta_2) < 1000$ and $z(\beta_3) > 1000$.

IN BRIEF

In this Chapter, I expanded upon the applications of a tomographic CDE model, this time leveraging the power of machine learning. We developed a Neural Network (NN) to perform model classification, where we generated mock $f\sigma_8(z)$ datasets with Stage IV survey specifications, assuming a ΛCDM and a tomographic CDE model. We then trained and tested our NN, and found that it was able to classify the data according to the model to a high level of accuracy, regardless of which epoch coupling is activated. We then tested it for multiclass classification, by combining all the datasets with coupling activated at different tomographic bins. We find that models with late-time coupling are more accurately distinguished compared to models with early-time coupling.

Current Stage IV surveys like DESI and *Euclid* will provide us with spectroscopic galaxy clustering data of unprecedented precision. Hence through this analysis, I have highlighted the power of machine learning techniques such as NNs as a robust cross-check of conventional Bayesian methods in detecting hints of beyond-ΛCDM physics.

8. Cosmology with *Euclid*

Sommaire

8.1 The *Euclid* survey

The *Euclid* space satellite is a Medium class mission commissioned by the European Space Agency (ESA) as part of its *Cosmic Vision* 2015-2025 programme. ESA *Euclid* is an ambitious project that will measure the shapes of 1.5 billion galaxies over $14,000$ deg^2 of the sky, up to a redshift of $z \sim 2$ [214]. It is equipped with the Visible Instrument (VIS), which will provide photometry in the optical range, and the Near-Infrared Photometer and Spectrometer (NISP) instrument, which will provide photometry in the near-infrared, as well as spectroscopy.

Being a mission aiming to investigate the dark sector of the Universe, the primary probes of *Euclid* are weak lensing, galaxy clustering (photometric and spectroscopic) and 3x2pt (the combination of weak lensing, photometric galaxy clustering and their cross-correlation galaxy-galaxy lensing). With *Euclid*, it is expected that the dark energy EoS parameters w_0 and w_a will be constrained with a precision of approximately 1% with 3x2pt alone [214]. Hence it is imperative that a robust analysis pipeline is established, which will allow us to maximally exploit the high-quality data *Euclid* that will provide, to obtain the most precise and accurate cosmological constraints to date.

8.2 CLOE : Cosmology Likelihood for Observables in *Euclid*

The official likelihood code of *Euclid*, Cosmology Likelihood for Observables in *Euclid* (CLOE), is thus an integral part of the mission's data analysis pipeline : it will generate theoretical forecasts for *Euclid*'s primary probes, compute the likelihood and establish fiducial constraints on the probability distributions of cosmological parameters. The Inter-Science Taskforce : Likelihood (IST :L) team within the *Euclid* consortium has been responsible for developing CLOE, by synergising between the scientific needs of the various Science Working Groups (SWGs) and communicating the required data products that will be produced by the *Euclid* Science Ground Segment (SGS) OU-LE3.

CLOE will calculate the theoretical predictions of the main *Euclid* probes based on the recipes provided by the SWGs, also incorporating the nonlinear prescription from IST :Nonlinear. IST :NL handles the analytical calculations of the covariance matrices for each probe. CLOE will then ingest the data vectors and data covariances, and conduct the likelihood calculation.

CLOE is currently integrated with `Cobaya` as the fiducial sampling platform, where all the specifications of the desired Bayesian inference pipeline to run are fully specified in a single `yaml` configuration file : the probe selection, data file paths, scale cuts, covariance matrices, parameters to sample over (both cosmological and nuisance), as well as a sampler to use (eg. Metropolis-Hastings or `PolyChord`). Using `Cobaya` also gives the advantage that it is easily interfaced with `Getdist` to enable straightforward post-processing of chains.

I have been actively involved in the development of CLOE, first as a code developer in IST :L, then as a co-lead of one of the IST :L Key Project papers on forecasts with CLOE. In the following subsections, I highlight my specific contributions towards these endeavours.

It should also be stated that the material in the following subsections is based on unpublished results, and has not yet been approved by the Euclid Consortium ; hence should be regarded as preliminary.

8.3 Cosmological Forecasts with CLOE

In this section, I present forecasts on the cosmological parameter constraints that CLOE will be able to provide with the main *Euclid* probes. This exercise also serves

as a validation of CLOE's readiness in processing data and deriving constraints for Data Release 1 of *Euclid*, the first of its kind for Stage IV surveys.

8.3.1 Photometric Probes

To simulate *Euclid* observations, we generate synthetic data in the form of harmonic space angular power spectra for the photometric probes, and Legendre multipole power spectra for the spectroscopic probe.

We generate synthetic angular power spectra of the weak lensing ($C_{ij}^{\epsilon\epsilon}(\ell)$), photometric galaxy clustering ($C_{ij}^{gg}(\ell)$) and galaxy-galaxy lensing ($C_{ij}^{g\epsilon}(\ell)$) probes using CLOE itself, referencing the values of the fiducial cosmology as given in the third column of Table 8.1. We model IA following a redshift-dependent nonlinear alignment model, and the nonlinear matter power spectrum using the HMCode emulator [215], which models the impact of baryonic feedback on the power spectrum as a change in its amplitude at small scales through the parameter $\log_{10}(T_{\rm AGN}/{\rm K})$. We plot the weak lensing, galaxy clustering, and the galaxy-galaxy lensing data vectors in Figs. 8.1, 8.2 and 8.3 respectively.

To simulate *Euclid* DR3 survey specifications, we assume 13 equipopulated redshift bins ranging between $z = (0.2, 2.5)$, with the redshift distributions measured from the *Euclid* Flagship 2 simulation [216]. Details of the mean redshift of each bin, $\bar{z}_i$, the survey area, shape noise σ_ϵ and limiting galaxy magnitude can be found in Table 8.2. The calculated power spectra are then binned in 32 logarithmically spaced multipole bins ranging between $\ell = (10, 3000)$.

We also derive analytically the data covariance matrix for the photometric probes. In harmonic space, the total covariance matrix can be written as a sum of all 3 contributions : a Gaussian term, a connected non-Gaussian term and a Super Sample Covariance (SSC) term. Therefore the total covariance matrix between two power spectra at ℓ bins ℓ_1 and ℓ_2 is given by :

$$\begin{aligned}\mathrm{Cov}\left[C_{ij}(\ell_1), C_{kl}(\ell_2)\right] \;=\; &\mathrm{Cov}_{\rm G}\left[C_{ij}(\ell_1), C_{kl}(\ell_2)\right] \;+\; \mathrm{Cov}_{\rm nG}\left[C_{ij}(\ell_1), C_{kl}(\ell_2)\right] \\ &+\; \mathrm{Cov}_{\rm SSC}\left[C_{ij}(\ell_1), C_{kl}(\ell_2)\right]\,. \end{aligned} \tag{8.1}$$

We shall only consider the Gaussian and SSC terms since the connected non-Gaussian term has been shown to be subdominant [217].

The first Gaussian term is given by [218] :

$$\mathrm{Cov_G}\left[C_{ij}^{AB}(\ell_1), C_{kl}^{CD}(\ell_2)\right] = \left[(2\,\ell_1+1)\,f_{\rm sky}\,\Delta\ell\right]^{-1}\delta^{\rm D}_{\ell_1\ell_2}\times\Bigg\{\left[C_{ik}^{AC}(\ell_1)+N_{ik}^{AC}(\ell_1)\right]$$
$$\left[C_{jl}^{BD}(\ell_2)+N_{jl}^{BD}(\ell_2)\right]+\left[C_{il}^{AD}(\ell_1)+N_{il}^{AD}(\ell_1)\right]\left[C_{jk}^{BC}(\ell_2)+N_{jk}^{BC}(\ell_2)\right]\Bigg\}\,, \quad (8.2)$$

for some fraction of the sky $f_{\rm sky}$, the noise contributions $N_{ij}^{AB}(\ell)$ for the different probe combinations are

$$N_{ij}^{AB}(\ell) = \begin{cases} (\sigma_\epsilon^2/2\bar{n}_i^{\rm L})\,\delta_{ij}^{\rm D} & A=B=\gamma\ \ (\mathrm{WL}) \\ 0 & A\neq B \\ (1/\bar{n}_i^{\rm G})\,\delta_{ij}^{\rm K} & A=B=g\ \ (\mathrm{GC}) \end{cases} \quad (8.3)$$

where $\bar{n}_i$ is the mean number density of source (G) or lens (L) galaxies and σ_ϵ the shape noise.

The SSC term, which essentially captures the uncertainty in the angular power spectrum due to a change in the background density at a mode larger than the survey area, is given by the modelling in [219] :

$$\mathrm{Cov_{SSC}}\left[C_{ij}^{AB}(\ell_1), C_{kl}^{CD}(\ell_2)\right] \simeq \frac{1}{f_{\rm sky}}\int d\chi\,\frac{q_i^A(\chi)q_j^B(\chi)q_k^C(\chi)q_l^D(\chi)}{\chi^4}\times$$
$$\frac{\partial P_{AB}(k_{\ell_1},z)}{\partial\delta_{\rm b}}\,\frac{\partial P_{CD}(k_{\ell_2},z)}{\partial\delta_{\rm b}}\,\sigma_{\rm b}^2(z) \quad (8.4)$$

where $\delta_{\rm b}$ is the background density, $q_i^{A,B,C,D}(\chi)$ is the cosmic shear lensing efficiency or the clustering weight function given by Eqs. (4.16) and (4.23) respectively depending on the field, and $\sigma_{\rm b}$ is the covariance of the background density given by [220]

$$\sigma_{\rm b}^2(z) = \frac{1}{2\pi^2}\int dk\;k^2\,P_{\delta\delta}\,(k,z)\;[j_0(kr)]^2\,, \quad (8.5)$$

where j_0 is the spherical Bessel function of the zeroth order. Here, only the linear matter power spectrum is considered when writing $P_{\delta\delta}(k,z)$.

8.3.2 Spectroscopic Probes

Adopting the same fiducial cosmology as was used for the photometric probes, we generate the spectroscopic power spectrum in terms of Legendre multipoles

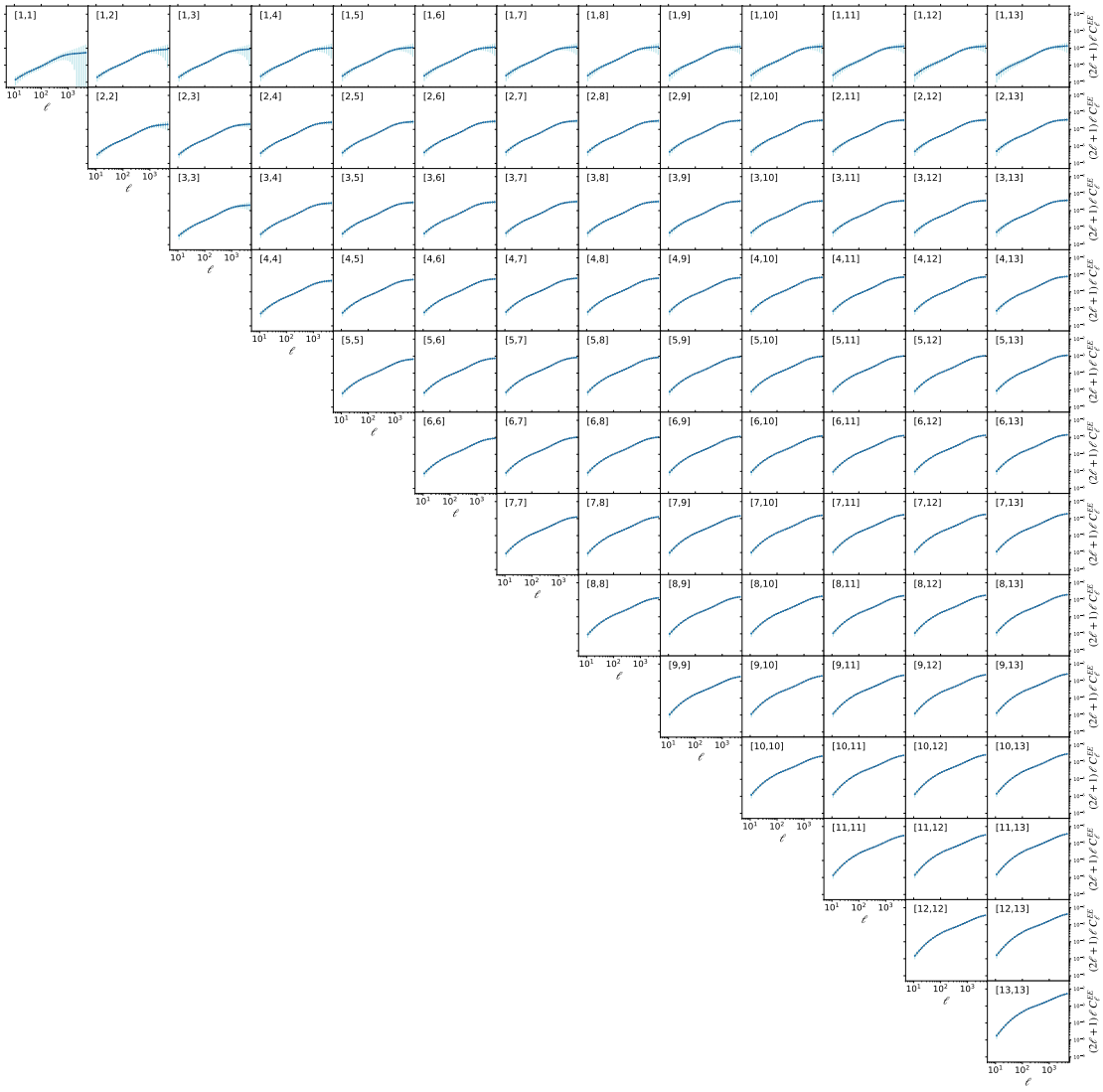

Fig. 8.1. Synthetic weak lensing angular power spectra, for the auto and cross-correlations between the 13 photometric redshift bins. The light blue error bars correspond to the uncertainty given by the analytical covariance matrix.

$P_\ell\,(k,z)$, given by

$$P_\ell(k,z) = \frac{2\ell+1}{2}\int_{-1}^{-1} d\mu_k\, L_\ell(\mu_k)\left[b_{\rm g}^{\rm sp}(z) + f(z)\mu_k^2\right]^2 P_{\delta\delta}(k,z) \tag{8.6}$$

where μ_k is the cosine of the angle between $\vec{k}$ and the line-of-sight direction, $b_{\rm g}^{\rm sp}(z)$ is the redshift-dependent linear bias parameter for the spectroscopic sample and $L_\ell(\mu_k)$ is the Legendre polynomial of order ℓ, for $\ell = [0,2,4]$ in four spectroscopic bins covering a redshift range $z = (0.9, 1.8)$. The theory model is generated at

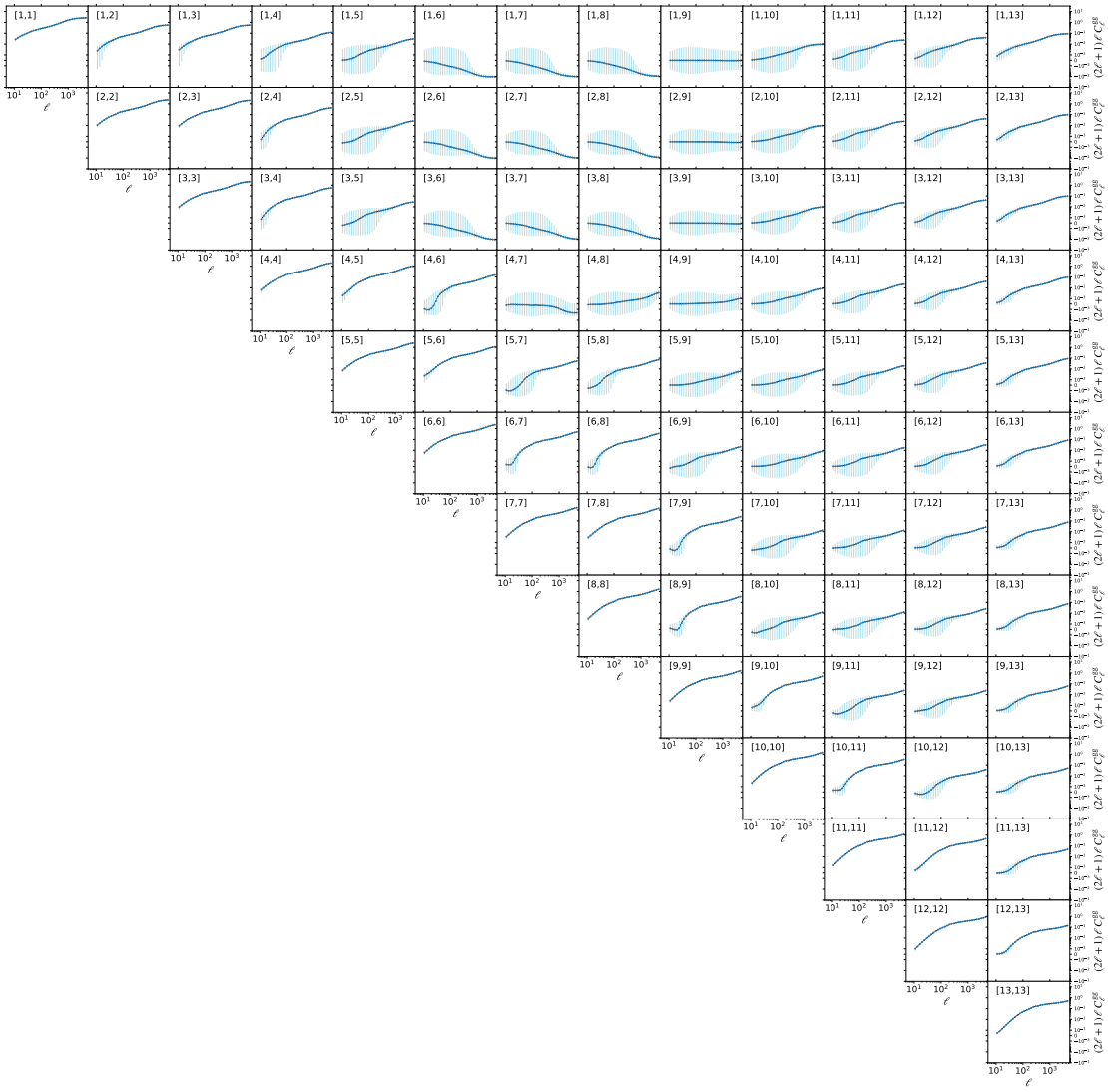

Fig. 8.2. Synthetic galaxy clustering angular power spectra, for the auto- and cross-correlations between the 13 photometric redshift bins. The light blue error bars correspond to the uncertainty given by the analytical covariance matrix.

the mean redshift of each bin, corresponding to the values $\bar{z} = [1.0, 1.2, 1.4, 1.65]$. The multipoles are then calculated over 100 linearly-spaced k bins between $k = (0.004, 0.3)h\,\text{Mpc}^{-1}$. We assume a Gaussian prescription for the data covariance matrix. The resultant spectroscopic galaxy clustering (GCsp) data vectors are shown in Fig. 8.4.

8.3.3 Models

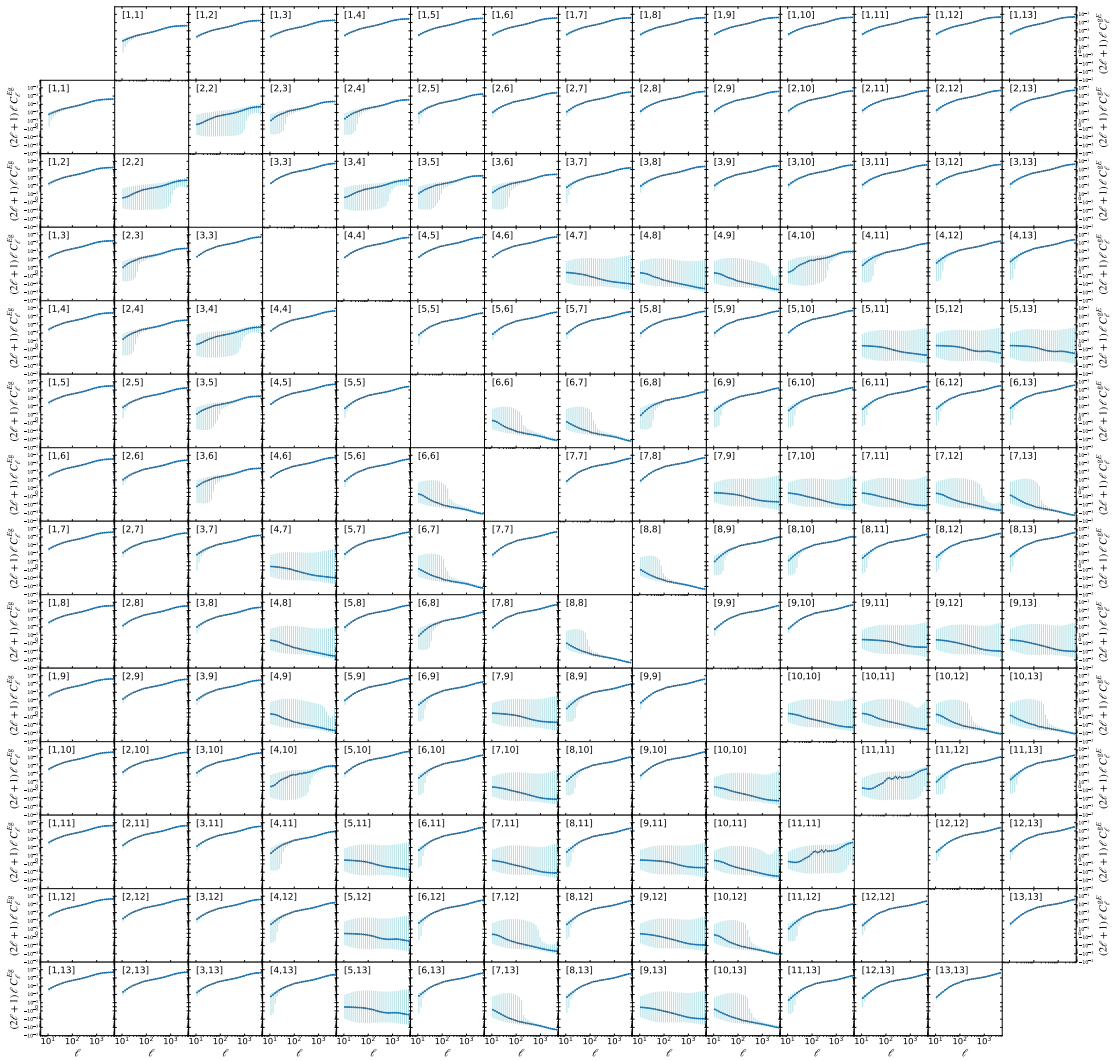

Fig. 8.3. Similar to Figs. 8.1 and 8.2, but showing the cross-correlation between WL and photometric GC (i.e. galaxy-galaxy lensing) for the auto- and cross-correlations between the 13 photometric redshift bins for both gE (upper triangle) and Eg (lower triangle).

We perform Bayesian inference with the mock data against 6 different models. On top of the concordance ΛCDM model, we consider minimal extensions by allowing variations in (1) curvature, (2) the dark energy EoS with parameters w_0 and w_a, and (3) General Relativity. In the first case, we relax the assumption of $\Omega_{\mathrm{k},0} = 0$ and sample the curvature energy density $\Omega_{\mathrm{k},0}$ as an additional cosmological parameter. In the second case, we vary the EoS $w(z)$ of dark energy, which we refer to as $w_0 w_a$CDM models. The most commonly used and well-tested Chevallier-Polarski-

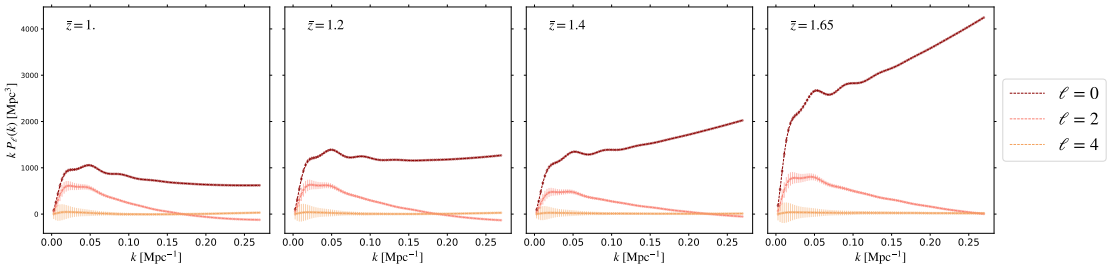

Fig. 8.4. Legendre multipoles $P_\ell(k)$ for the GCsp probe as a function of scale k for the 3 multipoles $\ell = 0$ (dark red), $\ell = 2$ (pink), and $\ell = 4$ (orange), corresponding to the 4 spectroscopic redshift bins. The error bars correspond to the data uncertainties given the analytical covariance matrix.

Linder (CPL) [7, 8] parameterisation of $w(z)$ gives

$$w(z) = w_0 + w_a \left(\frac{z}{1+z} \right) , \tag{8.7}$$

where w_0 is the present-day value of the EoS and w_a quantifies its redshift dependence as a function of the scale factor a.

Finally, we consider modifications to General Relativity by simplistically allowing variations in the structure growth through the index $\gamma_{\rm g}$, which governs the scaling relation between the growth rate $f(z)$ and the matter energy density $\Omega_{\rm m}(z)$:

$$f(z) = \Omega_{\rm m}(z)^{\gamma_{\rm g}} . \tag{8.8}$$

A value inconsistent with the fiducial of $\gamma_{\rm g} \approx 0.545$ in ΛCDM would point to a deviation in growth history, hence implying a gravitational theory different from that of General Relativity [12, 221].

In conclusion, we explicitly list the models we will be constraining with each probe (WL, 3x2pt and GCsp) :

1. ΛCDM
2. ΛCDM + Ω_k
3. ΛCDM + γ
4. $w_0 w_a$CDM
5. $w_0 w_a$CDM + Ω_k
6. $w_0 w_a$CDM + γ

8.3.4 Forecast Results with CLOE

We use the nested sampler `PolyChord` to conduct our cosmological inference. We present in Figs. 8.5, 8.6 and 8.7, preliminary results for selected model+probe combinations, where we plot the 2D marginalised contours for the sampled and derived cosmological parameters. Since we find that constraints on $\omega_{\rm b}$ were prior-dominated for all the cases, we report instead constraints on the combined present-day value of the matter density parameter, $\Omega_{\rm m,0}$. For a table of best-fit and 1σ values as well as additional constraints on the nuisance parameters, we refer the reader to Appendix C.

Our results prove that we are able to recover the fiducial cosmology to a high degree of fidelity for all the model+probe combinations, hence validating our likelihood pipeline.

For the case of the WL probe, we find that we are not able to constrain parameters such as H_0 and $n_{\rm s}$. However, we gain considerable constraining power going from the WL to the 3x2 probe. This demonstrates the strength of combining these two highly complementary probes to break parameter degeneracies, such as in the $\Omega_{\rm m} - \sigma_8$ plane. However, it should be noted that the setup we have adopted is a rather optimistic one (eg. going up to very small scales of $\ell = 3000$).

8.4 CLOE with `CosmoSIS`

I additionally implemented a pipeline to run CLOE with `CosmoSIS` as an alternative to the existing fiducial implementation with `Cobaya`. This gives the user flexibility to choose an alternative sampler while still relying on CLOE to produce the theoretical predictions and return the value of the log-likelihood. Using `CosmoSIS` furthermore allows the user to employ samplers that are not currently implemented within `Cobaya`, such as `emcee` [222], `Multinest` [223-225], `Nautilus` [226], `Zeus` [227], and `Pocomc` [228], on top of `PolyChord` and other regular Metropolis-Hastings samplers.

There are currently two approaches to interface CLOE with `CosmoSIS`, depending on user preference. In the first approach, the theory and likelihood calculations are decoupled, whereby at each point of the sampling step, an external Boltzmann code is called to calculate the theoretical matter power spectrum and growth functions, which are then input into CLOE to derive the C_ℓ's and the log-likelihood value. The

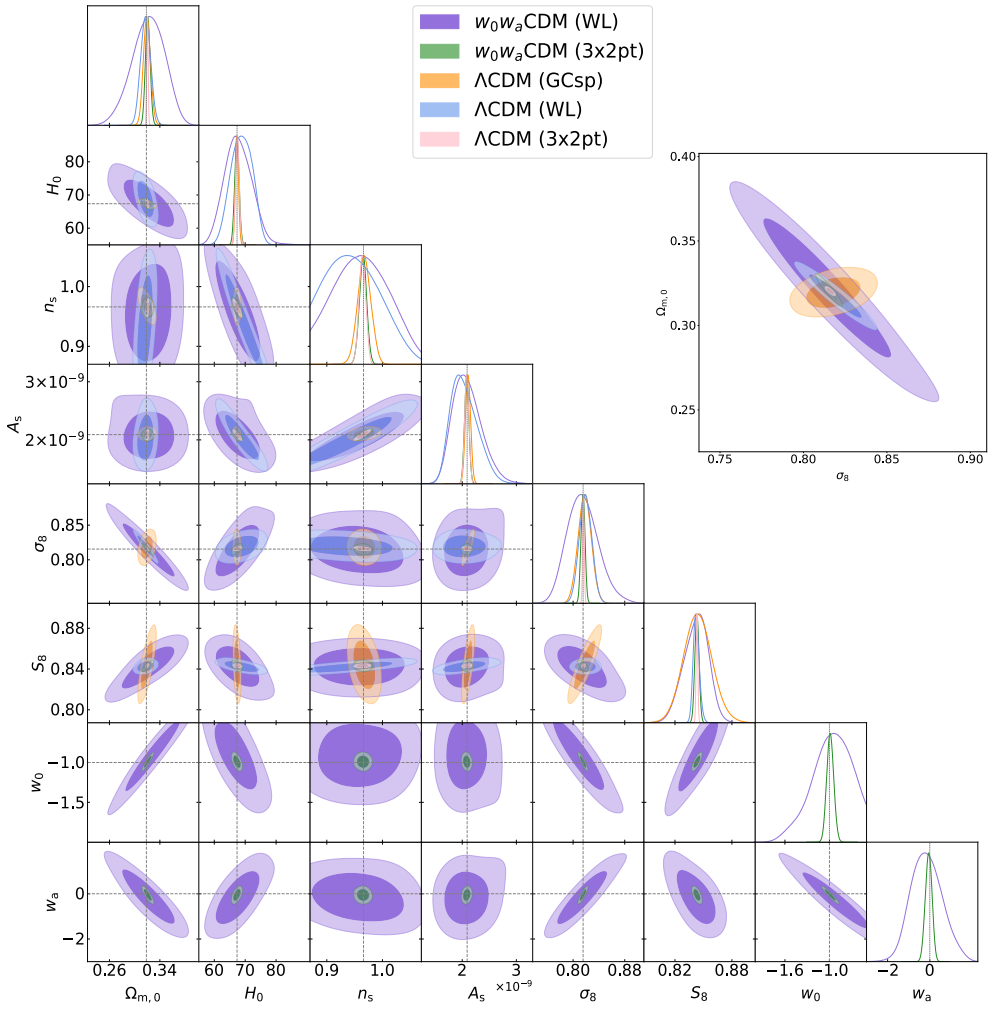

Fig. 8.5. 2D marginalised contours of the cosmological parameters, as well as derived parameters $\Omega_{\rm m}$, σ_8 and S_8, for the model+probe combinations of w_0w_aCDM (WL) (purple), w_0w_aCDM (3x2pt) (green), ΛCDM (GCsp) (yellow), ΛCDM (WL) (blue) and ΛCDM (3x2pt) (pink). We show a zoom-in of the $\Omega_{\rm m} - \sigma_8$ plane in the inset figure. The fiducial values have been marked out with grey lines. Please note that these results are preliminary and subject to change.

external Boltzmann code and CLOE are thus invoked by `CosmoSIS` as separate modules. This entails writing scripts that will interface `CosmoSIS` with `CAMB` and CLOE, which I have written in `camb_interface.py` and `cloe_interface.py` respectively.

I detail here the flow of the pipeline. The top-level default parameter file is given by `run_cosmosis.ini`. It requires two modules : the Boltzmann module, such as `[camb]` or `[class]`, and the `[euclid]` module that prompts CLOE to calculate

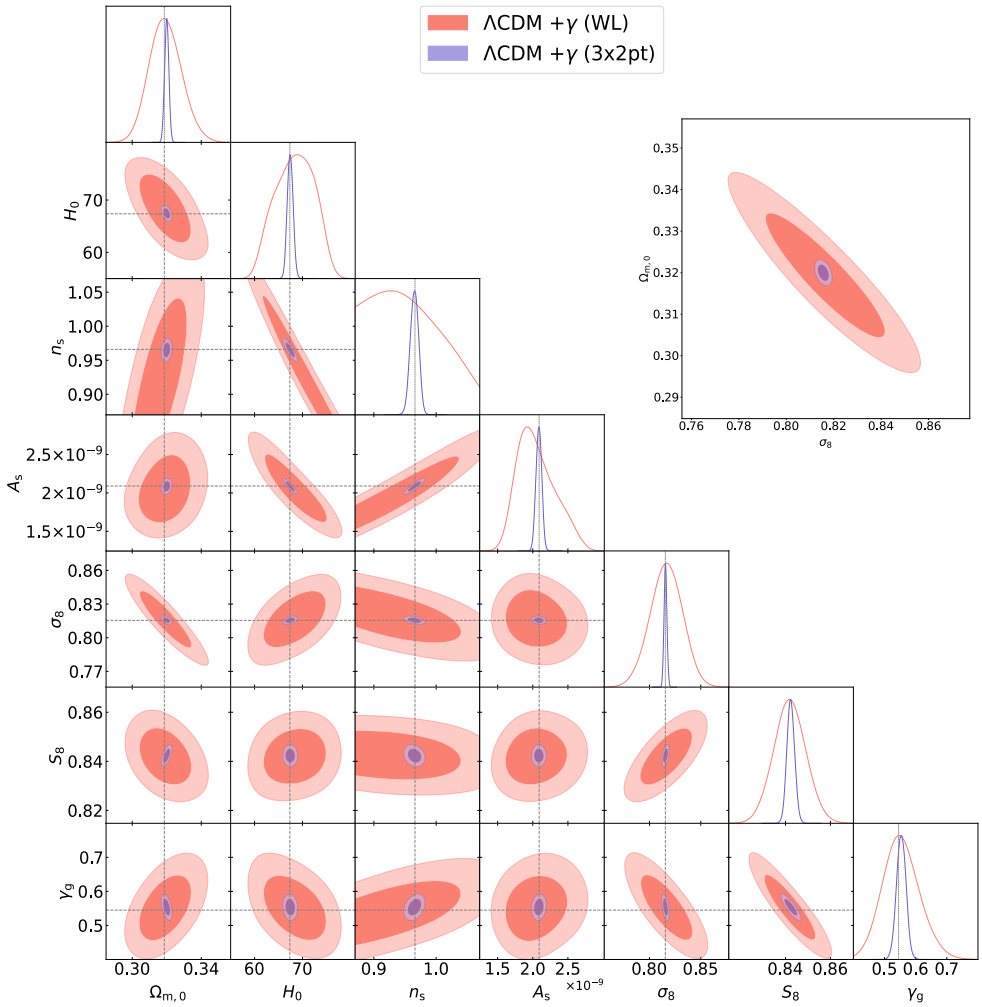

Fig. 8.6. 2D marginalised contours of the cosmological parameters, as well as derived parameters σ_8 and S_8, for the model+probe combinations of ΛCDM $+\gamma$ (WL) (pink) and ΛCDM $+\gamma$ (3x2pt) (purple). We show a zoom-in of the $\Omega_{\rm m} - \sigma_8$ plane in the inset figure. The fiducial values have been marked out with grey lines. Please note that these results are preliminary and subject to change.

the log-likelihood. The `[camb]` module is run first, which will call a Boltzmann solver (`CAMB` in this case) to calculate the matter power spectrum and background quantities, such as the angular diameter distance, $D_{\rm A}(z)$, linear growth rate, $f(z)$, and $\sigma_8(z)$, according to the user specifications in `cobaya_config_for_cosmosis.yaml`. This `yaml` file has been written in the same format as the regular `config.yaml` file for ease of understanding. These quantities are then stored in the `CosmoSIS` DataBlock. In the `[euclid]` module, where the script `cloe_interface.py` will be run,

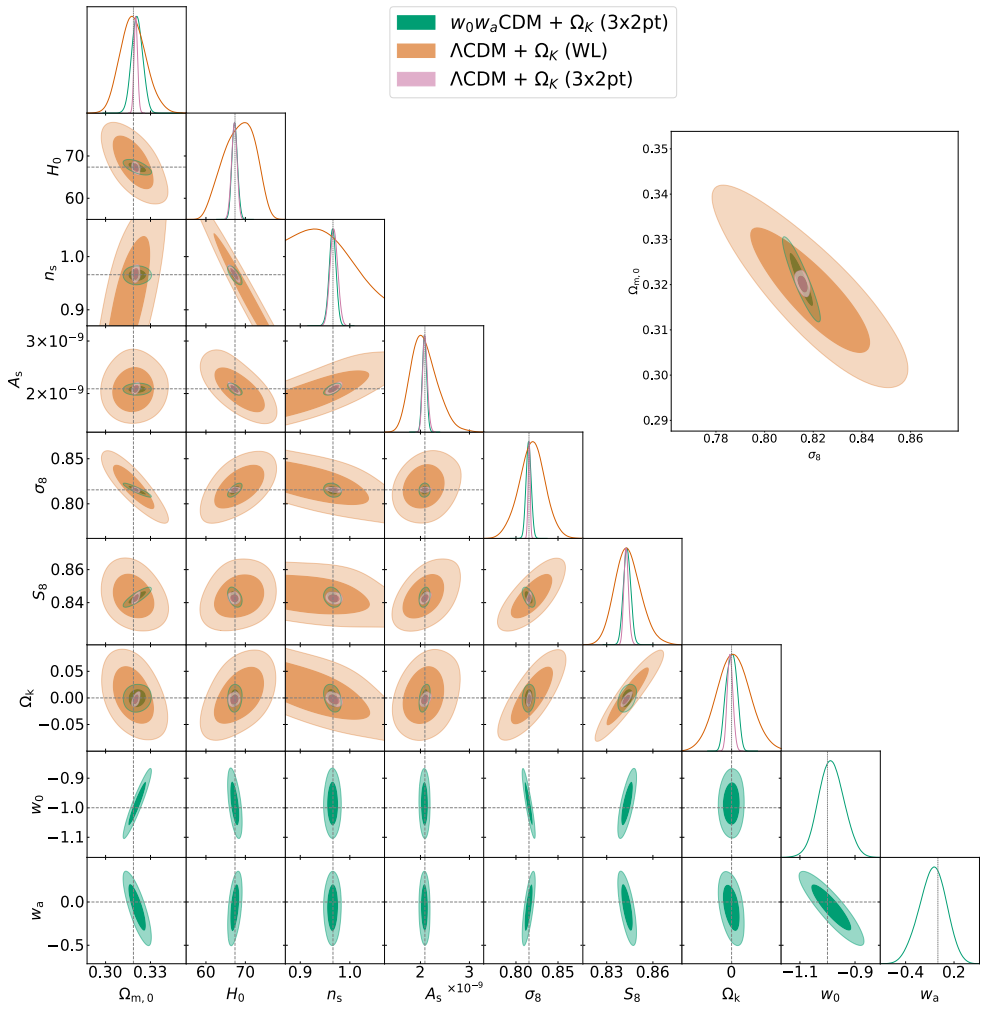

Fig. 8.7. 2D marginalised contours of the sampled cosmological parameters, as well as derived parameters σ_8 and S_8, for the model+probe combinations of w_0w_aCDM $+\Omega_k$ (3x2pt) (teal), ΛCDM $+\Omega_k$ (WL) (orange) and ΛCDM $+\Omega_k$ (3x2pt) (pink). We show a zoom-in of the $\Omega_\mathrm{m} - \sigma_8$ plane in the inset figure. The fiducial values have been marked out with grey lines. Please note that these results are preliminary and subject to change.

CLOE retrieves these quantities from the DataBlock, along with further user specifications for CLOE in `cobaya_config_for_cosmosis.yaml` (such as data file paths, scale cuts, and covariance matrices). It then calculates and returns the value of the log-likelihood, which is again stored in the `CosmoSIS` DataBlock. This process repeats for each step of the parameter sampling.

In the second approach, the CLOE $\times$ `Cobaya` pipeline performs every aspect of both the theory and likelihood calculations. As a result, the `CosmoSIS` parameter `ini`

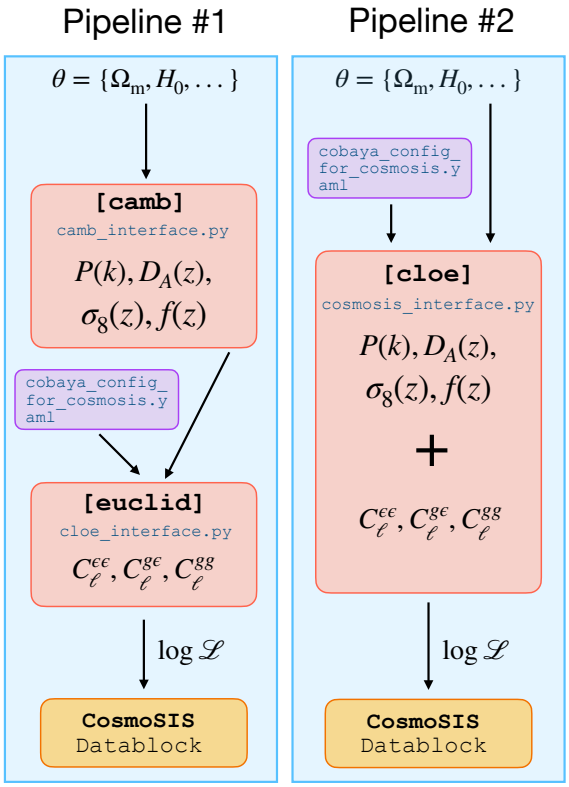

Fig. 8.8. Illustration of the structure of the interface between CLOE and `CosmoSIS`, for both pipelines (left : theory and likelihood split, right : theory and likelihood calculations combined). The diagram shows the process of one single step taken by the sampler, starting from the vector of currently sampled parameters θ and arriving at one value of the log-likelihood.

file only requires one module, `[cloe]`, as an input. The file specified within this module, `cosmosis_interface.py`, establishes the interface with `CosmoSIS` by first reading the `cobaya_config_for_cosmosis.yaml` config file in the form of a `Cobaya` `info` dictionary. It retrieves the parameters currently being sampled from the `CosmoSIS` DataBlock and updates the `info` dictionary with their values. With this, CLOE then calculates the matter power spectrum and relevant growth functions mentioned above using the Boltzmann solver within CLOE, after which it calculates the observable power spectra. `Cobaya` is invoked with the `evaluate` sampler to output the log-likelihood value, which is subsequently stored in the `CosmoSIS` DataBlock. Here, there is no explicit call to the Boltzmann code, as the calculations of the cosmological quantities are performed under the hood when the `model` instance is created. This approach effectively overlays a `CosmoSIS` wrapper over the CLOE $\times$ `Cobaya` pipeline. Fr clarity, I illustrate the flow of both pipelines in Fig. 8.8.

8.5 Theory Science Working Group synergies with CLOE

I am also part of Work Package (WP) 17 of the Theory Science Working Group (TWG), which is responsible for integrating the needs of the various TWG WPs into the CLOE analysis pipeline. Specifically, this involves modifying and validating CLOE according to the different extended ΛCDM models proposed by each WP, supporting the functionalities of modified Boltzmann solvers and deriving forecasts for these extended models.

One such project was to include, within the CLOE theoretical recipe, the effect of *lensing magnification* on the spectroscopic lens sample, which is currently being investigated in WP9.

Gravitational lensing affects the number density of galaxies that *Euclid* measures, by magnifying or de-magnifying the fluxes of observed galaxies. Therefore, since galaxy surveys can only detect sources above a certain magnitude threshold, galaxies that are intrinsically too faint to be observed might be included within the catalogue due to this effect. Moreover, magnification can increase the size of a galaxy, thus decreasing the number density of the overall sample. The total lensing effect on the observed galaxy counts is then known as *lensing magnification*, and the amplitude of the lensing contribution depends on the slope of the luminosity function of the galaxy population, known as the *magnification bias*.

There exists extensive literature showing that magnification has a significant impact on the analysis of current and future photometric galaxy surveys such as DES [229], LSST [230] and *Euclid* [231]. It was shown that for future galaxy redshift surveys, where the redshift range of the galaxies will extend up to $z \sim 2.5$, neglecting magnification can cause non-negligible bias in the estimate of cosmological parameters and the growth factor [232, 233]. Hence it is important to investigate its impact on *Euclid* data with CLOE and quantify the biases that might arise from such an effect.

Here, we describe the proposed recipe following [233] which I have implemented within CLOE, as well as the tests I have carried out to validate this implementation.

The contribution of lensing magnification to spectroscopic galaxy clustering can be expressed in real space, in terms of the multipole 2PCFs. It is split into two contributions : the cross-correlation of magnification and density, and the magnification-magnification auto-correlation. Therefore, we can include this effect by adding these two contributions to the multipoles of the correlation function already implemented

in CLOE, that is

$$\xi_{\mathrm{obs},\ell}(s,z) = \xi^{\mathrm{gg}}_{\mathrm{obs},\ell}(s,z) + 2\xi^{\mathrm{g}\mu}_{\ell}(s,z) + \xi^{\mu\mu}_{\ell}(s,z). \tag{8.9}$$

where $\xi^{\mathrm{gg}}_{\mathrm{obs},\ell}(s,z)$ refers to the pure galaxy-galaxy correlation term as a function of the real space separation between 2 galaxies s and redshift z.

The second term in the above equation is the contribution due to the cross-correlation of galaxy density and magnification, which can be written as follows :

$$\xi^{\mathrm{g}\mu}_{\ell}(s,z) = -C^{\mathrm{g}\mu}(\ell)\frac{3\Omega_{\mathrm{m},0}H_0^2}{4\pi}b^2_{\mathrm{mag}}(z)(1+z)s^2\times \sum_{n=0}^{\ell/2}\frac{(-1)^n}{2^n}\binom{\ell}{n}\binom{2\ell-2n}{\ell}\left[\frac{\ell}{2}-n\right]!\, I^{\ell/2-n+3/2}_{\ell/2-n+1/2}(s,z), \tag{8.10}$$

where $b_{\mathrm{mag}}(z)$ is the amplitude of the spectroscopic magnification bias at redshift z,

$$C^{\mathrm{g}\mu}(\ell) = \frac{2\ell+1}{2}\pi^{3/2}\frac{2^{3/2}}{2^{\ell/2}} \tag{8.11}$$

and

$$I^n_{\ell}(s,z) = \frac{1}{2\pi^2}\int_0^{\infty} dk\, k^2\, P_{\delta\delta}\,(k,z)\,\frac{j_{\ell}(ks)}{(ks)^n}, \tag{8.12}$$

where j_ℓ is the spherical Bessel function of order ℓ. Since the integrals in Eq. (8.12) involve integrals of the spherical Bessel function of half-integer orders, it is convenient to write them in terms of the Bessel function of the first kind, J_ℓ :

$$j_{\ell}(x) = \sqrt{\frac{\pi}{2x}}\,J_{\ell+1/2}(x). \tag{8.13}$$

Therefore, the 3 types of integrals that are relevant for the computation of Eq. (8.10) can be written as

$$I^{3/2}_{1/2}(s,z) = \frac{1}{2\pi^2}\sqrt{\frac{\pi}{2}}\int_0^{\infty} dk\, k^2\, P_{\delta\delta}\,(k,z)\,\frac{J_1(ks)}{(ks)^2} \tag{8.14}$$

$$I^{5/2}_{3/2}(s,z) = \frac{1}{2\pi^2}\sqrt{\frac{\pi}{2}}\int_0^{\infty} dk\, k^2\, P_{\delta\delta}\,(k,z)\,\frac{J_2(ks)}{(ks)^3} \tag{8.15}$$

$$I^{7/2}_{5/2}(s,z) = \frac{1}{2\pi^2}\sqrt{\frac{\pi}{2}}\int_0^{\infty} dk\, k^2\, P_{\delta\delta}\,(k,z)\,\frac{J_3(ks)}{(ks)^4} \tag{8.16}$$

The last term in Eq. (8.9) is the magnification-magnification contribution, which can

be expressed as

$$\xi_\ell^{\mu\mu}(s,z) = C^{\mu\mu}(\ell)\frac{9\Omega_{\mathrm{m},0}^2 H_0^4}{8\pi} b_{\mathrm{mag}}^2(z)\chi^3(z)\int_0^1 f_\ell(x,s,z)\mathrm{d}x, \tag{8.17}$$

where the the coefficient $C^{\mu\mu}(\ell)$ is defined as

$$C^{\mu\mu}(\ell) = (2\ell+1)\frac{\ell!}{2^\ell\left[(\ell/2)!\right]^2}, \tag{8.18}$$

with ! being the factorial operator, and the integrand in Eq. (8.17) is given by

$$f_\ell(x,s) = x^2(1-x)^2\left[1+z(\chi)\right]^2 K_\ell\left(xs\right), \tag{8.19}$$

where

$$K_\ell\left(xs\right) = (xs)\int_0^\infty \mathrm{d}k\, k^2\, P_{\delta\delta}(k,z(\chi))\frac{j_\ell(x\,ks)}{x\,ks}, \tag{8.20}$$

and $z(\chi)$ is the redshift corresponding to the radial comoving distance χ.

I thus implemented, within CLOE, the option to account for spectroscopic magnification when the cosmological parameter inference is carried out using the spectroscopic multipole correlation functions, specifically for the monopole, quadrupole and hexadecapole. Calculating the magnification bias contribution terms $\xi_\ell^{g\mu}$ and $\xi_\ell^{\mu\mu}$ would thus require the additional input nuisance parameters $b_{\mathrm{mag}}(\bar{z}_i)$, the amplitude of magnification bias at the mean redshift of each bin. This parameter can either be fixed or sampled over.

I validated my implementation against the external code `coffe` (COrrelation Function Full-sky Estimator; [234]), which calculates the 3D galaxy-galaxy 2PCF and its multipoles with linear perturbation theory. For a fiducial cosmology of $\Omega_{\mathrm{b},0} = 0.049$, $\Omega_{\mathrm{DM},0} = 0.27$, $H_0 = 67.0$, $n_\mathrm{s} = 0.96$, $\sigma_8 = 0.83$, linear galaxy bias values of $b_\mathrm{g}^\mathrm{sp} = [1.441, 1.643, 1.862, 2.078]$ and lensing magnification bias values of $b_\mathrm{mag} = [0.79, 0.87, 0.96, 0.98]$ estimated from the *Euclid* Flagship 2 simulations, I calculated the density and magnification auto- and cross-correlation functions, $\xi_\ell^{\mu\mu}(s,z)$ and $\xi_\ell^{\mathrm{g}\mu}(s,z)$, and compared the results between CLOE and `coffe` by plotting their relative differences in Fig. 8.9. I followed the fiducial *Euclid* setup of 4 spectroscopic redshift bins with mean redshifts $\bar{z} = [1.0, 1.2, 1.4, 1.65]$, plotting the monopole, quadrupole and hexadecapole for a separation range of $s = (40, 385)$ Mpc. We see that in the case of $\xi_\ell^{\mathrm{g}\mu}(s,z)$, the relative difference is well within 0.5% in all cases. For $\xi_\ell^{\mu\mu}(s,z)$, it is less than 2%. Hence we consider our implementation validated.

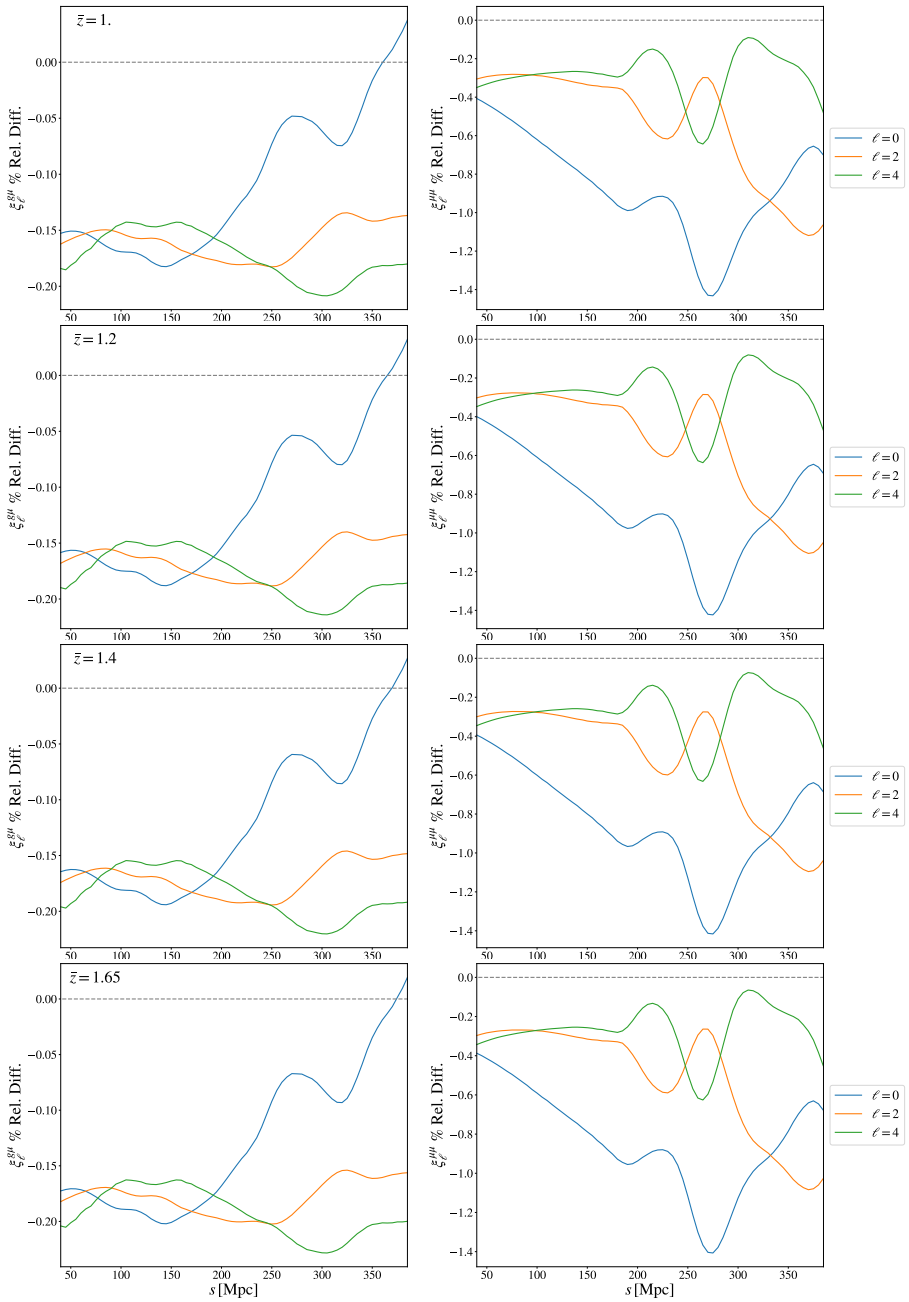

Fig. 8.9. Left column : Relative percentage difference between the density-magnification contribution $\xi_\ell^{g\mu}(s,z)$ as calculated by CLOE and `coffe`, for each of the multipole values $\ell = [0,2,4]$ and mean redshift bin values $\bar{z}_i$. Right : The same, for the magnification-magnification contribution $\xi_\ell^{\mu\mu}(s,z)$.

I subsequently ran CLOE to forecast the effect of lensing magnification contributions on the cosmological parameter posteriors. I produced mock spectroscopic

galaxy clustering multipole correlation functions $\xi_\ell(s, z)$ using CLOE, and their corresponding covariance matrices using `coffe`, assuming the same fiducial cosmology as above. In this case, I included the lensing magnification effect when creating the data. I then used these data vectors to run the Bayesian inference analysis with CLOE. For simplicity, I only sampled the cosmological parameters $\{H_0, A_\mathrm{s}, \Omega_\mathrm{m}\}$ while keeping all nuisance parameters fixed. Fig. 8.10 presents the marginalised posterior distributions for both cases when the magnification bias flag is activated or not in CLOE.

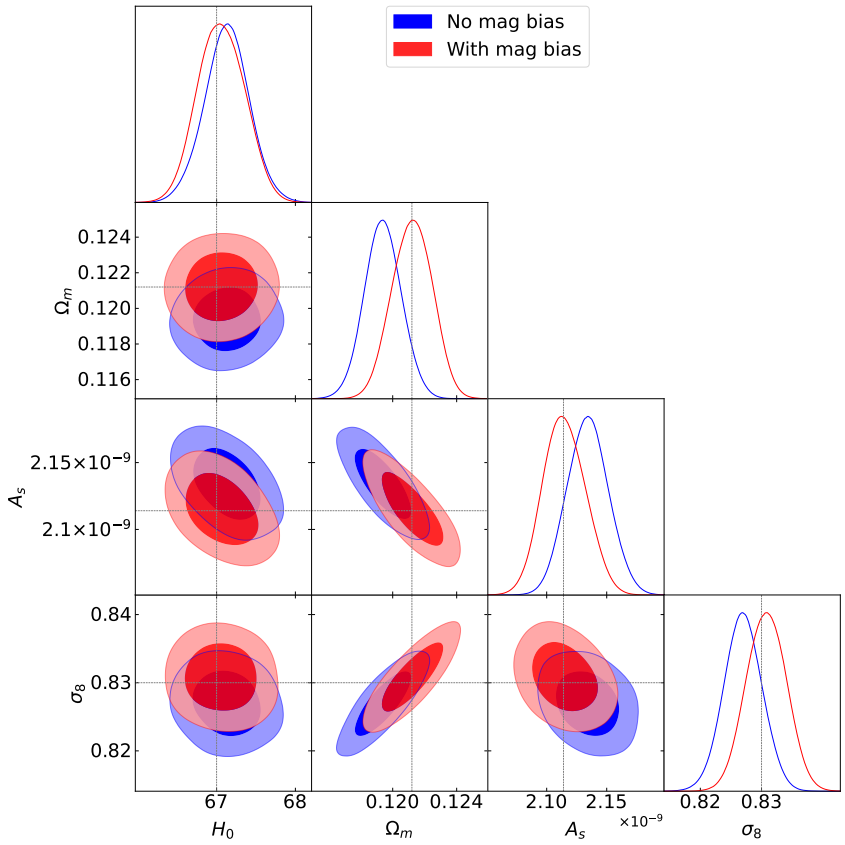

Fig. 8.10. 2D marginalised contours of the sampled cosmological parameters $\{H_0, A_\mathrm{s}, n_\mathrm{s}\}$ and derived parameter σ_8 obtained by CLOE, for a spectroscopic galaxy clustering dataset produced with magnification bias included. The horizontal and vertical lines mark the fiducial values. Blue : results for when the magnification bias flag is not activated in CLOE when conducting the inference. Red : when magnification bias is activated. We see a distinct shift away from the fiducial when magnification bias is not taken into account. Please note that these results are preliminary and subject to change.

As expected, we recover the fiducial parameter values when the magnification bias is properly considered within CLOE (i.e. when the analysis settings match those

when producing the data vectors). However, when lensing magnification bias is not taken into account, this causes a shift in the contours, most noticeably for $\Omega_{\rm m}$, $A_{\rm s}$ and σ_8, albeit still within the 1σ range. Hence this exercise serves as a useful investigation to quantify the impact of lensing magnification on cosmological parameter estimation. With incoming data that will only improve in quality and quantity hereafter, correctly accounting for systematic effects becomes increasingly important to ensure the robustness of our results.

IN BRIEF

In this Chapter, I have introduced the ESA *Euclid* space mission, specifically focusing on my contributions within the *Euclid* Consortium's Inter-Science Taskforce :Likelihood and Theory Science Working Groups, where I have played an active role in developing the likelihood analysis pipeline, CLOE.

Firstly, I discussed how we can obtain likelihood forecasts with CLOE, by first generating mock data and testing sampling strategies to obtain forecast contours, which will allow us to predict the constraining power of *Euclid*'s primary probes. Secondly, I described the CLOE$\times$`CosmoSIS` interface which I have implemented within CLOE, which will allow the user to run CLOE with an alternative sampling platform. Finally, within the TWG WP 17, I have worked with other WPs to modify CLOE to take into account the effects of lensing magnification when calculating the theoretical prescription of the spectroscopic galaxy clustering probe.

With *Euclid*, we expect to acquire large amounts of data of unprecedented precision, allowing us to illuminate the elusive dark sector of the Universe. I have hence demonstrated that my work within the IST :L and TWG constitutes a considerable effort towards this endeavour, especially with regard to the development of important infrastructural coding aspects of the mission.

Parameter		Fiducial	Prior
		Cosmology	
H_0		67.37	$\mathcal{U}(55.0, 91.0)$
ω_b		0.0227	$\mathcal{N}(0.0227, 0.00038)$
ω_DM		0.1219	$\mathcal{U}(0.01, 0.37)$
n_s		0.966	$\mathcal{U}(0.87, 1.07)$
$\ln 10^{10} A_\mathrm{s}$		3.04	$\mathcal{U}(1.6, 3.9)$
w_0		-1	$\mathcal{U}(-3.0, -0.5)$,
w_a		0	$\mathcal{U}(-3.0, -0.5)$,
γ_g		0.545	$\mathcal{U}(0.01, 1.1)$
$\log_{10}(T_\mathrm{AGN}/\mathrm{K})$	Baryonic feedback efficiency factor of the HMCode emulator	7.75	$\mathcal{N}(7.75, 0.17825)$
		Photometric sample nuisance parameters	
A_IA	Amplitude of intrinsic alignments	0.16	$\mathcal{U}(-2, 2)$
η_IA	Power-law slope of intrinsic alignment redshift evolution	1.66	$\mathcal{U}(0.0, 3.0)$
$b_{\mathrm{gal},i=0\ldots3}$	Coefficients of cubic polynomial for clustering bias	$[1.33291, -0.72414, 1.01830, -0.14913]$	$\mathcal{U}(-3, 3)$
$b_{\mathrm{mag},i=0\ldots3}$	Coefficients of cubic polynomial for magnification bias	$[-1.50685, 1.35034, 0.08321, 0.04279]$	$\mathcal{U}(-3, 3)$
$m_{i=1\ldots13}$	Per-bin shear multiplicative bias	0.0	$\mathcal{N}(0.0, 0.0005)$
$\Delta z_{i=1\ldots13}$	Per-bin mean redshift shift	$[-0.025749, 0.022716, -0.026032, 0.012594, 0.019285, 0.008326, 0.038207, 0.002732, 0.034066, 0.049479, 0.066490, 0.000815, 0.049070]$	$\mathcal{N}\left[z_i^\mathrm{fid}, 0.002\,(1 + z_i^\mathrm{fid})\right]$
		Spectroscopic sample nuisance parameters	
$b_{1,i=1\ldots4}$	Per-bin linear bias	$[1.412, 1.769, 2.039, 2.496]$	$\mathcal{U}(1.0, 3.0)$
$b_{2,i=1\ldots4}$	Per-bin second-order bias	$[0.695, 0.870, 1.162, 2.010]$	$\mathcal{U}(-5.0, 5.0)$
$\alpha_{P,i=1\ldots4}$	Poissonian shot noise for extra-stochastic parameters	$[0.056, 0.152, 0.144, 0.309]$	$\mathcal{U}(-1.0, 2.0)$
$c_{0,i=1\ldots4}$	Per-bin counter term for Legendre monopole	$[11.603, 14.475, 15.667, 26.413]$	Fixed
$c_{2,i=1\ldots4}$	Per-bin counter term for Legendre quadrupole	$[35.986, 44.914, 43.819, 62.353]$	Fixed
$c_{4,i=1\ldots4}$	Per-bin counter term for Legendre hexadecapole	$[56.943, 55.443, 44.214, 42.89]$	Fixed
$f_{i=1\ldots4}$	Per-bin purity factor (assuming Poisson distributed interlopers)	$[0.195, 0.204, 0.306, 0.121]$	$\mathcal{N}\left(f_i^\mathrm{fid}, 0.01\right)$

Table 8.1. Reference values and prior probability distributions for the cosmological and nuisance parameters. These fiducial values are used to compute the self-generated synthetic data. If the parameter is sampled, the corresponding prior probability distributions are either *uniform* $\mathcal{U}$ or *Gaussian* $\mathcal{N}$. Note that since we do not expect LSS probes to be able to give good constraints on the baryon energy density ω_b, we additionally imposed a BBN prior to speed up convergence.

Survey Specification	Fiducial Value
Survey Area	13245 deg^2
σ_ϵ	0.368
Magnitude	24.5
$\bar{z}_i$	$[0.27575,\ 0.37635,\ 0.44634,\ 0.54284,\ 0.62145,\ 0.70957,\ 0.79860,\ 0.86687,\ 0.97753,\ 1.09136,\ 1.24264,\ 1.47918,\ 1.89264]$
ℓ	$[10.00,\ 12.02,\ 14.45,\ 17.37,\ 20.88,\ 25.09,\ 30.16,\ 36.25,\ 43.58,\ 52.38,\ 62.96,\ 75.68,\ 90.97,\ 109.3,\ 131.4,\ 158.0,\ 189.9,\ 228.2,\ 274.4,\ 329.8,\ 396.4,\ 476.5,\ 572.7,\ 688.4,827.5,\ 994.7,\ 1195.5,\ 1437.1,\ 1727.4,\ 2076.4,\ 2495.8,\ 3000.0]$

Table 8.2. Assumed survey specifications (survey area, shape noise, limiting magnitude, mean redshift of each redshift bin and ℓ bin ranges) to generate the synthetic photometric data.

9. Cosmology with UNIONS

Sommaire

9.1 The Ultraviolet Near-Infrared Optical Northern Survey

The ground-based *Ultraviolet Near-Infrared Optical Northern Survey (UNIONS)* is a collaboration between the Canada-France Imaging Survey (CFIS), the Panoramic Survey Telescope and Rapid Response System (Pan-STARRS ; [235]) survey and the Wide Imaging with Subaru Hyper Suprime-Cam of the Euclid Sky (WISHES) survey. It will combine photometry from five optical bands : the u and r band data from CFIS using the Canada France Hawaii Telescope (CFHT), i band data from the Pan-STARRS1 and Pan-STARRS2 telescopes, z band imaging from WISHES and g band imaging from the Waterloo Hawaii IfA G-band Survey (WHIGS) with the Subaru Hyper Suprime Cam (HSC). Together, they will deliver the deepest dataset of galaxy photometry covering 4800deg^2 of the northern sky, providing ground-based optical data to complement *Euclid* observations in the northern hemisphere.

The high-quality imaging achieved by UNIONS telescopes will enable competitive weak lensing science. Hence considerable efforts have been made within the collaboration to process the galaxy images, measure their shapes, and create an accurate catalogue to ultimately obtain cosmological constraints from the data. I am part of this UNIONS collaboration, where I have been involved in developing the Bayesian inference pipeline to obtain cosmological constraints with UNIONS cosmic shear data. In the following sections, I detail the work that I have carried out in this respect.

9.2 Inference Pipeline Development

Here I present the tests I have conducted on the latest version of the UNIONS galaxy catalogue v1.3, containing approximately 84 million galaxies covering a 3200deg^2 footprint, which, after masking, has an effective area of 2138deg^2. It was processed using the `ShapePipe` software [236, 237], a fully modular end-to-end weak-lensing analysis pipeline which, from wide-field galaxy images, identifies galaxies, estimates the galaxy point spread functions (PSF) and conducts shape measurement, using software such as MCCD [238] and `ngmix` [239], ultimately delivering a galaxy catalogue robust enough for weak lensing science.

9.2.1 Cosmic Shear 2-Point Correlation Function

The main observable we will be using is the 2PCF in real space $\xi_{\pm}(\theta)$, as defined in Eq. (4.18). We use the `TreeCorr` software [240] to calculate $\xi_{\pm}(\theta)$, where we have binned the separation angle θ in 20 bins over a range $\theta = (1, 200)$ arcmin. For the current v1.3 catalogue we only consider 1 tomographic bin. In Fig. 9.1 below we plot the resultant $\xi_{\pm}(\theta)$. We also include the uncertainties of the measurement as calculated by `TreeCorr`, which were estimated using a jackknife approach, given by

$$\text{Cov}_{ij} = \frac{N}{N-1} \sum_{k}^{N} (\xi_i^k - \bar{\xi}_i)^T (\xi_j^k - \bar{\xi}_j), \tag{9.1}$$

where N is the number of patches the sky has been divided into, and ξ_i^k is the correlation function in the i-th θ bin of one k-th patch of the sky.

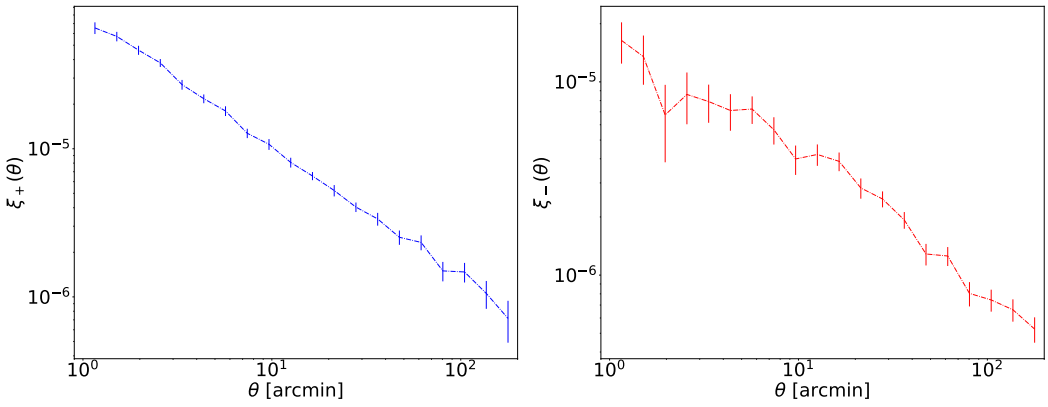

Fig. 9.1. Plot of real space 2PCF (left, blue : ξ_+, right, red : ξ_-) as a function of angular separation θ for one tomographic bin, calculated using `TreeCorr`. We also include the jackknife error bars on the measurement.

9.2.2 Photometric Redshift Distribution

Another key ingredient in weak lensing analyses is the photometric redshift distribution of the source galaxies, $n(z)$, which directly impacts the modelling of the weak lensing angular power spectrum, as seen from Eq. (4.15). The redshift distribution of the v1.3 catalogue was created based on a machine learning approach, specifically using *Self-Organising Maps (SOMs)* [241]. This involves estimating the redshift distribution of an ensemble of galaxies, instead of individually assigning an estimated photometric redshift (photo-z) to each of them. This is done by comparing the photometric sample to a given spectroscopic dataset with known spectro-z's. In order to most accurately estimate the $n(z)$ based on the spectro-z's, the spectroscopic sample is reweighted to closely match the photometric sample, typically based on galaxy colour. From there, it is then assumed that the redshift distribution of the photometric sample matches that of the spectroscopic one since there exists a strong correlation between a galaxy's magnitude in different optical bands, and its redshift.

This reweighting is carried out using SOMs [242], an unsupervised learning NN algorithm that maps a high-dimensional space into a lower-dimensional one, which in this case involves mapping the complex relations in the colour-redshift manifold. The SOM was trained on a spectroscopic dataset containing samples from the DEEP2 Redshift Survey [243], the VIMOS VLT Deep Survey [244] and the VIMOS Public Extragalactic Survey (VIPERS; [245]), since they overlap the UNIONS footprint and probe a similar colour-magnitude range as our photometric catalogue. We validate the SOM against the MICE2 mock catalogue [246] with appropriate magnitude cuts, and find a high level of fidelity.

In Fig. 9.2 I plot the resultant photometric $n(z)$. Since we have decided to conduct the blinding of the cosmological analysis on the level of the $n(z)$, I plot all 3 blinds of the redshift distribution.

9.2.3 Covariance Matrix

To derive the data covariance matrix, we use the `CosmoCov` software [247, 248], which calculates the covariance matrix of the 2PCFs in real space, taking into account the Gaussian and SSC contributions. We follow the methodology outlined in Sect. 8.3.1 to obtain $\mathrm{Cov}(C(\ell_1), C(\ell_2))$ for the cosmic shear observable ($\gamma\gamma$), transforming

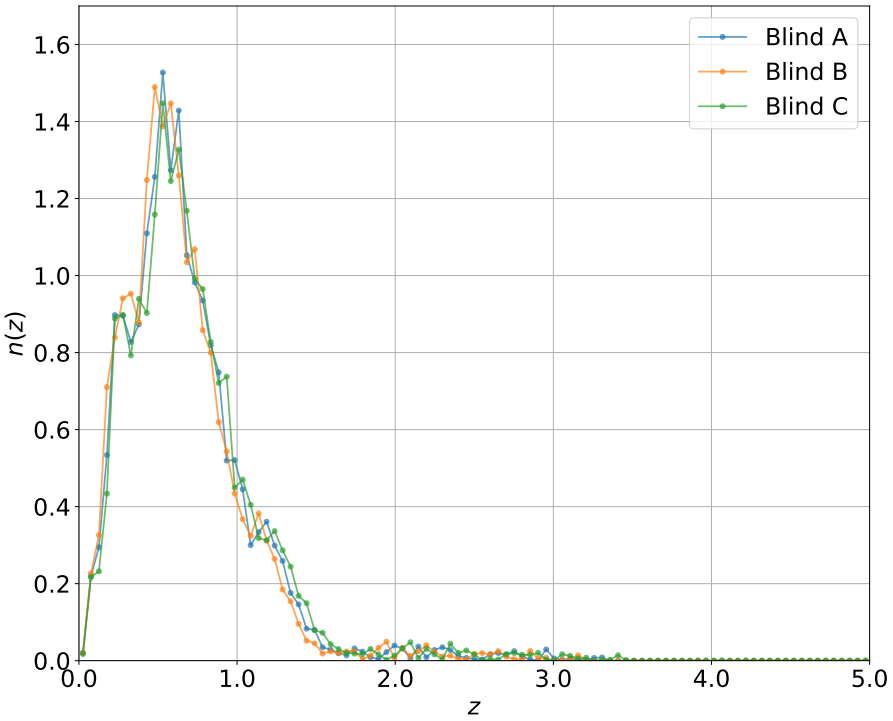

Fig. 9.2. Plot of the weighted redshift distributions of the galaxy samples in the v1.3 catalogue for all 3 blinds (A : blue, B : orange, C : green), calibrated using SOMs. We have created the histogram with 100 bins. Please note that these results are preliminary and subject to change.

them from harmonic space to real space by

$$\mathrm{Cov}\left(\xi_{ij}(\theta_1), \xi_{kl}(\theta_2)\right) = \frac{1}{4\pi^2} \int \frac{d\ell_1}{\ell_1} \int \frac{d\ell_2}{\ell_2} \ell_1^2\, \ell_2^2\, J_n(\ell_1\theta_1)\, J_n(\ell_2\theta_2) \times \\ \left[\mathrm{Cov}_{\mathrm{G}}(C_{ij}(\ell_1), C_{kl}(\ell_2)) + \mathrm{Cov}_{\mathrm{SSC}}(C_{ij}(\ell_1), C_{kl}(\ell_2))\right], \quad (9.2)$$

where in J_n, $n = 0$ for $\xi_+(\theta)$ and $n = 4$ for $\xi_-(\theta)$.

In Fig. 9.3 we plot the cosmic shear covariance matrix as obtained from `CosmoCov`, given the shape noise and galaxy density calculated by `ShapePipe` for one of the $n(z)$ blinds (blind A).

9.3 Cosmological Constraints with UNIONS Cosmic Shear

With the data vectors, redshift distributions and covariance matrix, we subsequently developed a cosmological inference pipeline based on `CosmoSIS`, which will allow us to obtain constraints on the cosmological parameters from UNIONS data. We per-

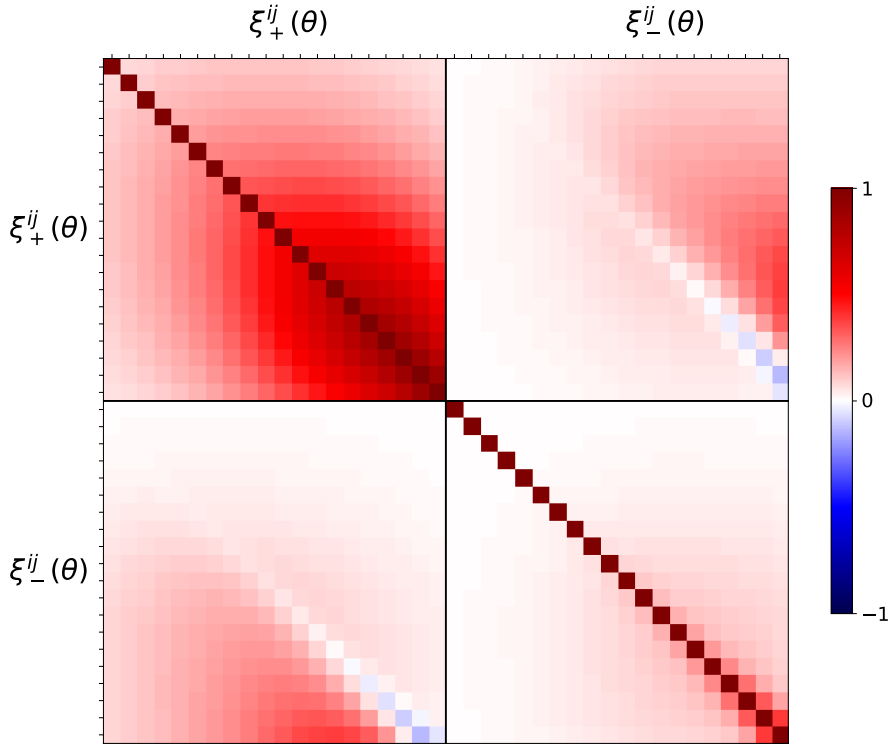

Fig. 9.3. Plot of the correlation matrices of $\xi_{\pm}(\theta)$ calculated by `CosmoCov` for the 20 θ separation bins, where $\mathrm{Corr}_{ij} = \mathrm{Cov}_{ij}/\sqrt{\mathrm{Cov}_{ii} \times \mathrm{Cov}_{jj}}$. Here we have assumed a fiducial cosmology of $\Omega_{\mathrm{m},0} = 0.25$, $\Omega_{\mathrm{b},0} = 0.044$, $\sigma_8 = 0.80$, $n_{\mathrm{s}} = 0.95$ and $h = 0.70$. Please note that these results are preliminary and subject to change.

formed a scale cut and considered only the scales $\theta = (10, 100)$ arcmin. We used `CAMB` as the fiducial Boltzmann solver, and sampled over the cosmological parameters $\{\Omega_{\mathrm{DM},0}, \Omega_{\mathrm{b},0}, h, n_{\mathrm{s}}, A_{\mathrm{s}}\}$. We adopted prior ranges similar to those of [82] and employed the `PolyChord` nested sampler. On top of one run where only the cosmological parameters are sampled (and assuming a `Halofit` model for the nonlinear power spectrum), we also investigated the impact of systematic effects such as IA, baryonic feedback, as well as uncertainties in the redshift distribution estimation. I detail in Table 9.1 the priors for all the cosmological and nuisance parameters sampled, for each of the different test cases we have considered.

I present the preliminary results in Fig. 9.4, where I plot the 2D marginalised constraints for all parameters sampled, for all the test cases. I also report their mean and 1σ values in Table 9.2.

We see that our results are largely similar between the various test cases, with the most distinct difference coming from the effect of sampling Δz (Test Case C),

Parameter		Prior
	Cosmology	
$\Omega_{\mathrm{b},0}$		$\mathcal{U}(0.03, 0.07)$
$\Omega_{\mathrm{m},0}$		$\mathcal{U}(0.1, 0.9)$
h		$\mathcal{U}(0.55, 0.91)$
n_{s}		$\mathcal{U}(0.87, 1.07)$
A_{s}		$\mathcal{U}(0.5 \times 10^{-9}, 5 \times 10^{-9})$
	Test Case A	
$\log_{10}(T_{\mathrm{AGN}}/\mathrm{K})$	Baryonic feedback efficiency factor of the HMCode emulator	$\mathcal{U}(6.5, 8.5)$
	Test Case B	
$\log_{10}(T_{\mathrm{AGN}}/\mathrm{K})$	Baryonic feedback efficiency factor of the HMCode emulator	$\mathcal{U}(6.5, 8.5)$
$\mathcal{A}_{\mathrm{IA}}$	Amplitude of intrinsic alignment (NLA Model)	$\mathcal{U}(-6.0, 6.0)$
	Test Case C	
$\log_{10}(T_{\mathrm{AGN}}/\mathrm{K})$	Baryonic feedback efficiency factor of the HMCode emulator	$\mathcal{U}(6.5, 8.5)$
$\mathcal{A}_{\mathrm{IA}}$	Amplitude of intrinsic alignment (NLA Model)	$\mathcal{U}(-6.0, 6.0)$
Δz	Per-bin mean redshift shift	$\mathcal{N}[0.0, 0.5]$

Table 9.1. Table of sampled parameters and their respective priors for the cosmological and nuisance parameters. We also investigated several test cases (A, B, C), in which we additionally sampled the listed nuisance parameters.

Parameter	Fiducial	Test Case A	Test Case B	Test Case C
$\Omega_{\mathrm{m},0}$	$0.252^{+0.043}_{-0.062}$	$0.245^{+0.040}_{-0.052}$	$0.249^{+0.046}_{-0.059}$	$0.285^{+0.072}_{-0.099}$
$\Omega_{\mathrm{b},0}$	$0.049^{+0.012}_{-0.013}$	0.0484 ± 0.013	$0.0477^{+0.011}_{-0.013}$	$0.0491^{+0.012}_{-0.013}$
h	0.72 ± 0.11	$0.73^{+0.11}_{-0.10}$	0.74 ± 0.12	0.72 ± 0.12
n_{s}	$0.988^{+0.054}_{-0.051}$	$0.986^{+0.066}_{-0.057}$	$0.99^{+0.062}_{-0.050}$	$0.973^{+0.064}_{-0.065}$
$10^9 A_{\mathrm{s}}$	$3.03^{+1.4}_{-1.2}$	$2.92^{+1.1}_{-1.2}$	3.02 ± 1.3	$3.02^{+1.3}_{-1.2}$
σ_8	$0.838^{+0.1}_{-0.085}$	$0.859^{+0.096}_{-0.088}$	$0.857^{+0.11}_{-0.097}$	0.912 ± 0.11
S_8	$0.755^{+0.020}_{-0.018}$	$0.767^{+0.019}_{-0.020}$	$0.768^{+0.021}_{-0.020}$	$0.874^{+0.120}_{-0.150}$
$\log_{10} T_{\mathrm{AGN}}$	$-$	$7.13^{+0.40}_{-0.49}$	$7.16^{+0.42}_{-0.52}$	$7.32^{+0.51}_{-0.60}$
$\mathcal{A}_{\mathrm{IA}}$	$-$	$-$	$-0.07^{+3.7}_{-3.9}$	$-0.4^{+3.7}_{-4.1}$
Δz	$-$	$-$	$-$	$-0.13^{+0.21}_{-0.16}$

Table 9.2. Table of mean and 1σ values of the sampled cosmological and nuisance parameters for each of the cases, for a redshift distribution blind A.

which works to widen the width of the contour in the $\sigma_8 - \Omega_m$ plane, consequently enlarging the S_8 posterior. We can also see this reflected in the strong degeneracy of the $\Delta z - S_8$ plane. Hence this demonstrates the importance of accurately estimating the galaxy redshift distribution, as it substantially impacts the theoretical modelling of the weak lensing kernel and can induce a bias in our results. However, since these results are still blinded, we will not comment on their accuracy.

We also see that the amplitude of the IA contribution, $\mathcal{A}_{\mathrm{IA}}$, is not well constrained with only 1 tomographic bin. We expect to be able to achieve tighter constraints with a tomographic analysis.

A possible cross-check to validate our results would be to conduct the analysis using the angular power spectra $C(\ell)$ in harmonic space, which although contains the same information of the shear field, is sensitive to different scales and systematic effects, hence yielding complementary information to its real space counterpart.

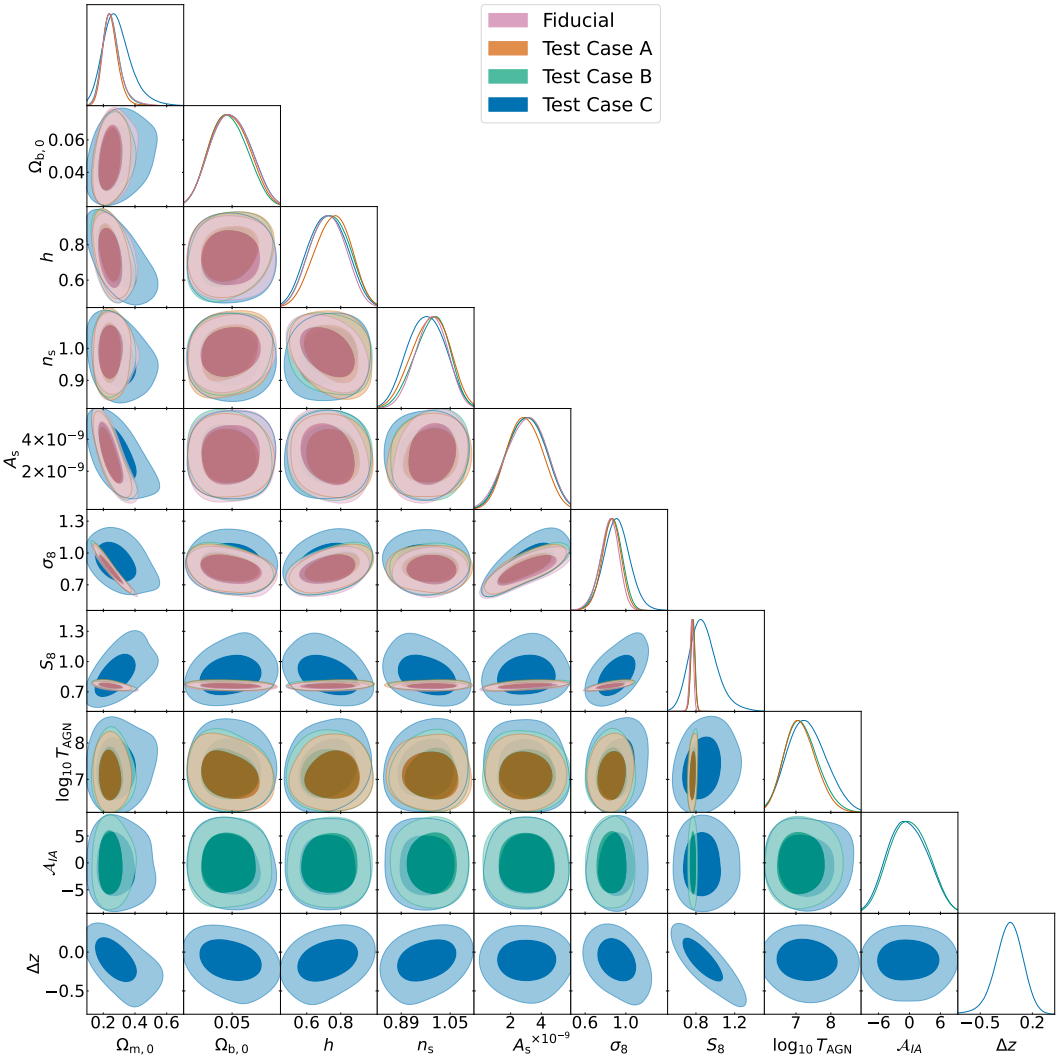

Fig. 9.4. 2D marginalised distributions of the sampled cosmological and nuisance parameters (assuming an $n(z)$ blind A), for a fiducial cosmological test case (pink), as well as test cases A (orange), B (green) and C (blue). Please note that these results are preliminary and subject to change.

IN BRIEF

In this Chapter, I have introduced UNIONS, a survey bringing together data from 3 different telescopes in Hawaii, which will deliver ground-based photometric data in the optical $ugriz$ bands in the northern hemisphere. It is one of the last Stage III surveys which, when completed, will provide a galaxy catalogue covering the largest area in the northern hemisphere to date. I especially highlight the work that I have been carrying out as a member of this collaboration, in terms of the development of the likelihood inference pipeline that will be used to derive cosmological constraints with UNIONS weak lensing data. This entails deriving the cosmic shear 2PCFs, the covariance matrices and the redshift distributions, and finally running the inference step using `CosmoSIS` to obtain preliminary cosmological constraints.

This is the first time cosmological weak lensing analysis is being conducted on data from UNIONS, and my contributions have been integral in this regard. With the launch of Stage IV surveys such as *Euclid* and LSST, cosmology with UNIONS could thus prove to be a fitting bridge to usher in a new era of weak lensing science.

10. Conclusions

The topic of my PhD involves exploring a novel parametrisation for a class of modified ΛCDM models, the *tomographic CDE model*, and probing it with LSS data from the *Euclid* satellite. This thesis has thus striven to achieve such a goal. To begin, I laid out the groundwork in Chapter 3 by expounding the relevant theoretical background of cosmology, such as the FLRW metric and the Friedmann Equations governing the evolution of the background matter-energy densities. After which, in Chapter 4, I discussed various cosmological probes, specifically that of weak lensing, galaxy clustering, 3x2pt and the Cosmic Microwave Background, as well as common statistical techniques employed in cosmological analyses.

With the stage now set, I moved on to introduce a novel parametrisation of the CDE model in Chapter 5, which I term a *tomographic CDE model*, and assessed its potential constraints from datasets encompassing a range of redshifts, particularly focusing on that which could be obtained with LSS probes. I found promising results whereby LSS data could deliver tight constraints on the strength of the scalar field-dark matter coupling parameter at low redshifts, comparable to that of the CMB at early times.

Hence I further expanded our investigations by exploring various applications of a tomographic CDE model : in Chapter 6, I introduced a subclass known as an ECQ model, where we restricted the coupling to only be activated during primordial times, which has interesting physical implications such as the formation of objects that could be potential candidates of dark matter. I found that for the first time, we were able to use observational data to verify an important relationship between the allowed strength of early time coupling and the redshift at which it is deactivated, which up till now has only been derived from first principles. In Chapter 7, I subsequently turned to machine learning techniques, by assessing its capabilities in differentiating between LSS data generated from a ΛCDM model as opposed to a tomographic CDE model. This exercise proved notable in demonstrating the validity of employing machine learning techniques in upcoming Stage IV survey analyses.

Having established this new tomographic CDE model, I shifted my sights to the data : specifically, data from upcoming surveys and the potential it has in constraining beyond-ΛCDM physics. With this in mind, I delved into the realm of observa-

tional cosmology in Chapters 8 and 9, where I detailed my contributions to the current galaxy collaboration *Euclid* and UNIONS respectively. Within the *Euclid* Consortium, I helped develop the official likelihood code CLOE, implementing features such as a `CosmoSIS` wrapper and spectroscopic magnification bias effects. I also worked on obtaining forecasts with *Euclid* data using CLOE, where we found that next-stage LSS data could deliver unprecedented precision in our analysis of cosmological constraints. Within the UNIONS collaboration, I am leading the efforts in developing a likelihood analysis pipeline for UNIONS cosmic shear data, where I have worked to obtain preliminary cosmological results with UNIONS cosmic shear data. These findings complement those of current Stage III surveys and pave the way for the exciting results that we can expect with current and upcoming Stage IV surveys.

10.1 Future Outlook

Looking ahead, the future holds much promise, and I foresee various potential extensions of my work.

10.1.1 Modelling the Nonlinear Power Spectrum in Tomographic CDE Models

Firstly, a natural step would be to develop a nonlinear prescription for the matter power spectrum in a tomographic CDE model. At small scales, astrophysical effects become dominant : active galactic nuclei eject baryons outside the dark matter haloes, leading to a suppression of the matter power spectrum [249]. Current LSS data, especially cosmic shear, contain valuable information on matter overdensities at the small scales [250], thus an accurate recipe is needed in order to ensure such effects are adequately accounted for [251]. Currently, emulators and fitting functions have been developed to model the nonlinear power spectrum in a constant CDE framework [252]. However, this is not the case for a tomographic CDE model. Therefore a possible avenue of extension would be to further develop these methods to include a tomographic CDE models as well.

10.1.2 Cosmology with 3x2pt UNIONS Data

With the full 4800deg^2 dataset of UNIONS estimated to be complete within the next two years, it will be the largest photometric survey in the northern hemisphere in five optical bands to date. Thus the next step would be to conduct cosmological

parameter inference with UNIONS tomographic cosmic shear data, and not just for one redshift bin. This would allow us to obtain improved constraints by breaking parameter degeneracies [253, 254]. It would also be of interest to cross-correlate UNIONS data with that of surveys like DESI or *Euclid* to carry out a 3x2pt analysis.

10.1.3 Extended ΛCDM Models with *Euclid* DR1

Forecasts have shown that *Euclid* will be able to put constraints on cosmological parameters like the dark energy EoS $w(z)$ at 0.1%, and the growth index $\gamma_{\rm g}$ at 0.08% uncertainty [255], thus ushering a new era of precision cosmology. With the first data release of *Euclid* slated for 2025, I hope to be able to continue developing CLOE in preparation for DR1, possibly even deriving constraints on extended ΛCDM models. In light of recent interesting results from another Stage IV survey DESI [256], it would be exciting to see if *Euclid* will reaffirm these findings, potentially unveiling new knowledge about our Universe.

In this PhD, I have just begun embarking on the humbling journey of exploring our Universe, and I believe that I still have much to learn and explore. I hope that this thesis has fairly demonstrated my efforts in this regard, paving the way for more exciting science to come.

A. Tomographic CDE Best Fit Cosmological Parameters

Here we present the tables with the best-fit, mean and 68% C.L. values for the various models we have tested.

3-bin Tomographic β						
	Planck (constant β)		**Planck**		**Planck +PlanckLens**	
Parameter	Best-Fit	Mean$\pm\sigma$	Best-Fit	Mean$\pm\sigma$	Best-Fit	Mean$\pm\sigma$
$100\,\omega_{\rm b}$	2.248	$2.241^{+0.018}_{-0.019}$	2.235	$2.252^{+0.020}_{-0.020}$	2.256	$2.244^{+0.022}_{-0.023}$
$\omega_{\rm DM}$	0.118	0.119 ± 0.002	0.121	$0.120^{+0.003}_{-0.004}$	0.119	$0.120^{+0.003}_{-0.004}$
$\ln 10^{10} A_s$	3.042	$3.048^{+0.014}_{-0.015}$	3.046	$3.049^{+0.018}_{-0.021}$	3.051	$3.051^{+0.026}_{-0.026}$
$n_{\rm s}$	0.970	0.967 ± 0.005	0.966	0.971 ± 0.007	0.972	$0.971^{+0.005}_{-0.004}$
$\tau_{\rm reio}$	0.052	$0.056^{+0.008}_{-0.009}$	0.053	$0.057^{+0.009}_{-0.012}$	0.054	$0.057^{+0.012}_{-0.013}$
σ_8	0.829	$0.822^{+0.013}_{-0.015}$	0.820	$0.825^{+0.014}_{-0.017}$	0.813	$0.817^{+0.013}_{-0.015}$
S_8	0.819	$0.829^{+0.023}_{-0.026}$	0.839	$0.831^{+0.033}_{-0.043}$	0.821	$0.828^{+0.018}_{-0.026}$
H_0	69.17	$68.15^{+1.21}_{-1.43}$	67.62	$68.51^{+1.42}_{-1.17}$	68.02	$67.93^{+0.97}_{-0.77}$
β_1	0.03	< 0.023	0.018	< 0.031	0.0	< 0.014
β_2	–	–	0.014	< 0.029	0.004	< 0.027
β_3	–	–	0.02	< 0.026	0.024	< 0.024
	Planck +ACT1800		**Planck +ACT1800+SPT**		**Planck650 +ACT+SPT**	
Parameter	Best-Fit	Mean$\pm\sigma$	Best-Fit	Mean$\pm\sigma$	Best-Fit	Mean$\pm\sigma$
$100\,\omega_{\rm b}$	2.247	$2.246^{+0.020}_{-0.022}$	2.258	$2.245^{+0.012}_{-0.014}$	2.229	2.250 ± 0.014
$\omega_{\rm DM}$	0.119	$0.119^{+0.003}_{-0.004}$	0.116	$0.119^{+0.002}_{-0.001}$	0.120	$0.118^{+0.002}_{-0.002}$
$\ln 10^{10} A_s$	3.069	$3.057^{+0.021}_{-0.022}$	3.052	$3.056^{+0.012}_{-0.014}$	3.043	$3.047^{+0.012}_{-0.014}$
$n_{\rm s}$	0.974	0.971 ± 0.005	0.973	0.973 ± 0.004	0.976	0.977 ± 0.005
$\tau_{\rm reio}$	0.058	$0.057^{+0.008}_{-0.009}$	0.053	$0.056^{+0.007}_{-0.008}$	0.051	0.055 ± 0.006
σ_8	0.86	$0.837^{+0.023}_{-0.028}$	0.841	$0.832^{+0.011}_{-0.014}$	0.819	$0.814^{+0.008}_{-0.009}$
S_8	0.843	$0.832^{+0.022}_{-0.033}$	0.811	$0.828^{+0.014}_{-0.016}$	0.842	0.8193 ± 0.018
H_0	69.89	$69.17^{+1.75}_{-1.65}$	70.48	$68.98^{+0.79}_{-1.03}$	66.99	$68.07^{+0.63}_{-0.71}$
β_1	0.027	< 0.042	0.057	< 0.033	0.031	< 0.059
β_2	0.03	< 0.037	0.036	< 0.029	0.042	< 0.042
β_3	0.112	< 0.036	0.066	< 0.066	0.071	< 0.068

Table A.1. Table of best-fit, mean and 68% C.L. values of the various cosmological parameters of the 3-bin tomographic model, for the CMB datasets Planck, Planck+ACT1800, Planck+ACT1800+SPT and Planck650+ACT+SPT. We also include the case of a constant coupling model using Planck data. For reference, the binning is defined by edges $z = \{0, 100, 1000\}$. In the last two rows, we include the $\Delta\chi^2 = \chi^2_{\rm min,cde} - \chi^2_{\rm min,\Lambda CDM}$ difference for each model (constant and tomographic CDE) and dataset, compared with ΛCDM using the same dataset, as well as the logarithm of the Bayes factor $\ln B = \ln E_{\rm CDE} - \ln E_{\Lambda\rm CDM}$ for one chosen dataset.

7-bin Tomographic β										
	Planck+ACT1800 +SPT+BSC (constant β)		**Planck+ACT1800 +SPT+BSC**		**Planck+ACT1800 +SPT+BSC RSD**		**Planck+ACT1800 +SPT+BSC SH0ES**		**Planck+ACT1800 +SPT+BSC RSD+SH0ES**	
Parameter	Best-Fit	Mean$\pm\sigma$	Best-Fit	Mean$\pm\sigma$	Best-Fit	Mean$\pm\sigma$	Best-Fit	Mean$\pm\sigma$	Best-Fit	Mean$\pm\sigma$
$100\,\omega_{\rm b}$	2.235	$2.244^{+0.012}_{-0.016}$	2.254	2.239 ± 0.014	2.239	$2.246^{+0.014}_{-0.013}$	2.235	$2.241^{+0.012}_{-0.010}$	2.252	$2.247^{+0.011}_{-0.013}$
$\omega_{\rm DM}$	0.117	$0.1178^{+0.0012}_{-0.0008}$	0.1172	$0.116^{+0.0022}_{-0.0015}$	0.1167	$0.1169^{+0.0014}_{-0.0009}$	0.1154	0.1167 ± 0.0008	0.1162	0.1159 ± 0.0011
$\ln 10^{10} A_{\rm s}$	3.047	$3.055^{+0.015}_{-0.017}$	3.047	$3.052^{+0.014}_{-0.015}$	3.030	$3.050^{+0.013}_{-0.015}$	3.046	$3.052^{+0.013}_{-0.015}$	3.050	$3.044^{+0.015}_{-0.020}$
$n_{\rm s}$	0.976	$0.971^{+0.005}_{-0.004}$	0.972	$0.970^{+0.005}_{-0.004}$	0.974	0.972 ± 0.005	0.969	0.969 ± 0.003	0.974	$0.972^{+0.004}_{-0.003}$
$\tau_{\rm reio}$	0.055	$0.058^{+0.006}_{-0.009}$	0.054	$0.054^{+0.007}_{-0.008}$	0.05	$0.057^{+0.007}_{-0.006}$	0.054	0.055 ± 0.007	0.057	$0.053^{+0.007}_{-0.009}$
σ_8	0.821	$0.818^{+0.010}_{-0.011}$	0.832	$0.845^{+0.013}_{-0.022}$	0.807	$0.822^{+0.003}_{-0.011}$	0.83	$0.834^{+0.010}_{-0.010}$	0.817	$0.828^{+0.012}_{-0.014}$
S_8	0.815	$0.817^{+0.014}_{-0.010}$	0.832	$0.834^{+0.015}_{-0.017}$	0.801	$0.814^{+0.010}_{-0.011}$	0.803	$0.818^{+0.010}_{-0.011}$	0.802	$0.809^{+0.011}_{-0.013}$
H_0	68.73	$68.49^{+0.46}_{-0.56}$	68.27	68.86 ± 0.59	68.51	$68.85^{+0.38}_{-0.60}$	70.06	$69.5^{+0.45}_{-0.43}$	69.18	$69.51^{+0.46}_{-0.55}$
β_1	0.023	$0.015^{+0.005}_{-0.014}$	0.185	$0.146^{+0.075}_{-0.081}$	0.03	$0.027^{+0.005}_{-0.026}$	0.014	< 0.017	0.01	< 0.038
β_2	$-$	$-$	0.036	< 0.124	0.057	< 0.015	0.033	$0.028^{+0.010}_{-0.023}$	0.088	< 0.038
β_3	$-$	$-$	0.078	< 0.094	0.012	$0.064^{+0.018}_{-0.023}$	0.019	$0.041^{+0.016}_{-0.016}$	0.051	< 0.048
β_4	$-$	$-$	0.024	< 0.031	0.031	< 0.016	0.067	$0.058^{+0.018}_{-0.015}$	0.03	< 0.041
β_5	$-$	$-$	0.005	< 0.028	0.054	$0.031^{+0.010}_{-0.011}$	0.055	$0.050^{+0.011}_{-0.013}$	0.008	< 0.048
β_6	$-$	$-$	0.029	< 0.054	0.011	$0.030^{+0.011}_{-0.019}$	0.022	< 0.027	0.048	< 0.049
β_7	$-$	$-$	0.059	$0.063^{+0.023}_{-0.054}$	0.001	< 0.018	0.006	$0.022^{+0.010}_{-0.014}$	0.03	< 0.042

Table A.2. Table of best-fit, mean and 68% C.L. values of the various cosmological parameters of the 7-bin tomographic model, using the baseline CMB dataset with a cut in ACT, i.e. Planck+ACT1800+SPT, in combination with BSC, BSC+RSD, BSC+SH0ES or BSC+RSD+SH0ES. The binning is defined in this case by edges $z = \{0, 1, 2, 5, 100, 500, 1000\}$. In the last two rows, we include the $\Delta\chi^2 = \chi^2_{\rm min,CDE} - \chi^2_{\rm min,\Lambda CDM}$ difference for each model (constant and tomographic CDE) and dataset, compared with ΛCDM using the same dataset, as well as the logarithm of the Bayes factor $\ln B = \ln E_{\rm CDE} - \ln E_{\Lambda\rm CDM}$ for one chosen dataset.

7-bin Tomographic β								
	Planck650+ACT +SPT+BSC (constant β)		**Planck650+ACT +SPT+BSC**		**Planck650+ACT +SPT+BSC+RSD**		**Planck650+ACT +SPT+BSC+SHoES**	
Parameter	Best-Fit	Mean$\pm\sigma$	Best-Fit	Mean$\pm\sigma$	Best-Fit	Mean$\pm\sigma$	Best-Fit	Mean$\pm\sigma$
$100\,\omega_{\rm b}$	2.263	$2.252^{+0.011}_{-0.012}$	2.251	2.247 ± 0.012	2.252	$2.255^{+0.012}_{-0.011}$	2.245	$2.239^{+0.017}_{-0.015}$
$\omega_{\rm DM}$	0.1175	0.1178 ± 0.0009	0.1172	$0.1157^{+0.0028}_{-0.0013}$	0.1171	$0.1165^{+0.0010}_{-0.0008}$	0.1173	$0.1153^{+0.0029}_{-0.0019}$
$\ln 10^{10} A_{\rm s}$	3.05	3.052 ± 0.005	3.049	$3.048^{+0.011}_{-0.013}$	3.036	$3.035^{+0.010}_{-0.012}$	3.064	$3.059^{+0.013}_{-0.018}$
$n_{\rm s}$	0.977	0.976 ± 0.005	0.975	0.977 ± 0.008	0.978	0.978 ± 0.004	0.973	0.971 ± 0.004
$\tau_{\rm reio}$	0.058	$0.057^{+0.004}_{-0.003}$	0.054	0.054 ± 0.006	0.051	$0.050^{+0.005}_{-0.006}$	0.057	$0.057^{+0.006}_{-0.008}$
σ_8	0.808	$0.816^{+0.003}_{-0.009}$	0.834	$0.844^{+0.015}_{-0.022}$	0.808	$0.813^{+0.007}_{-0.009}$	0.868	$0.870^{+0.020}_{-0.032}$
S_8	0.805	0.815 ± 0.010	0.828	$0.829^{+0.013}_{-0.017}$	0.802	0.803 ± 0.01	0.848	$0.842^{+0.015}_{-0.027}$
H_0	68.57	$68.47^{+0.45}_{-0.51}$	68.76	$69.10^{+0.46}_{-0.51}$	68.67	$68.94^{+0.39}_{-0.38}$	69.84	$70.00^{+0.42}_{-0.82}$
β_1	0.0	< 0.016	0.039	< 0.141	0.016	< 0.073	0.08	< 0.127
β_2	$-$	$-$	0.177	< 0.138	0.0	< 0.067	0.097	< 0.137
β_3	$-$	$-$	0.018	< 0.089	0.026	< 0.058	0.008	< 0.100
β_4	$-$	$-$	0.037	< 0.034	0.034	< 0.023	0.039	< 0.05
β_5	$-$	$-$	0.017	< 0.034	0.003	< 0.028	0.040	< 0.051
β_6	$-$	$-$	0.01	< 0.048	0.004	< 0.047	0.001	< 0.058
β_7	$-$	$-$	0.062	< 0.074	0.017	< 0.031	0.124	< 0.108

Table A.3. Table of best-fit, mean and 68% C.L. values of the various cosmological parameters of the 7-bin tomographic model, but using the baseline CMB dataset with a cut in Planck, i.e. Planck650+ACT+SPT. In the last two rows, we include the $\Delta\chi^2 = \chi^2_{\rm min,CDE} - \chi^2_{\rm min,\Lambda CDM}$ difference for each model (constant and tomographic CDE) and dataset, compared with ΛCDM using the same dataset, as well as the logarithm of the Bayes factor $\ln B = \ln E_{\rm CDE} - \ln E_{\Lambda\rm CDM}$ for one chosen dataset.

	Cosmic Shear (ΛCDM)		**Galaxy Clustering$_s$ (ΛCDM)**		**3x2pt (ΛCDM)**	
Parameter	Best-Fit	Mean$\pm\sigma$	Best-Fit	Mean$\pm\sigma$	Best-Fit	Mean$\pm\sigma$
$100\,\omega_{\rm b}$	2.052	$2.257^{+0.216}_{-0.220}$	2.249	$2.233^{+0.226}_{-0.224}$	2.433	$2.241^{+0.249}_{-0.225}$
$\omega_{\rm DM}$	0.139	$0.152^{+0.043}_{-0.055}$	0.129	$0.124^{+0.001}_{-0.010}$	0.136	0.123 ± 0.013
$n_{\rm s}$	0.991	$0.974^{+0.075}_{-0.076}$	0.863	$0.896^{+0.026}_{-0.049}$	0.864	$0.912^{+0.049}_{-0.060}$
H_0	67.37	$72.94^{+5.60}_{-5.50}$	70.21	69.48 ± 2.20	71.63	$69.30^{+2.70}_{-2.60}$
σ_8	0.709	$0.737^{+0.107}_{-0.141}$	0.724	$0.734^{+0.037}_{-0.042}$	0.755	$0.759^{+0.023}_{-0.025}$
S_8	0.770	$0.750^{+0.032}_{-0.022}$	0.734	$0.739^{+0.038}_{-0.041}$	0.772	$0.764^{+0.017}_{-0.014}$
	Cosmic Shear (constant β)		**Galaxy Clustering$_s$ (constant β)**		**3x2pt (constant β)**	
$100\,\omega_{\rm b}$	2.350	$2.436^{+0.151}_{-0.111}$	2.516	2.448 ± 0.049	2.521	$2.478^{+0.047}_{-0.033}$
$\omega_{\rm DM}$	0.1314	$0.1385^{+0.0275}_{-0.0389}$	0.1242	$0.1207^{+0.0050}_{-0.0054}$	0.1205	$0.1196^{+0.0065}_{-0.0055}$
$n_{\rm s}$	0.968	$0.953^{+0.057}_{-0.06}$	0.997	$0.970^{+0.017}_{-0.021}$	0.965	$0.975^{+0.011}_{-0.008}$
H_0	73.47	73.06 ± 5.7	71.02	$70.44^{+1.1}_{-1.2}$	71.75	$71.15^{+1.4}_{-1.3}$
σ_8	0.752	$0.753^{+0.091}_{-0.092}$	0.802	$0.763^{+0.037}_{-0.042}$	0.810	$0.795^{+0.020}_{-0.021}$
S_8	0.735	$0.748^{+0.026}_{-0.023}$	0.797	$0.753^{+0.034}_{-0.038}$	0.787	0.775 ± 0.018
β	0.02	< 0.064	0.002	< 0.019	0.004	$0.015^{+0.007}_{-0.011}$
	Cosmic Shear (4-bin β)		**Galaxy Clustering$_s$ (4-bin β)**		**3x2pt (4-bin β)**	
$100\,\omega_{\rm b}$	2.413	$2.440^{+0.104}_{-0.070}$	2.495	$2.459_{\pm}0.030$	2.294	$2.249^{+0.023}_{-0.024}$
$\omega_{\rm DM}$	0.1231	$0.1319^{+0.0358}_{-0.0445}$	0.1349	$0.1310^{+0.0080}_{-0.0084}$	0.1239	$0.1261^{+0.0049}_{-0.0047}$
$n_{\rm s}$	0.949	$0.981^{+0.029}_{-0.036}$	0.884	$0.902^{+0.025}_{-0.059}$	0.909	0.899 ± 0.008
H_0	71.88	$72.08^{+5.0}_{-5.6}$	71.96	71.18 ± 1.5	70.56	70.03 ± 1.1
σ_8	0.794	$0.753^{+0.111}_{-0.122}$	0.765	$0.772^{+0.048}_{-0.050}$	0.799	$0.772^{+0.020}_{-0.022}$
S_8	0.774	$0.737^{+0.036}_{-0.032}$	0.776	$0.781^{+0.049}_{-0.051}$	0.792	$0.775^{+0.016}_{-0.019}$
β_1	0.059	< 0.151	0.016	< 0.018	0.003	$0.014^{+0.007}_{-0.010}$
β_2	0.22	< 0.166	0.01	< 0.021	0.008	$0.018^{+0.007}_{-0.011}$
β_3	0.09	< 0.154	0.014	< 0.023	0.013	$0.016^{+0.007}_{-0.010}$
β_4	0.029	< 0.107	0.013	$0.016^{+0.007}_{-0.011}$	0.021	$0.015^{+0.006}_{-0.011}$

Table A.4. Table of best-fit, mean and 68% C.L. values of the various cosmological parameters, for weak lensing, spectroscopic galaxy clustering and 3x2pt datasets. We report the results obtained with the ΛCDM, the $\beta =$const. CDE model and the 4-bin tomographic model. For reference, the binning is defined by edges $z = \{0, 0.5, 1, 2\}$. In the last two rows of each model, we include the $\Delta\chi^2 = \chi^2_{\rm min,CDE} - \chi^2_{\rm min,\Lambda CDM}$ difference for each model (constant and tomographic CDE) and dataset, compared with ΛCDM using the same dataset, as well as the logarithm of the Bayes factor $\ln B = \ln E_{\rm CDE} - \ln E_{\Lambda\rm CDM}$ for one chosen dataset.

	Planck+ACT18oo +SPT+BSC+CS (ΛCDM)		**Planck+ACT18oo +SPT+BSC+CS (4-bin β)**	
Parameter	Best-Fit	Mean$\pm\sigma$	Best-Fit	Mean$\pm\sigma$
$100\,\omega_{\rm b}$	2.433	$2.276^{+0.244}_{-0.224}$	2.288	$2.326^{+0.224}_{-0.179}$
$\omega_{\rm DM}$	0.1492	$0.1617^{+0.0562}_{-0.057}$	0.1194	0.1194 ± 0.0008
$n_{\rm s}$	0.925	$0.971^{+0.084}_{-0.081}$	0.974	0.978 ± 0.003
H_0	71.37	$73.3^{+5.8}_{-6.0}$	69.55	$69.66^{+0.34}_{-0.36}$
σ_8	0.727	$0.72^{+0.130}_{-0.145}$	0.831	0.831 ± 0.007
S_8	0.774	$0.744^{+0.034}_{-0.030}$	0.823	$0.822^{+0.010}_{-0.009}$
β_1	$-$	$-$	0.057	$0.056^{+0.022}_{-0.052}$
β_2	$-$	$-$	0.154	< 0.092
β_3	$-$	$-$	0.033	$0.037^{+0.017}_{-0.024}$
β_4	$-$	$-$	0.027	< 0.032

Table A.5. Table of best-fit, mean and 68% C.L. values of the various cosmological parameters, obtained with the dataset Planck+ACT18oo+SPT+BSC+CS, for both a ΛCDM and tomographic CDE model. For reference, the binning is defined by edges $z = \{0, 0.5, 1, 2\}$. In the last two rows, we show the value of $\Delta\chi^2 = \chi^2_{\rm min,CDE} - \chi^2_{\rm min,\Lambda CDM}$, as well as the logarithm of the Bayes factor $\ln B = \ln E_{\rm CDE} - \ln E_{\Lambda\rm CDM}$.

B. Background Evolution of ECQ model

To better understand the individual effect of the coupling strength β, we present in Fig. B.1 additional plots of the energy fractions of the various species and the Hubble function for different values of β and fixed $z_{\rm OFF}$.

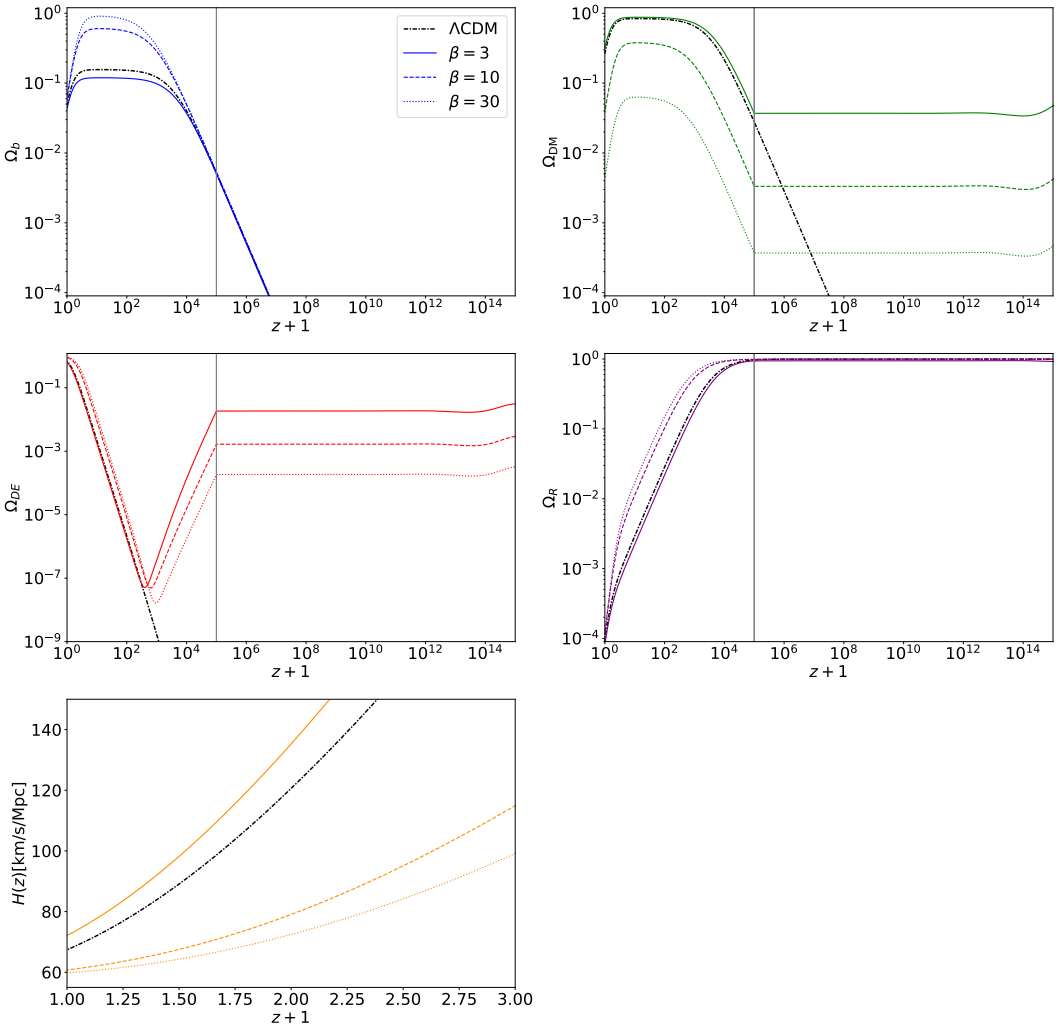

Fig. B.1. Evolution of the various density parameters Ω_i of (clockwise, from top left) : baryons, DM, radiation and the scalar field ϕ, for $\beta = \{3, 10, 30\}$. We fix $\Omega_{\rm b,0} = 0.02237$, $V_0 = 2.64 \cdot 10^{-47}$ GeV^4 and $z_{\rm OFF} = 10^5$. We include the ΛCDM case in black dashed-dotted lines for reference. In the last row we plot the Hubble function $H(z)$ in the redshift range $0 \leq z \leq 2$.

In Figs. B.2 we plot the background evolution of the Ω_i's for values of β and $z_{\rm OFF}$

along the degeneracy line, Eq. (6.16). We see how if we restrict values of β and $z_{\rm OFF}$ along this line, the values of $\Omega_{i,0}$'s are the same. Hence without data that can directly probe the evolution history at such high redshifts, these sets of β and $z_{\rm OFF}$ values are virtually indistinguishable.

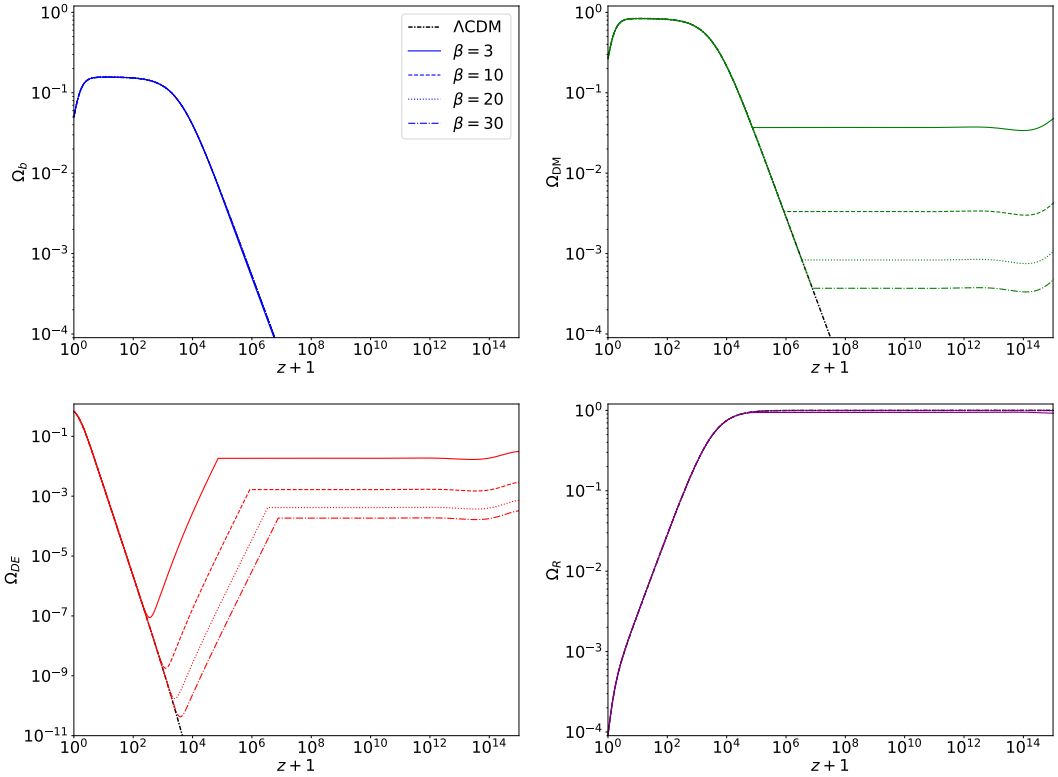

Fig. B.2. Evolution of the various density parameters Ω_i of (clockwise, from top left) : baryons, DM, radiation and the scalar field ϕ, for values of $\beta = \{3, 10, 20, 30\}$ and $z_{\rm OFF}$ on the corresponding degeneracy line, Eq. (6.16).

C. Additional Parameter Constraints on *Euclid* data with CLOE

We report in Table C.1 the mean and 1σ constraints on all the sampled cosmological parameters for the models and probes presented in Sec. 8.3.4.

In Figs. C.1−C.4, we present additional constraints in the form of 2D marginalised posteriors on the various nuisance parameters for the weak lensing (WL) and 3x2pt probes, for both ΛCDM and w_0w_aCDM models. We see that we are able to recover the fiducial values for all cases.

Parameter	Λ**CDM** (WL)	Λ**CDM** (3x2pt)	Λ**CDM** (GCsp)	w_0w_a**CDM** (WL)	w_0w_a**CDM** (3x2pt)
$\Omega_{\mathrm{m},0}$	0.317 ± 0.008	0.32 ± 0.001	0.32 ± 0.006	$0.322^{+0.027}_{-0.025}$	0.321 ± 0.004
H_0	$68.80^{+3.70}_{-3.50}$	$67.50^{+0.57}_{-0.59}$	$67.30^{+0.5}_{-0.52}$	$67.7^{+4.20}_{-4.60}$	67.30 ± 0.71
n_s	$0.949^{+0.037}_{-0.059}$	$0.964^{+0.0063}_{-0.006}$	0.967 ± 0.012	$0.963^{+0.048}_{-0.052}$	$0.965^{+0.0064}_{-0.0065}$
$10^9 A_\mathrm{s}$	$2.04^{+0.19}_{-0.29}$	2.08 ± 0.04	2.11 ± 0.05	$2.09 - 0.3^{+0.22}$	2.08 ± 0.04
σ_8	0.819 ± 0.0099	0.816 ± 0.0012	0.818 ± 0.01	$0.815^{+0.022}_{-0.026}$	0.815 ± 0.0031
S_8	$0.842^{+0.0028}_{-0.0034}$	$0.843^{+0.00085}_{-0.00087}$	0.844 ± 0.015	$0.842^{+0.014}_{-0.012}$	$0.843^{+0.0021}_{-0.0022}$
w_0	$-$	$-$	$-$	$-0.98^{+0.32}_{-0.21}$	-0.99 ± 0.05
w_a	$-$	$-$	$-$	$-0.15^{+0.68}_{-0.80}$	-0.05 ± 0.16
Parameter	Λ**CDM** $+\gamma_g$ (WL)	Λ**CDM** $+\gamma_g$ (3x2pt)	Λ**CDM** $+\Omega_k$ (WL)	Λ**CDM** $+\Omega_k$ (3x2pt)	w_0w_a**CDM** $+\Omega_k$ (3x2pt)
$\Omega_{\mathrm{m},0}$	$0.319^{+0.009}_{-0.010}$	0.32 ± 0.001	$0.319^{+0.008}_{-0.009}$	0.32 ± 0.001	0.321 ± 0.004
H_0	$68.40^{+4.60}_{-3.80}$	$67.40^{+0.6}_{-0.61}$	$68.50^{+4.5}_{-3.60}$	$67.20^{+0.64}_{-0.63}$	$67.30^{+0.68}_{-0.75}$
n_s	$0.954^{+0.026}_{-0.084}$	$0.965^{+0.0068}_{-0.0066}$	$0.954^{+0.025}_{-0.084}$	$0.968^{+0.0075}_{-0.0078}$	0.965 ± 0.0067
$10^9 A_\mathrm{s}$	$2.05^{+0.20}_{-0.33}$	2.09 ± -0.04	$2.08 - 0.31^{+0.21}$	$2.09^{+0.04}_{-0.05}$	2.08 ± 0.04
σ_8	0.816 ± 0.016	0.816 ± 0.001	0.819 ± 0.015	0.816 ± 0.001	0.815 ± 0.003
S_8	0.842 ± 0.007	0.842 ± 0.002	$0.844^{+0.008}_{-0.009}$	0.843 ± 0.001	0.843 ± 0.002
w_0	$-$	$-$	$-$	$-$	$-0.99^{+0.04}_{-0.05}$
w_a	$-$	$-$	$-$	$-$	$-0.06^{+0.18}_{-0.16}$
γ_g	$0.553^{+0.055}_{-0.063}$	0.554 ± 0.015	$-$	$-$	$-$
Ω_k	$-$	$-$	0.0041 ± 0.033	$-0.0029^{+0.0054}_{-0.0056}$	-0.0003 ± 0.011

Table C.1. Table of mean and 1σ values of the cosmological parameters, for the various model+probe combinations as reported in Sec. 8.3.4.

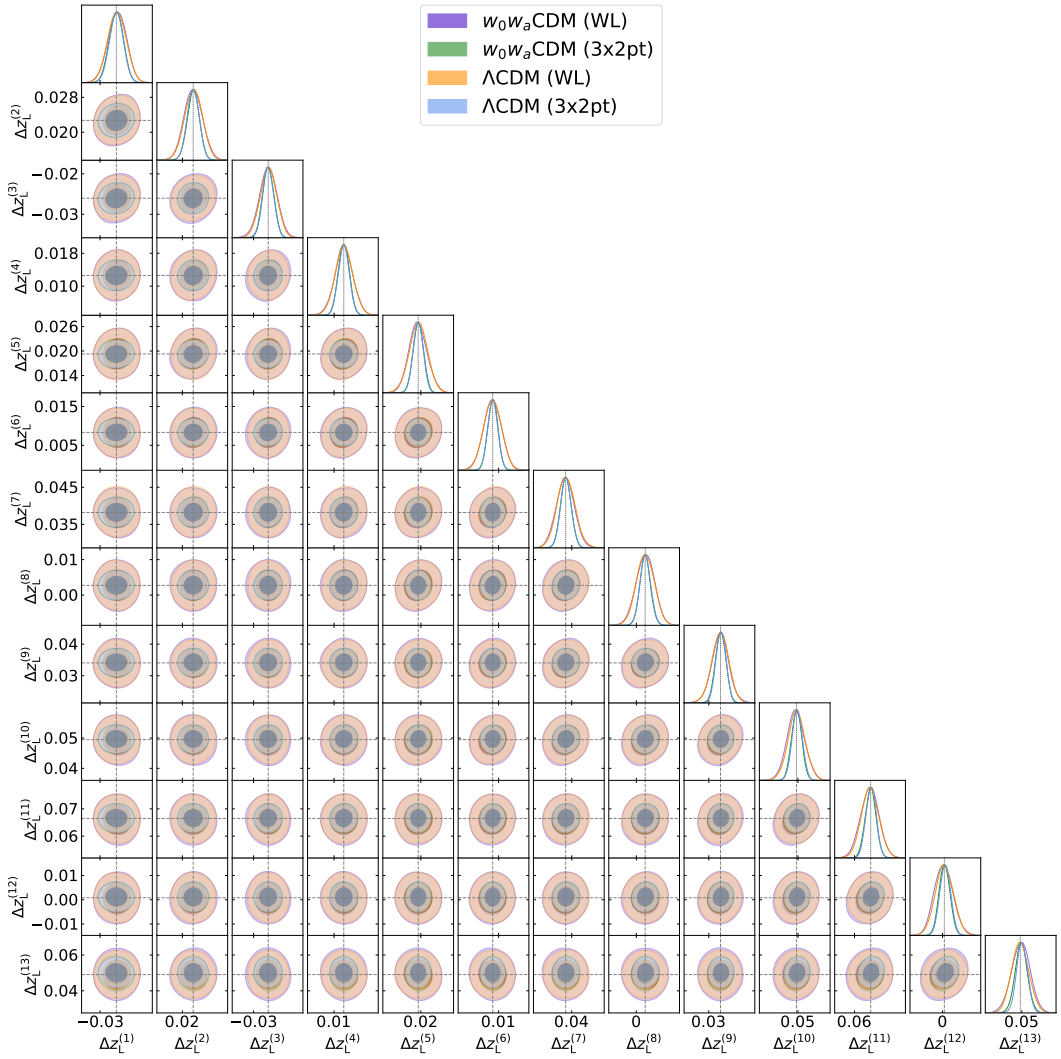

Fig. C.1. 2D marginalised contours of the per-bin mean redshift shift, $\Delta z^{(i)}$ of the 13 photometric redshift bins, for the model+probe combinations of w_0w_aCDM (WL) (purple), w_0w_aCDM (3x2pt) (green), ΛCDM (WL) (yellow) and ΛCDM (3x2pt) (blue). The fiducial values are marked out with grey lines. Please note that these results are preliminary and subject to change.

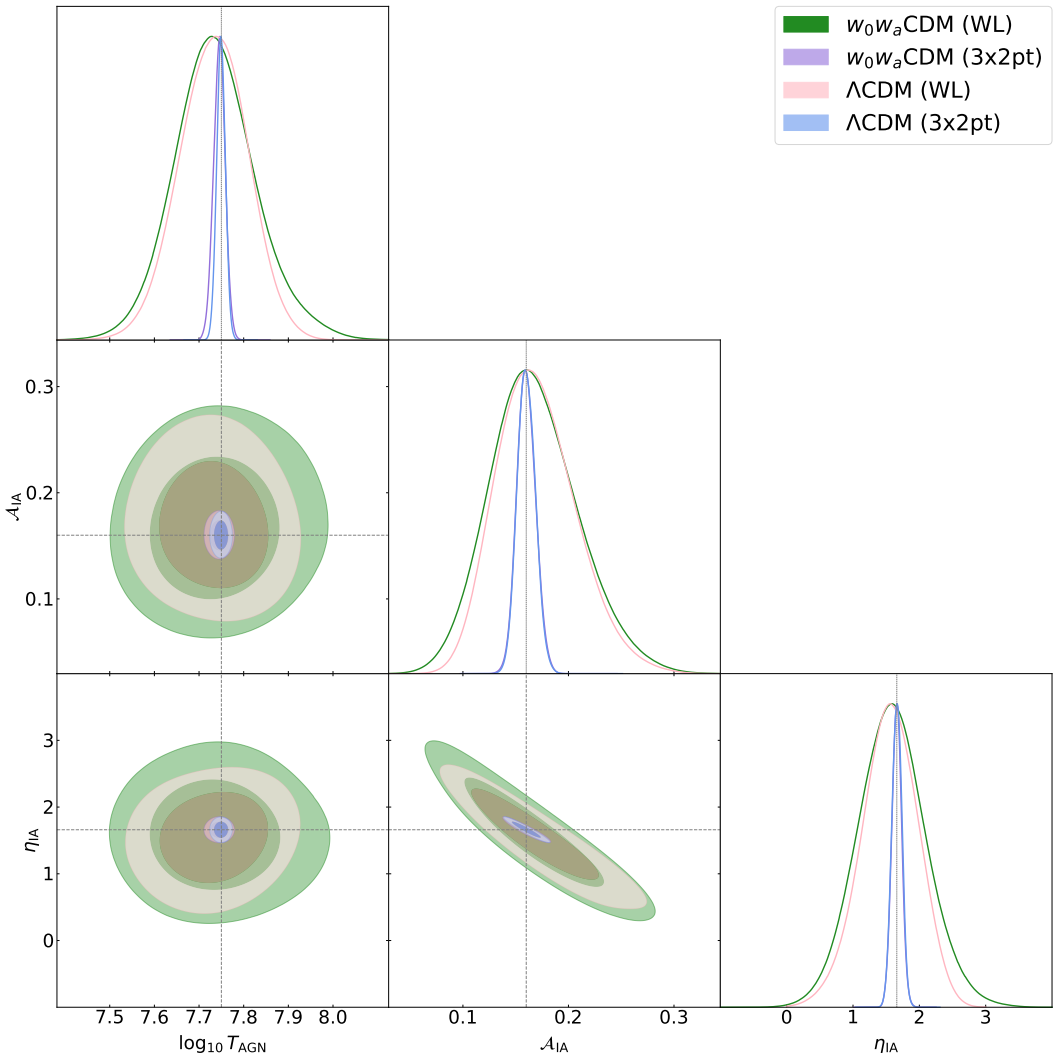

Fig. C.2. 2D marginalised contours of the HMCode feedback efficiency parameter $\log_{10} T_{\rm AGN}$ and IA parameters ($\mathcal{A}_{IA}$ and η_{IA}), for the model+probe combinations of w_0w_aCDM (WL) (green), w_0w_aCDM (3x2pt) (purple), ΛCDM (WL) (pink) and ΛCDM (3x2pt) (blue). The fiducial values are marked out with grey lines. Please note that these results are preliminary and subject to change.

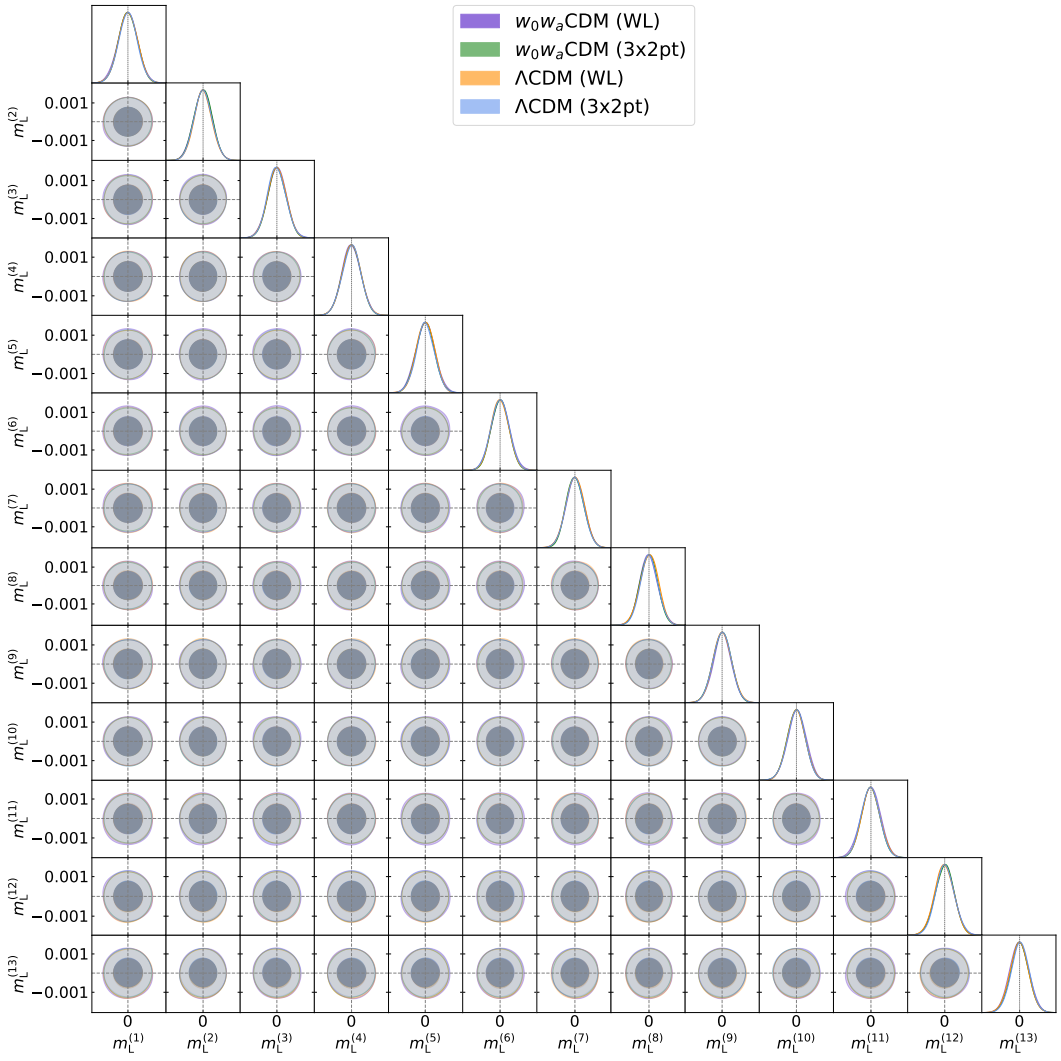

Fig. C.3. 2D marginalised contours of the per-bin multiplicative bias, $m^{(i)}$ of the 13 photometric redshift bins, for the model+probe combinations of w_0w_aCDM (WL) (purple), w_0w_aCDM (3x2pt) (green), ΛCDM (WL) (yellow) and ΛCDM (3x2pt) (blue). The fiducial values are marked out with grey lines. Please note that these results are preliminary and subject to change.

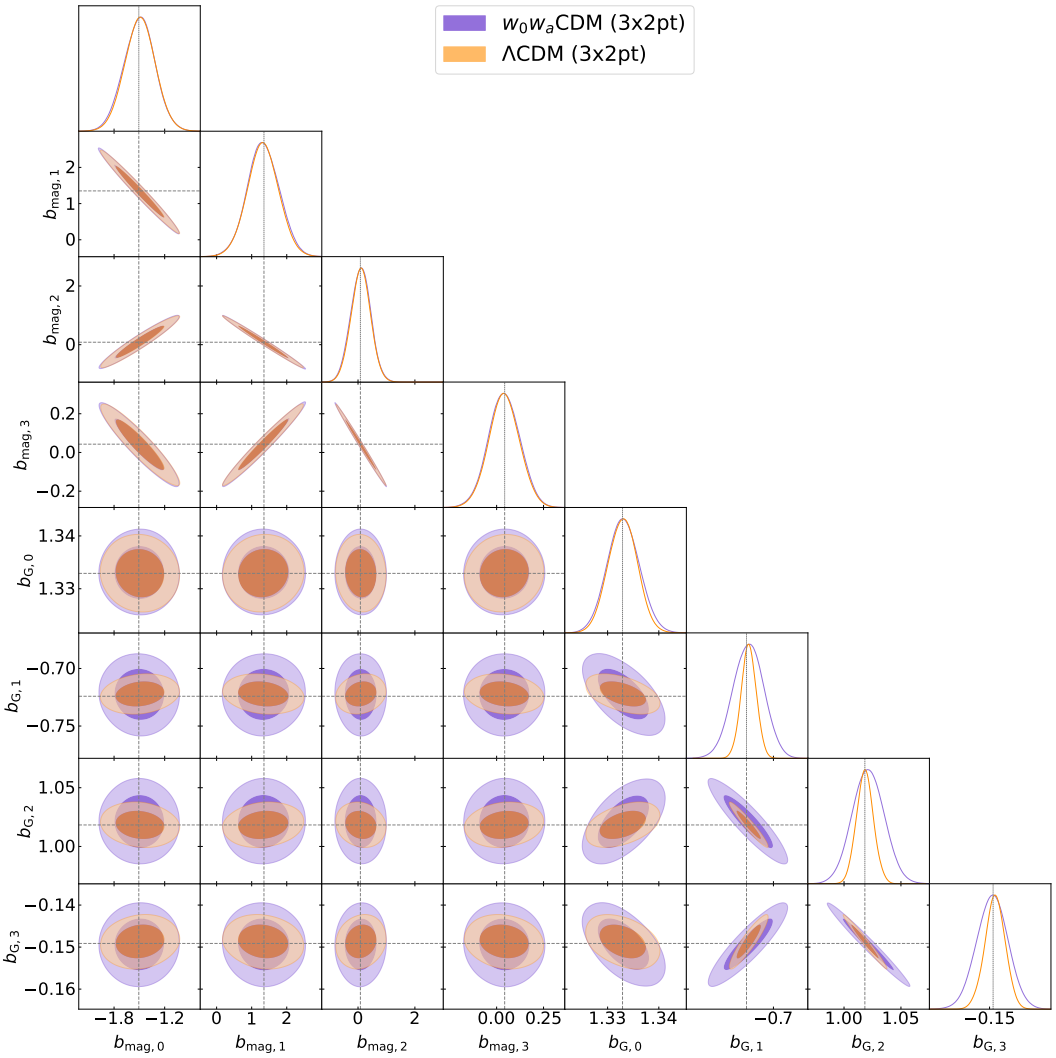

Fig. C.4. 2D marginalised contours of the coefficients of the cubic polynomial for the photometric clustering ($b_{\mathrm{G,i}}$) and magnification biases ($b_{\mathrm{mag,i}}$), for the model+probe combinations of w_0w_aCDM (3x2pt) (purple) and ΛCDM (3x2pt) (orange). The fiducial values are marked out with grey lines. Please note that these results are preliminary and subject to change.

Bibliographie

[1] A. Einstein. “Die Grundlage der allgemeinen Relativitätstheorie”. In : *Annalen der Physik* 354.7 (1916), p. 769-822. doi : https://doi.org/10.1002/andp.19163540702. eprint : https://onlinelibrary.wiley.com/doi/pdf/10.1002/andp.19163540702. url : https://onlinelibrary.wiley.com/doi/abs/10.1002/andp.19163540702.

[2] Scott Dodelson. *Modern Cosmology*. Academic Press, Elsevier Science, 2003.

[3] A. G. Riess et al. “Observational evidence from supernovae for an accelerating universe and a cosmological constant”. In : *Astron. J.* 116 (1998), p. 1009-1038. doi : 10.1086/300499. arXiv : astro-ph/9805201.

[4] S. Perlmutter et al. “Discovery of a supernova explosion at half the age of the Universe”. In : 391.6662 (jan. 1998), p. 51-54. doi : 10.1038/34124. arXiv : astro-ph/9712212 [astro-ph].

[5] V. C. Rubin et Jr. Ford W. K. “Rotation of the Andromeda Nebula from a Spectroscopic Survey of Emission Regions”. In : *Astrophys. J.* 159 (fév. 1970), p. 379. doi : 10.1086/150317.

[6] G. F. Smoot et al. “Structure in the COBE Differential Microwave Radiometer First-Year Maps”. In : *Astrophys. J.* 396 (sept. 1992), p. L1. doi : 10.1086/186504.

[7] M. Chevallier et D. Polarski. “Accelerating universes with scaling dark matter”. In : *Int. J. Mod. Phys. D* 10 (2001), p. 213-224. doi : 10.1142/S0218271801000822. arXiv : gr-qc/0009008.

[8] E. V. Linder. “Exploring the Expansion History of the Universe”. In : *Phys. Rev. Lett.* 90 (9 mars 2003), p. 091301. doi : 10.1103/PhysRevLett.90.091301. url : https://link.aps.org/doi/10.1103/PhysRevLett.90.091301.

[9] G. Zhao et al. “Dynamical dark energy in light of the latest observations”. In : *Nature Astron.* 1.9 (2017), p. 627-632. doi : 10.1038/s41550-017-0216-z. arXiv : 1701.08165 [astro-ph.CO].

[10] Edmund J. Copeland, M. Sami et Shinji Tsujikawa. “Dynamics of dark energy”. In : *Int. J. Mod. Phys. D* 15 (2006), p. 1753-1936. doi : 10.1142/S021827180600942X. arXiv : hep-th/0603057.

[11] P. J. E. Peebles. *Principles of Physical Cosmology*. 1993. doi : 10.1515/9780691206721.

[12] O. Lahav et al. “Dynamical effects of the cosmological constant.” In : *Mon. Not. Roy. Astron. Soc.* 251 (juill. 1991), p. 128-136. doi : 10.1093/mnras/251.1.128.

[13] A. H. Guth. “Inflationary universe: A possible solution to the horizon and flatness problems”. In : *Phys. Rev. D* 23.2 (jan. 1981), p. 347-356. doi : 10.1103/PhysRevD.23.347.

[14] A.D. Linde. “A new inflationary universe scenario: A possible solution of the horizon, flatness, homogeneity, isotropy and primordial monopole problems”. In : *Physics Letters B* 108.6 (1982), p. 389-393. issn : 0370-2693. doi : https://doi.org/10.1016/0370-2693(82)91219-9. url : https://www.sciencedirect.com/science/article/pii/0370269382912199.

[15] S. Dodelson. *Modern Cosmology*. Amsterdam : Academic Press, 2003. isbn : 978-0-12-219141-1.

[16] E. Di Valentino et al. “In the realm of the Hubble tension—a review of solutions *”. In : *Classical and Quantum Gravity* 38.15 (juill. 2021), p. 153001. issn : 1361-6382. doi : 10.1088/1361-6382/ac086d. url : http://dx.doi.org/10.1088/1361-6382/ac086d.

[17] N. Aghanim et al. “Planck 2018 results. I. Overview and the cosmological legacy of Planck”. In : *Astronomy & Astrophysics* 641 (2020), A1. doi : 10.1051/0004-6361/201833880. arXiv : 1807.06205 [astro-ph.CO].

[18] S. Aiola et al. “The Atacama Cosmology Telescope: DR4 Maps and Cosmological Parameters”. In : *JCAP* 12 (2020), p. 047. doi : 10.1088/1475-7516/2020/12/047. arXiv : 2007.07288 [astro-ph.CO].

[19] D. Dutcher et al. “Measurements of the E-mode polarization and temperature-E-mode correlation of the CMB from SPT-3G 2018 data”. In : *Phys. Rev. D* 104.2 (2021), p. 022003. doi : 10.1103/PhysRevD.104.022003. arXiv : 2101.01684 [astro-ph.CO].

[20] A. G. Riess et al. “A 2.4% Determination of the Local Value of the Hubble Constant”. In : *Astrophys. J.* 826.1 (2016), p. 56. doi : 10.3847/0004-637X/826/1/56. arXiv : 1604.01424 [astro-ph.CO].

[21] A. G. Riess et al. “A Comprehensive Measurement of the Local Value of the Hubble Constant with 1 km/s/Mpc Uncertainty from the Hubble Space Telescope and the SH0ES Team”. In : *Astrophys. J. Lett.* 934.1 (2022), p. L7. doi : 10.3847/2041-8213/ac5c5b. arXiv : 2112.04510 [astro-ph.CO].

[22] K. C. Wong et al. “H0LiCOW - XIII. A 2.4 per cent measurement of H_0 from lensed quasars: 5.3σ tension between early- and late-Universe probes”. In : *Mon. Not. Roy. Astron. Soc.* 498.1 (oct. 2020), p. 1420-1439. doi : 10.1093/mnras/stz3094. arXiv : 1907.04869 [astro-ph.CO].

[23] E. Di Valentino et al. “In the realm of the Hubble tension—a review of solutions”. In : *Class. Quant. Grav.* 38.15 (2021), p. 153001. doi : 10.1088/1361-6382/ac086d. arXiv : 2103.01183 [astro-ph.CO].

[24] M. Asgari et al. “KiDS-1000 Cosmology: Cosmic shear constraints and comparison between two point statistics”. In : *Astronomy & Astrophysics* 645 (2021), A104. doi : 10.1051/0004-6361/202039070. arXiv : 2007.15633 [astro-ph.CO].

[25] L. F. Secco et al. “Dark Energy Survey Year 3 results: Cosmology from cosmic shear and robustness to modeling uncertainty”. In : *Phys. Rev. D* 105 (2 jan. 2022), p. 023515. doi : 10.1103/PhysRevD.105.023515. url : https://link.aps.org/doi/10.1103/PhysRevD.105.023515.

[26] A. Amon et al. “Dark Energy Survey Year 3 results: Cosmology from cosmic shear and robustness to data calibration”. In : *Phys. Rev. D* 105.2, 023514 (jan. 2022), p. 023514. doi : 10.1103/PhysRevD.105.023514. arXiv : 2105.13543 [astro-ph.CO].

[27] X. Li et al. “Hyper Suprime-Cam Year 3 results: Cosmology from cosmic shear two-point correlation functions”. In : *Phys. Rev. D* 108.12 (2023), p. 123518. doi : 10.1103/PhysRevD.108.123518. arXiv : 2304.00702 [astro-ph.CO].

[28] R. Mandelbaum et al. “Weak lensing shear calibration with simulations of the HSC survey”. In : *Mon. Not. Roy. Astron. Soc.* 481.3 (déc. 2018), p. 3170-3195. doi : 10.1093/mnras/sty2420. arXiv : 1710.00885 [astro-ph.CO].

[29] A. Kannawadi et al. “Towards emulating cosmic shear data: revisiting the calibration of the shear measurements for the Kilo-Degree Survey”. In : *Astronomy & Astrophysics* 624, A92 (avr. 2019), A92. doi : 10.1051/0004-6361/201834819. arXiv : 1812.03983 [astro-ph.CO].

[30] N. MacCrann et al. “Dark Energy Survey Y3 results: blending shear and redshift biases in image simulations”. In : *Mon. Not. Roy. Astron. Soc.* 509.3 (jan. 2022), p. 3371-3394. doi : 10.1093/mnras/stab2870. arXiv : 2012.08567 [astro-ph.CO].

[31] A. Amon et G. Efstathiou. “A non-linear solution to the S_8 tension?” In : *Mon. Not. Roy. Astron. Soc.* 516.4 (2022), p. 5355-5366. doi : 10.1093/mnras/stac2429. arXiv : 2206.11794 [astro-ph.CO].

[32] C. Preston, A. Amon et G. Efstathiou. “A non-linear solution to the S8 tension – II. Analysis of DES Year 3 cosmic shear”. In : *Mon. Not. Roy. Astron. Soc.* 525.4 (2023), p. 5554-5564. doi : 10.1093/mnras/stad2573. arXiv : 2305.09827 [astro-ph.CO].

[33] N. Schöneberg et al. “The Ho Olympics: A fair ranking of proposed models”. In : *Phys. Rept.* 984 (2022), p. 1-55. doi : 10.1016/j.physrep.2022.07.001. arXiv : 2107.10291 [astro-ph.CO].

[34] P.J.E Peebles. *Principles of Physical Cosmology*. T. 99. Princeton University Press, 2019. isbn : 9780691209814. url : http://www.jstor.org/stable/j.ctvxrpxvb (visité le 13/05/2024).

[35] M. Kilbinger. “Cosmology with cosmic shear observations: a review”. In : *Rept. Prog. Phys.* 78 (2015), p. 086901. doi : 10.1088/0034-4885/78/8/086901. arXiv : 1411.0115 [astro-ph.CO].

[36] M. Bartelmann et P. Schneider. “Weak gravitational lensing”. In : *Phys. Rept.* 340 (2001), p. 291-472. doi : 10.1016/S0370-1573(00)00082-X. arXiv : astro-ph/9912508.

[37] B. Joachimi et S. L. Bridle. “Simultaneous measurement of cosmology and intrinsic alignments using joint cosmic shear and galaxy number density correlations”. In : *Astronomy & Astrophysics* 523, A1 (nov. 2010), A1. doi : 10.1051/0004-6361/200913657. arXiv : 0911.2454 [astro-ph.CO].

[38] R. G. Crittenden et al. “Discriminating Weak Lensing from Intrinsic Spin Correlations Using the Curl-Gradient Decomposition”. In : *Astrophys. J.* 568.1 (mars 2002), p. 20. doi : 10.1086/338838. url : https://dx.doi.org/10.1086/338838.

[39] L. J. King. “Cosmic shear as a tool for precision cosmology: minimising intrinsic galaxy alignment-lensing interference”. In : *Astronomy & Astrophysics* 441.1 (oct. 2005), p. 47-53. doi : 10.1051/0004-6361:20053330. arXiv : astro-ph/0506441 [astro-ph].

[40] N. Kaiser. “Weak Gravitational Lensing of Distant Galaxies”. In : *Astrophys. J.* 388 (avr. 1992), p. 272. doi : 10.1086/171151.

[41] S. Bridle et L. King. “Dark energy constraints from cosmic shear power spectra: impact of intrinsic alignments on photometric redshift requirements”. In : *New Journal of Physics* 9.12 (déc. 2007), p. 444. doi : 10.1088/1367-2630/9/12/444. arXiv : 0705.0166 [astro-ph].

[42] Christopher M. Hirata et Uro š Seljak. “Intrinsic alignment-lensing interference as a contaminant of cosmic shear”. In : *Phys. Rev. D* 70 (6 2004), p. 063526. doi : 10.1103/PhysRevD.70.063526. url : https://link.aps.org/doi/10.1103/PhysRevD.70.063526.

[43] D. N. Limber. “The Analysis of Counts of the Extragalactic Nebulae in Terms of a Fluctuating Density Field.” In : *Astrophys. J.* 117 (jan. 1953), p. 134. doi : 10.1086/145672.

[44] M. LoVerde et N. Afshordi. “Extended Limber approximation”. In : *Phys. Rev. D* 78 (12 déc. 2008), p. 123506. doi : 10.1103/PhysRevD.

78.123506. url : https://link.aps.org/doi/10.1103/PhysRevD.78.123506.

[45] P. Schneider. *Extragalactic Astronomy and Cosmology*. Springer, 2006.

[46] N. Kaiser. "On the spatial correlations of Abell clusters." In : *Astrophys. J. Lett.* 284 (sept. 1984), p. L9-L12. doi : 10.1086/184341.

[47] U.-L. Pen. "Reconstructing Nonlinear Stochastic Bias from Velocity Space Distortions". In : *Astrophys. J.* 504.2 (sept. 1998), p. 601-606. doi : 10.1086/306098. arXiv : astro-ph/9711180 [astro-ph].

[48] M. Tegmark et B. C. Bromley. "Observational Evidence for Stochastic Biasing". In : *Astrophys. J.* 518.2 (mai 1999), p. L69. doi : 10.1086/312068. url : https://dx.doi.org/10.1086/312068.

[49] S. D. Landy et A. S. Szalay. "Bias and Variance of Angular Correlation Functions". In : *Astrophys. J.* 412 (juill. 1993), p. 64. doi : 10.1086/172900.

[50] L. Anderson et al. "The clustering of galaxies in the SDSS-III Baryon Oscillation Spectroscopic Survey: baryon acoustic oscillations in the Data Release 9 spectroscopic galaxy sample". In : *Mon. Not. Roy. Astron. Soc.* 427.4 (déc. 2012), p. 3435-3467.

[51] J. Elvin-Poole et al. "Dark Energy Survey year 1 results: Galaxy clustering for combined probes". In : *Phys. Rev. D* 98.4 (2018), p. 042006. doi : 10.1103/PhysRevD.98.042006. arXiv : 1708.01536 [astro-ph.CO].

[52] M. Levi et al. "The Dark Energy Spectroscopic Instrument (DESI)". In : *Bulletin of the AAS* 51.7 (sept. 2019). https://baas.aas.org/pub/2020n7i057.

[53] M. Kilbinger et al. "CFHTLenS: combined probe cosmological model comparison using 2D weak gravitational lensing". In : *Mon. Not. Roy. Astron. Soc.* 430.3 (avr. 2013), p. 2200-2220. doi : 10.1093/mnras/stt041. arXiv : 1212.3338 [astro-ph.CO].

[54] J. T. A. de Jong et al. "The Kilo-Degree Survey". In : *Experimental Astronomy* 35.1-2 (jan. 2013), p. 25-44. doi : 10.1007/s10686-012-9306-1. arXiv : 1206.1254 [astro-ph.CO].

[55] H. Aihara et al. “The Hyper Suprime-Cam SSP Survey: Overview and survey design”. In : *Publications of the Astronomical Society of Japan* 70, S4 (jan. 2018), S4. doi : 10.1093/pasj/psx066. arXiv : 1704.05858 [astro-ph.IM].

[56] Dark Energy Survey Collaboration et al. “The Dark Energy Survey: more than dark energy - an overview”. In : *Mon. Not. Roy. Astron. Soc.* 460.2 (août 2016), p. 1270-1299. doi : 10.1093/mnras/stw641. arXiv : 1601.00329 [astro-ph.CO].

[57] R. Laureijs et al. “Euclid Definition Study Report”. In : *arXiv e-prints*, arXiv:1110.3193 (oct. 2011), arXiv:1110.3193. doi : 10.48550/arXiv.1110.3193. arXiv : 1110.3193 [astro-ph.CO].

[58] Ž. Ivezić et al. “LSST: From Science Drivers to Reference Design and Anticipated Data Products”. In : *Astrophys. J.* 873.2, 111 (mars 2019), p. 111. doi : 10.3847/1538-4357/ab042c. arXiv : 0805.2366 [astro-ph].

[59] J. Lesgourgues et al. *Neutrino Cosmology*. Cambridge University Press, 2013.

[60] Planck Collaboration et al. “Planck 2018 results. I. Overview and the cosmological legacy of Planck”. In : *Astronomy & Astrophysics* 641, A1 (sept. 2020), A1. doi : 10.1051/0004-6361/201833880. arXiv : 1807.06205 [astro-ph.CO].

[61] N. Aghanim et al. “Planck 2018 results. VI. Cosmological parameters”. In : *Astronomy & Astrophysics* 641 (2020). [Erratum: Astron.Astrophys. 652, C4 (2021)], A6. doi : 10.1051/0004-6361/201833910. arXiv : 1807.06209 [astro-ph.CO].

[62] T. Okamoto et W. Hu. “CMB lensing reconstruction on the full sky”. In : *Phys. Rev. D* 67 (2003), p. 083002. doi : 10.1103/PhysRevD.67.083002. arXiv : astro-ph/0301031.

[63] A. Lewis et A. Challinor. “Weak gravitational lensing of the CMB”. In : *Phys. Rept.* 429 (2006), p. 1-65. doi : 10.1016/j.physrep.2006.03.002. arXiv : astro-ph/0601594.

[64] D. S. Swetz et al. “OVERVIEW OF THE ATACAMA COSMOLOGY TELESCOPE: RECEIVER, INSTRUMENTATION, AND TELESCOPE SYSTEMS”. In : *Astrophys. J. Supplement Series* 194.2 (juin 2011), p. 41. issn : 1538-4365. doi : 10.1088/0067-0049/194/2/41. url : http://dx.doi.org/10.1088/0067-0049/194/2/41.

[65] B. A. Benson et al. “SPT-3G: a next-generation cosmic microwave background polarization experiment on the South Pole telescope”. In : *Millimeter, Submillimeter, and Far-Infrared Detectors and Instrumentation for Astronomy VII*. Sous la dir. de Wayne S. Holland et Jonas Zmuidzinas. T. 9153. Society of Photo-Optical Instrumentation Engineers (SPIE) Conference Series. Juill. 2014, 91531P, 91531P. doi : 10.1117/12.2057305. arXiv : 1407.2973 [astro-ph.IM].

[66] L. Balkenhol et al. “Measurement of the CMB temperature power spectrum and constraints on cosmology from the SPT-3G 2018 TT, TE, and EE dataset”. In : *Phys. Rev. D* 108.2 (2023), p. 023510. doi : 10.1103/PhysRevD.108.023510. arXiv : 2212.05642 [astro-ph.CO].

[67] Z. Ivezic et al. *Statistics, Data Mining, and Machine Learning in Astronomy: A Practical Python Guide for the Analysis of Survey Data*. USA : Princeton University Press, 2014. isbn : 0691151687.

[68] Roberto Trotta. “Bayesian Methods in Cosmology”. In : *arXiv e-prints*, arXiv:1701.01467 (jan. 2017), arXiv:1701.01467. doi : 10.48550/arXiv.1701.01467. arXiv : 1701.01467 [astro-ph.CO].

[69] N. Metropolis et S. Ulam. “The Monte Carlo Method”. In : *J. Am. Statist. Assoc.* 44.247 (1949), p. 335-341. doi : 10.1080/01621459.1949.10483310.

[70] N. Metropolis et al. “Equation of State Calculations by Fast Computing Machines”. In : *The Journal of Chemical Physics* 21.6 (juin 1953), p. 1087-1092. doi : 10.1063/1.1699114.

[71] W. K. Hastings. “Monte Carlo Sampling Methods Using Markov Chains and Their Applications”. In : *Biometrika* 57 (1970), p. 97-109. doi : 10.1093/biomet/57.1.97.

[72] A. Gelman et D.B. Rubin. “Inference from Iterative Simulation Using Multiple Sequences”. In : *Statistical Science* 7 (1992), p. 457. doi : 10.1214/SS/1177011136.

[73] S.P. Brooks et A. Gelman. “General Methods for Monitoring Convergence of Iterative Simulations”. In : *Journal of Computational and Graphical Statistics* 7 (1997), p. 434. doi : 10.1080/10618600.1998.10474787.

[74] B. Audren et al. “Conservative constraints on early cosmology: an illustration of the Monte Python cosmological parameter inference code”. In : *JCAP* 2013.02 (2013), p. 001. doi : 10.1088/1475-7516/2013/02/001.

[75] A. Lewis et S. Bridle. “Cosmological parameters from CMB and other data: a Monte-Carlo approach”. In : *Phys. Rev. D* 66 (2002), p. 103511. doi : 10.1103/PhysRevD.66.103511.

[76] J. Torrado et A. Lewis. *Cobaya: Code for Bayesian Analysis of hierarchical physical models*. 2019. doi : 10.5281/zenodo.3538990. arXiv : 1910.14090.

[77] J. Zuntz et al. “CosmoSIS: Modular cosmological parameter estimation”. In : *Astronomy and Computing* 12 (2015), p. 45-59. doi : 10.1016/j.ascom.2015.05.005.

[78] J. Skilling. “Nested sampling”. In : *Bayesian Analysis* 1.4 (2006), p. 833-859. doi : 10.1214/06-BA127.

[79] W. Handley, M. P. Hobson et A. N. Lasenby. “POLYCHORD: nested sampling for cosmology”. In : *Mon. Not. Roy. Astron. Soc.* 450.1 (2015), p. L61-L65. doi : 10.1093/mnrasl/slv047.

[80] W. Handley, M. P. Hobson et A. N. Lasenby. “POLYCHORD: next-generation nested sampling”. In : *Mon. Not. Roy. Astron. Soc.* 453.4 (2015), p. 4384-4398. doi : 10.1093/mnras/stv1911.

[81] R. M. Neal. “Slice sampling”. In : *Annals of Statistics* 31.3 (2003), p. 705-767. doi : 10.1214/aos/1056562461.

[82] DES Collaboration et al. “Dark Energy Survey Year 3 results: Cosmological constraints from galaxy clustering and weak lensing”. In : *Phys. Rev. D* 103.8 (2021), p. 083533. doi : 10.1103/PhysRevD.103.083533.

[83] W. Li et al. “Revisiting the Dark Energy Survey Year 1 cosmological results with robust and accurate MCMC sampling”. In : *Phys. Rev. D* 107.12 (2023), p. 123524. doi : 10.1103/PhysRevD.107.123524.

[84] P. Lemos et al. “Robust sampling for weak lensing and clustering analyses with the Dark Energy Survey”. In : *Mon. Not. Roy. Astron. Soc.* 521.1 (2023), p. 1184-1199. doi : 10.1093/mnras/stac2786. arXiv : 2202.08233 [astro-ph.CO].

[85] C. Wetterich. “An asymptotically vanishing time-dependent cosmological "constant"”. In : *Astronomy & Astrophysics* 301 (1995), p. 321. doi : 10.48550/ARXIV.HEP-TH/9408025. url : https://arxiv.org/abs/hep-th/9408025.

[86] L. Amendola. “Coupled quintessence”. In : *Phys. Rev. D* 62.4 (juill. 2000), p. 043511. doi : 10.1103/physrevd.62.043511. url : https://doi.org/10.1103%2Fphysrevd.62.043511.

[87] I. Zlatev, L. Wang et P. J. Steinhardt. “Quintessence, Cosmic Coincidence, and the Cosmological Constant”. In : *Phys. Rev. Lett.* 82 (5 fév. 1999), p. 896-899. doi : 10.1103/PhysRevLett.82.896. url : https://link.aps.org/doi/10.1103/PhysRevLett.82.896.

[88] V. L. Fitch, D. R. Marlow et D. M. A. Elisabeth. *Critical problems in physics: Proceedings of a conference celebrating the 250th anniversary of Princeton University Princeton, N. Jersey, O. 31, N. 1, N. 2, 1.* Princeton University Press, 1997.

[89] A. P. Billyard et A. A. Coley. “Cosmology and cosmic strings”. In : *Phys. Rev. D* 61.8 (2000), p. 083503. eprint : astro-ph/9908224.

[90] W. Zimdahl et D. Pavon. “Interacting quintessence”. In : *Physics Letters B* 521.2-4 (2001), p. 133. eprint : astro-ph/0105479.

[91] G. R. Farrar et P. J. E. Peebles. “Dark matter and the cosmic microwave background”. In : *Astrophys. J.* 604.1 (2004), p. 1. eprint : astro-ph/0307316.

[92] S. Matarrese, M. Pietroni et C. Schimd. “Nonlinear gravitational clustering in scalar field cosmologies”. In : *JCAP* 08 (2003), p. 005. doi : 10.1088/1475-7516/2003/08/005. arXiv : astro-ph/0305224.

[93] L. Amendola. “Linear and non-linear perturbations in dark energy models”. In : *Phys. Rev. D* 69.10 (2004), p. 103524. eprint : astro-ph/0311175.

[94] A. V. Maccio et al. “Nonlinear evolution of cosmological perturbations and its cosmological implications”. In : *Phys. Rev. D* 69.12 (2004), p. 123516. eprint : astro-ph/0309671.

[95] L. Amendola, M. Gasperini et F. Piazza. “Crossing the phantom divide with scalar tensor theories”. In : *JCAP* 2004.9 (2004), p. 014. eprint : astro-ph/0407573.

[96] L. Amendola, G. Camargo Campos et R. Rosenfeld. “Constraining interactions in cosmology’s dark sector”. In : *Phys. Rev. D* 75.8 (2007), p. 083506. eprint : astro-ph/0610806.

[97] Z.-K. Guo, N. Ohta et S. Tsujikawa. “Probing the dark energy via gravitation wave observation in brane world cosmology”. In : *Phys. Rev. D* 76.2 (2007), p. 023508. eprint : astro-ph/0702015.

[98] T. Koivisto. “Covariant conservation equations and stability in modified gravities”. In : *Phys. Rev. D* 72.4 (2005), p. 043516. eprint : astroph/0504571.

[99] S. Lee, G.-C. Liu et K.-W. Ng. “Background cosmological dynamics in a non-local relativistic dust model”. In : *Phys. Rev. D* 73.8 (2006), p. 083515. eprint : astro-ph/0601333.

[100] B. Wang et al. “Interacting holographic dark energy model”. In : *Nuclear Physics B* 778 (2007), p. 69. eprint : astroph/0607126.

[101] R. Mainini et S. Bonometto. “WIMP cosmological constraints in interacting dark energy cosmologies”. In : *JCAP* 2007.6 (2007), p. 020. eprint : astro-ph/0703303.

[102] V. Pettorino et C. Baccigalupi. “Constraints on growing neutrino quintessence from cosmological data”. In : *Phys. Rev. D* 77.10 (2008), p. 103003. eprint : 0802.1086.

[103] J.-Q. Xia. “Hubble parameter evolution in the DGP model”. In : *Phys. Rev. D* 80.10 (2009), p. 103514. eprint : 0911.4820.

[104] L. P. Chimento et al. “Interacting quintessence solution to the coincidence problem”. In : *Phys. Rev. D* 67.8 (2003), p. 083513. eprint : astro-ph/0303145.

[105] G. Olivares, F. Atrio-Barandela et D. Pavon. “Observational constraints on phantom cosmology”. In : *Phys. Rev. D* 71 (2005), p. 063523. eprint : astro-ph/0503242.

[106] H. M. Sadjadi et M. Alimohammadi. “Third order cosmic perturbations revisited”. In : *Phys. Rev. D* 74 (2006), p. 103007. eprint : gr-qc/0610080.

[107] A. Brookfield, C. van de Bruck et L. M. Hall. “Dilaton dark energy with event horizons”. In : *Phys. Rev. D* 77 (2008), p. 043006. eprint : 0709.2297.

[108] C. G. Boehmer et al. “Dynamics of dark energy with non-standard Lagrangians”. In : *Phys. Rev. D* 78 (2008), p. 023505. eprint : 0801.1565.

[109] G. Caldera-Cabral, R. Maartens et B. M. Schaefer. “The growth of structure in interacting dark energy models”. In : *JCAP* 2009 (2009), p. 027. eprint : 0905.0492.

[110] J.-H. He et B. Wang. “Dark energy constraints from the abundance of massive clusters”. In : *JCAP* 2008 (2008), p. 010. eprint : 0801.4233.

[111] M. Quartin et al. “Constraints on the dark energy equation of state from gravitational lensing statistics”. In : *JCAP* 2008 (2008), p. 007. eprint : 0802.0546.

[112] J. Valiviita, R. Maartens et E. Majerotto. “Observational constraints on an interacting dark energy model”. In : *Mon. Not. Roy. Astron. Soc.* 402 (2010), p. 2355. eprint : 0907.4987.

[113] S. Pereira et J. Jesus. “Constraining the dynamics of dark energy with standard rulers”. In : *Phys. Rev. D* 79 (2009), p. 043517. eprint : 0811.0099.

[114] R. Bean et al. “Non-linear growth of dark energy perturbations: a numerical study”. In : *Phys. Rev. D* 78 (2008), p. 123514. eprint : 0808.1105.

[115] M. Gavela et al. “Dark energy effects in neutrinophilic self-interacting dark matter”. In : *JCAP* 2009 (2009), p. 034. eprint : 0901.1611.

[116] E. R. Tarrant et al. “Cosmological perturbations in the presence of extra dimensions”. In : *Phys. Rev. D* 85 (2012), p. 023503. eprint : 1103.0694.

[117] M. Baldi et al. “Observational constraints on the nature of dark energy: static versus dynamic”. In : *Mon. Not. Roy. Astron. Soc.* 403 (2010), p. 1684. eprint : 0812.3901.

[118] F. Marulli, M. Baldi et L. Moscardini. “The impact of dark energy perturbations on cosmic microwave background anisotropies”. In : *Mon. Not. Roy. Astron. Soc.* 420 (2012), p. 2377. eprint : 1110.3045.

[119] V. Salvatelli et al. “New constraints on coupled dark energy from the Planck satellite experiment”. In : *Phys. Rev. D* 88 (2 juill. 2013), p. 023531. doi : 10.1103/PhysRevD.88.023531. url : https://link.aps.org/doi/10.1103/PhysRevD.88.023531.

[120] A. Pourtsidou, C. Skordis et E. J. Copeland. “Models of dark matter coupled to dark energy”. In : *Phys. Rev. D* 88.8 (2013), p. 083505. doi : 10.1103/PhysRevD.88.083505. arXiv : 1307.0458 [astro-ph.CO].

[121] L. W. K. Goh et al. “Constraining constant and tomographic coupled dark energy with low-redshift and high-redshift probes”. In : *Phys. Rev. D* 107.8 (2023), p. 083503. doi : 10.1103/PhysRevD.107.083503. arXiv : 2211.13588 [astro-ph.CO].

[122] C. M. Will. “The Confrontation between General Relativity and Experiment”. In : *Living Rev. Rel.* 17 (2014), p. 4. doi : 10.12942/lrr-2014-4. arXiv : 1403.7377 [gr-qc].

[123] B. Elder et al. “Classical symmetron force in Casimir experiments”. In : *Phys. Rev. D* 101.6 (2020), p. 064065. doi : 10.1103/PhysRevD.101.064065. arXiv : 1912.10015 [gr-qc].

[124] J. Bergé et al. “MICROSCOPE Mission: First Constraints on the Violation of the Weak Equivalence Principle by a Light Scalar Dilaton”. In : *Phys. Rev. Lett.* 120.14 (2018), p. 141101. doi : 10.1103/PhysRevLett.120.141101. arXiv : 1712.00483 [gr-qc].

[125] P. Brax et al. “Constraining screened fifth forces with the electron magnetic moment”. In : *Phys. Rev. D* 97.8 (2018), p. 084050. doi : 10.1103/PhysRevD.97.084050. arXiv : 1802.05545 [hep-ph].

[126] S. A. Bonometto et R. Mainini. “Growth and dissolution of spherical density enhancements in SCDEW cosmologies”. In : *JCAP* 2017.06 (juin 2017), p. 010-010. doi : 10.1088/1475-7516/2017/06/010. url : https://doi.org/10.1088%2F1475-7516%2F2017%2F06%2F010.

[127] S. Bonometto et R. Mainini. “Coupled DM Heating in SCDEW Cosmologies”. In : *Entropy* 19.8 (août 2017), p. 398. doi : 10.3390/e19080398. url : https://doi.org/10.3390%2Fe19080398.

[128] S.A. Bonometto, M. Mezzetti et R. Mainini. “Strongly coupled dark energy with warm dark matter vs. LCDM”. In : *JCAP* 2017.10 (oct. 2017), p. 011-011. doi : 10.1088/1475-7516/2017/10/011. url : https://doi.org/10.1088%2F1475-7516%2F2017%2F10%2F011.

[129] S. A Bonometto, R. Mainini et M. Mezzetti. “Strongly coupled dark energy cosmologies yielding large-mass primordial black holes”. In : *Mon. Not. Roy. Astron. Soc.* 486.2 (mars 2019), p. 2321-2335. doi : 10.1093/mnras/stz846. url : https://doi.org/10.1093%2Fmnras%2Fstz846.

[130] R. R. Caldwell et E. V. Linder. “Limits of Quintessence”. In : *Phys. Rev. Lett.* 95 (14 sept. 2005), p. 141301. doi : 10.1103/PhysRevLett.95.141301. url : https://link.aps.org/doi/10.1103/PhysRevLett.95.141301.

[131] M. Martinelli et al. “Constraints on the interacting vacuum–geodesic CDM scenario”. In : *Mon. Not. Roy. Astron. Soc.* 488.3 (2019), p. 3423-3438. doi : 10.1093/mnras/stz1915. arXiv : 1902.10694 [astro-ph.CO].

[132] N. B. Hogg et al. “Latest evidence for a late time vacuum–geodesic CDM interaction”. In : *Phys. Dark Univ.* 29 (2020), p. 100583. doi : 10.1016/j.dark.2020.100583. arXiv : 2002.10449 [astro-ph.CO].

[133] J. D. Barrow et T. Clifton. “Cosmologies with energy exchange”. In : *Phys. Rev. D* 73 (2006), p. 103520. doi : 10.1103/PhysRevD.73.103520. arXiv : gr-qc/0604063.

[134] M. Baldi et al. “Hydrodynamical N-body simulations of coupled dark energy cosmologies”. In : *Mon. Not. Roy. Astron. Soc.* 403 (2010), p. 1684-1702. doi : 10.1111/j.1365-2966.2009.15987.x. arXiv : 0812.3901 [astro-ph].

[135] G. Caldera-Cabral, R. Maartens et L. A. Urena-Lopez. “Dynamics of interacting dark energy”. In : *Phys. Rev. D* 79 (2009), p. 063518. doi : 10.1103/PhysRevD.79.063518. arXiv : 0812.1827 [gr-qc].

[136] M. Baldi. “Time dependent couplings in the dark sector: from background evolution to nonlinear structure formation”. In : *Mon. Not. Roy. Astron. Soc.* 411 (2011), p. 1077. doi : 10.1111/j.1365-2966.2010.17758.x. arXiv : 1005.2188 [astro-ph.CO].

[137] C. Wetterich. “Growing neutrinos and cosmological selection”. In : *Physical Letters B* 655 (2007), p. 201-208. doi : 10.1016/j.physletb.2007.08.060. arXiv : 0706.4427 [hep-ph].

[138] V. Pettorino et al. “Neutrino lumps and the Cosmic Microwave Background”. In : *Phys. Rev. D* 82 (2010), p. 123001. doi : 10.1103/PhysRevD.82.123001. arXiv : 1009.2461 [astro-ph.CO].

[139] D. Blas, J. Lesgourgues et T. Tram. “The Cosmic Linear Anisotropy Solving System (CLASS). Part II: Approximation schemes”. In : *JCAP* 2011.7, 034 (juill. 2011), p. 034. doi : 10.1088/1475-7516/2011/07/034. arXiv : 1104.2933 [astro-ph.CO].

[140] V. Pettorino et al. “Constraints on coupled dark energy using CMB data from WMAP and SPT”. In : *Phys. Rev. D* 86 (2012), p. 103507. doi : 10.1103/PhysRevD.86.103507. arXiv : 1207.3293 [astro-ph.CO].

[141] V. Pettorino. “Testing modified gravity with Planck: the case of coupled dark energy”. In : *Phys. Rev. D* 88 (2013), p. 063519. doi : 10.1103/PhysRevD.88.063519. arXiv : 1305.7457 [astro-ph.CO].

[142] A. Gómez-Valent, V. Pettorino et L. Amendola. “Update on coupled dark energy and the H_0 tension”. In : *Phys. Rev. D* 101.12 (2020), p. 123513. doi : 10.1103/PhysRevD.101.123513. arXiv : 2004.00610 [astro-ph.CO].

[143] A. Gómez-Valent et al. “Coupled and uncoupled early dark energy, massive neutrinos and the cosmological tensions”. In : *Phys. Rev. D* 106 (2022), p. 103522. doi : 10.1103/PhysRevD.106.103522. arXiv : 2207.14487.

[144] L. Amendola et al. “Testing coupled dark energy with next-generation large-scale observations”. In : *Phys. Rev. D* 85 (2012), p. 103008. doi : 10.1103/PhysRevD.85.103008. arXiv : 1111.1404 [astro-ph.CO].

[145] A. Lewis. “GetDist: a Python package for analysing Monte Carlo samples”. In : (oct. 2019). arXiv : 1910.13970 [astro-ph.IM].

[146] L. Balkenhol et al. “Constraints on ΛCDM extensions from the SPT-3G 2018 EE and TE power spectra”. In : *Phys. Rev. D* 104.8 (2021), p. 083509. doi : 10.1103/PhysRevD.104.083509. arXiv : 2103.13618 [astro-ph.CO].

[147] J. C. Hill et al. “Atacama Cosmology Telescope: Constraints on prerecombination early dark energy”. In : *Phys. Rev. D* 105.12 (2022), p. 123536. doi : 10.1103/PhysRevD.105.123536. arXiv : 2109.04451 [astro-ph.CO].

[148] V. Poulin, T. L. Smith et A. Bartlett. “Dark energy at early times and ACT data: A larger Hubble constant without late-time priors”. In : *Phys. Rev. D* 104.12 (2021), p. 123550. doi : 10.1103/PhysRevD.104.123550. arXiv : 2109.06229 [astro-ph.CO].

[149] T. L. Smith et al. “Hints of early dark energy in Planck, SPT, and ACT data: New physics or systematics?” In : *Phys. Rev. D* 106.4 (2022), p. 043526. doi : 10.1103/PhysRevD.106.043526. arXiv : 2202.09379 [astro-ph.CO].

[150] P. Carter et al. “Low Redshift Baryon Acoustic Oscillation Measurement from the Reconstructed 6-degree Field Galaxy Survey”. In : *Mon. Not. Roy. Astron. Soc.* 481.2 (2018), p. 2371-2383. doi : 10.1093/mnras/sty2405. arXiv : 1803.01746 [astro-ph.CO].

[151] H. Gil-Marín et al. “The clustering of galaxies in the SDSS-III Baryon Oscillation Spectroscopic Survey: RSD measurement from the power spectrum and bispectrum of the DR12 BOSS galaxies”. In : *Mon. Not. Roy. Astron. Soc.* 465.2 (2017), p. 1757-1788. doi : 10.1093/mnras/stw2679. arXiv : 1606.00439 [astro-ph.CO].

[152] C. Blake et al. “The WiggleZ Dark Energy Survey: joint measurements of the expansion and growth history at z < 1”. In : *Mon. Not. Roy. Astron. Soc.* 425.1 (sept. 2012), p. 405-414. doi : 10.1111/j.1365-2966.2012.21473.x. arXiv : 1204.3674 [astro-ph.CO].

[153] T. M. C. Abbott et al. “Dark Energy Survey Year 3 results: A 2.7% measurement of baryon acoustic oscillation distance scale at redshift 0.835”. In : *Phys. Rev. D* 105.4 (2022), p. 043512. doi : 10.1103/PhysRevD.105.043512. arXiv : 2107.04646 [astro-ph.CO].

[154] H. Gil-Marín et al. “The clustering of the SDSS-IV extended Baryon Oscillation Spectroscopic Survey DR14 quasar sample: structure growth rate measurement from the anisotropic quasar power spectrum in the redshift range $0.8 < z < 2.2$”. In : *Mon. Not. Roy. Astron. Soc.* 477.2 (2018), p. 1604-1638. doi : 10.1093/mnras/sty453. arXiv : 1801.02689 [astro-ph.CO].

[155] V. de Sainte Agathe et al. “Baryon acoustic oscillations at z = 2.34 from the correlations of Lyα absorption in eBOSS DR14”. In : *Astronomy & Astrophysics* 629 (2019), A85. doi : 10.1051/0004-6361/201935638. arXiv : 1904.03400 [astro-ph.CO].

[156] D. M. Scolnic et al. “The Complete Light-curve Sample of Spectroscopically Confirmed SNe Ia from Pan-STARRS1 and Cosmological Constraints from the Combined Pantheon Sample”. In : *Astrophys. J.* 859.2 (2018), p. 101. doi : 10.3847/1538-4357/aab9bb. arXiv : 1710.00845 [astro-ph.CO].

[157] A. G. Riess et al. “Type Ia Supernova Distances at Redshift > 1.5 from the Hubble Space Telescope Multi-cycle Treasury Programs: The Early Expansion Rate”. In : *Astrophys. J.* 853.2 (2018), p. 126. doi : 10.3847/1538-4357/aaa5a9. arXiv : 1710.00844 [astro-ph.CO].

[158] T. M. C. Abbott et al. “First Cosmology Results using Type Ia Supernovae from the Dark Energy Survey: Constraints on Cosmological Parameters”. In : *Astrophys. J. Lett.* 872.2, L30 (fév. 2019), p. L30. doi : 10.3847/2041-8213/ab04fa. arXiv : 1811.02374 [astro-ph.CO].

[159] R. Jimenez et A. Loeb. “Constraining cosmological parameters based on relative galaxy ages”. In : *Astrophys. J.* 573 (2002), p. 37-42. doi : 10.1086/340549. arXiv : astro-ph/0106145.

[160] A. Gómez-Valent. "Quantifying the evidence for the current speed-up of the Universe with low and intermediate-redshift data. A more model-independent approach". In : *JCAP* 05 (2019), p. 026. doi : 10.1088/1475-7516/2019/05/026. arXiv : 1810.02278 [astro-ph.CO].

[161] F. Qin, C. Howlett et L. Staveley-Smith. "The redshift-space momentum power spectrum – II. Measuring the growth rate from the combined 2MTF and 6dFGSv surveys". In : *Mon. Not. Roy. Astron. Soc.* 487.4 (2019), p. 5235-5247. doi : 10.1093/mnras/stz1576. arXiv : 1906.02874 [astro-ph.CO].

[162] F. Shi et al. "Mapping the Real Space Distributions of Galaxies in SDSS DR7. II. Measuring the Growth Rate, Clustering Amplitude of Matter, and Biases of Galaxies at Redshift 0.1". In : *Astrophys. J.* 861.2, 137 (juill. 2018), p. 137. doi : 10.3847/1538-4357/aacb20. arXiv : 1712.04163 [astro-ph.CO].

[163] F. Simpson et al. "Galaxy and mass assembly: Redshift space distortions from the clipped galaxy field". In : *Phys. Rev. D* 93.2 (2016), p. 023525. doi : 10.1103/PhysRevD.93.023525. arXiv : 1505.03865 [astro-ph.CO].

[164] C. Blake et al. "Galaxy And Mass Assembly (GAMA): improved cosmic growth measurements using multiple tracers of large-scale structure". In : *Mon. Not. Roy. Astron. Soc.* 436 (2013), p. 3089. doi : 10.1093/mnras/stt1791. arXiv : 1309.5556 [astro-ph.CO].

[165] F. G. Mohammad et al. "The VIMOS Public Extragalactic Redshift Survey (VIPERS). Unbiased clustering estimate with VIPERS slit assignment". In : *Astronomy & Astrophysics* 619, A17 (nov. 2018), A17. doi : 10.1051/0004-6361/201833853. arXiv : 1807.05999 [astro-ph.CO].

[166] L. Guzzo et al. "A test of the nature of cosmic acceleration using galaxy redshift distortions". In : *Nature* 451 (2008), p. 541-545. doi : 10.1038/nature06555. arXiv : 0802.1944 [astro-ph].

[167] T. Okumura et al. "The Subaru FMOS galaxy redshift survey (FastSound). IV. New constraint on gravity theory from redshift space distortions at $z \sim 1.4$". In : *Publications of the Astronomical Society of Japan* 68.3 (2016), p. 38. doi : 10.1093/pasj/psw029. arXiv : 1511.08083 [astro-ph.CO].

[168] E. Macaulay, I. K. Wehus et H. K. Eriksen. “Lower Growth Rate from Recent Redshift Space Distortion Measurements than Expected from Planck”. In : *Phys. Rev. Lett.* 111.16 (2013), p. 161301. doi : 10.1103/PhysRevLett.111.161301. arXiv : 1303.6583 [astro-ph.CO].

[169] K. Kuijken et al. “The fourth data release of the Kilo-Degree Survey: ugri imaging and nine-band optical-IR photometry over 1000 square degrees”. In : *Astronomy & Astrophysics* 625 (2019), A2. doi : 10.1051/0004-6361/201834918. arXiv : 1902.11265 [astro-ph.GA].

[170] C. Heymans et al. “KiDS-1000 Cosmology: Multi-probe weak gravitational lensing and spectroscopic galaxy clustering constraints”. In : *Astronomy & Astrophysics* 646, A140 (fév. 2021), A140. doi : 10.1051/0004-6361/202039063. arXiv : 2007.15632 [astro-ph.CO].

[171] S. Casas et al. “Fitting and forecasting coupled dark energy in the non-linear regime”. In : *JCAP* 01 (2016), p. 045. doi : 10.1088/1475-7516/2016/01/045. arXiv : 1508.07208 [astro-ph.CO].

[172] A. Mead et al. “Accurate halo-model matter power spectra with dark energy, massive neutrinos and modified gravitational forces”. In : *Mon. Not. Roy. Astron. Soc.* 459.2 (2016), p. 1468-1488. doi : 10.1093/mnras/stw681. arXiv : 1602.02154 [astro-ph.CO].

[173] S. Alam et al. “The clustering of galaxies in the completed SDSS-III Baryon Oscillation Spectroscopic Survey: cosmological analysis of the DR12 galaxy sample”. In : *Mon. Not. Roy. Astron. Soc.* 470.3 (2017), p. 2617-2652. doi : 10.1093/mnras/stx721. arXiv : 1607.03155 [astro-ph.CO].

[174] A. G. Sanchez et al. “The clustering of galaxies in the completed SDSS-III Baryon Oscillation Spectroscopic Survey: cosmological implications of the configuration-space clustering wedges”. In : *Mon. Not. Roy. Astron. Soc.* 464.2 (2017), p. 1640-1658. doi : 10.1093/mnras/stw2443. arXiv : 1607.03147 [astro-ph.CO].

[175] C. Blake et al. “The 2-degree Field Lensing Survey: design and clustering measurements”. In : *Mon. Not. Roy. Astron. Soc.* 462.4 (2016), p. 4240-4265. doi : 10.1093/mnras/stw1990. arXiv : 1608.02668 [astro-ph.CO].

[176] B. Joachimi et al. “KiDS-1000 methodology: Modelling and inference for joint weak gravitational lensing and spectroscopic galaxy clustering analysis”. In : *Astronomy & Astrophysics* 646 (2021), A129. doi : 10.1051/0004-6361/202038831. arXiv : 2007.01844 [astro-ph.CO].

[177] P. A. R. Ade et al. “Planck 2015 results. XIV. Dark energy and modified gravity”. In : *Astronomy & Astrophysics* 594 (2016), A14. doi : 10.1051/0004-6361/201525814. arXiv : 1502.01590 [astro-ph.CO].

[178] N. Aghanim et al. “Planck 2018 results. VIII. Gravitational lensing”. In : *Astronomy & Astrophysics* 641 (2020), A8. doi : 10.1051/0004-6361/201833886. arXiv : 1807.06210 [astro-ph.CO].

[179] A. Heavens et al. “Marginal Likelihoods from Monte Carlo Markov Chains”. In : (avr. 2017). arXiv : 1704.03472 [stat.CO].

[180] R. E. Kass et A. E. Raftery. “Bayes Factors”. In : *J. Am. Statist. Assoc.* 90.430 (1995), p. 773-795. doi : 10.1080/01621459.1995.10476572.

[181] L. W. K. Goh et al. “Observational constraints on early coupled quintessence”. In : *Phys. Rev. D* 109.2, 023530 (jan. 2024), p. 023530. doi : 10.1103/PhysRevD.109.023530. arXiv : 2308.06406 [astro-ph.CO].

[182] L. Amendola, J. Rubio et C. Wetterich. “Primordial black holes from fifth forces”. In : *Phys. Rev. D* 97.8 (avr. 2018), p. 081302. doi : 10.1103/physrevd.97.081302. url : https://doi.org/10.1103%2Fphysrevd.97.081302.

[183] S. Savastano et al. “Primordial dark matter halos from fifth forces”. In : *Phys. Rev. D* 100.8 (oct. 2019). doi : 10.1103/physrevd.100.083518. url : https://doi.org/10.1103%2Fphysrevd.100.083518.

[184] L. Amendola. “Scaling solutions in general nonminimal coupling theories”. In : *Phys. Rev. D* 60 (4 juin 1999), p. 043501. doi : 10.1103/PhysRevD.60.043501. url : https://link.aps.org/doi/10.1103/PhysRevD.60.043501.

[185] L. Amendola et T.-V. Domenico. “Baryon bias and structure formation in an accelerating universe”. In : *Phys. Rev. D* 66.4 (août 2002), p. 043528. doi : 10.1103/physrevd.66.043528. url : https://doi.org/10.1103%2Fphysrevd.66.043528.

[186] T.-V. Domenico et L. Amendola. “Stationary dark energy with a baryon-dominated era: Solving the coincidence problem with a linear coupling”. In : *Phys. Rev. D* 65.6 (fév. 2002). doi : 10.1103/physrevd.65.063508. url : https://doi.org/10.1103%2Fphysrevd.65.063508.

[187] S. A. Bonometto, G. Sassi et G. La Vacca. “Dark energy from dark radiation in strongly coupled cosmologies with no fine tuning”. In : *JCAP* 2012.08 (août 2012), p. 015-015. doi : 10.1088/1475-7516/2012/08/015. url : https://doi.org/10.1088%2F1475-7516%2F2012%2F08%2F015.

[188] J.-P. Uzan. “Varying Constants, Gravitation and Cosmology”. In : *Living Rev. Rel.* 14 (2011), p. 2. doi : 10.12942/lrr-2011-2. arXiv : 1009.5514 [astro-ph.CO].

[189] R. Bean, S. H. Hansen et A. Melchiorri. “Early universe constraints on a primordial scaling field”. In : *Phys. Rev. D* 64 (2001), p. 103508. doi : 10.1103/PhysRevD.64.103508. arXiv : astro-ph/0104162.

[190] J. Beringer et al. “Review of Particle Physics (RPP)”. In : *Phys. Rev. D* 86 (2012), p. 010001. doi : 10.1103/PhysRevD.86.010001.

[191] N. Aghanim et al. “Planck 2018 results. V. CMB power spectra and likelihoods”. In : *Astronomy & Astrophysics* 641 (2020), A5. doi : 10.1051/0004-6361/201936386. arXiv : 1907.12875 [astro-ph.CO].

[192] D. Scolnic et al. “The Pantheon+ Analysis: The Full Data Set and Light-curve Release”. In : *Astrophys. J.* 938.2 (2022), p. 113. doi : 10.3847/1538-4357/ac8b7a. arXiv : 2112.03863 [astro-ph.CO].

[193] R. Takahashi et al. “Revising the Halofit Model for the Nonlinear Matter Power Spectrum”. In : *Astrophys. J.* 761 (2012), p. 152. doi : 10.1088/0004-637X/761/2/152. arXiv : 1208.2701 [astro-ph.CO].

[194] A. Gómez-Valent. “Fast test to assess the impact of marginalization in Monte Carlo analyses and its application to cosmology”. In : *Phys. Rev. D* 106.6 (2022), p. 063506. doi : 10.1103/PhysRevD.106.063506. arXiv : 2203.16285 [astro-ph.CO].

[195] K. Moriwaki, T. Nishimichi et N. Yoshida. “Machine learning for observational cosmology”. In : *Rept. Prog. Phys.* (2023).

[196] T. Kacprzak et J. Fluri. “Deeplss: Breaking parameter degeneracies in large-scale structure with deep-learning analysis of combined probes”. In : *Phys. Rev. X* 12.3 (2022), p. 031029.

[197] F. Ertam et G. Aydın. “Data classification with deep learning using Tensorflow”. In : *2017 International Conference on Computer Science and Engineering (UBMK)*. 2017, p. 755-758. doi : 10.1109/UBMK.2017.8093521.

[198] U. Anders et O. Korn. “Model selection in neural networks”. In : *Neural Networks* 12.2 (1999), p. 309-323. issn : 0893-6080. doi : https://doi.org/10.1016/S0893-6080(98)00117-8. url : https://www.sciencedirect.com/science/article/pii/S0893608098001178.

[199] A. Peel et al. “Distinguishing standard and modified gravity cosmologies with machine learning”. In : *Phys. Rev. D* 100.2, 023508 (juill. 2019), p. 023508. doi : 10.1103/PhysRevD.100.023508. arXiv : 1810.11030 [astro-ph.CO].

[200] J. Merten et al. “On the dissection of degenerate cosmologies with machine learning”. In : *Mon. Not. Roy. Astron. Soc.* 487.1 (2019), p. 104-122. doi : 10.1093/mnras/stz972. arXiv : 1810.11027 [astro-ph.CO].

[201] K. Murakami et al. “Non-Linearity-Free prediction of the growth-rate $f\sigma_8$ using Convolutional Neural Networks”. In : (mai 2023). arXiv : 2305.12812 [astro-ph.CO].

[202] DESI Collaboration et al. “The DESI Experiment Part I: Science,Targeting, and Survey Design”. In : *arXiv e-prints* (oct. 2016). doi : 10.48550/arXiv.1611.00036. arXiv : 1611.00036 [astro-ph.IM].

[203] S. Yahia-Cherif et al. “Validating the Fisher approach for stage IV spectroscopic surveys”. In : *Astronomy & Astrophysics* 649 (2021), A52.

[204] M. Tegmark. “Measuring cosmological parameters with galaxy surveys”. In : *Phys. Rev. Lett.* 79.20 (1997), p. 3806.

[205] Y. Wang, C. Chuang et C. M. Hirata. “Towards more realistic forecasting of dark energy constraints from galaxy redshift surveys”. In : *Mon. Not. Roy. Astron. Soc.* 430.3 (fév. 2013), p. 2446-2453. issn : 0035-8711. doi : 10.1093/mnras/stt068. eprint : https://academic.oup.com/

mnras/article-pdf/430/3/2446/4935129/stt068.pdf. url : https://doi.org/10.1093/mnras/stt068.

[206] A. Blanchard et al. “Euclid preparation-VII. Forecast validation for Euclid cosmological probes”. In : *Astronomy & Astrophysics* 642 (2020), A191.

[207] J. Schmidhuber. “Deep Learning in Neural Networks: An Overview”. In : *arXiv e-prints*, arXiv:1404.7828 (avr. 2014), arXiv:1404.7828. doi : 10.48550/arXiv.1404.7828. arXiv : 1404.7828 [cs.NE].

[208] T. Akiba et al. “Optuna: A Next-generation Hyperparameter Optimization Framework”. In : *arXiv e-prints*, arXiv:1907.10902 (juill. 2019), arXiv:1907.10902. doi : 10.48550/arXiv.1907.10902. arXiv : 1907.10902 [cs.LG].

[209] D. Singh et B. Singh. “Feature wise normalization: An effective way of normalizing data”. In : *Pattern Recognition* 122 (2022), p. 108307.

[210] J. He et al. “ReLU Deep Neural Networks and Linear Finite Elements”. In : *arXiv e-prints*, arXiv:1807.03973 (juill. 2018), arXiv:1807.03973. doi : 10.48550/arXiv.1807.03973. arXiv : 1807.03973 [math.NA].

[211] N. Srivastava et al. “Dropout: a simple way to prevent neural networks from overfitting”. In : *The journal of machine learning research* 15.1 (2014), p. 1929-1958.

[212] A. Tato et R. Nkambou. *IMPROVING ADAM OPTIMIZER*. 2018. url : https://openreview.net/forum?id=HJfpZq1DM.

[213] F. Chollet et al. *Keras*. https://keras.io. 2015.

[214] Y. Mellier et al. “Euclid. I. Overview of the Euclid mission”. In : (mai 2024). arXiv : 2405.13491 [astro-ph.CO].

[215] A. J. Mead et al. “HMCODE-2020: improved modelling of non-linear cosmological power spectra with baryonic feedback”. In : *Mon. Not. Roy. Astron. Soc.* 502.1 (mars 2021), p. 1401-1422. doi : 10.1093/mnras/stab082. arXiv : 2009.01858 [astro-ph.CO].

[216] Euclid Collaboration et al. “Euclid. V. The Flagship galaxy mock catalogue: a comprehensive simulation for the Euclid mission”. In : *arXiv e-prints*, arXiv:2405.13495 (mai 2024), arXiv:2405.13495. doi : 10.48550/arXiv.2405.13495. arXiv : 2405.13495 [astro-ph.CO].

[217] A. Barreira, E. Krause et F. Schmidt. “Accurate cosmic shear errors: do we need ensembles of simulations?” In : *JCAP* 2018.10 (oct. 2018), p. 053. doi : 10.1088/1475-7516/2018/10/053. url : https://dx.doi.org/10.1088/1475-7516/2018/10/053.

[218] W. Hu et B. Jain. “Joint galaxy-lensing observables and the dark energy”. In : *Phys. Rev. D* 70 (4 août 2004), p. 043009. doi : 10.1103/PhysRevD.70.043009. url : https://link.aps.org/doi/10.1103/PhysRevD.70.043009.

[219] M. Takada et W. Hu. “Power spectrum super-sample covariance”. In : *Phys. Rev. D* 87.12, 123504 (juin 2013), p. 123504. doi : 10.1103/PhysRevD.87.123504. arXiv : 1302.6994 [astro-ph.CO].

[220] F. Lacasa et R. Rosenfeld. “Combining cluster number counts and galaxy clustering”. In : *JCAP* 2016.08 (août 2016), 005–005. issn : 1475-7516. doi : 10.1088/1475-7516/2016/08/005. url : http://dx.doi.org/10.1088/1475-7516/2016/08/005.

[221] E. V. Linder. “Cosmic growth history and expansion history”. In : *Phys. Rev. D* 72 (4 août 2005), p. 043529. doi : 10.1103/PhysRevD.72.043529. url : https://link.aps.org/doi/10.1103/PhysRevD.72.043529.

[222] P. G. Ferreira et J. Magueijo. “A new view of the theory of large-scale structure”. In : *Phys. Rept.* 533 (2013), p. 143-164. doi : 10.1016/j.physrep.2013.03.001. arXiv : 1211.3874 [astro-ph.CO].

[223] F. Feroz et M. P. Hobson. “Multimodal nested sampling: an efficient and robust alternative to MCMC methods for astronomical data analysis”. In : *Mon. Not. Roy. Astron. Soc.* 384 (2008), p. 449-463. doi : 10.1111/j.1365-2966.2007.12353.x. arXiv : 0704.3704 [astro-ph].

[224] F. Feroz, M. P. Hobson et M. Bridges. “MULTINEST: an efficient and robust Bayesian inference tool for cosmology and particle physics”. In : *Mon. Not. Roy. Astron. Soc.* 398 (2009), p. 1601-1614. doi : 10.1111/j.1365-2966.2009.14548.x. arXiv : 0809.3437 [astro-ph].

[225] F. Feroz et al. “Importance Nested Sampling and the MultiNest Algorithm”. In : *Open Journal of Astrophysics* 2 (2019), p. 10. doi : 10.21105/astro.1112.3039. arXiv : 1112.3039 [astro-ph.IM].

[226] J. U. Lange. “NAUTILUS: boosting Bayesian importance nested sampling with deep learning”. In : *Mon. Not. Roy. Astron. Soc.* 525.2 (2023), p. 3181-3194. doi : 10.1093/mnras/stad2441. arXiv : 2306.16923 [astro-ph.IM].

[227] M. Karamanis et A. Lewis. “Zeus: a robust, Python-based implementation of the affine-invariant ensemble sampling algorithm”. In : *Mon. Not. Roy. Astron. Soc.* 502.3 (2021), p. 3823-3839. doi : 10.1093/mnras/staa4210. arXiv : 2009.14815 [astro-ph.IM].

[228] M. Karamanis et al. “pocoMC: A Python package for accelerated Bayesian inference in astronomy and cosmology”. In : *The Journal of Open Source Software* 7.79, 4634 (2022), p. 4634. doi : 10.21105/joss.04634. arXiv : 2207.05660 [astro-ph.IM].

[229] J. Elvin-Poole et al. “Dark Energy Survey Year 3 results: magnification modelling and impact on cosmological constraints from galaxy clustering and galaxy-galaxy lensing”. In : *Mon. Not. Roy. Astron. Soc.* 523.3 (août 2023), p. 3649-3670. doi : 10.1093/mnras/stad1594. arXiv : 2209.09782 [astro-ph.CO].

[230] C. Mahony, M. C. Fortuna, B. Joachimi et al. “Forecasting the potential of weak lensing magnification to enhance LSST large-scale structure analyses”. In : *Mon. Not. Roy. Astron. Soc* 513.1 (2022), p. 1210-1228. doi : 10.1093/mnras/stac872. arXiv : 2112.01545 [astro-ph.CO].

[231] Euclid Collaboration et al. “Euclid preparation: XIX. Impact of magnification on photometric galaxy clustering”. In : *Astronomy & Astrophysics* 662 (jan. 2022), A93. doi : 10.1051/0004-6361/202142419. url : https://doi.org/10.1051/0004-6361/202142419.

[232] G. Jelic-Cizmek et al. “On the importance of lensing for galaxy clustering in photometric and spectroscopic surveys”. In : *JCAP* 04 (2021), p. 055. doi : 10.1088/1475-7516/2021/04/055. arXiv : 2004.12981 [astro-ph.CO].

[233] G. Jelic-Cizmek et al. “Euclid Preparation. TBD. Impact of magnification on spectroscopic galaxy clustering”. In : *Astronomy & Astrophysics* (nov. 2023). arXiv : 2311.03168 [astro-ph.CO].

[234] V. Tansella et al. “COFFE: a code for the full-sky relativistic galaxy correlation function”. In : *JCAP* 10 (2018), p. 032. doi : 10.1088/1475-7516/2018/10/032. arXiv : 1806.11090 [astro-ph.CO].

[235] K. C. Chambers et al. “The Pan-STARRS1 Surveys”. In : *arXiv e-prints*, arXiv:1612.05560 (déc. 2016), arXiv:1612.05560. doi : 10.48550/arXiv.1612.05560. arXiv : 1612.05560 [astro-ph.IM].

[236] S. Farrens et al. “ShapePipe: A modular weak-lensing processing and analysis pipeline”. In : *Astronomy & Astrophysics* 664 (2022), A141. doi : 10.1051/0004-6361/202243970. arXiv : 2206.14689 [astro-ph.IM].

[237] A. Guinot et al. “ShapePipe: A new shape measurement pipeline and weak-lensing application to UNIONS/CFIS data”. In : *Astronomy & Astrophysics* 666 (2022), A162. doi : 10.1051/0004-6361/202141847. arXiv : 2204.04798 [astro-ph.CO].

[238] T. Liaudat et al. “Multi-CCD modelling of the point spread function”. In : *Astronomy & Astrophysics* 646, A27 (fév. 2021), A27. doi : 10.1051/0004-6361/202039584.

[239] E. Sheldon. *NGMIX: Gaussian mixture models for 2D images*. Astrophysics Source Code Library, record ascl:1508.008. Août 2015.

[240] M. Jarvis, G. Bernstein et B. Jain. “The skewness of the aperture mass statistic”. In : *Mon. Not. Roy. Astron. Soc.* 352.1 (juill. 2004), p. 338-352. doi : 10.1111/j.1365-2966.2004.07926.x. arXiv : astro-ph/0307393 [astro-ph].

[241] A. H. Wright et al. “Photometric redshift calibration with self-organising maps”. In : *Astronomy & Astrophysics* 637 (mai 2020), A100. issn : 1432-0746. doi : 10.1051/0004-6361/201936782. url : http://dx.doi.org/10.1051/0004-6361/201936782.

[242] T. Kohonen. “Self-organized formation of topologically correct feature maps”. In : *Biological Cybernetics* 43.1 (jan. 1982), p. 59-69. issn : 0340-1200. doi : 10.1007/BF00337288. url : http://dx.doi.org/10.1007/BF00337288.

[243] J. A. Newman et al. “The DEEP2 Galaxy Redshift Survey: Design, Observations, Data Reduction, and Redshifts”. In : *Astrophys. J. Supplement Series* 208.1, 5 (sept. 2013), p. 5. doi : 10.1088/0067-0049/208/1/5. arXiv : 1203.3192 [astro-ph.CO].

[244] O. Le Fèvre et al. “The VIMOS VLT Deep Survey final data release: a spectroscopic sample of 35 016 galaxies and AGN out to z ~6.7 selected with $17.5 \leq i_{AB} \leq 24.75$”. In : *Astronomy & Astrophysics* 559, A14 (nov. 2013), A14. doi : 10.1051/0004-6361/201322179. arXiv : 1307.6518 [astro-ph.CO].

[245] B. Garilli et al. “The VIMOS Public Extragalactic Survey (VIPERS). First Data Release of 57 204 spectroscopic measurements”. In : *Astronomy & Astrophysics* 562, A23 (fév. 2014), A23. doi : 10.1051/0004-6361/201322790. arXiv : 1310.1008 [astro-ph.CO].

[246] P. Fosalba et al. “The MICE grand challenge lightcone simulation - I. Dark matter clustering”. In : *Mon. Not. Roy. Astron. Soc.* 448.4 (avr. 2015), p. 2987-3000. doi : 10.1093/mnras/stv138. arXiv : 1312.1707 [astro-ph.CO].

[247] E. Krause et T. Eifler. “cosmolike - cosmological likelihood analyses for photometric galaxy surveys”. In : *Mon. Not. Roy. Astron. Soc.* 470.2 (sept. 2017), p. 2100-2112. doi : 10.1093/mnras/stx1261. arXiv : 1601.05779 [astro-ph.CO].

[248] X. Fang, T. Eifler et E. Krause. “2D-FFTLog: efficient computation of real-space covariance matrices for galaxy clustering and weak lensing”. In : *Mon. Not. Roy. Astron. Soc.* 497.3 (juin 2020), 2699–2714. issn : 1365-2966. doi : 10.1093/mnras/staa1726. url : http://dx.doi.org/10.1093/mnras/staa1726.

[249] D. H. Rudd, A. R. Zentner et A. V. Kravtsov. “Effects of Baryons and Dissipation on the Matter Power Spectrum”. In : *Astrophys. J.* 672.1 (jan. 2008), p. 19-32. doi : 10.1086/523836. arXiv : astro-ph/0703741 [astro-ph].

[250] G. Aricò et al. “DES Y3 cosmic shear down to small scales: Constraints on cosmology and baryons”. In : *Astronomy & Astrophysics* 678, A109 (oct. 2023), A109. doi : 10.1051/0004-6361/202346539. arXiv : 2303.05537 [astro-ph.CO].

[251] A. Schneider et al. “Baryonic effects for weak lensing. Part I. Power spectrum and covariance matrix”. In : *JCAP* 2020.04 (avr. 2020), 019–019. issn : 1475-7516. doi : 10.1088/1475-7516/2020/04/019. url : http://dx.doi.org/10.1088/1475-7516/2020/04/019.

[252] S. Casas et al. “Fitting and forecasting coupled dark energy in the non-linear regime”. In : *JCAP* 01 (2016), p. 045. doi : 10.1088/1475-7516/2016/01/045. arXiv : 1508.07208 [astro-ph.CO].

[253] W. Hu. “Power spectrum tomography with weak lensing”. In : *Astrophys. J. Lett.* 522 (1999), p. L21-L24. doi : 10.1086/312210. arXiv : astro-ph/9904153.

[254] M. Takada et B. Jain. “Cosmological parameters from lensing power spectrum and bispectrum tomography”. In : *Mon. Not. Roy. Astron. Soc.* 348 (2004), p. 897. doi : 10.1111/j.1365-2966.2004.07410.x. arXiv : astro-ph/0310125.

[255] A. Blanchard et al. “Euclid preparation: VII. Forecast validation for Euclid cosmological probes”. In : *Astronomy & Astrophysics* 642 (2020), A191. doi : 10.1051/0004-6361/202038071. arXiv : 1910.09273 [astro-ph.CO].

[256] DESI Collaboration et al. “DESI 2024 VI: Cosmological Constraints from the Measurements of Baryon Acoustic Oscillations”. In : *arXiv e-prints*, arXiv:2404.03002 (avr. 2024), arXiv:2404.03002. doi : 10.48550/arXiv.2404.03002. arXiv : 2404.03002 [astro-ph.CO].